amU
Aix Marseille Université

NNT : 2024AIXM0001

THÈSE DE DOCTORAT

Soutenue à Aix-Marseille Université
le 20 décembre 2024 par

Charles GRAZIANI

Aerosols stability in ground and microgravity conditions

Discipline
Sciences chimiques

École doctorale
ED - 250
Sciences chimiques de Marseille

Laboratoire
MADIREL
(UMR 7246)

Composition du jury

Thodoris KARAPANTSIOS Université Aristote de Thessalonique	Rapporteur
Khellil SEFIANE Universtié d'Edinbourg	Rapporteur
Irina MARTIN Aix Marseille Université	Présidente du jury
Cecile FIACHETTI CNES	Examinatrice
Mickaël ANTONI Aix Marseille Université	Directeur de thèse
Mathieu NESPOULOUS Aix Marseille Université	Co-encadrant de thèse
Guilhem FAVRE SAFM LOCALICSOL	Invité

Affidavit

I, undersigned, Charles Graziani, hereby declare that the work presented in this manuscript is my own work, carried out under the scientific supervision of Mickael Antoni and Mathieu Nespoulous, in accordance with the principles of honesty, integrity and responsibility inherent to the research mission. The research work and the writing of this manuscript have been carried out in compliance with both the French national charter for Research Integrity and AMU charter on the fight against plagiarism.

This work has not been submitted previously either in this country or in another country in the same or in a similar version to any other examination body.

Marseille, November 15th, 2024



This work is licensed under Creative Commons Attribution-NonCommercial-NoDerivatives 4.0 International Public License.

Liste des publications et/ou brevets réalisées dans le cadre du projet de thèse:

1. Charles Graziani; Mathieu Nespoulous; Renaud Denoyel; Stephan Fauve; Christian Chauveau; Luc Deike; Mickaël Antoni. A new experimental set-up for aerosol stability investigations in microgravity conditions. Comptes Rendus. Mécanique, Volume 351 (2023) no. S2, pp. 183-197. doi : 10.5802/crmeca.159. https://comptes-rendus.academie-sciences.fr/mecanique/articles/10.5802/crmeca.159/

Participation aux conférences et écoles d'été au cours de la période de thèse:

1. GDR MFA, Carry le Rouet,
   le 04/11/2021, portée nationale.

2. ELGRA, Lisbonne, communication orale,
   le 06/09/2022, portée internationale.

3. GDR MFA, Hyeres, communication orale,
   le 03/11/2022, portée nationale.

4. Seminar for Multiphase Flows, Stuttgart, communication orale,
   le 17/11/2022, portée internationale.

5. ICMF, Kobe, communication orale,
   le 06/04/2023, portée internationale.

6. GDR MFA, Hyeres, communication orale,
   le 25/10/2023, portée nationale.

7. ELGRA, Liverpool, communication orale,
   le 04/09/2024, portée internationale.

Résumé

La description de l'évolution des aérosols est un défi important en climatologie. Plusieurs questions restent à ce jour sans réponse, notamment en ce qui concerne la microphysique des nuages. Depuis 2018, le CNES soutient le développement d'un nouvel instrument permettant la production d'aérosols dans des conditions contrôlées. Ce travail de thèse présente la littérature sur l'évaporation de gouttelettes sessiles et en lévitation, les aérosols, la formation de nuages par nucléation, la description du dispositif instrumental ainsi que sos développements instrumentaux réalisés au cours de cette thèse et l'expérience menée dans des conditions de microgravité à l'aide de vols paraboliques et les différents résultats recueillis en vol parabolique et au sol. Il se concentre sur le problème de la répétabilité expérimentale et sur la dynamique d'évaporation des gouttelettes à différentes humidités relatives.

Les aérosols étudiés sont comparables à des nuages et sont composés de gouttelettes d'eau micrométriques (d'un diamètre initial de 5 μm) évoluant dans l'air. Ils sont étudiés par microtomographie optique loin des bords de la cellule d'expérimentation. Pendant la phase de microgravité, les gouttelettes se déplacent très peu, ce qui se traduit par une grande cohérence entre les images tomographiques successives. Une reconstruction en 3D est donc possible, ce qui permet de suivre les gouttelettes dans le temps. Cela permet des investigations basées sur le nombre de gouttelettes et leur taille dans le volume sondé.

Les expériences ont été menées avec une humidité relative (H) variant de 65% à 100%. Un point froid à température contrôlée a été développé et utilisé pour contrôler l'humidité. Lorsque les conditions n'étaient pas saturées, les gouttelettes s'évaporent. La reproductibilité de ce processus a été étudiée lors des campagnes de vols paraboliques, réalisées en mars et octobre 2023. Enfin, un spectroscope infrarouge à transformée de Fourier a été ajouté au dispositif. Il permet d'effectuer des analyses chimiques à l'intérieur de la chambre expérimentale. L'étude du mélange binaire eau/HFE7100 a été réalisée lors de la campagne de vols paraboliques d'octobre 2024.

Mots clés : aérosols, évaporation, micro-gravité, vols paraboliques, gouttelettes d'eau, lévitation.

Abstract

Describing the evolution of aerosols is an important challenge in climatology. Several questions remain unanswered so far, particularly concerning cloud microphysics. Since 2018, CNES has supported the development of a new instrument that enables aerosol production under controlled conditions. This work presents: the literature around evaporation of sessile and levitating single droplets, aerosol, the formation of clouds via nucleation, the set-up and the instrumental development done during this thesis and the experiment conducted in microgravity conditions using parabolic flights and the different results gathered in parabolic flight and on the ground. It focuses on the problem of experimental repeatability and on the droplet evaporation dynamics at different relative humidities.

Aerosols under consideration are comparable to clouds and are composed of micrometric water droplets (with an initial diameter of $5\,\mu$m) evolving in air. They are investigated with optical microtomography far from the edges of the experimental chamber. During the microgravity phase, droplets move very little, resulting in a high degree of coherence between successive tomographic images. A 3D reconstruction is therefore possible, enabling the droplets to be tracked over time. This allows investigations based on the number of droplets and their sizes in the probed volume.

The experiments were conducted with varying relative humidity (H) ranging from 65% to 100%. A temperature-controlled cold point was developed and used to monitor the humidity. When the conditions were unsaturated, the droplets evaporated. The reproducibility of this process was studied during the parabolic flight campaigns, performed in March and October 2023. Lastly, a Fourier transform infrared spectroscope was added to the set-up. It allows for the investigation of chemical analysis inside the experimental chamber. The investigation of the binary mixture water/HFE-7100 was studied during the parabolic flight campaign of October 2024.

Key words: aerosols, evaporation, microgravity, parabolic flights, water droplets, levitation.

Remerciements

Voici donc venu le moment d'écrire cette toute dernière section de mon manuscrit de doctorat. Au terme de ce travail de thèse, je tiens à exprimer ma profonde gratitude envers toutes les personnes qui ont contribué, de près ou de loin, à sa réalisation.

Je remercie tout particulièrement mon directeur de thèse Mickaël Antoni, pour son encadrement, ses conseils avisés, et sa disponibilité tout au long de ces années. Je remercie mon codirecteur de thèse Mathieu Nespoulous pour son écoute et sa bienveillance. Vos expertises et vos soutiens ont été des piliers essentiels à l'accomplissement de ce projet.

Je souhaite également remercier les membres de mon jury : particulièrement mes rapporteurs Thodoris Karapantsios et Khellil Sefiane ainsi que mes examinatrices Irina Martin et Cecile Fiachetti, pour avoir accepté de juger ce travail.

Mes remerciements vont aussi au CNES et à la région Sud pour le financement de cette thèse. Je tiens à remercier aussi l'équipe de Novespace, en particulier les responsables de l'expérience Alexis Jolion et Thomas Villatte, pour m'avoir offert un cadre de recherche exceptionnel pendant les quatre campagnes de vol parabolique.

Un grand merci à mes collègues, amis du laboratoire ainsi que les doctorants que j'ai pu rencontrer en congrès, pour les échanges scientifiques fructueux, les moments de camaraderie et le soutien moral durant les moments difficiles.

Enfin, envers ma famille, mes proches et ma petite amie Sandra, je ne saurais trouver les mots pour exprimer ma reconnaissance. Votre soutien infaillible et votre présence à mes côtés, dans les moments de doute comme dans les instants de joie, ont été essentiels tout au long de ce long voyage.

Merci à tous.

List of symbols

Value	Meaning	Unit
A	Fitting constant	m^{-3}
m	Droplet mass	kg
t	Time	s
$t_{cooling}$	Time to cool down the temperature	s
$t_{warming}$	Time to return to initial temperature after expansion	s
t_{evap}	Lifetime of the aerosol	s
t_{th}	Diffusion characteristic time	s
$t_{ev,N}$	Half height time of the hyperbolic tangent	s
$t_{ev,R}$	Time for square diameter trend break	s
k_{exp}	Experimental factor to link t_{evap} to the humidity	s
k_{th}	Theoretical factor to link t_{evap} to the humidity	s
$k_{ev,N}$	Theoretical factor to link t_{evap} to the humidity	s
τ	Characteristic diffusion time	s
$\tau_{cooling}$	Characteristic thermal time	s
τ_h	Characteristic convective time	s
$\tau_{ev,N}$	Characteristic evaporative time of droplet number density	s
r	Position (cylindrical or spherical coordinates), radius	m
R	Droplet radius	m
R_0	Initial droplet radius	m
R_{EC}	Interior radius of the EC	m
d_{th}	Diffusion characteristic distance	m
R_{corr}	Correlation coefficient	
g	Gravity	$\mathrm{m.s}^{-2}$
N	Droplet number density	m^{-3}
ρ	Density	$\mathrm{kg.m}^{-3}$
ρ_{liquid}	Liquid density	$\mathrm{kg.m}^{-3}$
ρ_{water}	Liquid water density	$\mathrm{kg.m}^{-3}$
D_{va}	Diffusion coefficient of the vapour into air	$\mathrm{m}^2\mathrm{.s}^{-1}$
c	Concentration of a vapour	$\mathrm{kg.m}^{-3}$
$\mathcal{R}$	Ideal gas constant	$\mathrm{J.kg}^{-1}\mathrm{.mol}^{-1}$
$\mathbf{F}_{drag}$	Drag force	$\mathrm{kg.m.s}^{-2}$
$\mathbf{v}$	Droplet velocity vector	$\mathrm{m.s}^{-1}$
v_{term}	Droplet terminal velocity	$\mathrm{m.s}^{-1}$
$V_{1,2}$	Volumes of the EC and ECC with dead volumes	m^3
V_b	Balls Volume	m^3

Value	Meaning	Unit
h	Convective exchange heat coefficient	$\mathrm{W.m^{-2}.K^{-1}}$
h_0	Initial convective exchange heat coefficient	$\mathrm{W.m^{-2}.K^{-1}}$
h_f	Final convective exchange heat coefficient	$\mathrm{W.m^{-2}.K^{-1}}$
$h_{cooling}$	Convective exchange heat coefficient during cooling	$\mathrm{W.m^{-2}.K^{-1}}$
λ_{cond}	Thermal conductive coefficient	$\mathrm{W.m^{-1}.K^{-1}}$
λ_{eff}	Thermal conductive effective coefficient	$\mathrm{W.m^{-1}.K^{-1}}$
Φ_{conv}	Thermal heat flux	$\mathrm{W.m^{-2}}$
a_m	Moist air thermal diffusivity	$\mathrm{m^2.s^{-1}}$
L	Latent heat	$\mathrm{kJ.kg^{-1}}$
H	Humidity	
β_{avg}	Humidity corrective term for the average	
$\beta_{ev,N}$	Humidity corrective term for each box	
S	Saturation ratio	
f	Literature droplet evaporation rate	$\mathrm{kg.s^{-1}}$
s	Compensation mass flow	$\mathrm{kg.s^{-1}}$
ν_{air}	Air kinematic viscosity	$\mathrm{m^2.s^{-1}}$
μ_{air}	Air dynamic viscosity	$\mathrm{m^2.s^{-1}}$
μ_{water}	Water dynamic viscosity	$\mathrm{m^2.s^{-1}}$
$C_{p_{air}}$	Air heat capacity	$\mathrm{J.kg^{-1}.K^{-1}}$
M	Water molar mass	$\mathrm{kg.mol^{-1}}$
f_{ev}	Evaporation square diameter fitting function	$\mu\mathrm{m}^2$
T	Temperature	K
ΔT	Temperature drop during the expansion	K
$T_{min,init}$	Temperature minimal or initial in the EC	K
T_{EC}	Temperature in the EC	K
T_{ECC}	Temperature in the ECC	K
$T_{peltiers}$	Temperature of the Peltiers	K
T_{CP}	Temperature of the Cold Point	K
$dT_{ev,N}$	Temperature correction for delayed evaporation	K
$dT_{drop,th}$	Theoretical temperature drop for single droplet	K
P	Pressure	Pa
P_0	Atmospheric Pressure	Pa
$P_{1,b}^{comp}$	Pressure in the EC with a ball after the compression	Pa
P_v	Partial pressure of the vapour	Pa
P_v^{sat}	Saturation vapour pressure	Pa
P_v^{∞}	Vapour pressure far from the droplet	Pa

List of abbreviation

Acronym	**Meaning**
$CNES$	Centre national d'études spatiales
CO_2	Carbon Dioxide
ERF	Effective Radiative Forcing
LOS	Line of Sight
WMO	World Meteorological Organization
$IPCC$	Intergovernmental Panel on Climate Change
GHG	Greenhouse gases
ISS	International Space Station
CR	Constant Contact Radius
CA	Constant Contact Angle
SS	Stick-Slide
EC	Experimental Chamber
ECC	Expansion and Compression Chamber
EV	Electrovalves
IR	Infra Red
$FTIRS$	Fourier Transform Infra Red Spectroscope
$HFE-7100$	Perfluorobutyl Ether
PIV	Particle Image Velocimetry
VK	von Kármán

Contents

List of symbols 7
List of abbreviation 9

Introduction **13**

1 State of the art **20**
1.1 About evaporation in droplets 20
1.1.1 Sessile droplets 21
1.1.2 Levitating droplets 24
1.2 Aerosol Physics 38
1.2.1 Aerosol generation 39
1.2.2 Evaporation 47
1.2.3 Droplets evolution in von Kármán swirling flow 49
1.3 Cloud Microphysics 51
1.3.1 Nucleation 51
1.3.2 Mixed clouds and Wegener Bergeron Findeison effect . 61
1.3.3 Flows and turbulence in clouds 66

2 Description and qualification of the AEROSOL facility **70**
2.1 AEROSOL project 70
2.1.1 Microgravity relevance 70
2.1.2 Methods to access microgravity 71
2.2 General presentation 76
2.2.1 Experimentation Chamber 78
2.2.2 Pneumatic Circuit 78
2.2.3 Engines and magnetic transmission 79
2.3 Optical system and data acquisition 81
2.3.1 Microscope 82
2.3.2 Translation stage 84
2.3.3 Acquisition system 86
2.4 Imaging 86
2.4.1 Fortran image processing 87

2.4.2 Python image processing . . . 91
2.4.3 Comparison of the two methods . . . 93
2.5 Infrared source and Fourier Transform Infrared spectroscopy implementation . . . 94
2.5.1 Characteristics of the IR sources . . . 94
2.5.2 Set-up . . . 95
2.5.3 FTIRS set-up . . . 97
2.5.4 FTIRS calibration . . . 99
2.6 Measurement devices . . . 101
2.6.1 Pressure . . . 101
2.6.2 Relative Humidity . . . 101
2.6.3 Temperature . . . 103
2.7 Volumes determination . . . 103
2.8 Relative Humidity Regulation . . . 104
2.8.1 Humidity regulation protocol and humidity stabilisation 111
2.8.2 Consequences of a lack of thermal regulation . . . 112
2.9 Secondary vapour injection . . . 115
2.10 Ground Qualification Tests . . . 116
2.10.1 Aerosol production . . . 116
2.10.2 Impact of relative humidity on aerosol formation . . . 117

3 Parabolic Flights investigation 123
3.1 Course of a campaign . . . 123
3.2 Humidity evolution . . . 125
3.3 Initial flow and relaxation time . . . 126
3.4 Reproducibility of experiments . . . 127
3.5 Evaporation of droplets . . . 129
3.5.1 Global evolution . . . 129
3.5.2 Numerical resolution: Temperature evolution . . . 131
3.6 Local evaporation . . . 134
3.6.1 Local evolution of the droplet number . . . 135
3.7 Vapour diffusion . . . 142
3.7.1 Evaporation of a single drop in our experimental conditions . . . 142
3.7.2 Impact of the environment . . . 143
3.7.3 Equation adaptation . . . 144
3.7.4 Equation closure . . . 146
3.8 Radius evolution . . . 149
3.9 Infrared spectroscopy of water aerosols with HFE-7100 vapour 153
3.9.1 Evolution of the spectrum in the absence of HFE-7100 155
3.9.2 Evolution of the CO_2 peak . . . 157

3.9.3 Evolution of the spectrum in the presence of HFE-7100 159

Conclusion **163**

A NI MAX **165**
A.1 Control the leaks 166

B IOTool **167**
B.1 How to load and start a sequence 167
B.2 How to modify a sequence 168
B.2.1 Modify targeted pressure 168
B.2.2 Modify the maintaining pressure time 169
B.2.3 Modify the tomography length in time 169
B.2.4 Modify the speed and engines start 169
B.3 How to plug the COM port correctly 169
B.4 How to deal with errors 171
B.5 How to record with the camera live 171

C LAIRD **173**

D How to regulate the humidity inside the EC **174**
D.1 With IOTool 174
D.2 Manually controlling the humidity 174

E Operating the FTIRS **176**
E.1 Baseline 177
E.2 Prepare a series of measure 177
E.3 Exploit Spectrum values 178
E.4 Modify the parameters of the scan 178

F Impact of the engines on the temperature sensor **180**

G Diameter evolution during evaporation experiments **183**

H Scaled Nucleation Theory **185**

I Record of the different acceleration during parabolic flights **186**

J Record of Pressure, Temperature and Humidity during parabolic flights **190**

K Code to solve the heat equation **192**

Introduction

Aerosols are dispersed systems in which liquid and/or solid particles evolve in a continuous gas phase. They are naturally subject to the influence of gravity, which determines the settling speed of the particles they contain. Aerosols have many applications in the pharmaceutical and cosmetic industries (inhalers, sprays [1–3]), in metallurgy (spray drying [4–6]) and in agriculture (pesticides [7–9]). From an academic point of view, they are the subject of intense research activity. The description of their evolution is, for example, a major issue in climatology. This thesis will focus on the new instrument developed in the MADIREL laboratory and financed by CNES to produce water aerosols in controlled thermodynamic conditions. The objective of the project named DECLIC/CNES is to develop an experiment for the ISS to investigate cloud microphysics for long duration. This thesis is the first phase of the project. The aerosol evolution is captured via optical tomography microscopy. To cope with the draining action of gravity, experiments are done using microgravity via parabolic flights. Due to climate change, clouds will have a growing incidence on the evolution of the climate. This study is done to understand on a microscopic level the cloud microphysics and will articulate over three main chapters: In the first chapter, the state of the art. It will start with the presentation of the evaporation physics of a single droplet on a substrate or levitating. It will then go on with the physics of the aerosols through a description from their creation to their evaporation and their evolution in a von Kármán (VK) swirling flow. The last part of this chapter will be the description of the cloud microphysics. The second chapter is dedicated to the description of the aerosol facility, the different devices and sensors, the optical system, the imaging technique, the humidity regulation, the installation of a Fourier transform infrared spectrometer and the ground qualification tests. The third chapter is about the results obtained during the parabolic flight campaigns.

Context: climate change

The climate is usually defined as the average weather, or more rigorously as the statistical description in terms of the mean and variability of relevant quantities over a period of time ranging from months to thousands or millions of years. The classical period for averaging these variables is 30 years, as defined by the World Meteorological Organization (WMO). The relevant quantities are often surface variables such as temperature, precipitation and wind [10]. As mentioned previously, the idea would be to study the cloud microphysics and to understand how the droplets interact with each others on a microscopic scale. To do so, it is important to understand the context in which clouds evolve in nature. Understanding the context would mean understanding the climate or at least the different trends in which clouds evolve. We will be focusing on the Intergovernmental panel on climate change (IPCC) report from 2021 and 2023. The first focus is the overall impact of the carbon dioxide (CO_2) emissions on the evolution of climate. It is key to understand why the CO_2 consumption is so high in most developed countries. Well, the first and second industrial revolutions could be summarized by the mastery of one thing, the fossil fuel (oil, coal and gas) combustion for industrial purposes. Those revolutions brought with them the mechanization of many manual works, leading to a higher productivity in the primary and secondary sectors (agriculture and heavy manufacturing especially) and therefore the possibility for the emergence of the tertiary sector that dominates the workforce today in western countries. According to the data gathered by the World Bank in 2021, 80% to 90% in the western country population works in the service sectors [11]. Figure 1 shows the percentage of the work force in the agriculture as a function of the tonnes oil equivalent per capita. The more a society uses machines and engines, the more this society consumes fuel or oil. As a result fewer people are working in the agriculture as they are replaced by more efficient machines, as the figure 1 demonstrates.

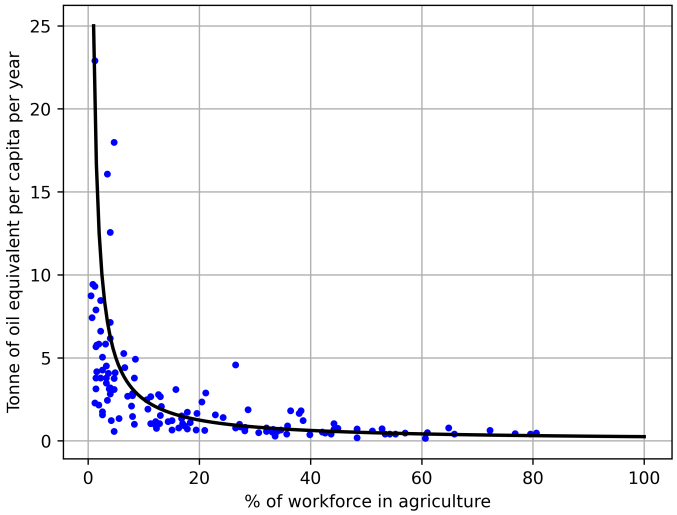

Figure 1: Consumed tonnes of oil equivalent per capita per year as a function of the percentage of the work force in the agriculture each point represent a country, the black line is added to guide the eye. Data gathered from the world bank [11].

This kind of society comes at a cost, the high use of energy per capita. This energy, mostly coming from fossil fuel, is emitting CO_2 into the atmosphere via its combustion. This CO_2 is absorbed by three possible ways. The first way to absorb CO_2 is via plants that will use the CO_2 for photosynthesis, the second is the acidification of the ocean via a dissolution of the CO_2 inside the ocean. Those two effects may take a significant part for low CO_2 emission. However, their ability to absorb the CO_2 is limited and if the emission of CO_2 is very high (scenarios SSP3-7.0 and SSP5-8.5, see figure 2), the atmosphere will have to take the remaining part. In these two scenarios, the limitation of the first two mechanisms is deeply felt as the atmosphere has to directly absorb the difference in terms of CO_2 emissions (see figure 2).

This CO_2 adds up over time and contributes more and more to the green house effect. It modifies the transmission spectrum from the earth to space by enlarging the absorption band of the atmosphere. This enlargement and overall impact over the temperature could be computed by using the code MODTRAN [13] which is a software that computes line-of-sight (LOS) atmospheric spectral transmittances and radiances over the ultraviolet through long wavelength infrared spectral regime (10 - 50,000 cm^{-1}). MODTRAN solves the radiative transfer equation including the effects of molecular and particulate absorption/emission and scattering, surface reflections and emission, solar/lunar illumination, and spherical refraction. As the MODTRAN code suggests, doubling the CO_2 concentration (from 400 ppm to 800 ppm)

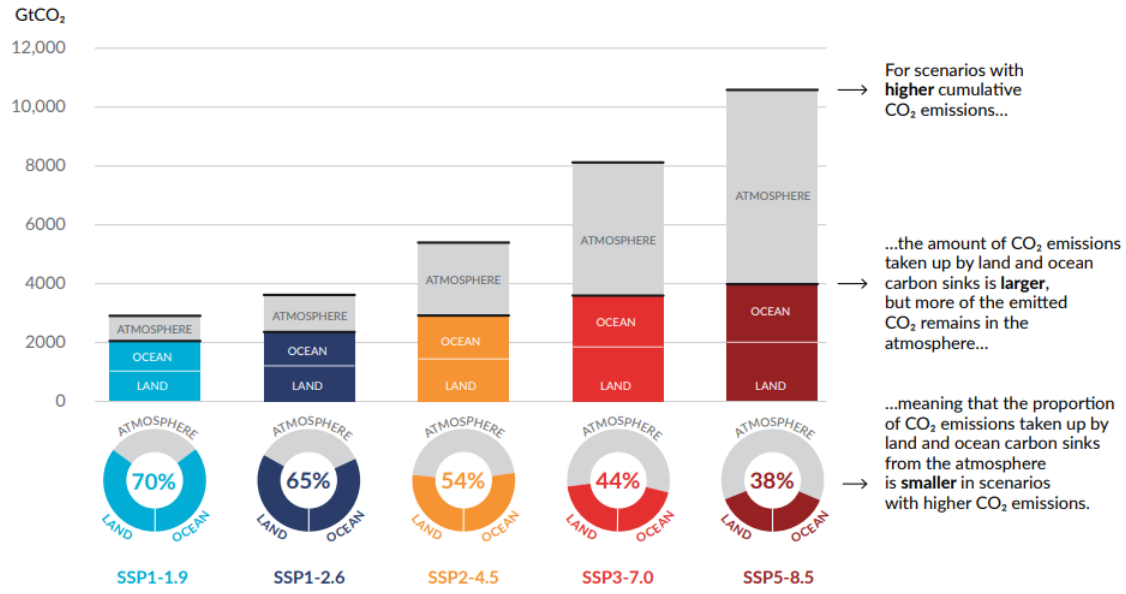

Figure 2: Total cumulative CO_2 emissions taken up by land and ocean (colours) and remaining in the atmosphere (grey) under the five illustrative scenarios from 1850 to 2100. Figure copied from ref [12].

would result in a decrease of 3.01 $W.m^{-2}$ in the heat loss going out of the earth towards space (from 289.6 $W.m^{-2}$ to 286.588 $W.m^{-2}$). This effect is known as effective radiative forcing (ERF). To keep the heat loss towards space the same, the ground would have to heat up by 0.715 K which is already high considering that when CO_2 is released, other green-house gases are also emitted like methane, nitrous oxide or sulfur dioxide that also have a greenhouse effect. Anthropogenic emissions of greenhouse gases and their precursors contributed to an ERF of 3.84 [3.46 to 4.22] $W.m^{-2}$ over the industrial era (1750–2019). Most of this total ERF (3.03 to 3.61 $W.m^{-2}$) comes from the well-mixed greenhouse gases, with changes in ozone and stratospheric water vapour (from methane oxidation) contributing the remainder. The ERF of greenhouse gases is composed of 1.90 to 2.41 $W.m^{-2}$ from carbon dioxide, 0.43 to 0.65 $W.m^{-2}$ from methane, 0.33 to 0.49 $W.m^{-2}$ from halogenated species, and 0.18 to 0.24 $W.m^{-2}$ from nitrous oxide. The ERF for ozone is 0.24 to 0.71 $W.m^{-2}$ [12]. The IPCC, has then developed scenarios for the evolution of the different pollutant, they are presented in the figure 3 from the 2021 report [12].

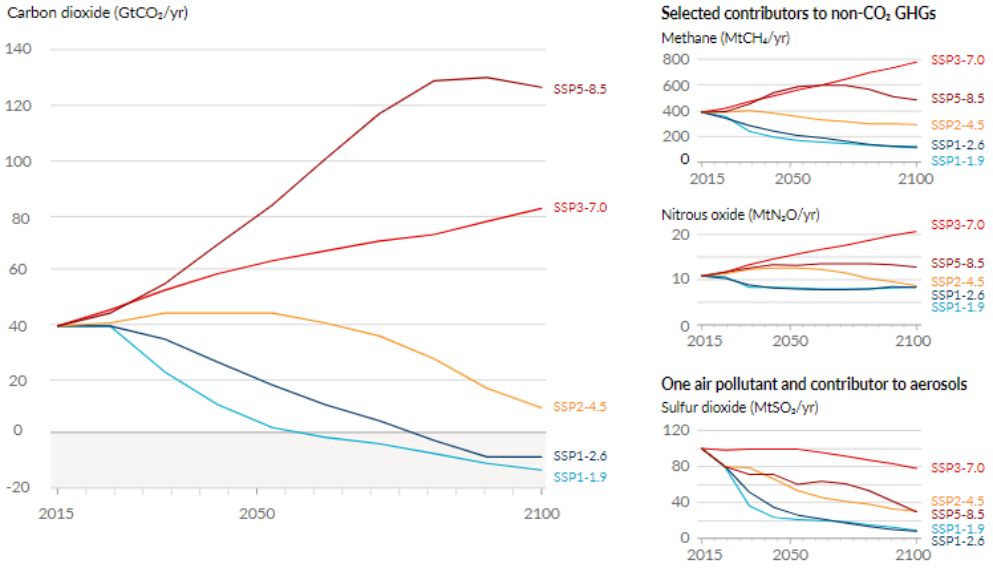

Figure 3: Future annual emissions of CO_2 (left) and of a subset of key non-CO_2 drivers (right), across five illustrative scenarios. These projections (2021–2100) of greenhouse gases (GHG) are shown for very low (SSP1-1.9), low (SSP1-2.6), intermediate (SSP2-4.5), high (SSP3-7.0) and very high (SSP5-8.5) GHG emissions scenarios. Figure copied from ref [12].

This is linked to a raise in terms of temperature described in the figure 4. Each future emission of greenhouse gases, will affect the temperature over the long term as suggested by the chart. The five future scenarios are the ones described in figure 3. Each scenario has an estimation of the temperature evolution for the near term (2021-2040), mid-term (2041-2060) and long term (2081-2100) and a very likely range. The first scenario (SSP1-1.9) would likely entails an increase of $1.5 \pm 0.25\,°C$ in the near term, $1.6 \pm 0.4\,°C$, in the mid term and $1.4 \pm 0.4\,°C$ in the long term. The second scenario (SSP1-2.6) would likely entails an increase of $1.5 \pm 0.25\,°C$ in the near term, $1.7 \pm 0.45\,°C$, in the mid term and $1.8 \pm 0.5\,°C$ in the long term. The third scenario (SSP2-4.5) would likely entails an increase of $1.5 \pm 0.2\,°C$ in the near term, $2.0 \pm 0.45\,°C$, in the mid term and $2.7 \pm 0.6\,°C$ in the long term. The fourth scenario (SSP3-7.0) would likely entails an increase of $1.5 \pm 0.3\,°C$ in the near term, $2.1 \pm 0.5\,°C$, in the mid term and $3.6 \pm 0.9\,°C$ in the long term. The last scenario (SSP5-8.5) would likely entails an increase of $1.6 \pm 0.3\,°C$ in the near term, $2.4 \pm 0.6\,°C$, in the mid term and $4.4 \pm 1.1\,°C$ in the long term.

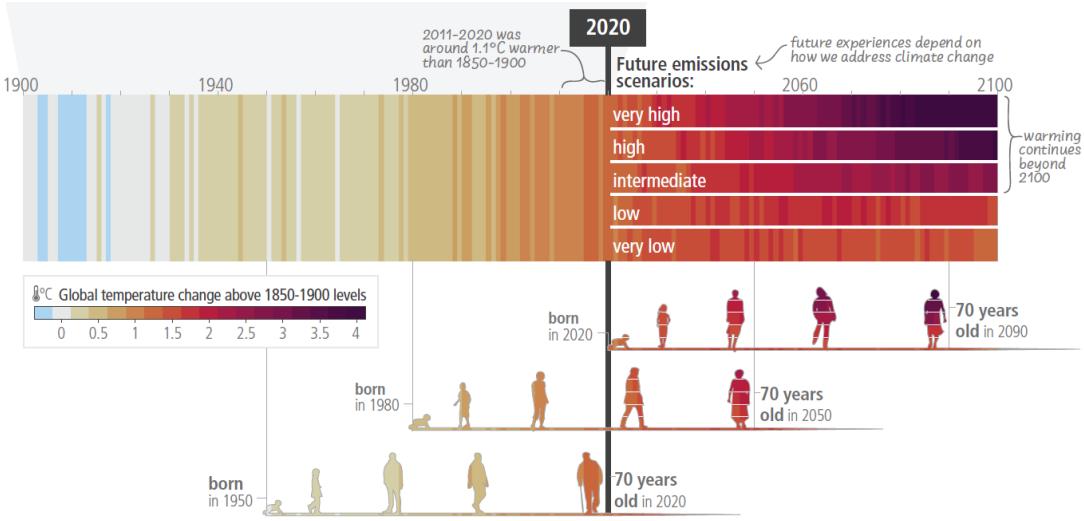

Figure 4: Observed (1900–2020) and projected (2021–2100) changes in global surface temperature (relative to 1850-1900), which are linked to change in climate conditions and impacts, illustrate how the climate has already changed and will change along the lifespan of three representative generations (born in 1950, 1980 and 2020). Changes in annual global surface temperatures are presented as 'climate stripes', with future projections showing the human-caused long-term trends and continuing modulation by natural variability (represented here using observed levels of past natural variability). Colours on the generational icons correspond to the global surface temperature stripes for each year, with segments on future icons differentiating possible future experiences. Figure copied from ref [10].

This raise on temperature implies changes in the climate feedback depending on its sensitivity and the change in temperature occurring (see figure 4). As the temperature is raising, so does the water vapour saturation pressure which will increase the water quantity evaporating from the ocean into the air. This water quantity will gain altitude with upward movement, and tend to nucleate and form clouds. This will lead to a higher impact of the clouds and aerosols on the evolution of climate. The figure 5 presents the impact of clouds on the climate and the role that they play in the thermal balance of the earth.

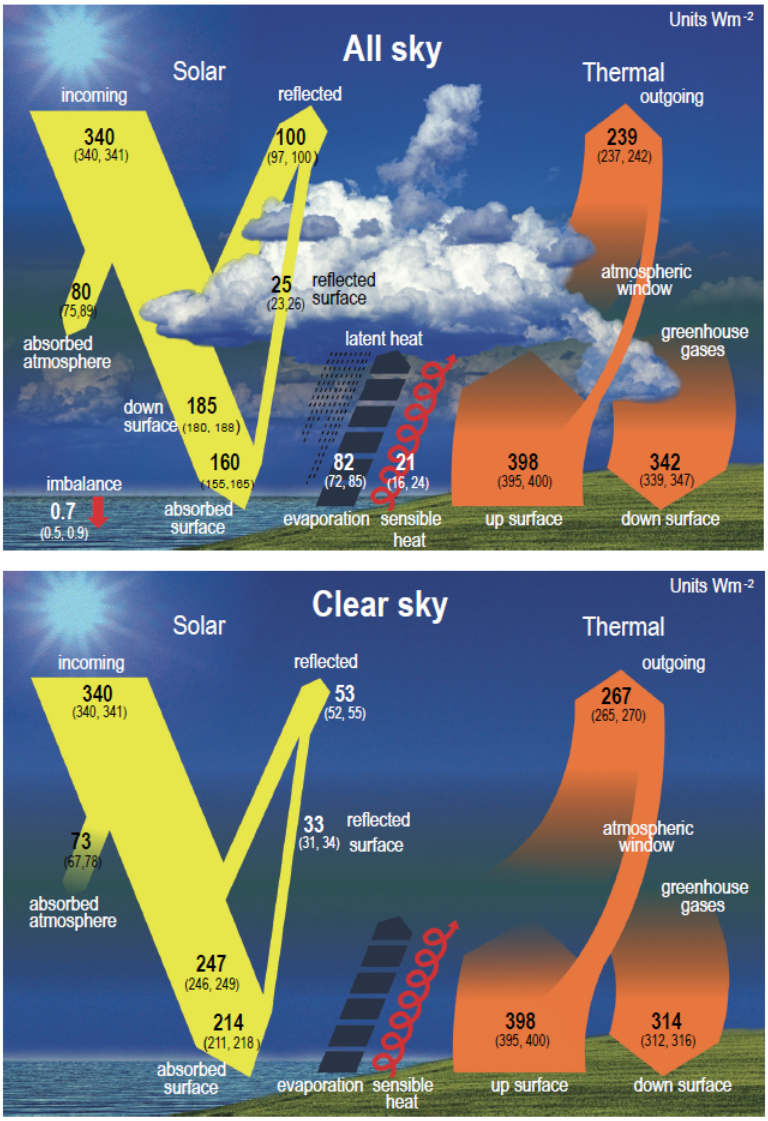

Figure 5: Global mean energy budget (W.m^{-2}), and its equivalent without consideration of clouds effects. The values in parenthesis are the confidence range. Figure copied from ref [14].

The global impact of those clouds is understood. However, some uncertainties remains. The hypothesis we make is that understanding the mechanisms of clouds at the droplet scale will help the understanding of much broader phenomenons.

Chapter 1

State of the art

The study of aerosol dynamics, particularly the evaporation of liquid droplets, has gained significant attention in recent decades due to its broad implications in environmental sciences, atmospheric chemistry, and industrial processes. Aerosols are playing a crucial role in climate modelling, air quality assessments, and the transport of pollutants. Evaporation in aerosols specifically influences particle size distribution, chemical composition, and their interaction with the surrounding environment, making it a critical phenomenon to understand in multiple contexts.

Recent studies have focused on the role of environmental factors, such as temperature, humidity, and gas-phase composition. Experimentally, the literature studies have been focussing on the evaporation dynamics of single droplets or large clouds. Simultaneously, investigations into multi-component droplets and their non-ideal behaviour have uncovered new complexities in the evaporating process. Despite these advancements, several challenges remain unresolved, particularly in the accurate modelling of aerosols evaporation at a droplet level.

This chapter will first provide an overview of the key theoretical models of droplet evaporation either sessile or levitating. It will then present the way aerosol could be created, the physical behaviour of aerosol when evaporating or under a von Kármán flow. Lastly, this work will present the cloud mechanisms occurring in nature and responsible of the nucleation of liquid or ice droplets.

1.1 About evaporation in droplets

Droplet evaporation is crucial for a wide range of applications such as spray drying, spray cooling, fire suppression, combustion, crystallization, painting,

medical aerosols or prevention of aircraft icing. Many papers highlight the need for a simple analytical model that quantitatively describes multiple droplet evaporation [10, 12]. Indeed, even the evaporation of a suspended drop involves complex phenomena: phase change coupled with heat and mass transfers. The heat is transferred by conduction and convection between the surrounding gas and the drop interface, while the vapour is transported away from the interface by diffusion and convection. The following sections will present the evaporation of a single droplet either sessile or levitating in ground and in microgravity conditions.

1.1.1 Sessile droplets

Although sessile drops have simple geometries, the physics involved in their evaporation process is complex owing to their numerous intricate interactions and their fluid nature. For example, a droplet could be made of complex or pure fluids, colloids or biological matter [15]. This droplet could be affected or not via an electric field [16], gravity or a microgravity environment [17]. It could be placed on a heated substrate that will have special wettability properties [18–21]. This substrate could be rough, soft or even soluble. These parameters induce a complex physics that occurs in the evaporation of a sessile droplet. On this part, the focus will be put on the evaporation of a water droplet without heating the substrate for an easy start. The lifetime of an evaporating droplet depends on the manner in which it evaporates. As Picknett and Bexon described in their pioneering work in 1977 [22], there are two extreme modes of droplet evaporation, namely the 'constant contact radius' (CR) mode, in which the contact angle $\theta = \theta(t)$ $(0 < \theta < \pi)$ decreases with time t but the contact radius $R = R_0$ remains constant, and the 'constant contact angle' (CA) mode, in which the contact radius $R = R(t)$ decreases but the contact angle $\theta = \theta_0$ remains constant; here R_0 and θ_0 denote the initial values of R and θ, respectively.
However, as Picknett and Bexon [22] also described (and as Bourgès-Monnier and Shanahan [24] and many other authors have subsequently confirmed), in practice a droplet usually evaporates in a so called 'stick–slide' (SS) mode, made up of one or more of two phases, the first phase is a CR evaporation phase where the radius is constant and after the critical contact angle 'transition contact angle' θ^* is reached, a CA phase starts as shown in figure 1.1. Various SS modes have been observed experimentally, but perhaps the most commonly reported is the one (referred to as the 'combined pinned–receding mode' by Nguyen and Nguyen [23]) where there is an initial stick phase in which the droplet evaporates in a CR phase, followed by a first slide phase in which the droplet evaporates in a CA phase, followed in turn by a second

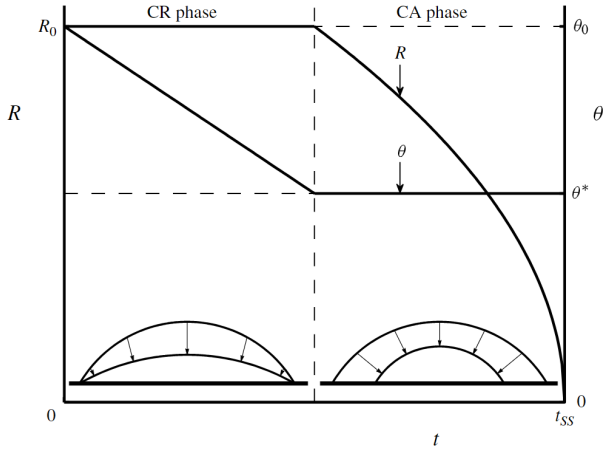

Figure 1.1: Evolution of the droplet radius R through the two phases in the 'stick–slide' evaporation mode, first the contact angle decrease (CR phase) to its critical value and then the radius of the drop decreases (CA phase). Figure copied from ref [23].

slide phase in which both R and θ vary simultaneously. In practice, the second slide phase is often of relatively short duration compared with the stick and the first slide phases, in which case it can be neglected when determining the lifetime of the droplet (as discussed by, for example, Nguyen and Nguyen [23], Sefiane [18], Stauber [25–27], Dash and Garimella [28], Hu and Wu [29], Debuisson [30], Wilson at al. [31]). The different mathematical models developed in those evaporations situation (CA or CR only or SS) leads to an evaporation time proportional to $\frac{\rho_{liquid} R_0^2}{D_{va}(c_{sat}-c_\infty)}$ where ρ_{liquid} is the liquid density, R_0 is the initial radius of the droplet, D_{va} is the diffusion coefficient of the liquid into the surrounding gas and c_{sat} the concentration of its vapour at the droplet interface, c_∞ the concentration away from the droplet [32].

Sessile droplet in microgravity

In microgravity, the evaporation rate for a heated-substrate evaporation experiment is approximately divided by two [33] (see figure 1.2). This is mostly due to the absence of natural convection in the vapour phase that develops due to buoyant forces, forces that are absent in microgravity. The purely diffusive-controlled evaporation model does not take into account the natural convection, it naturally underestimates the experimental evaporation rate. The natural convection increases the mass transfer in the vapour phase, by modifying the vapour field around the droplet via the creation of a flow motion around the droplet. This renews the gas around the droplet diminishing

the vapour quantity around the droplet. This naturally leads to an increase in the evaporation rate as the evaporation is controlled by the difference in the vapour concentration at the interface and in the far field and is generally controlled more by the mass transport in the vapour phase [17].

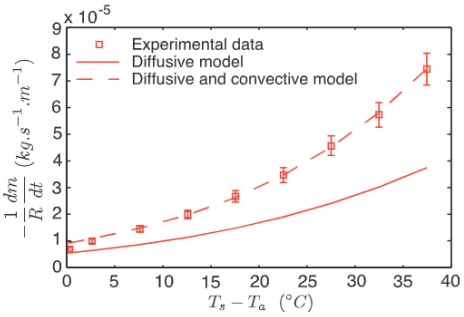

(a) Terrestrial gravity conditions, ($a = 1.36 \cdot 10^{-9}\,\mathrm{kgs^{-1}m^{-1}K^{-1}}$ and $b = 2.62$)

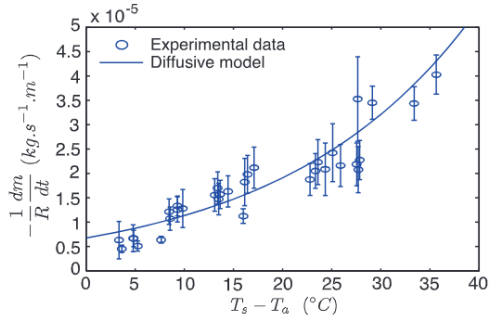

(b) Micro-gravity conditions (μg), ($a = 8.75 \cdot 10^{-9}\,\mathrm{kgs^{-1}m^{-1}K^{-1}}$ and $b = 2.061$)

Figure 1.2: Evaporation rate for an ethanol droplet divided by its radius as a function of the difference between the substrate temperature and the surrounding air temperature. The two fitting curves are a power law ($y = ax^b$), the fitting parameters (a and b) are indicated in their respective graphs. Figure copied from ref [17].

This leads to a mass flux with two contributions, the standard one that depends in particular on the radius, the diffusion coefficient and the temperature of the substrate. And the second term that will depend of gravity. With the help of the experimental data, the evaporation rate could be estimated as eq 1.1 suggests:

$$E = \frac{4RD_{va}MP_v}{\mathcal{R}T_s}\left(1 + 0.333\left[\frac{P_vMg}{(P_a - P_v)M_a\nu_{air}^2}R^3\right]^{0.186}\right) \tag{1.1}$$

where R is the droplet radius, D_{va} is the vapour diffusion coefficient into the air, M is the molar mass of the vapour, P_v is the partial vapour pressure (supposed to be at saturation), T_s is the substrate temperature, M_a is the molar mass of the air, P_a is the air pressure, g is the gravity and ν_{air} is the air kinematic viscosity. With a similar approach on heptane, cyclohexane heptane and 3-methylpentane, P.L. Kelly-Zion [34] arrived to a similar conclusion with the equation 1.2:

$$E = \frac{4RD_{va}MP_v z}{\mathcal{R}T_s}\left(1 + 0.310\left[\frac{P_v Mg}{(P_a - P_v)M_a\nu_{air}^2}\right]^{0.216} R^{0.648}\right) \tag{1.2}$$

where $z = \frac{P_a}{P_v}\ln\left(\frac{1}{1-P_v/P_a}\right)$.

1.1.2 Levitating droplets

The substrate has a strong influence on the shape of the droplet [20, 21] and the evaporation of sessile droplets [19]. To approach the aerosol physics, the substrate has to be removed. For pending droplets in microgravity, the work from C. Chauveau [35] demonstrated that the droplet radius is following a d^2 law so that the square radius of the droplet diminishes linearly ($R(t)^2 = R_0^2 - Kt$). However, at high temperature (above 700 K), a departure from that law is observed and the value of K diminishes. From then on, the idea is to leave the substrate or any contact with some kind of support for the droplets. The droplet will then evolve freely in levitation. There are multiple ways to have levitating droplets. The standards methods are to do acoustic levitation, an other option is to use magnetic fields to create levitation, the last but not least possibility is to use microgravity via parabolic flights, drop towers, sounding rockets or the development of an insert for the ISS that will be explained in detail during this thesis. In this part, the idea is to focus on the description of the different equations that dictate the evolution of a levitating droplet. The first focus will be on the description of a droplet without gravity. Two theories will be presented. First the basic droplet evaporation is presented in the review done by Erbil [36]. Then a second model is developed by Sobac [37]. The levitation of a droplet could be obtained via the Leidenfrost effect or acoustic waves both techniques will be presented. This will give an idea of the different techniques used to create an artificial removal of gravity.

Basic theory of drop evaporation

The first approach to describe a droplet evaporation is to use the ideas developed by Maxwell almost 130 years ago in his book [38] where he showed that the local evaporative flux is uniform at the bulb surface of a thermometer. This leaded him to an approach based on the evaporative flux with an analogy between the rate of diffusion and the rate of heat conduction. He then derived the general diffusion rate equation with the assumption that the concentration at the interface c_i is equal to the equilibrium concentration or saturated vapour concentration at the temperature of the droplet interface.

Fuchs pointed out the validity of this hypothesis for droplets much larger than the mean free path of the vapour molecules in the case of stationary evaporation [39]. The spherical nature of the drop was studied also numerically and even if the droplet is not spherical at the beginning, after a short time, the drop reaches its spherical shape [40, 41]. The evaporation rate is given by:

$$\frac{dm}{dt} = -4\pi r^2 D_{va} \frac{dc}{dr} \tag{1.3}$$

where m is the droplet mass (kg), t the time (s), D_{va} the diffusion coefficient of the water vapour into air ($m^2.s^{-1}$), c is the vapour concentration $kg.m^{-3}$. With the evaporation process, the gas will have a water vapour component leading to droplet evaporating into a gas mixture of air and water vapour.

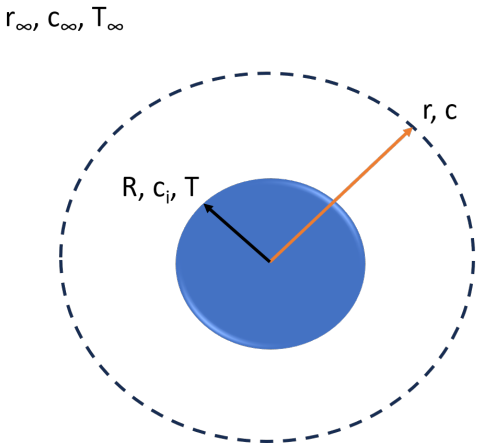

Figure 1.3: Sketch of the droplet parameters r is the radius, c the concentration T the temperature. The index i stand for interface and ∞ is to indicate the conditions far from the droplet.

The next step is to use the mass continuity equation in a stationary regime to integrate using the following boundary conditions:

- $c = c_i$ when $r = R$
- $c = c_\infty$ when $r = \infty$

As a result of the integration:

$$\frac{dm}{dt} = -4\pi R D_{va}(c_i - c_\infty) \tag{1.4}$$

By using the fact that the outer layer of the droplet is evaporating the small mass dm can be expressed as $dm = 4\pi\rho_{water}R^2dR$ where ρ_{water} is the density of water. With the hypothesis that the water vapour could be seen as an ideal gas $c = \frac{MP_v}{\mathcal{R}T}$ (M the vapour molar mass, P_v the partial pressure of the vapour, $\mathcal{R}$ the ideal gas constant and T the temperature). The evaporation rate is transformed from eq 1.4 into:

$$\frac{dm}{dt} = \frac{-4\pi M D_{va}(P_v^{sat} - P_v^{\infty})R}{\mathcal{R}T_{\infty}} \tag{1.5}$$

By using the fact that $\frac{P_v^{\infty}}{P_v^s} = H(\%)$ and after integrating, it leads to the following equation:

$$R_0^2 - R^2 = \frac{2D_{va}MP_v^{sat}(T_{\infty})(1-H)}{\rho_{water}\mathcal{R}T_{\infty}}t \tag{1.6}$$

Using R_0 as the initial radius of the droplet. The lifetime t_{evap} is obtained when $R = 0$ in eq 1.6. This leads us to the form used for the fitting where t_{evap} is equal to a function of the relative humidity H and a theoretical factor k_{th}:

$$t_{evap} = \frac{k_{th}}{1-H} \tag{1.7}$$

The factor k_{th} could also be evaluated from eq 1.6 with $k_{th} = \frac{R_0^2\rho_{water}\mathcal{R}T_{\infty}}{2DMP_v^{sat}(T_{\infty})}$. The equation 1.7 will be used for the description of the evaporation regimes to understand the data gathered during the experiment made in parabolic flights in section 3.5. However, even if this model might be a good first approach, it does not take into account the heat transfer that will cool down the droplet. The evaporative cooling occurs as the droplet is evaporating due to the liquid water latent heat L. If the droplet is levitating inside still air then the heat transfer with the exterior only occur via heat diffusion. The thermal equation governing the evaporation regime is:

$$-L\frac{dm}{dt} = 4\pi R\lambda_{cond}(T - T_{\infty}) \tag{1.8}$$

with λ_{cond} the air thermal conductivity, T_{∞} the air temperature far from the droplet, R the droplet radius and T the droplet temperature. The equation 1.6 and 1.8 are the two equations that build a complete description of the evaporation dynamic.

Sobac molar approach

The approach by Sobac [37] includes other parameters and is focused on a molar approach. First, it is taking into account the receding speed of the interface in the Fick's diffusion law [42] and secondly the heat exchanges with the droplet. The Fick's law is given as

$$j^* = -c_g^* D_{va} \frac{\partial X}{\partial r} + c_v^*(u^* - u_i) \tag{1.9}$$

where j^* is the local molar flux of evaporation leaving the interface (mol.m^{-2}.s^{-1}), c_g^* the local molar gas mixture concentration (mol.m^{-3}), c_v^* the local molar vapour concentration (mol.m^{-3}), $X = \frac{c_v^*}{c_g^*}$ is the vapour mole fraction in the gas phase. The subscripts l is for the liquid (liquid water), g is for the gas mixture and v, a are for the vapour and air. The total gas pressure is given by the Dalton's law $P_g = P_v + P_a$ (with $P_n = c_n^* \mathcal{R} T$ the n value could be replaced by either g,v or a), the receding velocity of the interface due to evaporation $u_i = \dot{R}$ and the molar averaged velocity of the gas $u^* = u_a(1 - X) + u_v X$ where u_v and u_a are the vapour and air velocities, respectively. The mass continuity equation applied to the gas gives:

$$\frac{\partial c_g^*}{\partial t} + \frac{1}{r^2}\frac{d(r^2 c_g^* u^*)}{dr} = 0 \tag{1.10}$$

In a stationary regime, it leads to $u^* = \frac{\epsilon}{c_g^* r^2}$ with ϵ an unknown coefficient. There is continuity of the local flux of evaporation at the surface this flux is linked on both sides to the receding speed u_i at the interface when $r = R$.

$$j^* = -c_l^* u_i = c_g^*(u^* - u_i) \tag{1.11}$$

Considering $c_g^* \ll c_l^*$ it leads to the following expression of the average molar velocity of the gas:

$$u^* = \frac{j^* R^2}{c_g r^2} \tag{1.12}$$

The consideration of the continuity equation for the vapour gives:

$$\frac{\partial c_v^*}{\partial t} + \frac{1}{r^2}\frac{d}{dr}\left[r^2\left(c_v^* u^* - c_g^* D_{va}\frac{\partial X}{\partial r}\right)\right] = 0 \tag{1.13}$$

In a stationary regime and with the use of eq 1.10 it results in:

$$c_g^* u^* \frac{dX}{dr} = \frac{1}{r^2}\frac{d}{dr}\left(c_g^* D_{va} r^2 \frac{\partial X}{\partial r}\right) \tag{1.14}$$

The boundary conditions are the following:

- $X(r \to \infty) = X_\infty$
- $X(r = R) = X_i$
- $j^* = -\frac{c_g^* D_{va}}{1-X_i} \frac{dX}{dr}\Big|_{r=R}$

The third equation is obtained by a combination of eq 1.9 and eq 1.11. At the interface, the partial pressure P_v is supposed to be the saturation pressure at the temperature of the droplet. As a result it could be estimated as $X_i = P_v^{sat}(T_i)/P_g$. The Clapeyron equation gives:

$$X_i = \exp\left(-\frac{L}{\mathcal{R}}\left(\frac{1}{T_i} - \frac{1}{T_b}\right)\right) \tag{1.15}$$

where L is the latent heat of vaporization, T_i is the temperature of the interface and T_b is the boiling temperature at the pressure P_g. The curvature impact of the radius R on the saturation pressure variation is neglected [43]. The steady state heat equation including convection and diffusion gives:

$$c_g^* C_{p,g}^* u \frac{dT_g}{dr} = \frac{1}{r^2}\frac{d}{dr}\left(\lambda_g r^2 \frac{dT_g}{dr}\right) \tag{1.16}$$

where T_g, $C_{p,g}^*$ and λ_g are the temperature, the molar heat capacity and the thermal conductivity of the gas, respectively. The heat transport is advected with the average speed u and not the molecular one. However, the two are linked: $u = u^* M/M_g$, where $M_g = (1-X)M_a + XM$ is the local molar mass of the mixture. As a result $j = Mj^*$, $j^* = c_g u^*$ and $j = \rho_g u$ with $\rho_g = c_g M_g$ is the gas density. Regarding eq 1.16, the boundary conditions are the following:

- $T(r \to \infty) = T_\infty$
- $T(r = R) = T_i$
- $j^* L = \lambda_g \frac{dT_g}{dr}\Big|_{r=R}$

From that point on, the idea is to solve the two main equations eq 1.16 and eq 1.14, that are respectively, the heat transport equation and the molar transport equation. They are linked in terms of boundary condition by eq 1.15. The resolution of those equations is done here with homogeneous physico-chemical properties, the expression of those gas physico-chemical properties as functions of the gas composition and temperature is done in the work of Sobac [37] that is followed for this theoretical explanation given in this part. With homogeneous properties and eq 1.12, eq 1.14 become :

$$\frac{dX}{dr} = \frac{c_g^* D_{va}}{j^* R^2} \frac{d}{dr}\left(r^2 \frac{dX}{dr}\right) \tag{1.17}$$

This second order differential equation is solved with the boundary conditions given for eq 1.14. The local molar flux of evaporation j^* is then expressed as:

$$j^* R = -c_g^* D_{va} \ln\left(\frac{1 - X_i}{1 - X_\infty}\right) \tag{1.18}$$

Similarly, the heat conduction is simplified using the same method once the properties are considered constant:

$$\frac{dT_g}{dr} = \frac{M_g}{M} \frac{c_g^* \alpha_g}{j^* R^2} \frac{d}{dr}\left(r^2 \frac{dT_g}{dr}\right) \tag{1.19}$$

where $\alpha_g = \lambda_g / (c_g^* C_{p,g}^*)$ is the thermal diffusivity of the gas. By using the boundary conditions of eq 1.16, it is possible to solve this equation, it is a second order differential equation in r. The gas temperature is expressed as:

$$T_g(r) = T_\infty - \frac{T_\infty - T_i}{1 - \exp\left(-\frac{M}{M_g}\frac{C_{p,g}^* j^* R}{\lambda_g}\right)} \left(1 - \exp\left(-\frac{M}{M_g}\frac{C_{p,g}^* j^* R^2}{\lambda_g}\frac{1}{r}\right)\right) \tag{1.20}$$

The third equation which describes the boundary conditions of equation 1.16 allows the determination of the interface temperature T_i:

$$T_i = T_\infty - \frac{M_g L}{M C_{p,g}^*} \left(\exp\left(-\frac{M}{M_g}\frac{C_{p,g}^* j^* R}{\lambda_g}\right) - 1\right) \tag{1.21}$$

For the resolution of this equations (transport and heat) the physico-chemical quantities ($c_g^*, C_{p,g}^*, D_{va}, L, \lambda_g, M_g, M, \mathcal{R}, T_b, T_\infty, X_\infty$) are supposed known. L is evaluated at the temperature T_i and the other variables are evaluated at T_∞. This leads to a set of four equations (eq 1.15, eq 1.18, eq 1.21 and eq 1.22) that are solved together to determinate the different quantities: j^*, T_i, X_i, L. It is important to note that j^* and R always appear grouped in those equations as a result $j^* R, T_i, X_i, L$ are independent of R and therefore they are not time dependant. The latent heat equation as a function of the temperature is given by the book written by Yau (T is the temperature in degree °C between $-25\,°C$ to $40\,°C$) [44]. For higher temperatures the law from Torquato [45] could be used.

$$L(T) = 2500.8 - 2.36T + 0.0016T^2 - 0.00006T^3 \,(\mathrm{kJ/kg}) \tag{1.22}$$

The description of this model will be used later to analyse the parabolic flight data and to have access to the interface temperature via a measurement of the temperature far from the droplet, the humidity far from the droplet and the evolution of the averaged radius evolution over time. Measuring the evaporation flux is hard, however, it is possible to link it to the mass evaporation:

$$-c_l^* \frac{dV_{drop}}{dt} = 4\pi R^2 j^* = -4\pi R c_g^* D_{va} \ln\left(\frac{1-X_i}{1-X_\infty}\right) \tag{1.23}$$

where V_{drop} is the volume of the droplet so that $V_{drop} = \frac{4}{3}\pi R^3$. By integrating eq 1.23 it results in:

$$R^2 = R_0^2 - 2D_{va}\frac{c_g^*}{c_l^*} \ln\left(\frac{1-X_i}{1-X_\infty}\right) t \tag{1.24}$$

where t is the time and R_0 is the initial radius of the drop. Thanks to eq 1.24, it would be possible to link the droplet radius evolution to the different parameters, especially X_i that will leads to the determination of T_i for example. With these two approaches, it is possible to have a relatively good estimation on how the droplets will behave under microgravity.

Leidenfrost effect

To have access to a levitating droplet different techniques will be seen. The first one investigated is the levitation via the Leidenfrost effect. This effect happens when a drop of liquid is deposited on a hot solid, with a temperature much higher than the boiling point, the drop is then not any more in contact with the solid, but levitates above its own vapour. Because of the insulating properties of the film, the evaporation is rather slow: a millimetric droplet of water on a metallic surface at 200 °C is observed to float for more than a minute (see figure 1.4). In addition, the absence of contact between the liquid and the solid prevents the nucleation of bubbles, so that the drop does not boil but just quietly evaporates. Such floating drops are called Leidenfrost drops, after the name of the German physicist who first reported the phenomenon around 1750 [46].
In that situation the capillary forces are key and the main number to look at is the Bond number (Bo) or the ratio between the buoyancy forces and the surface tension of the liquid.

$$Bo = \frac{\Delta\rho g l^2}{\gamma} = \left(\frac{l}{l_c}\right)^2 \tag{1.25}$$



Figure 1.4: Large water droplet deposited on a silicon film at 200 °C. Figure copied from ref [47].

where $\Delta\rho$ is the density difference between the droplet and its surrounding gas (approximated as ρ_{liquid} because the air density is really small compared to the droplet density), l is the characteristic length (usually the radius of the droplet) and γ is the surface tension. The value l_c is the capillary length so that $l_c = \sqrt{\gamma/\rho_{liquid}g}$. If the radius of the droplet is bellow the capillary length then the droplet is mostly spherical and a little flattened at the bottom. This shape is accurately modelled in the article by Sobac [48]. In the study done by Biance [47], the temperature of the droplet reported is 99 ± 1 °C. This leads to an estimation of the water density at $960\,\mathrm{kg.m^{-3}}$, a surface tension of $59\,\mathrm{mN.m^{-1}}$ and therefore a capillary length of 2.5 mm. It is observed that for a certain size, the droplet will break into several smaller droplet. This is attributed to Rayleigh-Taylor instabilities of the lower interface. The critical radius (R_c) of a Leidenfrost droplet is given as 3.84 l_c or 9.6 mm in radius [47]. The evaporation of a heated droplet smaller than the capillary length will occur in the entire surface of the droplet compared to larger droplet (larger than the capillary length which will have an evaporation rate similar to the one of a film not a sphere). The evaporation rate is given as:

$$\frac{dm}{dt} \propto \frac{\lambda_v}{L}\frac{\Delta T}{R}R^2 \tag{1.26}$$

where λ_v is the thermal conductivity of the vapour, L the latent heat of vaporization, ΔT the temperature difference between the support and the

boiling temperature of the liquid and R the radius of the droplet. After the integration for a sphere the result is given by:

$$R^2(t) = R_0^2 \left(1 - \frac{t}{\tau_L}\right) \tag{1.27}$$

where $\tau_L \propto \rho_{liquid} L R_0^2 / \lambda_v \Delta T$. This evaporation time and overall evolution is an other application of the d^2 law. The impact of gravity on the Leidenfrost effect is rather important as this effect highly depends on the capillary length and therefore on the gravity level applied to the droplet. Experiment conducted at the Large Diameter Centrifuge (LDC) (facility of the ESA) allows investigations up to $20\,g$. This study was done by Maquet [49]. The main effect of gravity is to modify the apparent weight of the drop, i.e. to affect the capillary length l_c. This capillary length has to be modified to account for the hypergravity: $l_c = \sqrt{\gamma / \rho_{liquid} g G}$, where γ and ρ_{liquid} are the surface tension and the density of the liquid, g the Earth gravity acceleration and G the hypergravity ratio defined as $G = 1 + R_g \omega^2 / g$, i.e. the ratio between the apparent gravity and the Earth gravity (where R_g is the radius of the centrifuge and ω the rotation speed). In microgravity environment, the capillary effects are enhanced as the capillary length l_c diverges. On the other hand, high-gravity conditions increase the gravity effect and the capillary length decreases. This means that the droplet would tend to behave like a pebble because the radius of the droplet will exceed the one of the capillary length (see figure 1.5). This situation is particularly interesting regarding the Leidenfrost effect because, during the evaporation, the drop successively experiences three regimes: very large drop ($R > R_c$), large drop ($l_c < R < R_c$), and small drop ($R < l_c$), where R_c is the critical radius for chimney formation, over this value of radius, an instability will develop and break the droplet into smaller ones [47]. As a result, for the same volume of liquid, different evaporation regimes could be investigated only by applying different gravity levels. The theoretical impact of gravity on the droplet shape is drawn in fig 1.6 by Maquet [49], based on the computation done by Sobac [48].

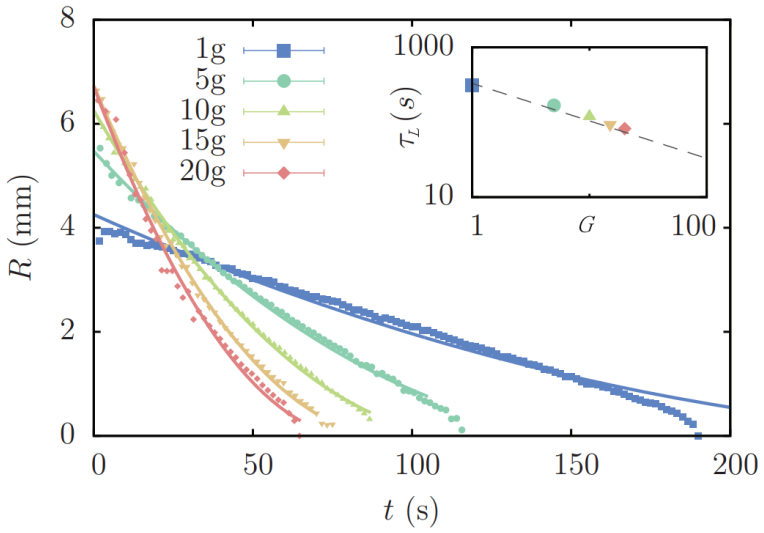

Figure 1.5: Radius evolution for a 10 μL Leidenfrost drop for five different hypergravity ratio: $G = 1$, 5, 10, 15 and 20. The temperature of the substrate is 300 °C. The inset represents the lifetime of the droplet as a function of the hypergravity ratio. The dashed line is a power law fit with exponent -1/2. Figure copied from ref [49].

As a result, the radius evolution will turn from the evolution of a sphere evaporating (seen previously described in eq 1.27) to the one of a pebble (see figure 1.6). It entails that the radius evolution is then varying at a much faster rate as $R(t) = R_0\left(1 - \frac{t}{\tau_L}\right)^2$ with a lifetime τ_L defined by:

$$\tau_L = 2\left(\frac{4\rho_{liquid} l_c L}{\kappa_v \Delta T}\right)^{3/4}\left(\frac{3\eta_v}{\rho_v G}\right)^{1/4} R_0^{1/2} \tag{1.28}$$

where η_v is the dynamic viscosity and ρ_v the vapour density. If the droplet is assumed to be a flat pancake, the conservation of volumes gives $R_0 = \sqrt{V/2\pi l_c} \propto G^{1/4}$. This evolution of the initial radius along with the definition of τ_L explains the reason why $\tau_L \propto G^{-1/2}$ as shown in figure 1.5.

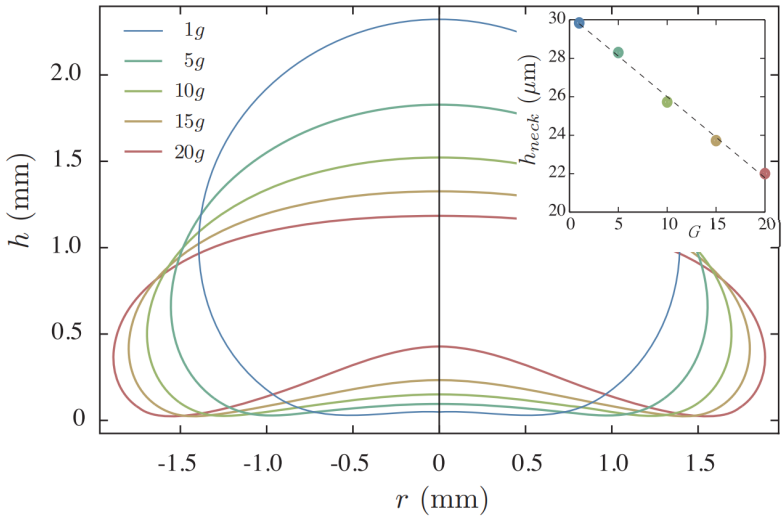

Figure 1.6: Theoretical shapes of a 10 μL Leidenfrost drop for five different hypergravity ratio: G = 1, 5, 10, 15 and 20. The temperature of the substrate is 300 °C. These shapes are numerically determined using theoretical modelling [48]. The inset represents the thickness of the vapour film at the location where it is thinnest, h_{neck}, as a function of the hypergravity ratio G, using the same model. Figure copied from [49].

The Leidenfrost effect is one way to have a levitating droplet. However, this technique imposes different conditions around the droplet (boiling temperature, high evaporation rate...) that do not correspond to the the best way to study an aerosol adapted to cloud evolution and formation as the temperature is then equal to a maximum 25 °C. It is also important to note that in microgravity, the vapour film may push the droplet away from its support, creating a free moving droplet cooling in the surrounding air.

Acoustic Levitation

The acoustic levitation method (ALM) is a method that consists in using pressure waves to levitate a sample. This method of manipulation is critical in the industry for microassembly since the classical assembly processes are no longer usable for very small components, typically ranging from 10 μm to 10 mm. There the cost of the assembling becomes the most expensive task, owing to the difficulties of automation since usually neglected surface forces disturb the handling task by inducing adhesion between the component and the gripper [50]. The advantages of this contactless handling approach can be summarized as follow. Some of the advantages listed are not limited to the handling of microcomponents [51].

- Surface forces can be completely neglected.
- The friction effect is drastically reduced, which enables high resolution and accuracy motion devices by avoiding the stick-slide effects (see section 1.1.1).
- Handling of tricky (fragile, freshly painted, sensitive or micron-sized structured surfaces) components is feasible because high local contact pressure by direct mechanical contact is avoided [52]. Handling of non-rigid products is also possible due to the force field [53].
- Contamination from and of the manipulation can be totally avoided. This can be important in food handling [53].
- In material science, measurements of some physical properties are allowed on very small liquid or solid samples avoiding undesired contamination from the container and eliminating wall-driven heterogeneous nucleation [54].

The objective in our case is to study the levitation of droplets, therefore we will focus on the pressure field necessary for the levitation to occur. To do so, we will follow the work of M. Andrade [55]. The idea is to play on the pressure by creating a wave via a transducer and a reflector (shown in figure 1.7)
To describe the propagation of mechanical waves of small amplitudes in a fluid medium and the acoustic radiation pressure, let us consider that in the absence of perturbation, the fluid is at rest ($u_0 = 0$) and has constant pressure (p_0) and constant density (ρ_0). Let us also assume that when a wave propagates in the fluid, the fields p, u, and ρ present small variations in relation to the unperturbed fluid. In this case, we can express the total fields (p, u, and ρ) as a sum of the unperturbed fields (p_0, u_0, and ρ_0), the first-order perturbation fields (p_1, u_1, and ρ_1) and the second-order perturbation fields (p_2, u_2, and ρ_2), as follows:

- $p = p_0 + p_1 + p_2$ with $|p_1| \ll p_0$ and $|p_2| \ll p_0$
- $u = u_1 + u_2$
- $\rho = \rho_0 + \rho_1 + \rho_2$

with the continuity and momentum equation, the pressure wave responsible for the levitation could be found via the Gorkov [56] hypothesis ($R \ll \lambda$)

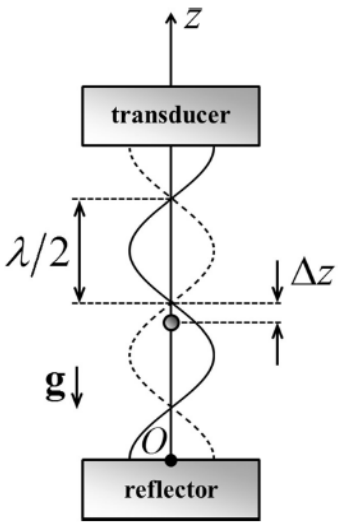

Figure 1.7: Acoustic levitation of a small rigid sphere at the pressure node of a plane standing wave established between a transducer and a reflector. Figure copied from [55].

so that $p_1(z,t) = p_{ampl}\cos(\omega t)\sin(kz)$ with p_{ampl} the acoustic pressure amplitude and $k = \omega/c_0 = 2\pi/\lambda_{acc}$ (c_0 being the speed of sound inside the considered material here air). The minimal pressure amplitude to levitate a small droplet could then be calculated as:

$$p_{ampl} = \sqrt{\frac{8\rho_0\rho_{liquid}c_0^2 g}{5k}} \tag{1.29}$$

where ρ_{liquid} is the liquid droplet density and g the gravity field. So if the minimal pressure amplitude is applied, the droplet will levitate. However, it is important to keep in mind that along with the pressure comes a speed flow around the droplet called acoustic streaming. This flow will promote the evaporation of the droplet. The evaporation of water droplet mixed with NaCl, ethanol was studied by Sasaki [57] and Maruyama [58] recently. There the droplet is put in place with a syringe and kept levitating with acoustic levitation. Two set-ups are experimented and are similar in both studies. The figure 1.8 a shows a schematic of the measurement visualization system for the droplet external flow, which correspond to the first set-up. A nebulizer produced water mist (diameter $5\,\mu$m) in the form of tracer particles to visualize the external flow. The vertical cross section of a levitated droplet was illuminated using a sheet laser, and the droplet flow field was measured using a high-speed camera. The flow field was recorded at 500 frames per second (fps). The figure 1.8 b shows a diagram of the surface temperature

measurement system which corresponds to the second set-up. The droplet contour and its surface temperature were obtained using a high-speed camera, with a spatial resolution of 19.8 μm/pixel, and an IR camera, with a temperature resolution of approximately 0.02 °C, respectively. To obtain information about the diameter, the droplet contour was measured using an LED back light [57].

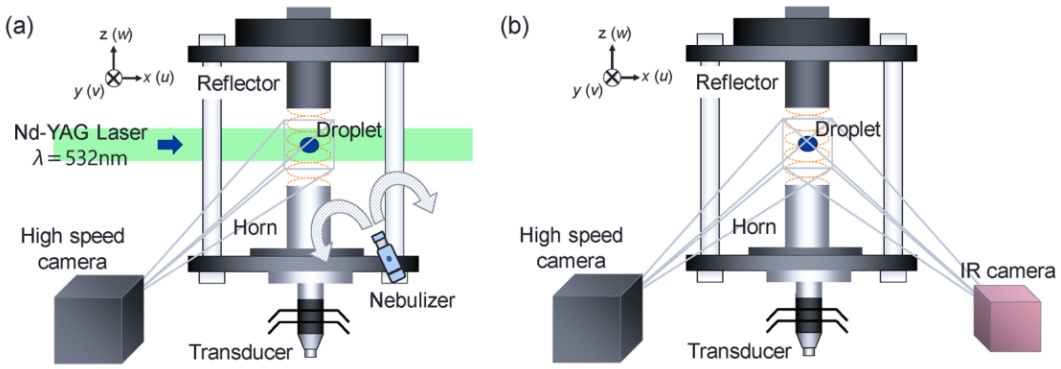

Figure 1.8: Acoustic levitation of a small rigid sphere, the first set-up (a) allows the investigation of the flow around the droplet via a nebulizer and a PIV technique. The second set-up (b) allows the investigation of the temperature evolution via an IR camera. Figure copied from [57].

In both studies, the droplet size is millimetric (between 1.0 mm and 2.0 mm) with a resonance frequency of the ultra sonic waves at 19.3 − 19.4 kHz. When the evaporating droplet is composed of pure water, the radius follows a d^2 law where the square radius decreases linearly. When the water is mixed with salt, the evaporation follows a d^2 law and then after the evaporation of the water is completed, the salt crystallizes and a pure salt droplet is left floating. As the salt is stable in its solid form, the evaporation stops and the diameter does not evolve any more (see fig 1.9a). When the water is mixed with ethanol, things change as the ethanol is also a liquid that will evaporate (see fig 1.9b). It appears that the ethanol will tend to evaporate first (higher saturation pressure, lower latent heat, lower surface tensions are in favour of a higher evaporation rate) causing a shift from the d^2 law as this evaporation in different proportions will change the physical behaviour of the droplet (changes in the diffusion coefficient as the composition of the droplet varies, changes in the average molar mass and density). Those changes are driving the linear coefficient responsible for the d^2 law. As a result, three main phases are observed. During the first phase, the ethanol will evaporate preferentially. Then, as the temperature of the droplet is decreased due to the ethanol evaporation, the surrounding water present in the air will condensate

on the droplet. And in a last phase the droplet is mostly made of water and will tend to behave like so. During that phase an increase in temperature is observed mostly due to viscous dissipation inherent to the levitation method.

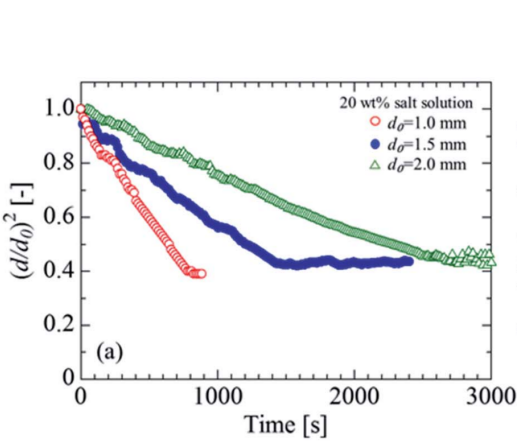

(a) Effect of initial droplet diameter on droplet evaporation and precipitation, and visualisation of the plateau that happens when the salty droplet is fully crystallized. Figure copied from [58].

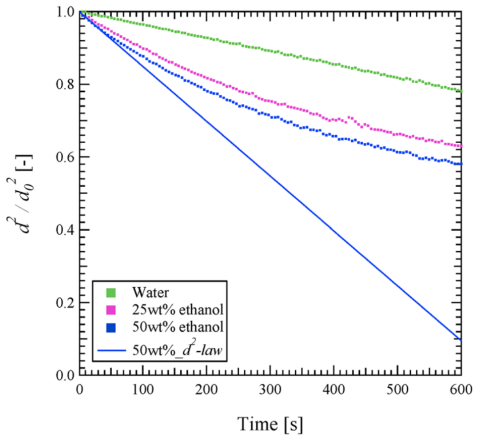

(b) Effect of the ethanol concentration on the evaporation of a droplet, the constant d^2 law is witnessed for the pure water but the ethanol concentration is causing a deviation. Figure copied from [57].

Figure 1.9: Evaporation rate for two different solutions, a salt solution and an ethanol solution. d is the diameter and d_0 its initial value.

The three different phases could be seen on the figure 1.9b, first (for a time lower than 50 s) the curves indicates that the 50wt% ethanol droplet tend to behave like the d^2 law at the same composition. Then this droplet evaporation is slowed and gradually will tend to behave like the pure water droplet by having the same evaporation rate. The same phenomenon occurs with the curve at 25wt% ethanol.

1.2 Aerosol Physics

The idea of this section is to understand the physics of an aerosol made from multiple droplets. The first section describes the way droplets are generated (via nebulizer, cloud chamber or spray) and the size distribution that result from these methods. The second section is about the evaporation of aerosols. The third section is about the droplet evolution in a VK swirling flow.

1.2.1 Aerosol generation

There are numerous ways to produce an aerosol experimentally. The generation of aerosols could be done by playing on the temperature of a gas to nucleate the droplets. Typically, it could also be done by expanding a volume between two pistons [59]. It is also possible to have these results by just applying a temperature gradient on a two stage system [60], or in the case of this study, expanding a volume of gas brutally to create this temperature drop. The second principle used to create an aerosol, is to start with a liquid and nebulize it via ultra-sonic waves [61]. The third and last possibility is to generate it via a spray or jet [62]. An aerosol could also be generated via uncontrolled processes such as bronchoscopy [63] or sea spray aerosol in nature [64].

Aerosol creation by ultra-sonic nebulizers

Ultrasonic nebulizers or atomizers are very important due to their many applications such as drug delivery, mass spectrometry, humidity control, spray pyrolysis, coating, etc. In almost all cases, the distribution of droplet sizes is an important parameter. For example, in many drug delivery systems, droplets need to be sufficiently small to reach the lower parts of the pulmonary tract, as larger droplets are deposited predominantly at the start of the airways [65]. The droplet size distribution plays an important role for many applications, as for example in mass spectrometry large droplets can lead to a loss of sensitivity and if not properly desolvated may lead to vacuum fluctuations, while small droplets will not. The work done by Kooij [62] is analysed here as a way to present the different techniques of nebulizers. This is also the first study that focusses primarily on the droplet size distribution for ultrasonic nebulization. This process is mostly explained by the capillary wave mechanism. The formation of capillary waves on the surface of a fluid supported by a vibrating solid was first described by Faraday in 1831, and are therefore also referred to as Faraday waves [66]. Later, Kelvin derived the formula for the capillary wavelength λ [67], relating it to the surface tension σ, density of the fluid ρ, fluid depth h and frequency f of the standing waves to obtain the following relation:

$$\lambda \tanh\left(\frac{2\pi h}{\lambda}\right)^{-1/3} = \left(\frac{2\pi\sigma}{\rho f}\right)^{1/3} \tag{1.30}$$

For a sufficiently deep liquid layer ($h/\lambda \ll 1$), one can take $\tanh(2\pi\lambda/h) = 1$. As with many parametric oscillators, the frequency of the non-linear standing waves is half the excitation frequency F, i.e. $f = F/2$. For ultrasonic

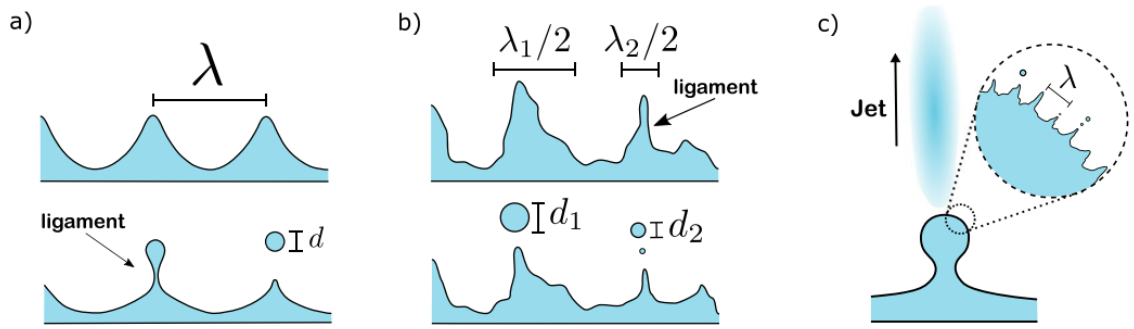

Figure 1.10: (a) Ideal case of standing capillary waves of wavelength λ. It leads to a monodisperse droplets distribution of size $d \simeq \lambda$. (b) Capillary waves in a system with maximum interference. This results in a broader distribution of droplet sizes. (c) Faraday waves are superposed on larger waves of the order of the wavelength of the chip material. The motion of these larger waves initiates breakup of the smaller superposed capillary waves. Figure copied from [62].

nebulizers, according to the capillary wave mechanism, the amplitude of the oscillation is large enough to cause droplet pinch-offs, thereby nebulizing the fluid (figure 1.10a). Since the size of the pinch-off droplets is proportional to the capillary wavelength, the median droplet size (designated as D_{50}) is given by

$$D_{50} = \kappa \left(\frac{8\pi\sigma}{\rho F^2} \right)^{1/3} \tag{1.31}$$

with F is the frequency of the nebulizer and κ a proportionality constant. Lang was the first to experimentally determine this constant as $\kappa = 0.34$ [68]. The different ways to produce the nebulization are shown in figure 1.11 and will be described bellow.

Nebulizers SAWN. The Surface Acoustic Wave Nebulizer (SAWN) consists of two interdigital transducers (IDT) with lithium niobate as the piezoelectric substrate. Between the two IDTs there is a space (delay zone) where a droplet can be placed for nebulization (figure 1.11b with holder and figure 1.12a). For this particular chip, the resonance frequency is 9.6 MHz . The distance between the metallic electrodes of the IDT sets the wavelength of the acoustic waves at $\lambda = 0.36$ mm. The surface acoustic waves can either be created by one of the IDTs (single mode) or both (dual mode). In this work, one IDT is used to create the waves and the other IDT as a transceiver. The SAWN creates plumes of droplets with ionized molecules, which after the

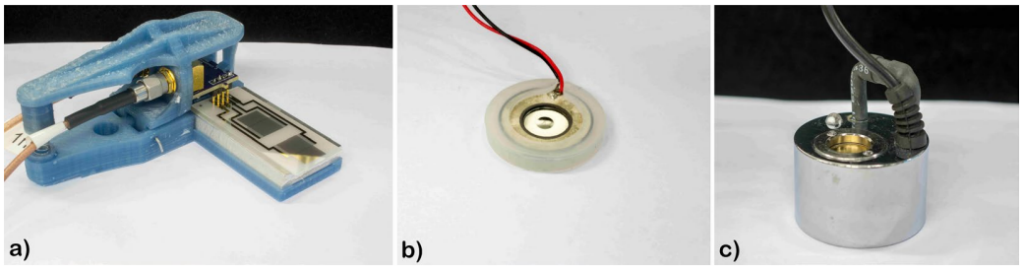

Figure 1.11: Nebulizer types investigated. (a) SAWN chip with holder. (b) Nebulizer chip. (c) Mist maker. The gold-colored part is the vibrating membrane. The transducer is placed roughly 4 cm under water. Figure copied from [62].

evaporation of the solvent, can be directly used by the mass spectrometer.

Nebulizer chip. The nebulizer chip is a low-frequency (105±5 kHz), low-power (2 W) and low-cost type of atomizer (see figure 1.11b). The transducer has a coin shape with and a rubber ring for isolation and a small reservoir to contain the fluid to be nebulized. If the transducer is placed in a small bath of water, water will be absorbed from under the chip into the reservoir such that the nebulizer can work continuously. In the middle of the chip there is a small bump where the nebulization takes place (see figure 1.12b).

Mist maker. The mist maker is a widely used commercial type of nebulizer mostly used for decoration and terraria (figure 1.11c). Unlike the other nebulizers investigated, this type is submerged. We immersed a Nebler nebulizer in water, placing it about 4 cm under the water surface where it produces a small cone-shaped fountain accompanied by a large amount of micron-sized droplets, seen as mist (figure 1.12c). The depth of the transducer follows from the fact that when the nebulizer is placed near the surface, it produces a lot of splashing, while if it is placed to deep, attenuation of the waves will reduce its effectiveness. The frequency of the nebulizer is 1700±50 kHz with a power of 30 W.

What determines the droplet size distribution in different types of fluid breakup, such as spray and jets, is well understood. In fluid fragmentation, where ligaments are of equal size, the rescaled droplet size distribution is given by a gamma function:

$$\Gamma(x = d/\langle d\rangle, n) = \frac{n^n}{(n-1)!} x^{n-1} e^{-nx} \tag{1.32}$$

where $\langle d\rangle$ is the mean droplet size and n a parameter that sets the ligament oscillation parameter. For systems with highly oscillating ligaments, the

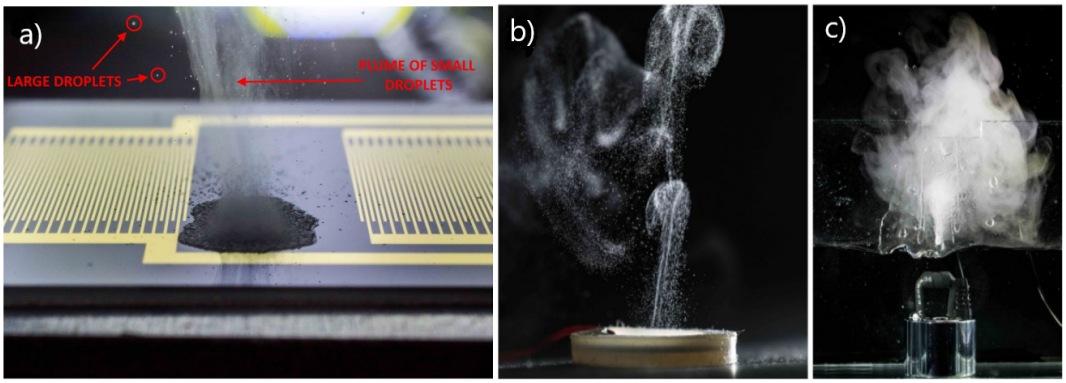

Figure 1.12: (a) Picture of the nebulization of a droplet on the SAWN chip taken with a 5 μs fash light. Two droplet size regimes can be observed as indicated by the red arrows. (b) Nebulization process for the nebulizer chip. (c) Mist maker producing large amounts of small droplets. As can be seen, the mist maker is the only submerged nebulizer, while for the other nebulizers small amounts of fuids are placed on top of the transducer. Figure copied from [62].

distribution is broad and $n = 4-5$, while for very smooth ligaments $n = \infty$, which would result in a delta peak. For more complicated fluid breakup, such as in agricultural sprays, the ligaments themselves can also be distributed in size [61], leading to a two-parameter compound gamma distribution:

$$\mathcal{P}_{m,n}\left(x = \frac{d}{\langle d \rangle}\right) = \frac{2(mn)^{\frac{m+n}{2}} x^{\frac{m+n}{2}-1}}{\Gamma(m)\Gamma(n)} \mathcal{K}_{m-n}(2\sqrt{mnx}) \tag{1.33}$$

where m sets the width of the ligament size distribution, n the ligament oscillation parameter and $\mathcal{K}_{m-n}$ is a Bessel function of order $m-n$ [69]. The ultrasonic atomization is similar to other fluid fragmentation processes according to Kooij, since here there can be a spread in ligament sizes due to a spread in wavelengths (see figure 1.10b), and the pinch-of ligaments can be either smooth or rough.

Figure 1.13 shows the rescaled size distributions for the different nebulizers for three consecutive measurements. The laser diffraction method (Malvern Spraytec) does not allow for error bars on the data points, the setup averages hundreds of measurements per run, and the standard deviation between such measurements is typically small. The agreement between the three different runs shows however that there is little variability between measurements. The droplet sizes are fitted with eq. 1.33 to obtain the parameters m and n. Due to the form of eq. 1.33, exponents can become large, leading to numerical problems in evaluating the distribution function. Stan-

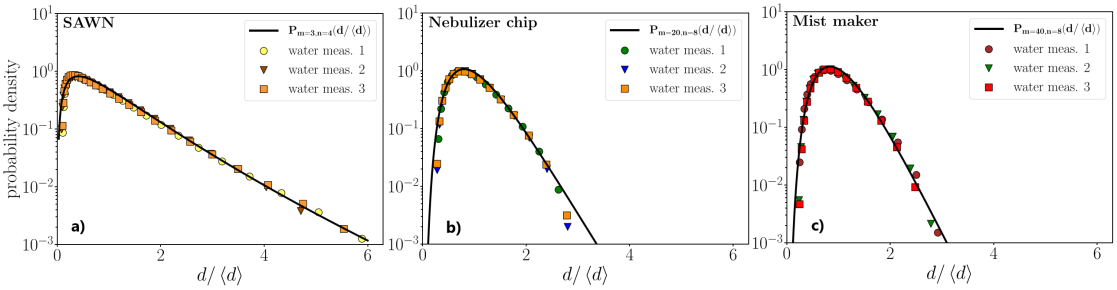

Figure 1.13: Rescaled droplet size (d) distributions for the three different nebulizers, each of which measured three consecutive times. Solid lines are fits to a two-parameter compound Gamma distribution $\mathcal{P}_{m,n}$, eq. 1.33 (a) Size distribution of the SAWN for the smallest droplets with a median droplet size at 1.1 μm. (b) Size distribution of the nebulizer chip and a median droplet size of 9.5 μm. (c) Size distribution for the mist maker and a median droplet size of 5.6 μm. Figure copied from [62].

dard minimization algorithms therefore do not work properly, since they are sensitive to the values of the initial guess. Fitting parameters were therefore obtained by manually fitting the distribution function. This however does not affect the results, since minor changes of the parameters does not alter the conclusions in any way. The first graph is the size distribution of the SAWN for the smallest droplets, with fitting parameters $m = 3$ and $n = 4$. The fitting parameters indicate a very large spread in pinch-of ligament sizes and very corrugated ligaments, which can be expected for the nebulization of a droplet by the violent mechanism. Median droplet size for the smallest droplets of the SAWN is 1.1 μm. The second graph corresponds to the size distribution of the mist maker with fitting parameters $m = 40$ and $n = 8$ and a median droplet size of 5.6 μm. These parameters indicate that the wavelengths are very similar to the graph (c) and the pinch-of ligaments reasonably smooth, in accordance with the capillary wave mechanism of a free surface such as present in case of the the mist maker. This shows that the nebulizer chip also has similar-sized pinch-of ligaments, although less so than the mist maker.

Aerosol creation by spray

Spraying is one of the most common processes in everyday life. It is important for agriculture, drug administration, printing, firefighting, spray painting, etc. [70] The droplet size and distribution in sprays are of paramount importance for effective spray application; it is important in agriculture pesti-

cide spraying, for instance, that the drop sizes are small for a good deposition and coverage [71], but not too small because of the environmental hazards of airborne spray drift [72, 73]. For drug delivery [74–76], one needs small drops that can easily be inhaled, but not so small that evaporation is almost instantaneous. Much work has been done on the optimization of drop sizes in sprays, but most research so far only deals with a few specific aspects of the droplet formation. The formation of droplets in sprays ultimately results from the breakup of liquid ligaments, which are often themselves transiently formed during the destabilization of jets or sheets [77]. In particular, it was understood that one of the main breakup mechanisms for nozzles is due to waves on the surface of the sheet that are produced by friction with the surrounding air (see figure 1.14). These waves, which were first described by Squire [78], grow in amplitude, causing thickness modulations of the sheet. The modulations will cause the sheet to thin to such an extent that it will break, creating sheet fragments of a well-defined size, the Squire wavelength. These fragments will contract to form ligaments, which subsequently break up into droplets. The Rayleigh-Taylor instability [79] describes the instability of the sheet accelerated perpendicular to its plane, which then forms ligaments. These ligaments then break into droplets through a Rayleigh-Plateau instability driven by surface tension [80]. Depending on the initial corrugation of the ligaments, this instability is more or less noisy, producing droplets more or less distributed in size [77]. A similar sequence of events governs the breakup of a liquid jet [81].

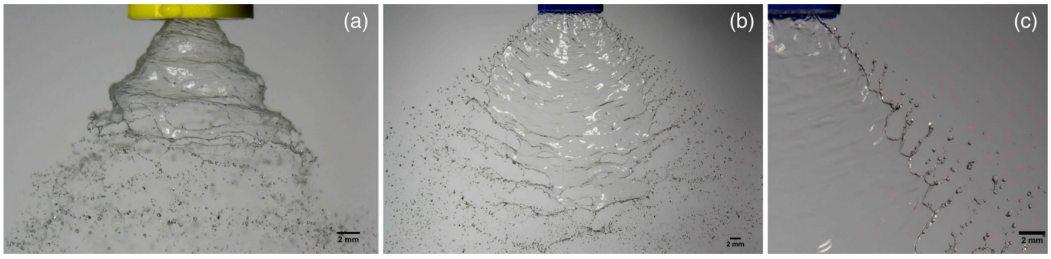

Figure 1.14: (a) Picture of the conical nozzle with an operating pressure of 2.0 bar. The Squire wave is clearly visible, with a wavelength in agreement with the prediction. (b) The flat fan nozzle at 2.0 bar, with flapping and breakup occurring near the bottom of the picture. (c) Zoomed-in picture of the flat fan nozzle at low pressure (1.0 bar), showing droplets coming from the sheet's rim that are of the order of the nozzle size. The scale is 2 mm. Figure copied from [61].

Here, the work done by Kooij [61] is followed about the examination of the spray formation as a function of all relevant parameters: nozzle type,

spraying pressure, and fluid properties. They show that the drop size can be predicted from the Weber number (which gives the competition between fluid inertia and surface tension) and the geometrical properties of the spray nozzle. Their findings allow one to directly calculate the drop size as a function of both of these parameters. In addition, the size distribution is found to be mostly universal (see figure 1.15a and b), implying that all distributions for different parameters collapse when scaled with the mean drop size. The results presented here allow the obtention of the drop size and its entire drop-size distribution without adjustable parameters.

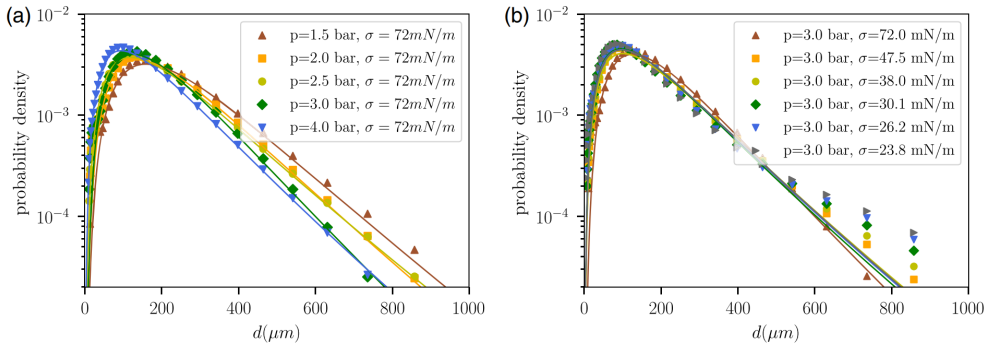

Figure 1.15: (a) The droplet size distribution for pure water with pressures from 1.5 to 4.0 bar for the Teejet 110-03 nozzle (flat liquid sheet). Fitting lines are the global size distribution (eq 1.33) with parameters m and n around 5. (b) Droplet size distributions of water-ethanol mixtures with different surface tensions (Teejet 110-03, flat liquid sheet). The fitting parameters are similar to those for pure water. Figure copied from [61].

It was established that the droplet size is insensitive to the liquid viscosity, which is not unexpected when the drop formation results from a competition between fluid inertia and surface tension. For the working range of pressures, the flow speeds in the nozzle are of the order of 20 m/s, implying that the nozzles operate in a regime where the Squire instability will occur meaning that the liquid sheet makes a flapping motion due to interaction with the surrounding air [78]. Two dimensionless numbers are expected to be relevant: the Weber number $We = \rho_{water} v^2 b/\sigma$ and the density ratio $\alpha_\rho = \frac{\rho_{air}}{\rho_{water}}$ where ρ_{water} is the liquid density, ρ_{air} is the air density, σ is the surface tension, $v = q/A_{hyd}$ the liquid velocity, b is the characteristic length ($b = \sqrt{2A_{hyd}/3\pi}$), q is the volumetric flow rate, and $A_{hyd} = q/\sqrt{2p/\rho_{water}}$ the effective hydraulic area. The different results are showing that the median droplet size D_{50} is equal to:

$$D_{50} = C_0 A_{hyd} q^{-2/3} \tag{1.34}$$

where C_0 is a constant that depends only of the geometry of the nozzle. The observed dependence of D_{50} on the flow rate directly suggests that:

$$D_{50} = C_1 b \alpha_\rho^{-1/6} We^{-1/3} \tag{1.35}$$

where C_1 is a dimensionless constant, this constant is the slope of the dashed line in figure 1.16 and has a value of approximately 1.95. The Weber number at the scale of the droplets is approximately 1200. Thus, these arguments allow for a determination of the droplet size without any adjustable parameters.

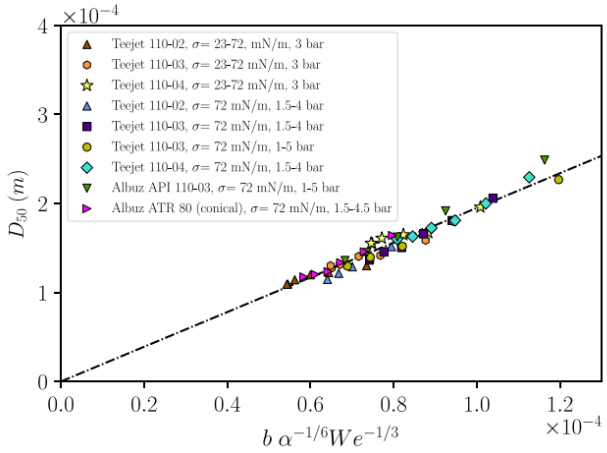

Figure 1.16: The median droplet size, D_{50}, plotted as indicated in eq 1.35 for all nozzles and various pressures and surface tensions. Figure copied from [61].

The median droplet size can be changed without altering the overall shape of the distribution. It can be done by changing the nozzle or pressure or by adding ethanol to lower the surface tension. Because of the relatively weak dependence of the median droplet size on the spraying parameters, the most effective and practical way of changing the median droplet size is by changing the pressure and, hence, the flow rate. Changing the surface tension has a limited effect, since for most fluids, the surface tension cannot be changed significantly, without adding a substantial amount of another liquid. Even if the surface tension could be changed by a factor of 3, keeping other parameters the same, the resulting change in droplet size would be no more than 44%. However, adding another liquid to lower the surface tension often changes the density of the solution as well, which generally

has the opposite effect. For the case of ethanol-water mixtures, adding as much as 80 wt% ethanol results in a theoretical change of only 36% in the droplet size due to the variation of σ/ρ_{liquid}. The measured change is a little lower, because of an increase of the largest droplets for high ethanol volume fraction, which is probably due to enhanced coalescence of droplets driven by Marangoni stress gradients [61].

1.2.2 Evaporation

Regarding the evaporation of aerosols once they are created, the literature always mention models for single droplets and considers that because droplets are distant at more than a certain multiple of their radius (usually five to ten), one can use single droplets models.

Numerical resolution

This issue has been studied a lot for combustion chambers in diesels engines [82] where numerical models can include the interaction between droplets via the resolution of the basic hydrodynamics equations for an unsteady, viscous, heat conducting fluid. The conservation equations for mass and momentum are written as followed according to the model proposed by Haselman and Westbrook in 1978 [83]:

$$\frac{\partial \rho_g}{\partial t} + \boldsymbol{\nabla} \cdot (\rho_g \mathbf{v}) = f \tag{1.36}$$

$$\rho_g \frac{\partial Y_i}{\partial t} + \rho_g \boldsymbol{\nabla} \cdot (\boldsymbol{\nabla} Y_i) = \boldsymbol{\nabla} \cdot \rho_g D_i \boldsymbol{\nabla} Y_i + f_i + K_i \tag{1.37}$$

$$\frac{\partial \mathbf{v}}{\partial t} + \mathbf{v}\boldsymbol{\nabla} \cdot \mathbf{v} = -\frac{1}{\rho_g}\boldsymbol{\nabla} P_g + \frac{\mathbf{F}}{\rho_g} + \frac{1}{\rho_g}\boldsymbol{\nabla} \cdot \overline{\tau} + f_m \tag{1.38}$$

with ρ_g the gas density, $\mathbf{v}$ the velocity vector, P_g the gas pressure, f the mass source per unit of volume, $\mathbf{F}$ the body force per unit of volume, $\overline{\tau}$ the viscous stress tensor, Y_i the mass fraction of species i, D_i the diffusion coefficient, f_i the mass source rate and K_i the gain or loss rate of species i due to chemical reaction. f_m is the momentum source. These equations have to be coupled with the control equations:

$$\sum_i Y_i = 1 \tag{1.39}$$

$$\sum_i f_i = f \tag{1.40}$$

$$\sum_i K_i = 0 \tag{1.41}$$

$$\sum_i \boldsymbol{\nabla} \cdot \rho_g D_i \boldsymbol{\nabla} Y_i = 0 \tag{1.42}$$

The effects of liquid droplet spray motion and vaporization can be described by the spray equation:

$$\frac{\partial N}{\partial t} + \frac{\partial N e_{rate}}{\partial R} + \boldsymbol{\nabla} \cdot (N \mathbf{v_d}) + \boldsymbol{\nabla}_\mathbf{v} \cdot (N \mathbf{F}) = N_{source} \tag{1.43}$$

with N the droplet number density, e_{rate} is the droplet evaporation rate (comparable to $\frac{\partial_R}{\partial t}$), R the droplet radius, $\mathbf{v_d}$ the droplet velocity, $\mathbf{F}$ the sum of the external body forces on each droplet and N_{source} the generalized source and droplet interaction term. The objective of the evaporation experiment done in this manuscript are to form an equation that is similar to the equation 1.43.

The work from Vaillancourt et al. [84, 85] presents a more complex model that is including the turbulence to investigate its effect on the growth of droplets in a cloud aerosol. The supersaturation is computed using an implicit method based on the Newton–Raphson method. In the Vaillancourt study, the average interdroplet distance is of the same order of magnitude as the typical Kolmogorov length scale in clouds (1 mm). Turbulence is therefore expected to be as important as molecular diffusion in determining the ambient conditions in which an individual droplet grows. Consequently, neglecting turbulence would seem unrealistic unless the flow is near laminar. However, in a first time, this approach is still very useful because it offers a much simpler context to interpret the effect of sedimentation and the sensitivity of spectral broadening to various initial conditions. There the objective is to analyse the evolution of a population of droplets. The grid size used is 0.125 cm, the time step is 10^{-2} s, and the number of grid points is 120^3. The dimension of the computational domain is therefore 15^3 cm^3 and there are approximately 50000 droplets in the domain.

Experimental investigations

Regarding the experimental investigation of evaporation of aerosol, in the literature, the different papers mostly consider aerosol of a single droplet, which is similar to the evaporation bibliography seen in section 1.1.2 [86–90].

1.2.3 Droplets evolution in von Kármán swirling flow

The von Kármán flow is not the most famous flow especially when you compare it to the Taylor-Couette flow or the Poiseuille flow inside a cylinder. Throughout time, this flow developped and does not have a lot in common with the initial problem done by Theodore von Kármán (VK) in 1921[91]. The hypothesis of this flow are simple:

- The flow is following the Navier-Stokes law.
- The flow is contained between a rotating flat disks and a stationary one.
- Their rotation speed is controlled.

Theodore von Kármán knew that those hypothesis allowed for an analytical simplification of the Navier-Stokes equation. In 1951, G.K. Batchelor proposed a generalization to two contra-rotating flat disks (see figure 1.17) [92].

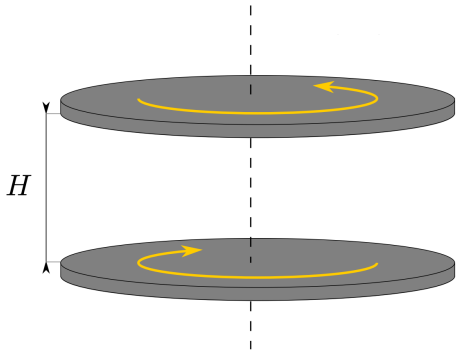

Figure 1.17: Configuration proposed by Batchelor 1951 [92]. Two flat infinite disks separated by a distance H are stirring the fluid.

Each of the flat disk then drives one half of the fluid in quasi-solid rotation, and a shear layer at the center ensures the continuity of the velocity field. This configuration makes it possible to give a definition of the Reynolds number of the flow, where the characteristic length is chosen as the distance between the discs [93]. Particle Image Velocimetry has shown the possibility to investigate extreme inertial dissipation events which are associated with the existence of velocity fronts, saddle points, spirals, jets and, in some cases, suggestive of cusps [94]. As predicted by the theory [95] of critical points, these kinds of topologies are typically associated with special configurations

of eigenvalues of the velocity strain tensors around critical points of flow patterns. At such points, it is often the case that Lagrangian trajectories cross with no speed (see figure 1.18). With that in mind, in a flow composed of air and microscopic water droplet, the crossing of the Lagrangian trajectories mean that the water droplets can come in contact with each other and coalesce eventually. In warm (i.e., above-freezing) clouds, droplets grow by collision-coalescence to form drizzle droplets or raindrops, a few hundred micrometers to several millimeters in diameter [96]. Rainfall produced in such a way (referred to as warm rain, in contrast to precipitation formed by ice processes) accounts for approximately 30% of the total rainfall on the planet and roughly 70% of the total rain in the tropics area [97].

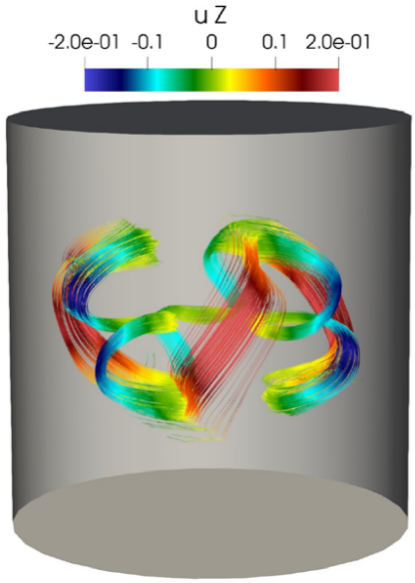

Figure 1.18: Three-dimensional streamlines coloured by u_z, $Re = 29000$. It is referred to as helical mode. Figure copied from [98].

The unique conditions in which our experiment takes place is close to mimic the conditions in clouds where turbulence is occurring and creates movement of the droplets, the von Kármán flow might be able to create the conditions to observe the collision-coalescence mechanisms. There is no literature for this type of flow with droplets in gas as it requires microgravity to create a stable aerosol first. The idea is to use the microgravity conditions to create reference experiment.

1.3 Cloud Microphysics

From aerosol in a lab, the idea is to enlarge the objective and look at clouds. Especially the real microphysics happening inside them. The clouds have different names based on their altitude, temperature and shape. They are briefly described in figure 1.19. In this section, the focus will be on three key aspects of cloud microphysics: the nucleation of water or ice, the Wegener Bergeron Findeison effect and turbulence inside clouds.

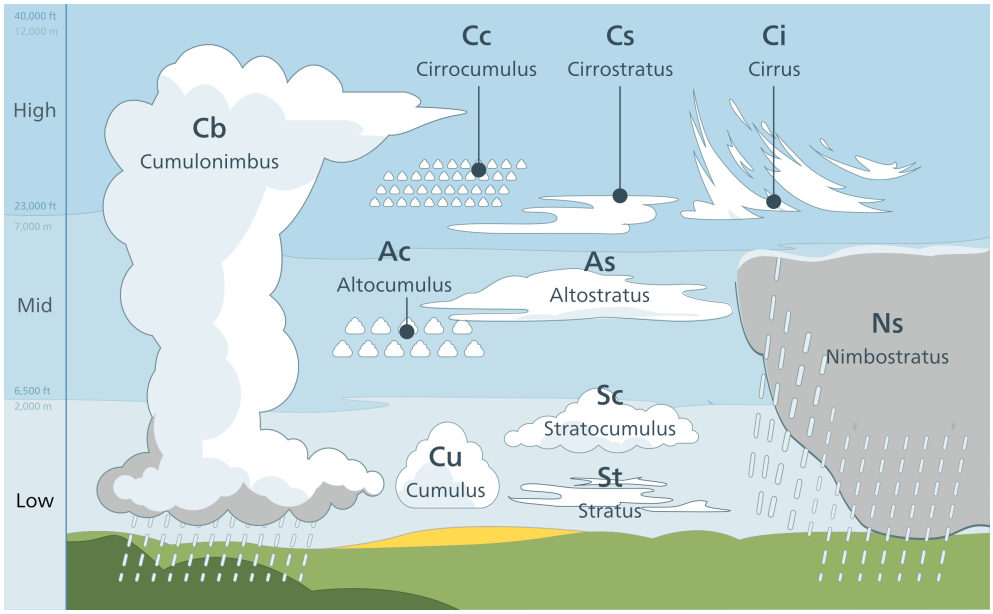

Figure 1.19: Visualization of the different cloud types in their respective altitudes. Figure copied from [99].

1.3.1 Nucleation

The phenomenon chosen for the creation of the aerosol is the nucleation of the droplet, in this part homogeneous and heterogeneous nucleation will be presented. In the experiment, heterogeneous nucleation is the most likely of the two to occur. Condensation of a vapour, evaporation of a liquid, melting of a crystal, crystallization of a liquid are examples of phase transition process occurring in clouds. Generally speaking, phase transition reflect the ability of physical systems to explore a huge range of microscopic configurations in accordance with the second law of thermodynamics. A characteristic feature of a phase transition is an abrupt change of properties. An example could be a gas cooled at constant pressure: first, the gas state changes continuously up

to a certain temperature at which condensation begins transforming gas into a liquid with different properties (density, viscosity, heat capacity...). The states of a component between which a phase transition takes place are called phases. If the difference between phases is of quantitative nature, it can in principle be detected through a microscope. In this case one speaks of a first-order transition. Condensation of gas is an example of such a transition in which coexisting vapour and liquid phases have essentially different densities. Close to the two-phase coexistence lines of a first-order phase transition one can find domains of metastable states. In particular, it is possible to raise the vapour pressure above the saturation pressure, so that in the domain where the liquid phase is thermodynamically stable, a metastable supersaturated vapour can exist. Similarly, where the vapour phase is stable, a metastable superheated liquid can exist. In the same fashion, where the crystalline phase is stable, a metastable supercooled liquid can exist.

The occurrence of these metastable states originates from the requirement for nucleation. The phenomenon of nucleation is associated with the nonequilibrium first-order transitions transforming a metastable parent phase to a thermodynamically stable daughter phase. The transformation takes place through the creation of small clusters of molecules of the daughter phase out of the parent phase by thermal fluctuations. Although the parent phase is metastable with respect to the bulk daughter phase, it can remain stable with respect to small clusters of the daughter phase. The reason for this is that the thermodynamic properties of the clusters differ from those of the bulk because of the presence of an interface between the phases. Whenever there is an abrupt change in the parent and daughter phases, there is a thermodynamic cost in creating this interface. Due to this reason the parent phase can remain present in conditions where the bulk daughter phase should be more stable [100].

Homogeneous nucleation and classical nucleation theory

At atmospheric pressure, a little below 0 °C, water will tend to freeze into ice but it needs nucleation to start the process, resulting in the presence of both ice droplets and liquid droplets. At lower temperature, below −35 °C, ice crystals appears instantly [101]. The same physical phenomenon will occur with a supersaturated water vapour nucleating into liquid water droplets.
Physically a supersaturated vapour corresponds to a local minimum of the free energy (illustrated in figure 1.20). Metastability means that the system in this state (state A in figure 1.20) is stable to small fluctuations in the thermodynamic variables but after a certain time will evolve to state B corresponding to the global minimum of the free energy (bulk liquid). In

order to perform this transformation, this system has to overcome a barrier, representing a local maximum of the free energy. The latter corresponds to an unstable equilibrium state in which the system is unstable with respect to small fluctuations of the thermodynamic variables. To overcome the energy barrier a fluctuation is required which causes a formation of a small quantity (cluster) of the new phase called nucleus, and then the growth of the droplet over the nucleus can start.

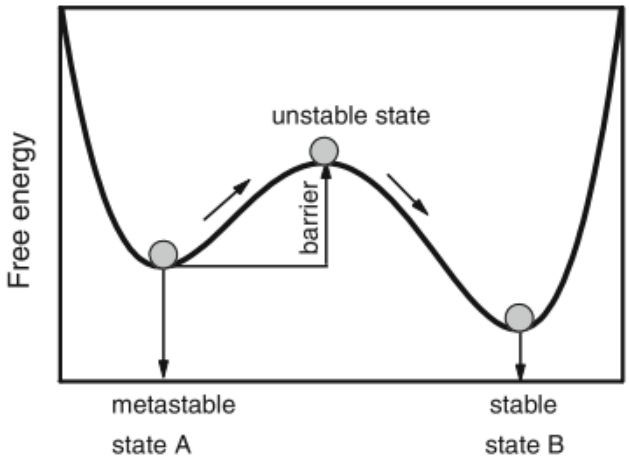

Figure 1.20: Free energy evolution as a function of an order parameter, the transition between A and B involves overcoming the free energy barrier. Figure copied from [100].

The driving thermodynamic force for this transformation of one mole is the difference in chemical potential (noted $\Delta\mu$) between the metastable state A where the vapour is supersaturated but does not have received the extra energy to nucleate and the unstable state that will lead to the stable state B in figure 1.20. This driving force could be expressed as a function of the supersaturation S, the temperature T and k_b the Boltzmann constant so that:

$$\Delta\mu = k_b T \ln(S) \tag{1.44}$$

From then on, the idea will be to focus on the formation of the cluster itself and the growth of the droplet. The key approximation of the classical nucleation theory (developed by Volmer, Weber, Becker, Döring and Zeldovich) [102–104] is the capillarity approximation. This approximation could be declined as:

- A cluster is viewed as a large homogeneous spherical droplet of a well defined radius with the bulk liquid properties inside of it and the bulk vapour properties outside it.
- The liquid is incompressible.
- The surface energy of the cluster containing n molecules (n-cluster) is presented as the product of the planar interfacial tension at the temperature T, $\gamma(T)$, and the surface area of the cluster $A(n)$.

The minimum work to form an n-cluster is equal to the change of the Gibbs free energy, with the previous assumptions, this energy could be expressed as:

$$\Delta G = -n\Delta\mu + \gamma A(n) \tag{1.45}$$

where $A(n) = 4\pi r_n^2$ with r_n the radius of the cluster. v_1 is the volume occupied by a single molecule

$$r_n = \left(\frac{3v_1}{4\pi}\right)^{1/3} n^{1/3} \tag{1.46}$$

The Gibbs free energy ΔG could then be expressed as a function of the number of molecules in the cluster $\Delta G(n)$. At small n the positive surface term dominates, making it energetically unfavourable to create a very small droplet in view of the large uncompensated surface energy. For large n the negative bulk contribution prevails. This function $\Delta G(n)$ has a maximum that will be n_c the critical number of molecules present in the cluster. The cluster containing n_c molecules is called a critical cluster; $\Delta G(n_c) = \Delta G^*$ represents an energy barrier which a system has to overcome to form a new stable (liquid) phase. Droplets with $n < n_c$ molecules on average dissociate whereas those with $n > n_c$ on average grow into the new phase [100]. The critical number n_c could be expressed as:

$$n_c = \left(\frac{2\gamma s_1}{3k_B T \ln(S)}\right)^3 \tag{1.47}$$

with $s_1 = (36\pi)^{1/3} v_1^{2/3}$ the "surface area of a monomer". The energy ΔG^* could be expressed as a function of the critical number n_c or by measurable parameters:

$$\Delta G^* = \frac{1}{3}\gamma A(n_c) = \frac{16\pi v_1^2 \gamma^3}{3(k_B T \ln(S))^2} \tag{1.48}$$

The last step to look at when there is nucleation is the nucleation rate or the number of droplets created by unit of volume. Within the classical nucleation theory, the following assumptions are made:

- the elementary process which changes the size of a nucleus is the attachment to it or loss by it of one molecule
- if a monomer collides a cluster it sticks to it with probability unity
- there is no correlation between successive events that change the number of particles in a cluster.
- the nucleation is a Markov process

With the hypothesis done by Becker and Döring [102], leading to the Becker-Döring equations, the nucleation rate could be calculated as:

$$J = J_0 \exp\left(\frac{-\Delta G^*}{k_B T}\right) \tag{1.49}$$

where J_0 is a constant pre-factor dependent of the surface tension, the mass of a molecule, the density of the liquid and the density of the vapour. It is important to keep in mind that the nucleation rate does not depends on size but is observed at the critical cluster size [100].

Miller's experimental approach

The theoretical approach explained previously has to be confirmed by experiment. To do so, Miller and associates used an expansion cloud chamber [105]. The expansion is done by a controlled movement of a piston, this movement will create an expansion of the the available volume for the gas. This technique was used initially by pioneers such as Wilson [106] or Coulier [107] to observe the phenomenon. A hundred years later, the process used is still the same but this time the objective is to quantify the nucleation process over a wide range of temperature (230 K-290 K). The design of the expansion cloud chamber is drawn bellow (see fig.1.21a). The objective of Miller's experiment was to quantify the homogeneous nucleation rate in the expansion cloud chamber. The detailed description of the chamber were done by Kassner [108] and Schmitt [109] and won't be described here. The main result of Miller's experiment is the establishment of an empirical law which link the nucleation rate to the supersaturation and the expansion minimal temperature. The nucleation rate is the derivation over time of the number of droplets created during the expansion. The number of droplets is counted by photography (timing indicated in figure 1.21b).

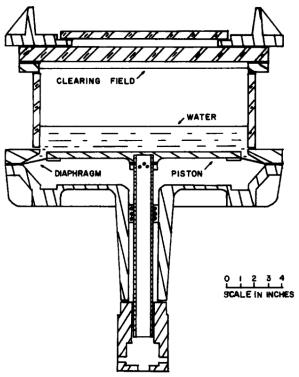

(a) Expansion cloud chamber used in Miller's experiments. Figure copied from [105]

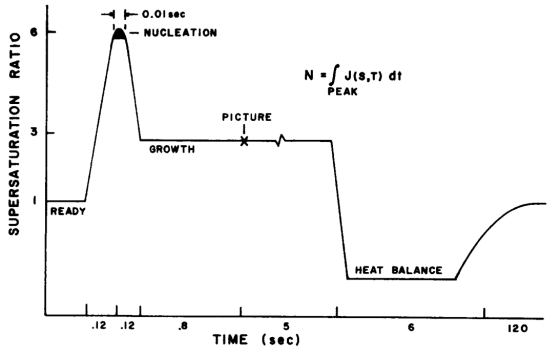

(b) Evolution of the supersaturation over time. Figure copied from [105].

Figure 1.21: Scheme and evolution of the saturation in Miller's experiment.

The nucleation process is controlled in terms of pressure and temperature. The pressure evolution in time is controlled and as a result the supersaturation (S) and the temperature (T) are known as a function of time.

$$S(P) = C_{S1} + C_{S2}Z + C_{S3}Z^2 + C_{S4}Z^3 \tag{1.50}$$

$$T(P) = C_{T1} + C_{T2}Z + C_{T3}Z^2 + C_{T4}Z^3 \tag{1.51}$$

$$P(t) = P_{min} + C_{p1}t + C_{p2}t^2 \tag{1.52}$$

where $Z = (1200/P) - 1.29$ with P in mmHg, the coefficients C_{Si} and C_{Ti} are fixed for each initial temperature. The main result of the study proposed by Miller is the fitting to the experiment of the equation 1.53, proposed by Hale and Plummer [110]

$$J(S,T) = S^2 \exp(A(T) + B(T)/\ln(S^2)) \tag{1.53}$$

Here, A and B are temperature polynomials.

$$A = x_0 + x_1T + x_2T^2 + x_3T^3 \tag{1.54}$$

$$B = x_4 + x_5T + x_6T^2 \tag{1.55}$$

The x_i coefficients are calculated via a non-linear least squares fits on the entire data set.

$$Y = \sum_{i=1}^{N_{exp}} \left[\int J(S_i(t), T_i(t))dt - N_i \right]^2 \tag{1.56}$$

N_{exp} is the total number of expansions, S_i and T_i are respectively the supersaturation ratio and the temperature profiles of the i-th expansion and N_i the number of droplets counted during this i-th expansion. As expected the non-linear least squares fits produces great results to fit Miller's data. In figure 1.22, the temperature is a parameter, here it seems that to have the best fitting conditions, the minimal temperature recorded was used.

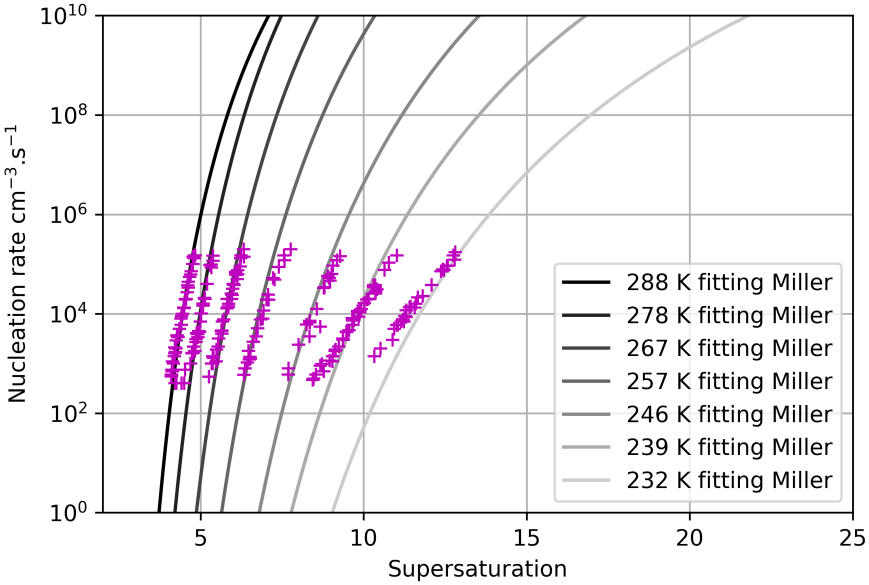

Figure 1.22: Evolution of the supersaturation over time and the fit from miller's law [105] the experimental points are in purple and the fitting law (eq 1.53) is in full line in grey.

Limit on the temperature validity domain for other experiments The fit is nice for Miller's data on a large range of temperature (230 K-290 K). However, the equation developed by Miller, to predict the nucleation rate, struggles to predict other experimental results especially when the temperature is at the limit of the validity domain. In fig 1.23, the objective was to use Miller's experimental law to fit the data from Viisanen [111] in red dots. As the figure 1.23 shows, Miller's experimental law is correct inside the temperature validity range. However, outside of the validity domain, the experimental law is less accurate.

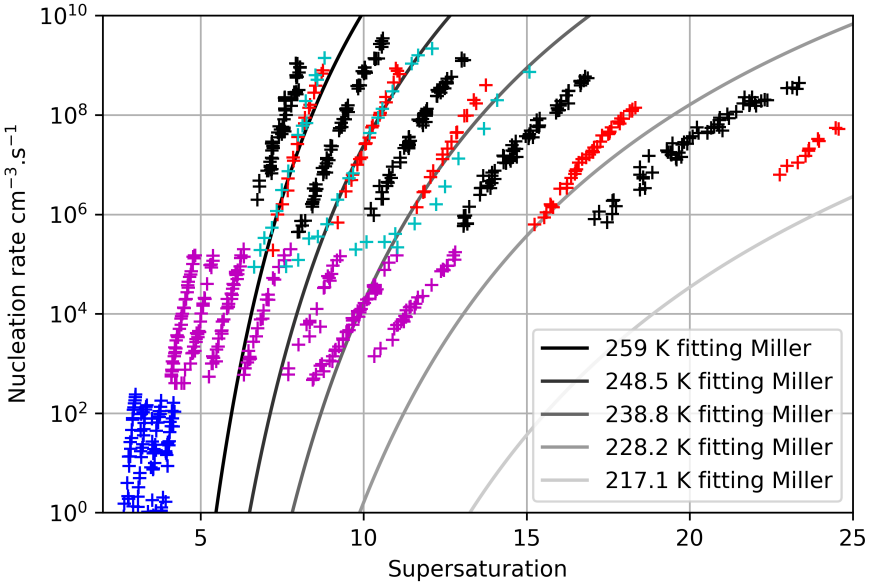

Figure 1.23: Evolution of the nucleation rate over the supersaturation and the fit from miller's law [105]. The experimental points from Viisanen [111] are in red, the experimental point from Wölk [112] are in black, the points in blue are from Brus [113] and the points in light blue are from Wagner [59].

The figure 1.23 is a record of the different experiment done by multiple teams. The techniques used are varying from one team to an other along with the carrier gas that's why the comparison should not be pushed too far, even if the carrier gas has little to no effect on the nucleation [111].

Heterogeneous Nucleation

Nucleation is very sensitive to the presence of impurities in the system. As a result, between homogeneous and heterogeneous nucleation, the latter is the most likely to occur in the AEROSOL experiment. As said previously in section 1.3.1, the nucleation is a phenomenon that happens when there is an excess of water vapour compared to the saturation pressure in the gas. As a result, the excess water in the gas has to change phase and form water droplets to decrease the supersaturation. The droplets are forming after a growth period from a nucleus. Either this condensation nucleus is a small water droplet formed by water molecules or this nucleus is an extra compound included in the present gas. When the droplets are growing from a nucleus not made of the vapour, the nucleation is qualified as heterogeneous nucleation. These pre-existing foreign particles are usually called condensation nuclei (CN). Clusters as well as CN can be liquid or solid. CN can be a planar

macroscopic surface, a spherical particle (liquid or solid). Here, the CN is considered to be electrically neutral and insoluble chemical compound in to the cluster formed on its surface, i.e. there is neither reactivity nor mass transfer between the CN and the liquid or vapour phases [100]. An example of heterogeneous nucleation, one experiences in the everyday life, is vapour-liquid nucleation on the surface of aerosol particles in atmosphere, leading to trails after planes reactors.

The process of condensational growth of aerosol particles got considerable experimental and theoretical attention due to its role in the environmental effects [114]. Classical theory of single-component homogeneous nucleation was explained previously. Later on, Lazaridis [115] extended Fletcher's theory (The size effect of the particle is significant for a radius between 0.01 to 0.1 μm , the nucleation efficiency is stable above this range but sharply reduced below it. [116]) to binary systems. The general approach to kinetics of nucleation processes remains valid for the heterogeneous case. The steady-state nucleation rate has the general form of eq 1.49 with a different prefactor leading to eq 1.57:

$$J(T) = J_{Het} \exp\left(\frac{-\Delta G^*}{k_B T}\right) \tag{1.57}$$

with J_{Het} the kinetic prefactor, ΔG^* the free energy of formation of the critical embryo from the foreign particle. As in the case of homogeneous nucleation, heterogeneous nucleation rate is determined mainly by the energy barrier ΔG^*. The presence of this "cloud condensation nuclei" (CCN) reduces the energy cost to build the cluster surface. Leading it to be the most predominant form of nucleation in nature, especially in clouds. Water vapour can condense on a soluble aerosol particle, because the Raoult effect (equilibrium water vapour pressure over a solution is lower than that over pure water) opposes the Kelvin effect that results from the small radius of curvature of the nascent droplet.

The classical Köhler theory [117] of cloud droplet formation is based on the concept that for each dry soluble particle size there is a "critical supersaturation" (supersaturation is defined as the saturation ratio minus one), SS on the figure 1.24, at which the difference between the Raoult and Kelvin effects is at a maximum (see figure 1.24). At this point, any infinitesimal increase in the size of the droplet will lead to spontaneous growth into a cloud droplet, since the Kelvin effect decreases with further increase of drop radius. Köhler theory predicts that SS decreases with increasing size of a soluble particle, or with increasing mass of a soluble substance contained in a mixed particle containing both soluble and insoluble components. Köhler theory predicts also that this subset is selected based on the amount of soluble matter in the

particle. For organic aerosols, however, a series of additional chemical effects can modify the ability of a particle to act as a CCN [118, 119]. Organic compounds in aerosols can influence CCN activity by several mechanisms: contribution of soluble matter, reduction of surface tension, and formation of hydrophobic surface films [120].

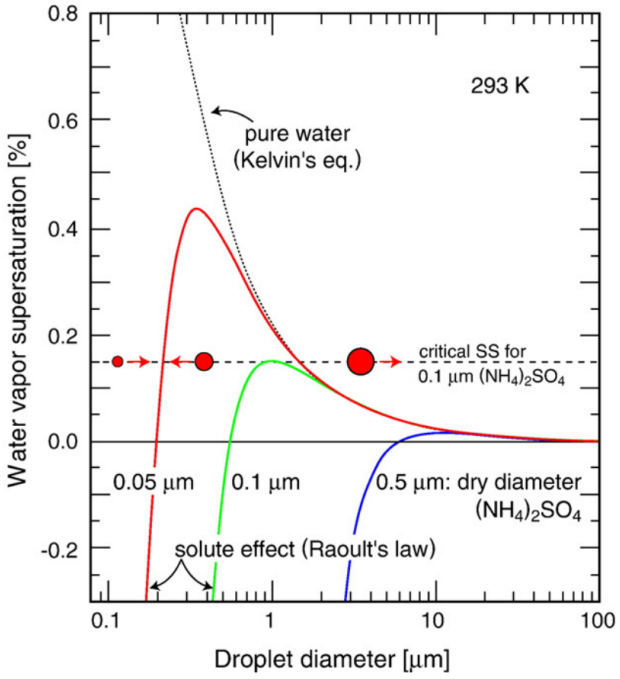

Figure 1.24: Köhler curves showing the equilibrium water vapour supersaturation at 293 K for droplets of pure water (dotted curve) and for droplets containing various masses of dissolved salts $(NH_4)_2SO_4$ (solid curves) vs. diameter of the droplet [121]. Here an ambient water vapour S of 0.15% (dashed line) exceeds the critical value for all ammonium sulfate aerosols with dry diameter $\geq 0.1\,\mu$m. These aerosols will therefore activate and grow into cloud droplets, whereas smaller particles remain nonactivated. Droplets below their corresponding equilibrium curve will shrink by evaporation whereas those above will grow by condensation (the indicated droplets correspond, for example, to a dry diameter of $0.05\,\mu$m). Figure copied from [120].

As an example, sea spray aerosols are formed by breaking waves via bubble bursting and by tearing of wave crests. When a wave breaks, air is entrained into the water and dispersed into a cloud of bubbles [64, 122]. In this fashion, it is possible to create the CCN that may or not be activated via the adapted nucleation conditions (see figure 1.24). Differences between the CCN in clean marine and polluted continental environments are primarily

responsible for the observed differences between microphysical characteristics of clouds developing in these environments [123].

1.3.2 Mixed clouds and Wegener Bergeron Findeison effect

One of the objectives of the AEROSOL project is to investigate the Wegener Bergeron Findeison effect directly. Although experiment were done, they are either using simulation, indirect measurement such as the scavenging efficiency or aircrafts [124–126]. There is a lack of microgravity duration that prevent the the observation of mixed phase clouds in parabolic flight.

The higher the cloud, the lower the temperature, for a standardised troposphere profile, the temperature decreases by 6.5 K every kilometre. This means that clouds gathered at a lower temperature are more likely to be made of ice as the figure 1.25 suggests. This could also be seen by analysing the Liquid Water Content (LWC) and the Ice Water Content (IWC). Around $-15\,°C$ the water density lines crosses each other suggesting that the cloud became more an ice cloud in mass majority. This evolution along the Total Water Content (TWC) evolution could be seen in fig 1.25.

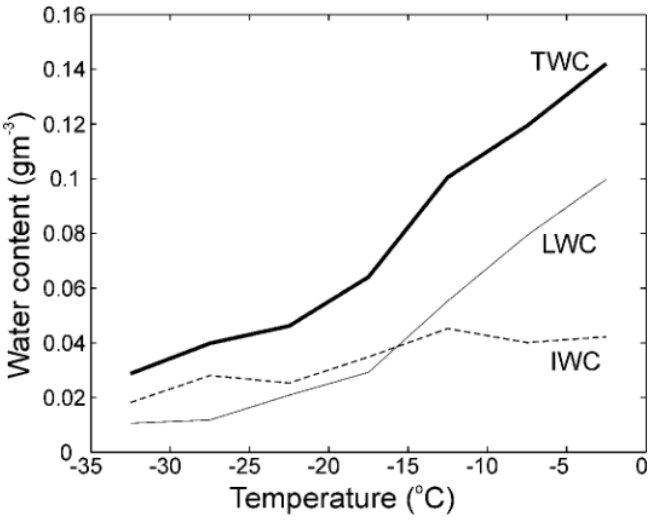

Figure 1.25: Visualisation of the evolution of the Liquid Water Content (LWC), the Ice Water Content (IWC) and the Total Water Content (TWC) as a function of the temperature. Figure copied from [127].

At lower temperatures and therefore lower pressures, the total water content decreases. The total pressure equation is given using the hydrosatic equation:

$$\frac{dP}{dz} + \rho_{air} g = 0 \tag{1.58}$$

As the air density is dependent of the temperature and pressure through the ideal gas law:

$$\rho_{air}(z) = \frac{P(z)}{r_{air} T(z)} \tag{1.59}$$

with $T(z) = T_0 - \alpha_T z$ where T_0 is the ground temperature and α_T is the decrease of temperature as altitude increases. The integration gives:

$$P(z) = P_0 \exp\left(\frac{g}{\alpha_T r_{air}} \ln\left(1 - \frac{\alpha_T z}{T_0}\right)\right) \tag{1.60}$$

with the use of the equation 1.62, it is possible to link the saturation pressure to the TWC using the total pressure equation. With this quite basic theory, the evolution of the TWC is captured. It decreases with the altitude in an exponential manner. The review from Korolev [127] also gives information about the droplet themselves, especially their number per unit of volume and mean radius. To analyse the particles diameter, the forward-scattering spectrometer probes (FSSP) along Nevzorov probes are used (see figure 1.26).

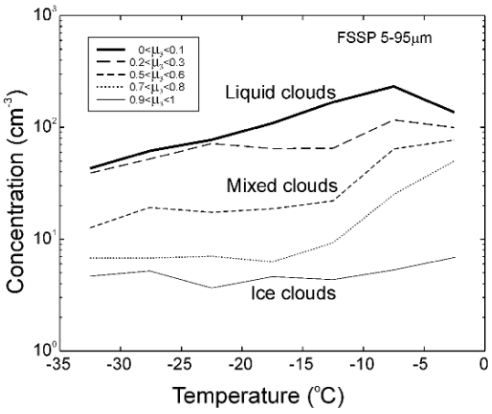

(a) Concentration for different cloud type as a function of the temperature using FSSP.

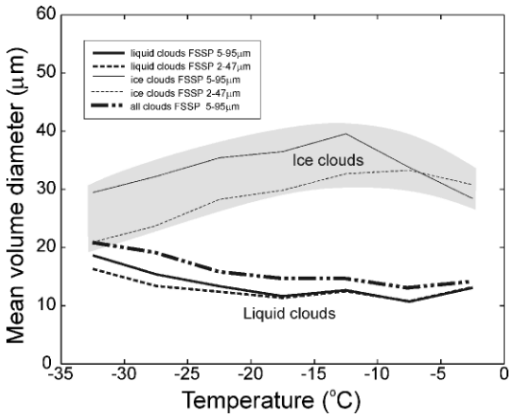

(b) Mean volume diameter as a function of the temperature recorded using FSSP.

Figure 1.26: Characteristics of the droplets (concentration and diameter) as a function of the temperature. Figure copied from [127].

Mixed-phase clouds (where ice particles, water droplet and vapour coexist) play an important role in the formation of precipitation, radiative transfer

for cloudy atmospheres, Earth's radiation budget, and climate. The relative proportion of water in the ice and liquid phases (or the 'phase composition') of clouds is an important cloud microphysical parameter. The phase composition affects the rate of precipitation formation and the life cycle of clouds [128]. Mixed-phase clouds are thermodynamically unstable and the process of phase transformation in them is often referred to as the "ice crystal theory," which originated in the works of Wegener [129], Bergeron [130], and Findeisen [131]. The Wegener-Bergeron-Findeisen (WBF) effect is the process where in these mixed phased clouds, ice particles grows at the expense of the water droplets. The basis of this theory is that the WBF effect will occur if the equilibrium water vapour pressure is higher than the saturation pressure over ice and lower than the saturation pressure over liquid water. As a result, within the mixture of these (ice and liquid) particles, and if the total water content is sufficiently high, the ice crystals would gain mass by vapour condensation at the expense of the liquid drops that would lose their mass by evaporation [132]. The condensation (or evaporation) rate is proportional to the difference between the cloud vapour pressure (P_v), the equilibrium pressure over the liquid water (P_v^{sat}) and the equilibrium pressure over ice (P_i). At sub freezing temperatures the equilibrium pressure over ice is larger than the one on the liquid giving: $P_v^{sat} > P_i$ [133].

$$P_i = 611.21e^{\frac{22.587T}{T+273.86}} \tag{1.61}$$

$$P_v^{sat} = 610.94e^{\frac{17.625T}{T+243.04}} \tag{1.62}$$

It leaves room for only three possibilities for P_v that will entail three evolutions of clouds:

$$P_v > P_v^{sat} > P_i \tag{1.63}$$

$$P_v^{sat} > P_v > P_i \tag{1.64}$$

$$P_v^{sat} > P_i > P_v \tag{1.65}$$

When eq 1.63 is satisfied, both droplets and ice particles grow because the vapour pressure is over the thermodynamical limit. Korolev and Mazin [134] showed that this occurs when the mixed-cloud phase is moving upwards at a speed u_z over the limit of u_z^* ($u_z > u_z^*$).

$$u_z^* = \frac{P_v^{sat} - P_i}{P_i}\eta^*(P_g, T)N_i \langle R_i \rangle \tag{1.66}$$

where η^* is a coefficient dependent of the gas pressure P_g and the temperature of the cloud phase T, N_i and $\langle R_i \rangle$ are the number of particle per unit of volume and the mean radius of ice particles. For typical values of $N_i \langle R_i \rangle$ in clouds ($10^{-2} - 10^2\,\mu$m.cm^{-3}) [135] the vertical velocity required to grow ice and water droplet simultaneously ranges from a few cm.s^{-1} to a few m.s^{-1}. Such velocities are often observed in clouds (see section 1.3.3). These conditions are also satisfied during isobaric mixing at velocities close to zero but with different temperatures [134].

When eq 1.65 is satisfied, the particles whether made of ice or liquid will evaporate to saturate the local volume as the partial vapour pressure is below saturation pressure of either ice or liquid water.

The WBF effect occurs when equation 1.64 is verified. The water droplet and ice particle will then play opposite roles and the liquid water droplet will feed the ice particle growth. This may occur in both upward and downward cloud movement if the condition ($u_z^0 < u_z < u_z^*$) is valid with:

$$u_z^0 = \frac{P_i - P_v^{sat}}{P_v^{sat}} \eta_0(P_g, T) N_w \langle R_w \rangle \tag{1.67}$$

where η_0 is a coefficient dependent of the gas pressure P_g and the temperature of the cloud phase T, N_w and $\langle R_w \rangle$ are the number of particle per unit of volume and the mean radius of liquid water droplets. The different velocities are plotted in the fig 1.27, the speed u_z^* is always increasing in the range 10 to 12000 m altitude. This range is taken arbitrarily here at the end of the troposphere, this is where most of the liquid water content is and as this is the subject in the study, there is no need to focus on the evolution of the different parameters further in altitude.

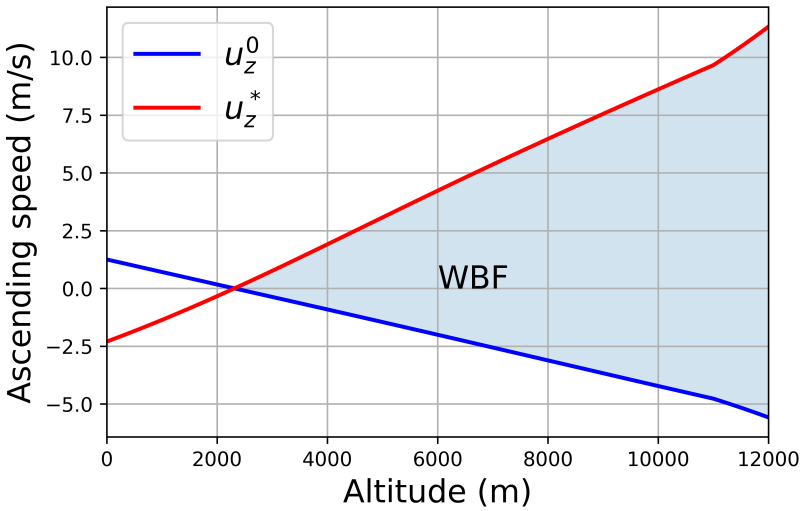

Figure 1.27: Visualisation of the different speeds as a function of the altitude, the blue curve represents the speed u_z^0, the red curve represents the speed u_z^*. Droplets, in the blue coloured area experience the WBF effect. The speeds are plotted for representatives concentration ($N_i = 2\,\mathrm{cm}^{-3}$ and $N_w = 80\,\mathrm{cm}^{-3}$) and radius ($R_i = 15\,\mu\mathrm{m}m$ and $R_w = 7.5\,\mu\mathrm{m}$).

As this is an unstable process (because $P_{sat} > P_v > P_i$), the liquid water droplets will evaporate and the ice particles will grow. According to Korolev and Mazin [134], this process shall last a few minutes. However, up to $-40\,^\circ\mathrm{C}$ liquid and ice particles may coexist [136]. The record in figure 1.28 shows that for different in-situ measurements, the bulk density (μ_3) is usually either low (inferior to 0.2 leading to a liquid in majority) or high (superior to 0.7 leading to a icy cloud in majority). This suggests that the WBF effect does not transform all the liquid droplets into ice but a majority of the glaciating process is done as liquid and ice water droplets do not coexist in equivalent ratios. However, the minima in frequency suggests that for every travel, the WBF process is fully done as a result, the glaciating time is necessarily inferior to the residence time of the cloud parcel in a given position.

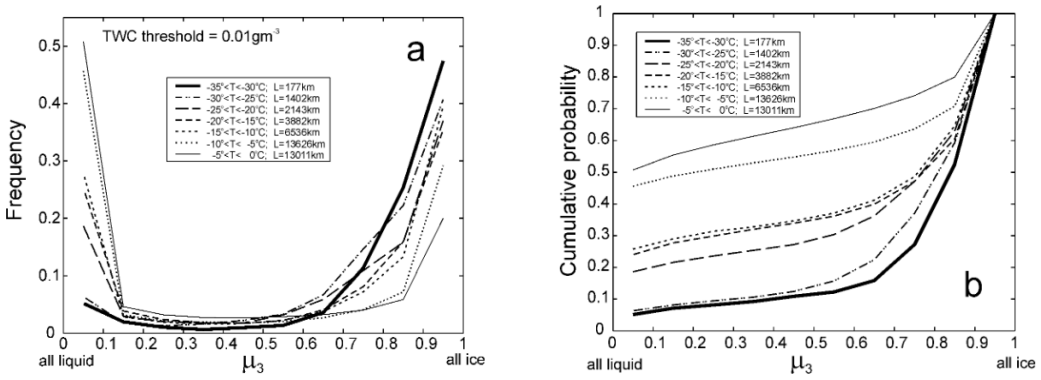

(a) Frequency of the observed clouds (ice or liquid)

(b) Cumulative probability of the observed clouds (ice or liquid)

Figure 1.28: Probability distributions of mixed-phase composition coefficient μ_3 for different temperature intervals. The value L is the length of clouds the measurement went through. Figure copied from [127].

1.3.3 Flows and turbulence in clouds

The differences in pressure and temperature, create movements throughout the clouds that impact the evolution of the present droplets. The different convection types are presented by Korolev in the review of 2017 [137], the figure 1.29 displays the different types of flows occurring in clouds that imply mixing between the phases. The clouds droplets after being created are subject to growth before falling to the ground in the form of rain or snow. Two key mechanisms are responsible for the droplet growth, the first to occur is the diffusion process, the second one is the growth by coalescence. During the diffusional growth, the rate at which the droplet radius increases is inversely proportional to the radius (see section 1.1.2). This implies that a larger droplet grows more slowly than a smaller one, and this mechanism favours a narrow droplet-size distribution if one considers only growth by diffusion. In warm (i.e., above-freezing) clouds, droplets can further grow by collision-coalescence to form drizzle droplets or raindrops, of a few hundred micrometers to several millimetres in diameter. Rainfall produced in such a way (referred to as warm rain, in contrast to precipitation formed by ice processes) accounts for approximately 30% of the total rainfall on the planet and roughly 70% of the total rain area in the tropics [97]. After an initial growth due mostly to diffusion, the collision process will take the lead in the growth of the droplets. Gravitational collisions between cloud droplets, in which larger droplets grow by capturing smaller droplets by collision-coalescence, are effective when the droplet radius reaches approximately $40\,\mu$m [123].

The collision-coalescence of droplets is greatly affected by the cloud convection on different scales. When droplets are suspended in a turbulent cloud, they are transported and dispersed by large-scale energy-containing turbulent eddies of the order of 100 m. At the same time, they alter the local environment through mass (condensation and evaporation), momentum (viscous drag), and energy (latent heat) transfer at the scale of individual droplets. For example, the phase transformation between water vapour in the air and the liquid water in the droplets, taking place at the droplet scale, introduces bulk buoyancy effects that drive cloud-scale motions. The great density contrast between the droplet and the air implies a significant droplet inertia and terminal velocity, making the droplet-turbulence interaction non-local and multi-scale by itself. Therefore, interactions between cloud dynamics and cloud microphysics in a turbulent cloud represent complex multi-scale and multi-phase problems [138].

The radius of a cloud droplet is typically in the order of 1 to $20\,\mu$m, with volume and mass fractions of approximately 10^{-6} and 10^{-3}, respectively. Therefore, the presence of cloud droplets has a negligible effect on the

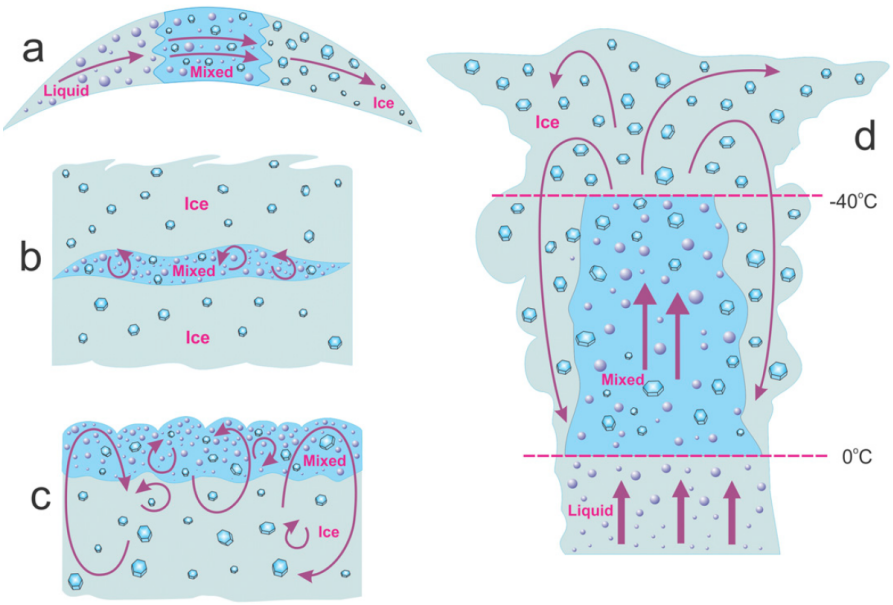

Figure 1.29: Conceptual model of the effect of dynamic forcing on the formation of the mixed-phase in different types of cloud: (a) Wave clouds, occuring in slow altocumulus; (b) frontal clouds, cirrostratus–nimbostratus; (c) boundary layer clouds, stratus–stratocumulus; and (d) deep convective clouds, cumulonimbus, convective storms. Figure copied from [137].

air turbulence. However, when water vapour condenses or evaporates from cloud droplets, the mass and energy transfers between the moist air and the dispersed phase are crucial for the dynamics of clouds through the buoyancy effect. Air turbulence in clouds is characterized by large flow Reynolds numbers, small energy dissipation rates (compared to many engineering flows), moderate velocity fluctuations, and a wide inertial sub-range [138]. The dissipation rate ϵ is a key parameter and depends on the cloud type and age, the typical ϵ values are $10^{-3}\,\mathrm{m^2.s^{-3}}$ in stratocumulus, $10^{-2}\,\mathrm{m^2.s^{-3}}$ in cumulus, and $10^{-1}\,\mathrm{m^2 s^{-3}}$ or higher in cumulonimbus clouds [123, 135]. The root-mean square velocity u' is typically $1\,\mathrm{m.s^{-1}}$ and appears to increase with ϵ [139]. The Taylor micro-scale Reynolds number is given by the equation:

$$Re_\lambda = u'^2 \sqrt{\frac{15}{\nu\epsilon}} \tag{1.68}$$

with a typical value of $u' = 1\,\mathrm{m.s^{-1}}$ and $\epsilon = 0.01\,\mathrm{m^2.s^{-3}}$, Re_λ is in the order of 10^4, the integral length scale or the scale of entraining eddies is equal to $l = u'^3/\epsilon = 100\,\mathrm{m}$, and integral timescale T_e is equal to $l/u' = 100\,\mathrm{s}$. In contrast, the Kolmogorov characteristics η, τ_k and v_k are equal to $\eta =$

$(\nu^3/\epsilon)^{0.25} = 0.8\,\text{mm}$, $\tau = \sqrt{\nu/\epsilon} = 0.04\,\text{s}$, and $v_k = (\nu\epsilon)0.25 = 2\,\text{cm.s}^{-1}$ respectively. Therefore, the typical scale separations are $l/\eta = 105$, $T_e/\tau_k = 2,500$, and $u'/v_k = 50$.

We note that the smallest scales governing the temperature and water-vapour fluctuations are similar to η as the thermal diffusivity κ of air and the diffusivity D_{va} of water vapour are similar in magnitude to the kinematic viscosity ν of air, with $\nu/\kappa = 0.71$ and $\nu/D_{va} = 0.60$ under atmospheric conditions. Even if cloud droplets are small ($R < \eta$), their motion is tightly coupled with the air turbulence. This can be seen by comparing the droplet inertial response time $\tau_p = 2\rho_w R^2/(9\mu_{air})$ and still-fluid terminal velocity $V_{term} = \tau_p g$ to the Kolmogorov scales. For droplets with radius R varying between $10\,\mu$m and $60\,\mu$m, the Stokes number varies from 0.01 to 2, and the non dimensional settling parameter V_{term}/v_k varies from 1 to 40 [140]. Hence the gravitational settling is almost always important, whereas the inertial effect is weak for small ϵ and significant for large ϵ. Both parameters increase rapidly with droplet size, which demonstrates the strong non-linear nature of droplet-turbulence interactions. It is also important to keep in mind that cloud turbulence most likely exhibits strong large scale inhomogeneity and non stationarity. For instance, interfacial instabilities responsible for the cauliflower-like appearance of cumulus clouds provide a strong and intermittent source of turbulent kinetic energy [141].

Cloud simulations, are usually climatological simulations limited in the domain size/resolution because they are dealing with fairly large domains ($1000^2\,\text{km}^2$ for the COSMO-DE [142]), as a result the microphysics is modelled and the thermodynamical conditions are averaged over the grid resolution (7 km in that case). Having such models in general is not that much of an issue as the validation parameters are done by satellites or ground stations that can't have a resolution to the droplet level [142–144]. At the scale of clouds, it is important to keep in mind that all cloud droplets are not exposed to the same supersaturation because the droplets are not homogeneously distributed in space, there is a range of droplet sizes, or there are small-scale vertical velocity fluctuations along with small temperature and pressure fluctuations within the parcel. In those situations, individual droplets are expected to experience different supersaturations. This inhomogeneity in thermodynamical conditions forces accurate models to describe the growth of droplets individually [145]. Elementary considerations demonstrate that the humidity and temperature gradients in the droplet vicinity are established rapidly i.e., with a characteristic timescale of milliseconds or smaller, leading to homogeneous thermodynamical conditions in the vicinity of the droplet [84, 85]. Vaillancourt [85] reported the first study that uses DNS (Direct Numerical Simulation) of homogeneous isotropic turbu-

lent flows carrying a large number of droplets growing by diffusion of water vapour. The study considered a small volume (approximately 1 litre) from the adiabatic (i.e., undiluted) cloud. The statistically stationary 3D turbulent flow field is obtained from DNS using the pseudospectral technique [146] as implemented in Bartello et al. [147]. The flow is forced by a method of Sullivan et al. [148]. To obtain statistically stationary 3D turbulent flows, the forced incompressible Navier–Stokes equations in 3D are solved. The parameters that must be specified for these turbulent flow simulations are the momentum viscosity coefficient, the forcing radius, which determines how many modes are forced, and the initial mean kinetic energy per unit mass. In contrast to previous studies of particle-laden turbulent flows, Vaillancourt included droplet sedimentation. The typical droplet sedimentation velocity is approximately $1\,\mathrm{cm.s^{-1}}$ and is comparable to the Kolmogorov velocity scale for typical turbulent dissipation rates in clouds. Only for significantly larger dissipation rates, typical for laboratory experiments with particle-laden turbulent flows, the sedimentation can be neglected [149].

The simulations reported by Vaillancourt also clearly show the effect of turbulence on droplet clustering. The effects of the turbulence on the droplet growth magnitude by diffusion only are small, if not insignificant. However, the turbulent flow significantly decreases the dispersion of the instantaneous distribution of supersaturation perturbation. The reduction is even more significant in terms of the dispersion of the degree of growth. The key argument is that the negligible effect of the small-scale turbulence can be understood as a rapid rearrangement of droplet positions. Turbulence influences cloud droplets that grow faster in one region (because the local droplet number concentration is lower and the supersaturation higher) by subsequently moving them to a region where the local droplet number concentration is higher and the supersaturation is lower, averaging the growth overall. Such changes occur rapidly, with typical times for supersaturation perturbation of less than a few seconds. The key point is that diffusional growth is reversible and position dependent, in contrast to irreversible growth by collision-coalescence that was not taken into account in these simulations. Similar simulations reported by Lanotte [150] led to broadly similar conclusions.

Chapter 2

Description and qualification of the AEROSOL facility

This chapter presents the AEROSOL facility, the first part describes the need for microgravity and the different ways to access it. Then this chapter will present the experiment carried inside parabolic flights.

2.1 AEROSOL project

The creation of the prototype for this project represents an initial step towards developing a more comprehensive instrument specifically designed for the study of aerosols. This instrument will incorporate diagnostics from optical microscopy, and Fourier-transform infrared spectroscopy. The primary goal of this project was the development of an insert dedicated to aerosol research within the scope of the DECLIC-Evolution program in the ISS.

2.1.1 Microgravity relevance

To study the stability of a cloud and eventually mass and heat transfer between droplets, the first thing is to have a stable aerosol. Here, we consider a single water droplet of radius R inside air at a temperature of 20 °C, as the aerosol is a dispersed media there is sufficiently low interactions between the droplets to consider the following argumentation valid for a complete aerosol. According to the Stokes law, for a hard sphere and a Reynolds number much lower than one, the drag force resulting of a flow around a spherical body is given by equation 2.1 with μ_{air} the air dynamic viscosity and $\mathbf{v}$ the velocity of the droplet.

$$\mathbf{F}_{drag} = -6\pi\mu_{air}\mathbf{v}R \tag{2.1}$$

The balance of the forces, projected along the vertical axis, gives first order derivative equation 2.2.

$$\frac{4}{3}\pi\rho_{water}R^3\frac{dv}{dt} = \frac{4}{3}\pi(\rho_{water} - \rho_{air})R^3g - 6\pi\mu_{air}\mathbf{v}R \tag{2.2}$$

The equation 2.2 will settle the speed (named terminal speed) of a falling droplet inside air to v_{term} shown in eq 2.3 with R the radius of the droplet, g the gravity constant.

$$v_{term} = \frac{2(\rho_{water} - \rho_{air})R^2g}{9\mu_{air}} \tag{2.3}$$

A more precise approach would lead to the Hadamard-Rybczynski law by considering a soft sphere with its own viscosity. Here v_{term} is adjusted in equation 2.4 with the dynamic viscosity of the sphere. The difference in between the two approaches is lower than 1% in this case, so we will keep the hard sphere model.

$$v_{term} = \frac{2(\rho_{water} - \rho_{air})R^2g}{3\mu_{air}}\frac{\mu_{air} + \mu_{water}}{2\mu_{air} + 3\mu_{water}} \tag{2.4}$$

As a result, the lower the gravity, the lower the terminal speed is. A droplet that is moving slowly is easily tracked and reconstructed using optical tomography microscopy. The radius of the droplet is directly linked to the formation process used to form the aerosol. In the end, a reduced gravity is the only way to study the stability of an aerosol and to prevent a settlement phenomenon. In Low-Level Stratiform Clouds, the record of the cloud droplet size distributions given by N. Miles [151] gives a average radius of approximately 10 μm for falling droplets. The Stokes law (equation 2.3) gives a settling velocity of 2.989 mm.s^{-1}. This speed is way too high to track the evolution of the droplets with a camera which has a field of view of 1 mm^2 and with velocimetry software. As the droplets created in this study are approximately the same size, it is required to have microgravity to study the aerosol stability.

2.1.2 Methods to access microgravity

As the previous section showed, there is a need for micro gravity to study the stability of aerosols and their evolution throughout time. There are different ways to access microgravity for different time periods and different duration

of experiment overall. The need for repeated experiment is a key factor in the choice that has to be made for the AEROSOL project. Here, four solutions are described. The first solution is the sounding rocket. Sounding rockets derive their name from the nautical term "to sound," meaning to measure or explore. Since 1959, NASA has employed these vehicles for space and Earth science research, utilizing them to test instruments intended for satellites and spacecraft and to gather data on the Sun, stars, galaxies, and the Earth's atmosphere and radiation. One of the main advantages of sounding rockets is their simplicity, cost-effectiveness, and efficiency. Developing experiments for the payload can be accomplished in approximately six months.

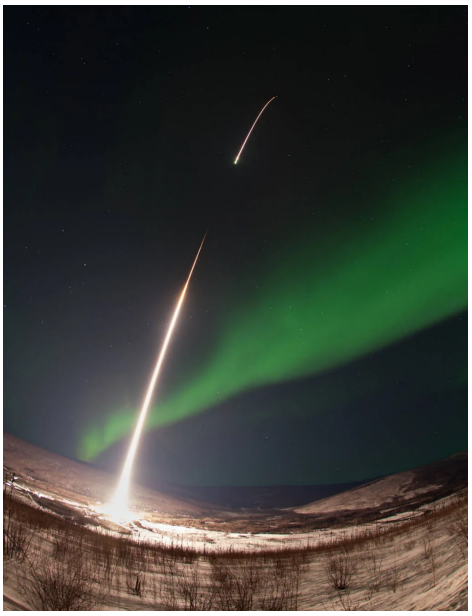

Figure 2.1: A heliophysics sounding rocket launches into an aurora in the early morning of March 3, 2014, over Venetie, Alaska. Credit: NASA/Christopher Perry [152]

A sounding rocket consists of two primary components: the payload and a solid-fuelled rocket motor. Many of these motors are surplus military motors, which helps keep costs low. Upon launching (see figure 2.1), the rocket uses its fuel, causing the motor to detach from the payload, which continues its ascent into space to conduct experiments. After completing its mission, the payload typically re-enters the atmosphere and descends safely back to Earth via parachute, allowing for recovery. This ability to refurbish and reuse components of the payload significantly reduces expenses. Scientific payloads can reach altitudes ranging from 48 km to over 1280 km. Although the time spent in space is relatively brief (usually between 5 to 20 min-

utes) the payload is ideally positioned to perform its intended experiments effectively. Data collected during the flight are transmitted back to Earth through telemetry links, similar to how radio signals work, relaying valuable information directly to researchers on the ground. This fast turnaround time makes sounding rocket testing an invaluable opportunity for students engaged in scientific research. Furthermore, sounding rockets provide the flexibility to conduct experiments in specific locations and times since they can be launched from temporary sites worldwide, including aircraft carriers. NASA's Wallops Flight Facility in Virginia hosts approximately 25 sounding rocket launches each year and boasts a 98 percent launch success rate. The Sounding Rocket Program has made significant contributions to the nation's space endeavours through its technical, scientific, and educational achievements [153].

The second possibility to have access to microgravity is by using drop towers. When an experiment is released from the top of a drop tower and before it lands on the padded ground below, it enters a state of free fall, effectively removing the influence of gravity. These brief moments of microgravity are available to scientists around the globe, serving as a budget-friendly alternative to space exploration and accessible throughout the year. The European Space Agency (ESA) operates the ZARM drop tower in Bremen, Germany (see figure 2.2).



Figure 2.2: The ZARM drop tower in Bremen, Germany. Operated by the ESA [154].

Standing at 146 meters, this concrete tower is on the Bremen University campus, and have been launching over 5,000 experiments since it opened in 1990. ZARM provides 4.74 seconds of near-weightlessness up to three times daily, with the option to extend this period using a catapult system that launches the experiments upward before they descend. The drop tube is crafted to be detached from the outer framework, allowing it to move freely with the wind while keeping the inner tube and the experiments shielded from vibrations. The experiment capsules have a diameter of 80 cm and can reach lengths of 2.4 meters. They are securely sealed under pressure with an aluminium cover, and the drop tube is under vacuum to reduce air drag during the fall. It takes 18 pumps about 90 minutes to evacuate the air from the 1700 m^3 tower. Throughout the 110 meters of free fall, experiments experience a mere 10^{-6} times the gravitational pull felt on Earth. Weightlessness ends when polystyrene beads cushion the container's landing. Afterward, it takes around 20 minutes to refill the drop tower with air, enabling researchers to collect their experiments [155].

The third possibility to have access to microgravity is with the use of planes, like the Airbus A310 Zero G (see figure 2.3) from Novespace which support parabolic flight programs, designed to support various scientific needs in microgravity. It caters to users starting microgravity experiments, those collecting data for potential long-duration space studies, users needing to test experiments before space flights, as well as research involving human subjects and student-led experiments. The Airbus A310 Zero G features the largest experimental microgravity area in the world, with a floor space of 100 m^2 and a volume of 200 m^3. It can host 10 to 15 experiments for a payload per rack up to 140 kg and up to 40 experimenters per flight. The area is fully padded, equipped with fixation rails for experiments, safety nets, and straps. Cabin pressure stabilizes 10 to 20 minutes after take-off at 825 ± 5 hPa until the end of parabolic flights. The cabin temperature ranges from 17 to 20 °C during flight and remains unregulated on the ground. In-flight humidity can reach up to 15%, while vibration levels depend on flight phases and the experiments conducted. Noise levels vary between 70 to 75 dB during weightless phases and reach 80 dB during $1.8g$ phases. The precision of achieving weightlessness is ± 0.02 g in the X-axis (from end to nozzle of the plane), $\pm 0.01g$ in the Y-axis (from right wing toward left wing), and $\pm 0.03g$ in the Z-axis (from floor to ceiling of the cabin) [156]. This is the solution chosen for the experiment done in microgravity in the context of this manuscript as the multiple parabolas allow for long duration of microgravity (around 22 seconds) and reproducibility of experiment with the 93 parabolas per campaign.

The last possibility to have access to microgravity is with an insert inside



Figure 2.3: Side view of the Airbus A310 Zero G from Novespace [157].

the International Space Station(ISS). The concept of a space station evolved over centuries, beginning with early theoretical contributions from figures like Johannes Kepler and Edward Everett Hale. By the mid-20th century, both the US and the Soviet Union were actively developing plans for such structures, culminating in the construction of the International Space Station (ISS). Officially approved in 1984, the ISS emerged from a collaborative effort involving multiple international partners, including NASA, Roscosmos, the European Space Agency, the Japan Aerospace Exploration Agency, and the Canadian Space Agency. The construction of the ISS began in earnest in 1998, following a phased approach that included collaboration with the Russian Mir Orbital Station.

The ISS provides long-term access to microgravity, which is invaluable for scientific research across various disciplines. This unique environment enables experiments that examine the effects on living organisms and materials, free from the influence of Earth's gravity. For instance, in microgravity, flames behave differently, fluids exhibit altered behaviours due to surface tension, and biological processes can be studied in ways that reveal new insights about life. Research opportunities aboard the ISS include studies in human physiology, radiation effects, fluid dynamics, material science, and the examination of advanced states of matter, such as Bose-Einstein Condensates. The ISS's low Earth orbit enables detailed observations of Earth's features, weather patterns, and environmental changes, allowing researchers to collect real-time data during significant events, such as storms or volcanic eruptions. In summary, the ISS functions as a powerful laboratory where scientists can leverage the advantages of microgravity to conduct innovative experiments that would not be possible on Earth, ultimately contributing to advancements in knowledge that benefit humanity. The facility continues to thrive as a symbol of international collaboration in space exploration, with its operational life extending through at least 2030.

As described earlier, the objective of the project is to create an insert for

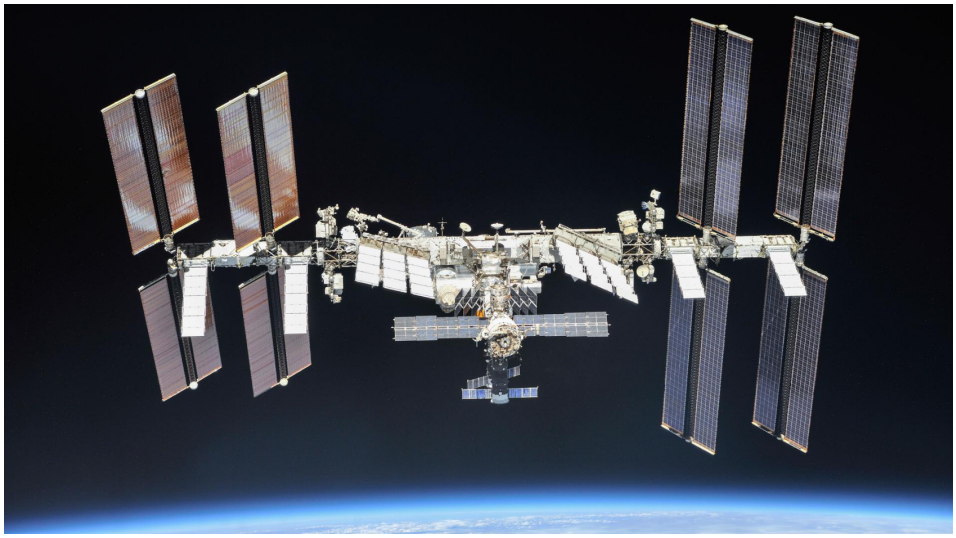

Figure 2.4: The International Space Station photographed by Expedition 56 in November 2018 [158].

the ISS, due to the cost and amount of preparation required to have an insert flying, in a first time, the experiment will go to its phase A where the objective is to prove the feasibility of the ISS insert. During this phase, experiments that only require short periods of microgravity are used to acquire experience for the preparation/conception of the ISS insert. The selected means to access microgravity is by parabolic flights.

2.2 General presentation

The experiment done during CNES 59th parabolic flight campaign demonstrated the possibility of stabilising the aerosol over sequences of about 22 seconds and studying their evolution. The solution used for aerosol formation is a device involving two separate chambers: An experimentation chamber (EC) of approximately $90\,cm^3$ in which the aerosol is created and a compression/expansion chamber (ECC) of $240\,cm^3$ for the control of the pressure changes necessary for the expansion and an isolation from the exterior. A diaphragm pump is used to achieve the compression from the ECC to the EC. The expansion is creating the droplets by nucleation inside the EC. The droplets are visualized inside the EC via optical tomography microscopy. Von Kármán (VK) swirling flows are generated in the EC using motors on the bases of the cylindrical EC. A schematic diagram is presented in figure 2.5. This approach has the advantage of producing drops that are uniformly

distributed in the experimental volume. The AEROSOL Rack can be seen in figure 2.6.

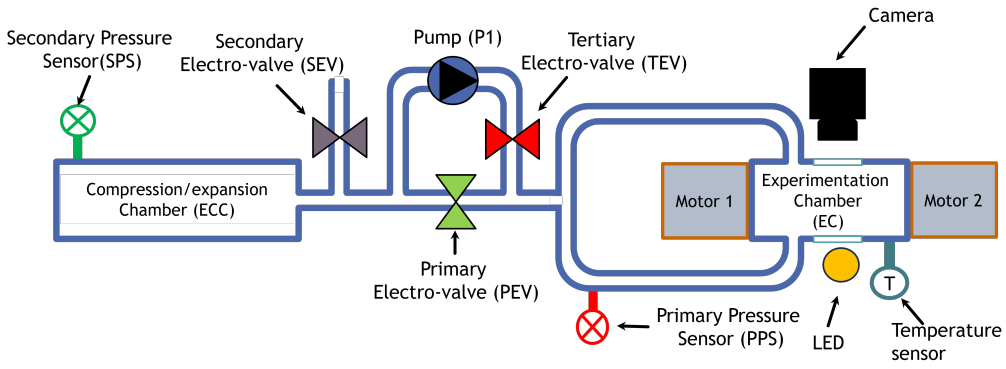

Figure 2.5: Scheme of the chamber and the pneumatic system used to control the pressure inside the EC.

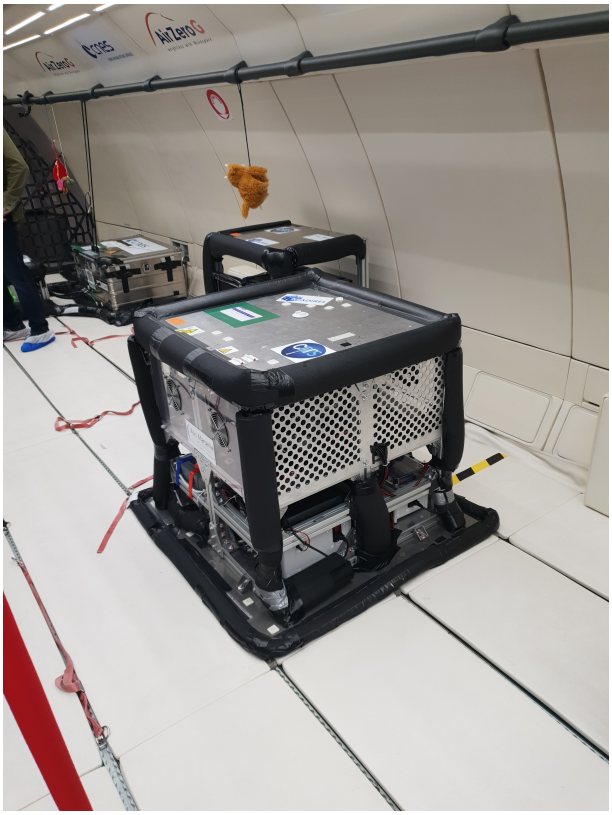

Figure 2.6: View of the AEROSOL Rack in the Airbus A310 Zero G.

2.2.1 Experimentation Chamber

The inside of the EC is a cylinder (3 cm diameter and 6 cm long) with its circular bases open to include engines with flat rotor on each side. This engines addition allows the creation of a VK flow inside the EC. This chamber also has two windows for microscopic analysis, one thermocouple and one hydrometric sensor

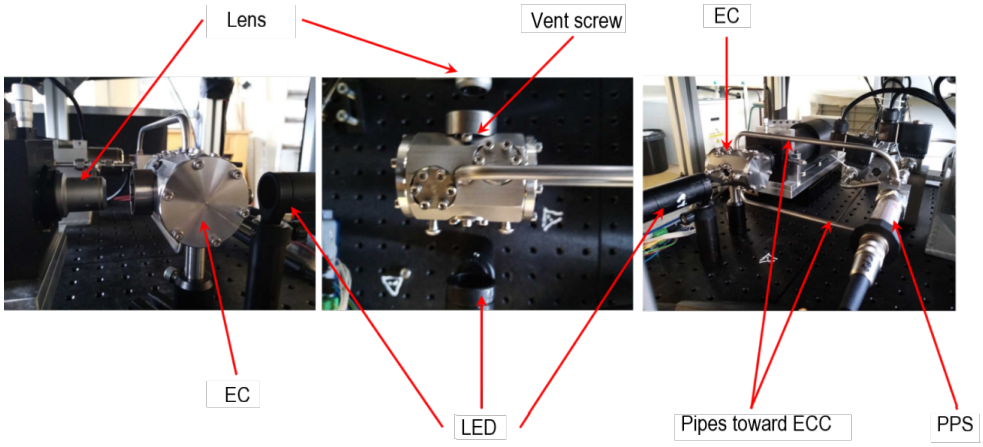

Figure 2.7: View of the EC, and different instruments.

2.2.2 Pneumatic Circuit

To create the expansion, a pneumatic circuit is necessary. The idea is to have two chambers, the EC and the ECC as described previously. During the compression phase, a pump compresses the air from the ECC into the EC (by starting the Pump P1 and opening the TEV, see figure 2.5). As a result, this system works in a close circuit and there is no reason to connect to the atmosphere (by opening the SEV). Therefore, once the humidity of the system is set-up on the ground, only leaks can impact the composition of the air inside the circuit.

Pump

The pump used is a membrane pump N86KNCD from the compagny KNF (see figure 2.8). This pump works with a power supply of either 12 V or 24 V and a required current of 1.3 A and 0.65 A respectively. The pump is powered by a RS PRO-3005 P supply and piloted by BE1 (Electrical Box 1).



Figure 2.8: View of the pump N86KNCD.

Electro-valve

The electro-valves used are the model Burkert 6013 (see fig 2.9) and piloted by BE2. BE2 has one electrical outlet, a circuit breaker of 30 mA, three independents outlets to pilot PEV, SEV, TET, one Com connexion towards the computer, and three outlets to power the PEV, SEV, TEV (see figure 2.5).



Figure 2.9: View of the valve Burkert 6013.

2.2.3 Engines and magnetic transmission

To create the VK flow, engines have to be used. The stirring device consists of two FAULHABER servomotors (4221G 024EXTH, see figure 2.10) equipped with an encoder (IE3-2024) and each controlled by a motion controller (MC5005 S RS).

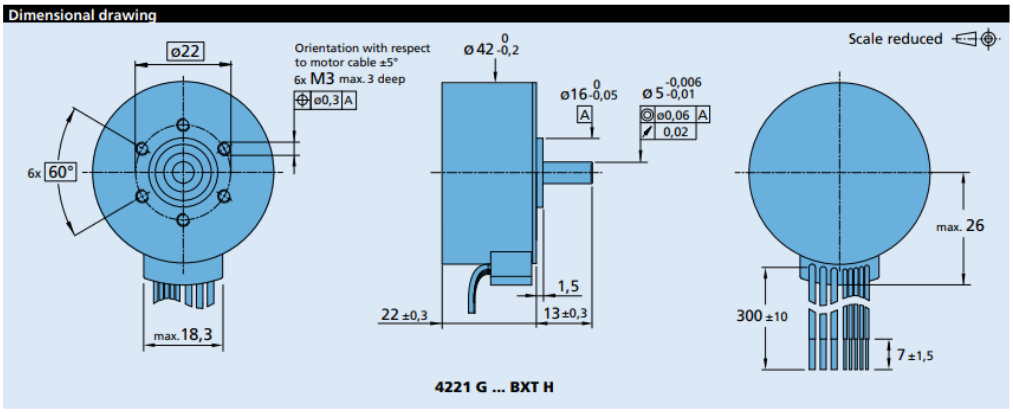

Figure 2.10: Technical drawing of the engines from the Faulhaber documentation.

This system allows the rotation of two flat disks of 29 mm diameter facing each other (see figure 2.11). Both are attached to a relay magnetically driven by a movement transmitter attached to the motors, making it possible to rotate at frequencies in the range 1 to 75 Hz (4500 rpm). The sealing of this device is obtained by a sealing flange which separates the relay, and therefore the EC, from the outside. Magnetic bearings with 5x20 mm neodymium segmental arc magnets provide the magnetic coupling. The advantage of this configuration is that it allows for an optimal level of sealing since no transmission shaft is required. This adaptation of the Faulhaber motors was developed in the laboratory. The movement transmitter (see figure 2.11a) is long due to the impact of the magnets on the hall effect velocity sensor in the Faulhaber motor.

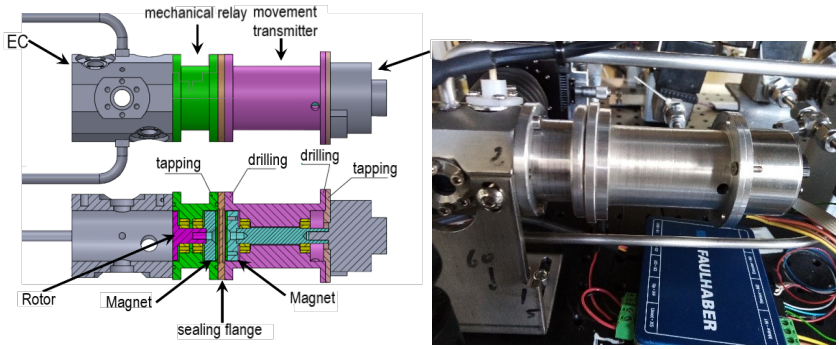

(a) Sectional diagram to display the pieces of the motors.

(b) Design of the engines and the transmission system.

Figure 2.11: Design of the motors used to create the VK flow in a controlled environment.

Other systems were tested (Neyco and Bal Seal joints) but leaks were present and therefore disqualified these products for their use in the experimental set-up. The possible issues that may have happened during these tests is a mechanical leak where the rotor is not in perfect contact with the joint.

2.3 Optical system and data acquisition

To observe the droplets after their creation, an observation system is necessary. To have an optimal set-up and then recreate the aerosol numerically, the tomography technique is used. The tomography technique consists in a series of shots at a given acquisition rate, the focal point of the camera being moved from one shot to another. In the present experiment, the camera focal point is moved, not by changing the objectives characteristics, but directly by moving the camera, therefore the position of the focal point is known at all time. The camera used for the tomography is a fast camera (Optronis CP70-1HS-MC-1900) described in more details in section 2.3.1.

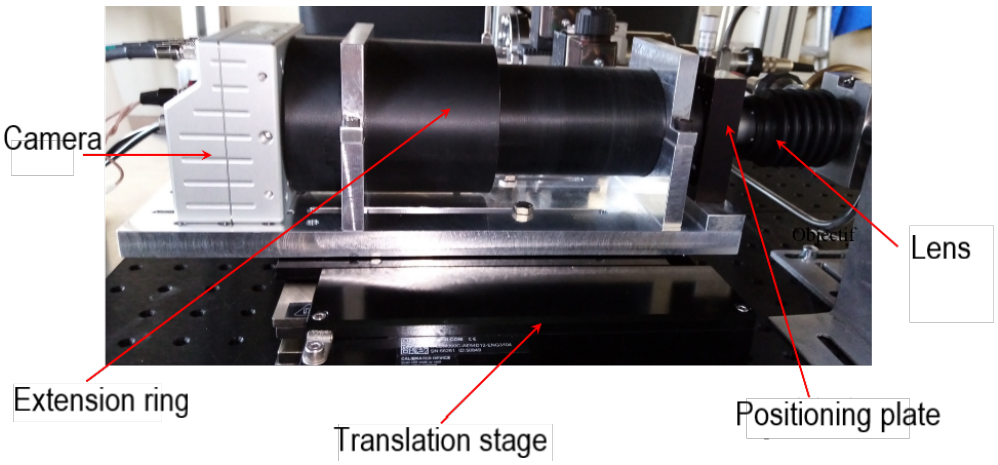

Figure 2.12: Camera system described with every components.

The objective used is a LEICA N-Plan 10x/0,25 (∞/-/B). The camera and the objective are fixed to a platform THORLABS, moved by Zaber X-LDM-AE technology (see section 2.3.2). An extension ring isolates from stray light between the camera and the objective. The illumination is a white light and obtained by an ILH-ON01 VA LED mounted with a focusing lens and an optical support (see fig 2.13). The components of this assembly are THORLABS materials.



(a) Separated view of the LED.

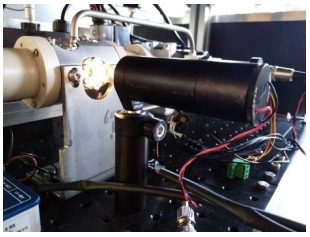

(b) Lighting system in place.

Figure 2.13: Global view of the lighting system.

2.3.1 Microscope

The camera used in the optical system has the following characteristics: 1280 × 860 pixels and 1980 images/second, interface CoaXPress, Cable CoaXPress (4 connectors DIN at each end). The camera has to be fast enough to capture movement of the droplet in order to keep coherent images throughout time. The figure 2.14 displays the technical drawing of the camera used. The focus is set with objective to have a field of view of $1280 \times 860\,\mu m^2$.

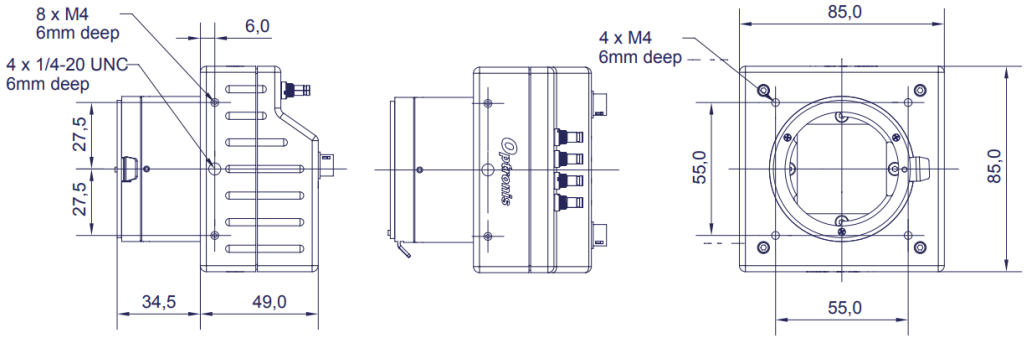

Figure 2.14: Camera system described from the outside.

The imaging issue, that has to be addressed first, is the definition of the optical parameters that are directly linked to the phenomenon we are willing to observe. In this case, the droplets are a few microns in diameter, the resolution is chosen to be fixed at 1 μm/px and verified at the end of this section. Resolution below that value would entails more complex data processing (approximation of the radius via a polynomial fitting, if the number of pixels to determine the radius in not high enough the margin for error would be quite large). To have a global view of the droplet environment, the size of the image is 1280 $\times$ 860 pixels. This is limited by the number of images taken per second (1980 images per second) and the total disk space to store those data during the parabolic flight campaign (1.86 Tb). The volume scanned is the blue volume displayed in the picture 2.15. The scanning back and forth is done on a 2 mm run as explained in section 2.3.2, the volume scanned is then 1280 μm $\times$ 860 μm $\times$ 2 mm. To have an idea of the scale on the pictures the tilted tip of the needle is 0.32 mm wide and 4.46 mm high. The needle is placed 8.4 mm inside the chamber (measure done from the left of the lunar steel piece to the needle).

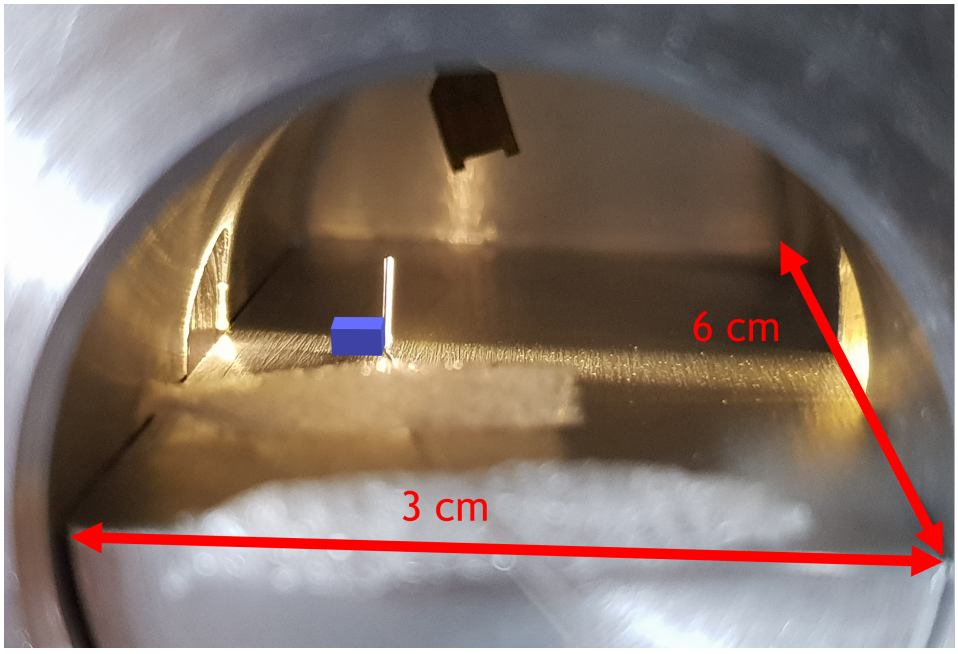

Figure 2.15: Visualization of the probed volume volume (in blue), the needle indicator is 4.46 mm high and 0.32 mm wide. The inner part of the probed volume points towards the centre of the EC (or the needle tip), the outer part of the probed volume is the closest part to the walls of the EC.

The visualization of the probed volume in the EC, is showing that this probed volume if far from the centre of the EC, this changes the nature of the possible results that could be observed with the use of the VK flow. During the parabolic flight investigation, several spinning frequencies were investigated, giving information on the time necessary to create a flow in the aerosol but the coalescence of the droplets was not observed.

Evaluation of a pixel size

The verification of a pixel size is determined via the camera itself, the idea is to focus on an object of a known size, here the tip of a microlitre needle. The width is measured to be 0.32 mm and correspond to an average of 317.5 pixels (average of 5 different heights, only one is illustrated on the picture 2.16) leading to a pixel value of 1.008 μm.

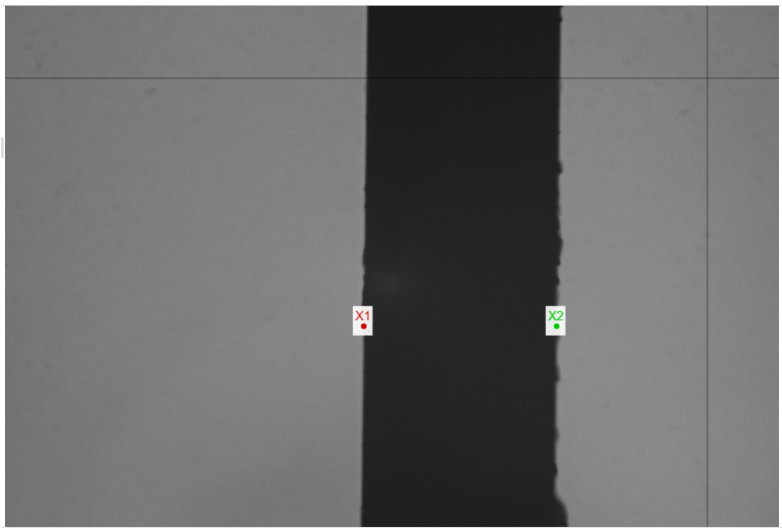

Figure 2.16: Visualization of the needle in the focal plane.

2.3.2 Translation stage

The translation stage (X-LDM060C-AE54D12-ENG3104) is manufactured by Zaber. The quality of the translation stage is crucial as it is the key element to realize optical tomography. All features of interest of the platform are displayed in the table 2.1 bellow. In the current experiment, the translation stage is used to scan back and forth on a 2 mm travel range. This brings the volume scanned to 2 mm^3.

Characteristic	**Value**
Travel Range	60 mm
Travel Range used	$2 - 6$ mm
Accuracy (unidirectional)	1 μm
Repeatability	$< 0.08\,\mu$m
Minimum Incremental Move	25 nm
Maximum Acceleration	34.3 m.s^{-2} or 3.50 g
Maximum Speed	1200 mm.s^{-1}
Speed Resolution	0.61 nm.s^{-1}
Peak Thrust	60 N
Maximum Centred Load	120 N
Pitch,Roll,Yaw	0.003 °
Moving Mass	1.74 kg
Weight	3.76 kg

Table 2.1: Record of the translation platform parameters.

The position of the translation stage is recorded and plotted in figure 2.17. The target for the translation stage is to travel the 2 mm range back and forth in 0.4 s. The figure is only showing a part of the signal, as it just repeat itself until the end of the parabola. A scan of the aerosol is complete when the translation stage travelled the range in one way. As a result a scan is composed of 400 images.

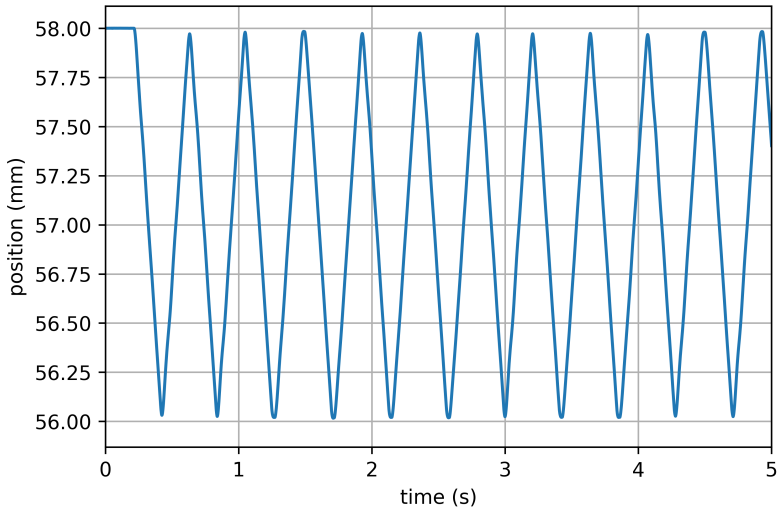

Figure 2.17: Evolution of the position of the translation stage throughout time.

2.3.3 Acquisition system

During, the experiment, the camera speed is set to its maximum (for image coherence) and the resolution is set at 1 micron per pixel. The field of view is the trade off factor used in this study. The objective is to have the largest possible field of view but enough pixels per droplets. As a result, every parabola generates 50 Gb of raw image data with the characteristics previously established. The disk used to stored the data has to have the capacity to store a day of parabolic flight, so 31 parabolas. A few extra parabolas are taken as a reserve. As a result, the disk used to store the data is a raid system of 1.86 Tb.

2.4 Imaging

The next following subsections will describe the two methods and results they give for the analysis and reconstruction of the aerosol from images like the one in figure 2.18. For this study, one code was already done in Fortran for previous experiments [159, 160] and I developed the other code in Python using the trackpy package during this thesis. The Fortran code is presented first.

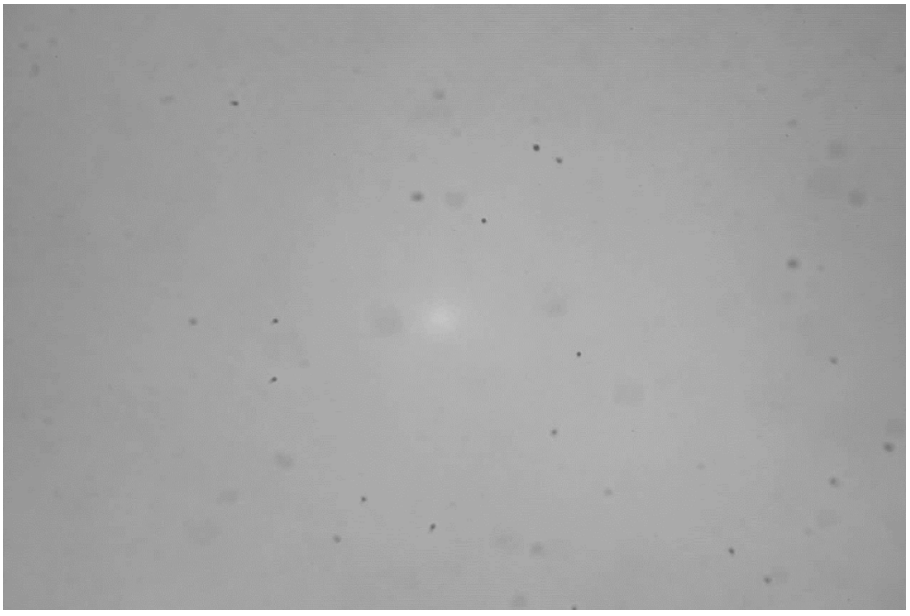

Figure 2.18: Image extracted from the 60th parabolic flight campaign from CNES. The water droplets are the dark spots. The field of view is 1280 μm $\times$ 860 μm.

2.4.1 Fortran image processing

The first step in the processing of the images is to correct the background. To do so, the first image is subtracted to the other images. This step is done to reduce the impact of the background inhomogeneities.

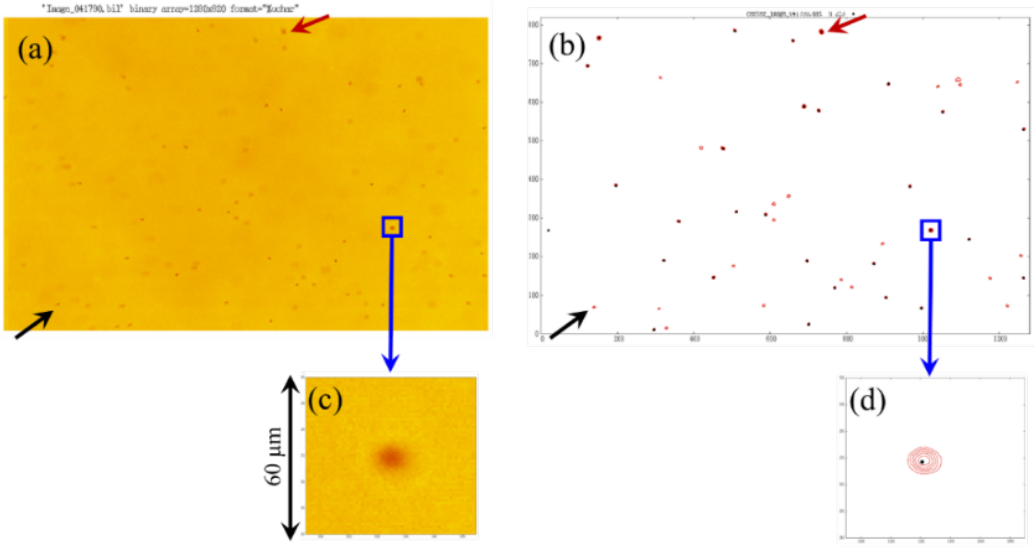

Figure 2.19: Image after background subtraction (a) and after treatment (b). The black and red arrows indicate two droplets and their signature after treatment. (c) and (d) correspond to a zoom on a droplet and illustrate the grey levels produced by a drop of about 5 μm in diameter. The black point is the centre of the contours.

Images are encoded on 8 bits and correspond to a field of view of 1280 μm by 860 μm (see figure 2.19(a) and section 2.3.1 for the pixel size). Each image presents a sufficient contrast (on at least 128 grey levels) for reliable post-processing. Vignetting may remain despite the optical quality and the collimation of the incident light beam. It is eliminated by subtracting a reference image acquired before the aerosol formation (the first image the camera gives). The identification of the droplets and their location in the images is performed by thresholding predetermined grey levels (about ten). An image of the contours generated by each droplet is then obtained (see figure 2.19(c) and 2.19(d)). The spherical geometry of the droplets and the fact that they are distant from each other produces typical circular contours, which is very helpful for the accuracy and CPU time effort.

The principle is then to detect the position of the centre of each of the contours, regardless of whether the corresponding droplet is focused or not, and then to construct, from the set of the centres of all the droplets and

all the images of a given scanning shot, the individual optical axis of each droplet. The quality of the image contrasts allows the detection of droplets with a diameters down to 3 μm.

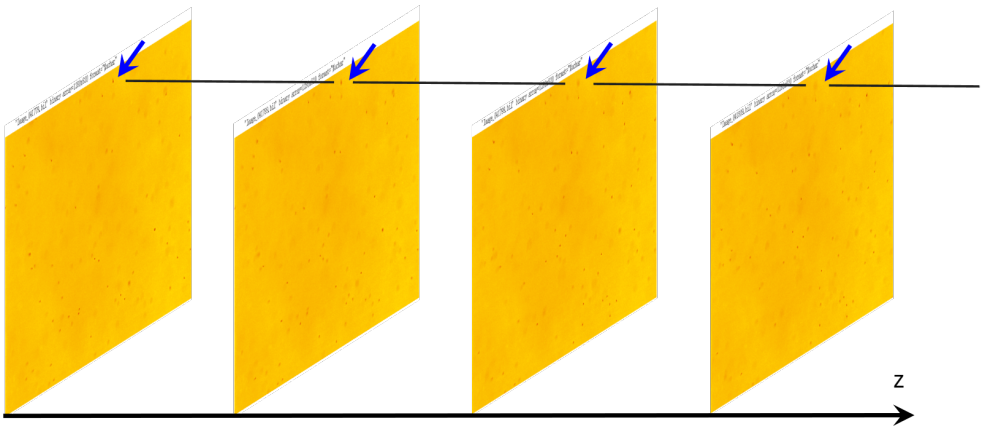

Figure 2.20: Schematic illustration of droplet tracking. The horizontal line correspond to the optical trajectory of one droplet indicated by the arrows. The actual distance (resp. time interval) between each image of this figure is about 5 μm (resp. 0.5 ms). The coordinates (x,y) are in the plane of the images and z indicates the position of the microscope working plane.

Individual optical axis are processed one by one determine droplet location in the scanning direction. This procedure is iterated for all the droplets (figures 2.20 and 2.21). Optical axis construction requires coherence between consecutive images and thus an aerosol evolving on slow characteristic times when compared to those of the acquisition system. This constraint is not satisfied immediately after droplet formation because of the fast flows generated by the initial expansion. As these flows decay after a few seconds, sequences of several tens of thousands of coherent images are produced and therefore usable for post processing. For the post processing reasons, a droplet has to be present on a sufficient number of images (in this case, 5 is chosen) for a precise radius computation along the optical axis, any optical axis smaller than 5 is removed. Droplets whose optical axis is crossing the limit and is too close from the end of the domain in the z axis (0.05 mm from the end is the limit) are removed. Droplets from the firsts 5 pixels on the x and y axis are also removed due to format issue.

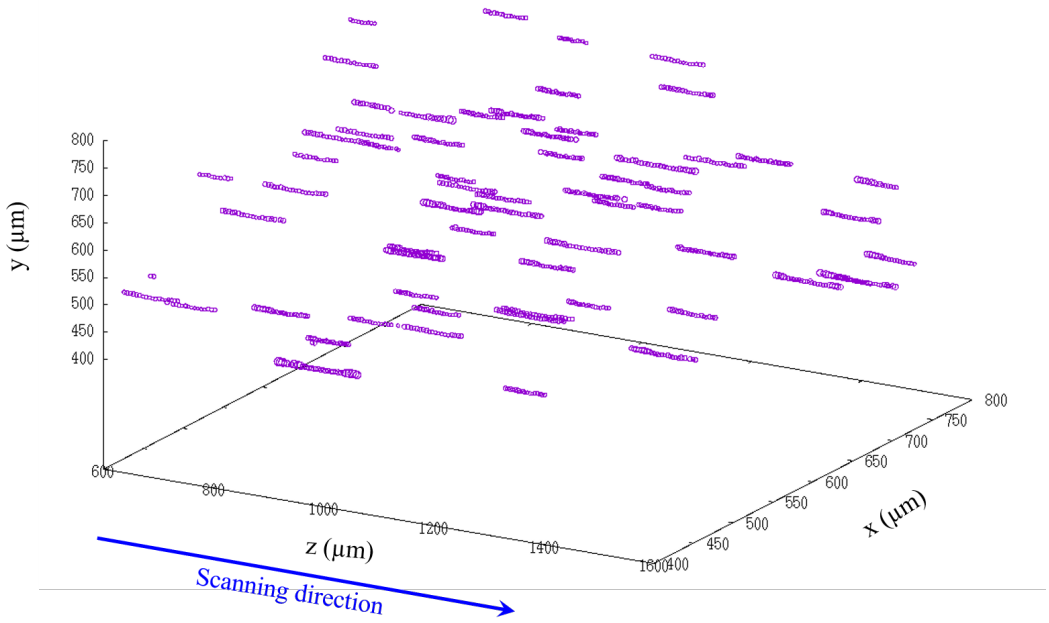

Figure 2.21: Optical axes resulting from the droplets of a tomographic sequence. Their orientation in the direction of the tomographic analysis (z direction) is a signature of the aerosol stability and good image coherence. This image is a zoom into the domain 400<x<800 (μm), 400<y<800 (μm), 600<z<1600 (μm) for more visibility.

Figure 2.21 represents a selection of the optical axes for a single tomographic sequence. It shows approximately a hundred optical axes and illustrates the precision of the analyses. This imaging technique is further used to obtain animations of the aerosol behaviour in periods of reduced gravity. A typical reconstructed snapshot for the entire probed volume is given in figure 2.22. The identification of the optical response produced by each droplet leads to optical axes of length depending upon their diameter.

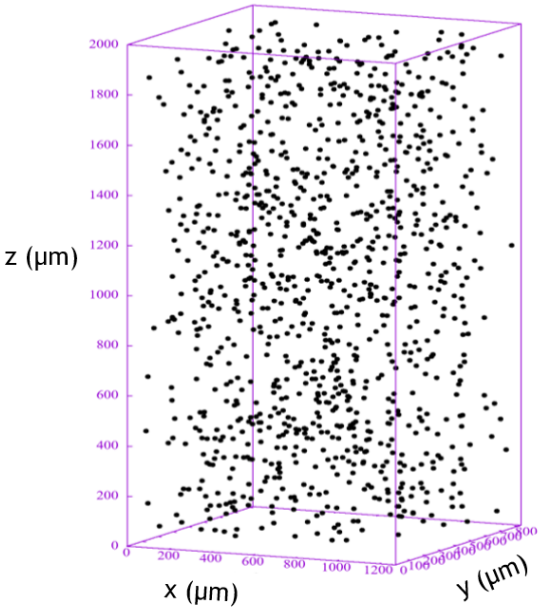

Figure 2.22: Snapshot of the aerosol reconstructed. The droplet size is multiplied by a factor 10 for visibility.

The larger the radius of droplets, the longer their optical axis. Figure 2.21 illustrates this fact in a representation showing the radius obtained from the optical response from one part of the domain, the rest of the domain is following the same pattern. When the working plane of the microscope is in the vicinity of the actual droplet location, the measured apparent radius reaches a minimum (see figure 2.23). This property is used in the last phase of the analysis to estimate the radius of the droplets. The apparent radius of a given droplet is obtained from the value at steepest tangent of the radial average of the grey levels of its optical response. This radius becomes larger when the droplet is out of focus and reaches a minimum value when it is in focus. Its actual radius is finally computed from the minimum of a quadratic fitting of the apparent radius when running along its optical axis. At this minimum contrast is the sharpest. Beside droplet radius, this procedure also determines the location of the droplet along its optical axis. At the end of the optical axis, this technique may be too rough as shown by the comparatively large fluctuations in figure 2.23.

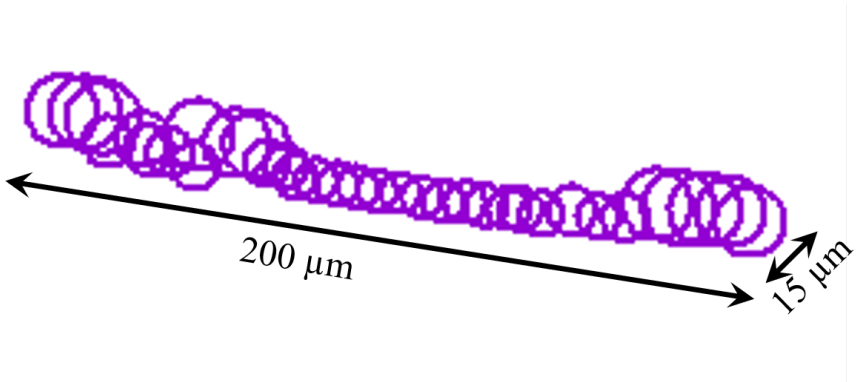

Figure 2.23: Focus on one optical axis resulting from the droplets of a tomographic sequence in figure 2.21. The figure shows the behaviour of the apparent radius of one random droplet as a function of the position of the microscope working plane.

2.4.2 Python image processing

The fortran code is slow and require to start multiple programs, generates an excess of data and is not optimised. These reasons motivated the development of a python code to improve the time necessary to extract data after a campaign and reduce the space necessary to do it. The treatment from the code I made in python is following the same steps as the Fortran procedure. First, the idea is to determine the start and end from each scan using the python library scipy. Then, using the python library trackpy, detect the droplets on each image of each scan and have a rough estimation of their radius using the function trackpy.batch that locate Gaussian-like blobs of some approximate size in a set of images. This is done by performing a band pass filter and a thresholding. The function locates all peaks of brightness (respectively in our case darkness), characterizes the neighbourhood of the peaks and takes only those with given total brightness ("mass").

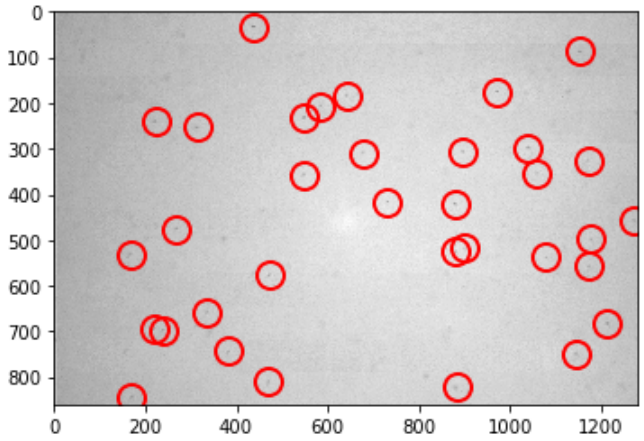

Figure 2.24: Droplet detected that are meeting the requirement of a minimal "mass".

Finally, the function refines the positions of each peak [161]. This method is the implementation of the paper published in 1995 by Crocker and Grier [162]. Then using trackpy.link, the idea is to link the previous data that were only coordinates of droplets and transform them into trajectories [161]. This action will create the optical axis like in the Fortran method, the result for one scan of 400 images could be seen on figure 2.25.

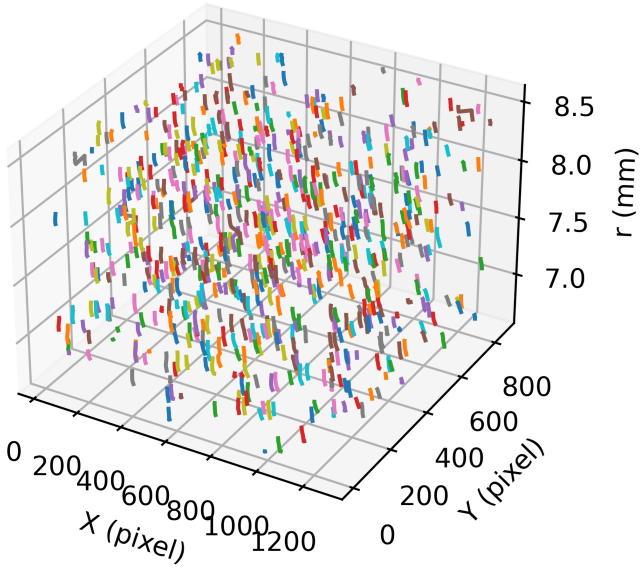

Figure 2.25: Droplet optical axis, the reconstruction is done in the entire probed volume. The r axis is for the position in the EC (cylindrical coordinates).

From then on, the idea is to have the best estimation of the radius of the droplet. To do so, the estimation of each droplet radius is plotted for each image of their optical axis. Similarly to the Fortran code approach, the radius is then fitted with a polynomial estimation of a degree two or four. The radius of the droplet is then taken as the minimum for each of those two polynomial. The estimated error on the square diameter is $0.05\mu m^2$. A typical radius distribution is shown in figure 2.26.

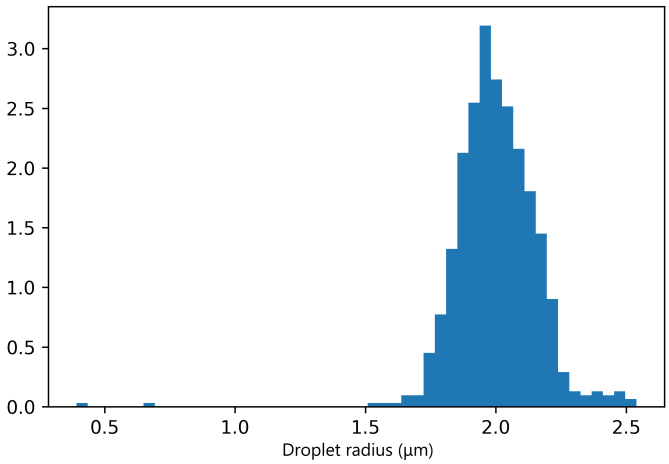

Figure 2.26: Droplet size distribution (Parabola 6, 64th campaign, scan 17).

The average droplet radius in this scan is 2.01 μm with a standard deviation of 0.17 μm. This distribution is fairly centred around the average, that will justify taking the average droplet size as representative for every droplet in the volume.

2.4.3 Comparison of the two methods

The comparison between the two methods is done on the droplet density and the radius of the droplet. The results are plotted in the graph 2.27.
The two codes are giving approximately the same values, as the python code runs 36 times faster (1 hour to treat a parabola in python versus 36 hours in Fortran), it was decided to keep the python results for any calculation that need the radius evaluation.

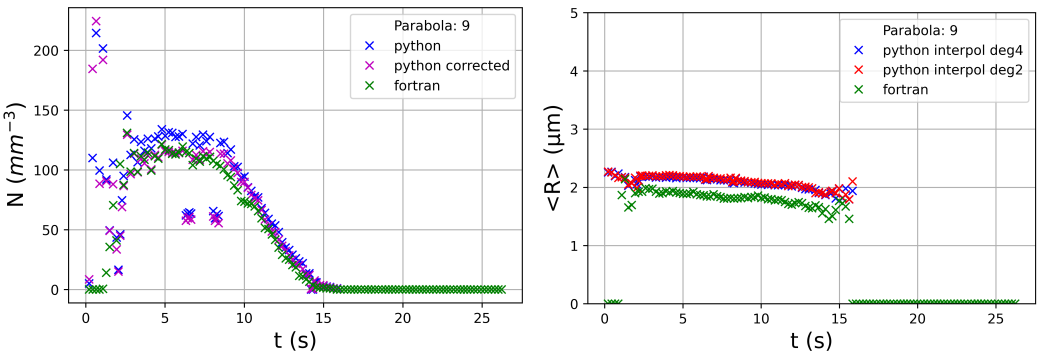

(a) Droplet density inside the probed volume for different methods.

(b) Droplet average radius inside the probed volume for different methods.

Figure 2.27: Method comparison for parabola 9 of CNES 64th parabolic flight campaign.

2.5 Infrared source and Fourier Transform Infrared spectroscopy implementation

The implementation of an IR source on the facility has two objectives. First, if the power is high enough, it would be possible to replicate the radiative power of the sun on the clouds [163]. The other objective is the implementation of an Fourier transform infrared spectroscope (FTIRS) in the ISS to analyse chemical reactions within aerosols during a prolonged microgravity phase. Both of these techniques require the implementation of an IR source onboard.

2.5.1 Characteristics of the IR sources

Before implementing the entire FTIRS in the AEROSOL rack, the idea is to use first the source present inside the FTIRS to evaluate the feasibility of having such a system on the rack. The characteristics of the system are listed down bellow (see figure 2.28). The two sources are tested first (see figure 2.28) only the MIR source is the one that is used in the final set-up, in the FTIRS.

Product code	ARCLIGHT-NIR	ARCLIGHT-MIR
Light emitting element	QTH (Halogen)	SiC globar
Source temperature [K]	2'850	1'550
Spectral range [µm]	0.4-4	1-25
Spectral range [cm^{-1}]	25'000-2'500	10'000-400
Rated lifetime [hours]	4'000	10'000
Removable fiber-optic coupler	NA = 0.25, CaF2 lens	NA = 0.3, gold-coated off-axis parabolic mirror
Power consumption [W]	20 (electrical)	
Power requirement	12V via OD 2.5mm/ID2.1mm power jack (100-240 VAC to 12 VDC converter included)	
Output beam diameter [mm]	12.7	
Operational temperature [°C]	5-40	
Attenuator	Manual Iris Diaphragm	
Dimensions [mm]	92x92x43 (w/o fiber coupler), 140x92x43 (w/ fiber coupler)	
Weight [kg]	0.4	

Figure 2.28: Characteristics of the IR sources used.

2.5.2 Set-up

The idea is to place the source like the camera with a window that will let the IR radiation enter the EC and warm up the small droplets after that window, as the water is absorbing in the IR domain. To do so, the window chosen is in zinc-selenide (ZnSe) as this material has a large transmission band in the IR domain [164]. To prevent gas leaks, the window is pressed between two joints. On the EC, at the end of the hole, there is a flat surface to apply the pressure from the turquoise piece in figure 2.29 and prevent the leaks. The set-up is presented in figure 2.29. The top yellow piece is the one in contact with the IR source, it will guide the signal and set it straight to enter the canal (turquoise). The green piece is an obturator, it will open or close on command. The set-up is pointing towards the centre of the cell, that is close to the probed volume.

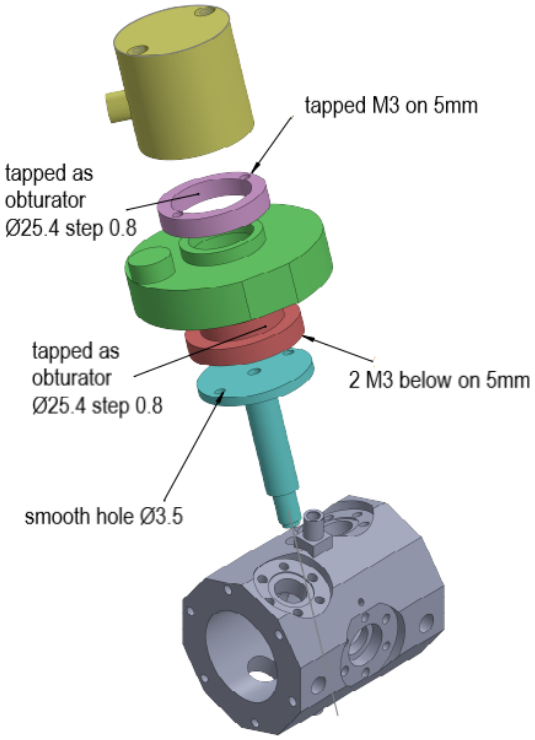

Figure 2.29: First set-up used to test the IR radiation impact on the aerosol, the IR source is placed after the yellow piece, the green one is an obturator that will let the signal pass on electrical command, the turquoise piece is the canal that connects the obturator to the EC.

The radiative power output of this set-up was measured with a calorimeter at 8 mW for the NIR source at the end of an optic fibre. During the 64th parabolic flight campaign, this set-up was tested. The objective was to see if the source would resist the gravity evolution and the effect this source would have on the evaporation dynamic of the aerosol. As a result, the source showed no issue or failure during the flight but the power output was not sufficient to have a visible effect on the evaporation dynamic of the aerosol. That means that the set-up could be used in parabolic flights to implement an FTIRS as the power output is not high enough to perturb the aerosol evaporation. The IR source used inside the FTIRS is the MIR source (see characteristics in figure 2.28).

In a second set-up, the IR source was replaced by the FTIRS, it turned out that the power output was not high enough to have a relevant signal to noise ratio. The main cause to this failure is the surface of the hole in the canal piece and the window size, the flat surface on the top of the canal piece reflects up to 85 % of the power output.

2.5.3 FTIRS set-up

To counter the previous issue, the idea is then to have access to a much larger surface, by putting a larger window and use a gold covered reflector to increase the signal to noise ratio, the reflector is placed inside the EC to avoid going through too many windows that will decrease the signal intensity. To have such a set-up, the motors on the side were removed (as showed in figure 2.30).

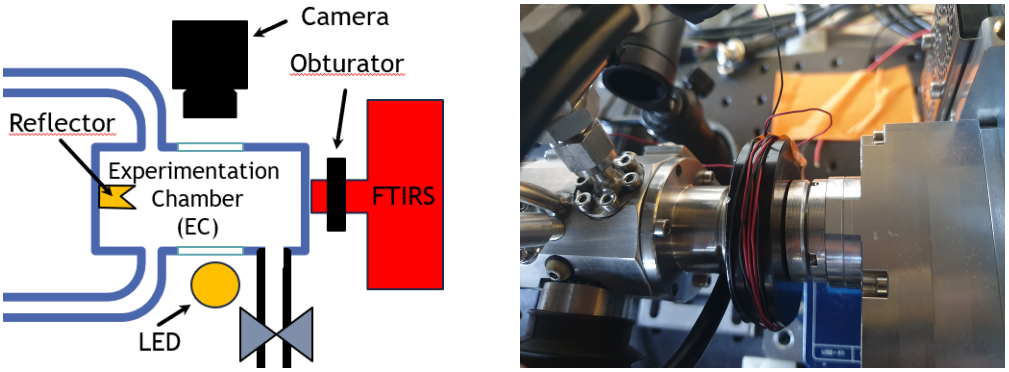

(a) Adapted set-up with motors removed, the reflector is inside the EC.

(b) Picture of the FTIRS set-up. The obturator is in black.

Figure 2.30: FTIRS set-up used for the 67th parabolic flight campaign.

To control the leaks the same idea is put in place and the set-up is showed in figure 2.31. The window used is 25 mm wide for a thickness of 3 mm, the diameter used for the light to enter is 20 mm and corresponds to the output beam of the FTIRS. On the figure 2.31, the green part is connected to the EC on the left, the leak prevention is made with a joint and compressed by BTR M3 screws. The ZnSe window is in grey pressing on a joint on its left and compressed by a nylon washer on its right, this piece limits the torque on the window that may damage it or create leaks. The last part on the right is connected the obturator as in the previous set-up.

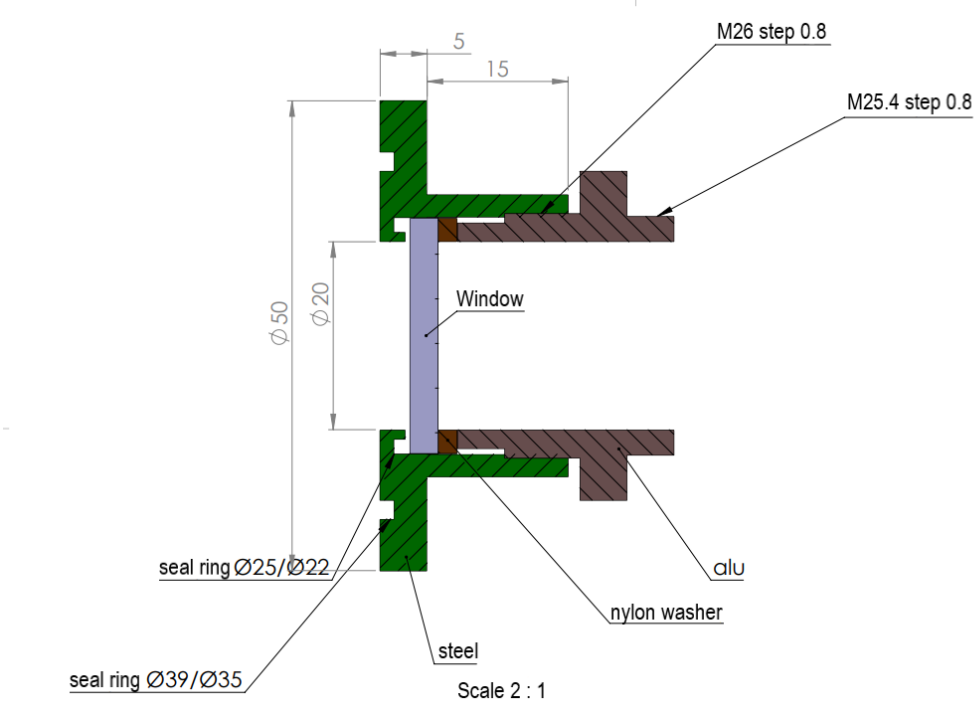

Figure 2.31: Fixation set-up for the obturator and the FTIRS on the side of the EC, the green piece on the left is screwed to the EC, the window is compressed on the green piece via the nylon washer.

On the other side, the reflector has to be set in place and maintained. To maintain the reflector, several options were possible. The first option consists in using the screws at the back of the reflector by screwing it through the flange, this option is elegant but will be the cause of leaks and as the leak will be on the flange of the EC, it may deteriorate heavily the quality of the pressure control in the EC. The second option is to use epoxy to glue the reflector to the interior of the flange, nothing is screwed through so nothing can leak. However, this is a definitive solution as it won't be possible to remove it without damaging one of the piece. The solution chosen for the parabolic flight campaign of October 2024 (67th CNES parabolic flight campaign) is to use a needle screw to maintain the reflector inside a cylindrical section tapped in a flange. The chosen solution is displayed in figure 2.32.



Figure 2.32: Chosen solution to maintain the reflector: An M3 needle screw is used to maintain the reflector in the middle of the sealing flange.

2.5.4 FTIRS calibration

To use the FTIRS, it is important to first do a calibration. To do a calibration, it is key to know the volume injected to be able to have the same response after multiple tests or know the volume to inject to have the answer that you want. The protocol to inject the secondary vapour (HFE-7100 being chosen for the 67th parabolic flight campaign) is the following: open the manual valve. Start the injection via the syringe pump. When the injection is done, circulate the gas (see section 2.9).

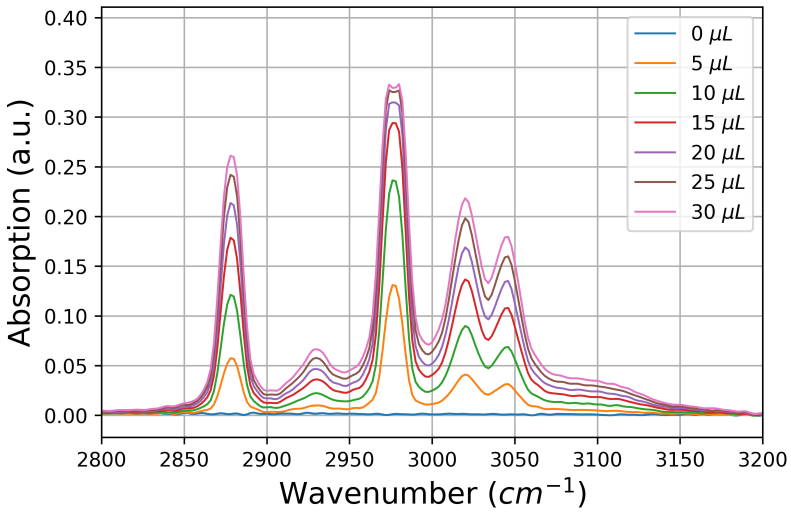

Figure 2.33: Calibration response for different injections of controlled volumes directly inside the EC (0 to 30 μL). The response observed is for the C-H vibration mode of the HFE-7100.

Via the software "ARCspectro Rocket" (the way to use it is described in appendix), the absorption of the gas for each injected volume of HFE-7100 is plotted in figure 2.33. For these graphs, the spectral wave investigated ranges from 834 to 5000 cm^{-1}. As the studied gas is HFE-7100, only the spectral range 2800 to 3200 cm^{-1} is represented with a typical absorption band from the molecule. To do the calibration, the maximal absorption is recorded over the restricted spectral range (2950 to 3000 cm^{-1}), corrected with the baseline each time and plotted in figure 2.34.

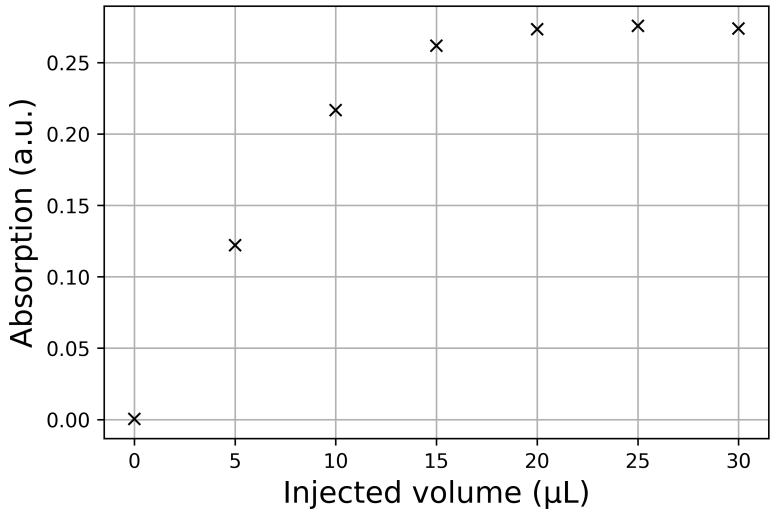

Figure 2.34: Absorbance as a function of the volume of HFE-7100 injected inside the EC. Before the plateau, the behaviour of the system is linear.

The first thing seen is the globally linear behaviour and the saturation of the FTIRS at 0.28 u.a. With this curve, it is easy, even in flight to know approximately the percentage of HFE-7100 inside the EC compared to the saturation, based on the calibration curve (ratio of the absorbance observed to the one at saturation). With this calibration, the FTIRS could be used like the humidity sensor. Furthermore, being precise on the injected volume means that the correct quantity of HFE-7100 could be injected via the syringe pump, in order to go from 50% to 70% of the saturation for example.

2.6 Measurement devices

Multiple sensors are necessary to create in controlled conditions the aerosol and to understand the evolution of this aerosol once created. Several parameters are tracked, like pressure, temperature and humidity throughout time.

2.6.1 Pressure

The pressure inside the EC and ECC are known thanks to two pressure sensors with polynomial compensation KELLER PAA-33X. The pressure sensor inside the EC is not directly plugged into it due to place restriction, this sensor is put a little further after the exits towards the ECC (see fig 2.7). The pressure sensor, in the ECC, is directly plugged in as the intrusion of such measurement sensor there does not cause any issue to the experiment. This way, the pressure inside the ECC is known more accurately as there is no intermediate pipe that could reduce the pressure recorded due to linear or singular pressure losses. An insulated and encapsulated piezo-resistive pressure sensor is used to transform the physical pressure value into an electric signal. According to the manufacturer of the system and after the sum of all the uncertainties, the margin of error is 0.47 %. These sensors are used at a high frequency (up to 2500 Hz) to allow a complete description of the pressure evolution inside the system.



(a) Picture of the pressure sensors.

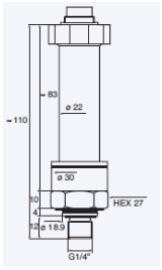

(b) Schematic view of the pressure sensor.

Figure 2.35: View of the sensor KELLER PAA-33X.

2.6.2 Relative Humidity

The hydrometric sensor is represented in fig 2.36a. This sensor is able to detect and measure the temperature and hydrometry of the gas. The sensor

is a SEK-SHT35 developed by the company SENSIRION. This sensor has an accuracy tolerance of ±1.5% (see fig 2.36b). In the experiment conducted in this work, it might be a better choice to use ±1.75% as a tolerance. The characteristic response time of the sensor, named $\tau_{63\%}$, is 8 s. So when the humidity is evolving, there is a need to wait at least 24 s to be sure that the final humidity is close (±5%).

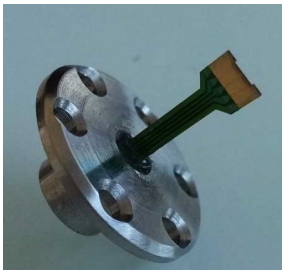

(a) Hydrometric sensor in green, glued with epoxy resin to a steel support which is fixed on the EC.

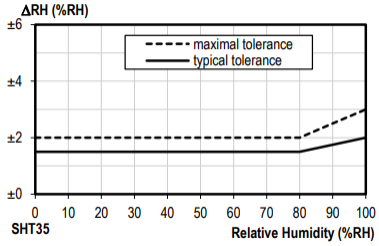

(b) Tolerance of relative humidity at 25 °C for different humidities (Constructor data sheet).

Figure 2.36: View and Relative humidity tolerance for the SHT35 Sensor used.

On fig 2.36a, it is possible to note that to ensure that the EC remain sealed, the sensor is glued to a steel flange with epoxy. This ensures no leaks in the EC. If the sensor is partially covered in epoxy it will impact the sensor. This impact is minor but whenever two sensors are set in place, this impact shall be considered along with the inherent differences between two sensors. The schematic drawing (figure 2.37) from the manufacturer, gives explanation on the physical principal used in the porous ship.

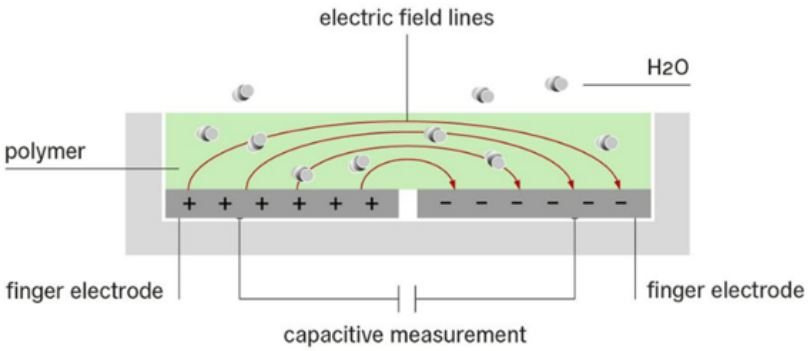

Figure 2.37: Manufacturer schematic drawing explaining the physical principle used for the humidity measurement.

The sensor characteristics, indicates that the sensor does not take into account the pressure inside the system. As the pressure plays an important role in the saturation pressure and the sensor is fairly slow with an 63% characteristic time response of 8 s, when doing compression and expansion during the parabolic flight, the value taken as true is the value at the end of the parabola.

2.6.3 Temperature

A temperature measurement with a K thermocouple driven by an Agilent 34972A LXI system is also implemented. The thermocouple used is a type K (397-1589). The cable consists of 0.0076 mm conductors with durable, colour-coded PFA Teflon and an insulation conforming to ANSI regulation. There is also an integrated temperature sensor in the relative humidity sensor, this other measurement creates redundancy which is always key in experiments.

2.7 Volumes determination

The volume of the cylinder that mostly compose the EC is known, as well as the volume of the ECC. However, additional "dead" volumes have to be added to these values in order to account for the pipes that are linked to the EC and ECC. To accurately measure the volumes, the idea is to add a known volume (calibrated balls, each of them has a volume of 7.0699 cm^3, see figure 2.38) to the EC and measure the differences in pressure to the situation without the balls.

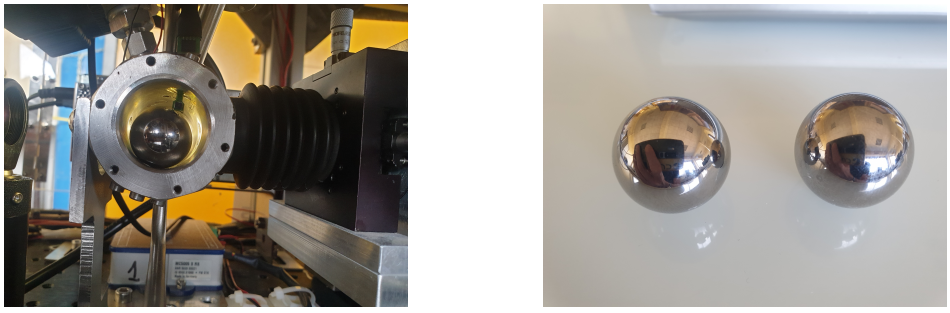

(a) Visualisation of the EC with a ball inside.

(b) Balls used for the determination of the dead volumes in the EC and ECC.

Figure 2.38: Determination of the dead volumes in the EC and ECC using calibrated balls.

The hypothesis made here is to say that there is no leaks inside the

volumes and that the compression is isothermal. For the following equations: the index 1 is for the EC and the dead volumes, the index 2 is for the ECC and the dead volumes. The exponent *comp* is to indicate that the volume is compressed and the index b is to indicate the presence of a ball inside the EC. As the same gas quantity is kept, before and after the compression, one can write:

$$P_1V_1 + P_2V_2 = P_1^{comp}V_1 + P_2^{comp}V_2 \tag{2.5}$$

The idea is to have the same equation but to add a calibrated sphere inside the volume V_1. This will impact the pressure after compression. As a result, with a ball in the EC, equation 2.5 becomes:

$$P_{1,b}(V_1 - V_b) + P_{2,b}V_2 = P_{1,b}^{comp}V_1 + P_{2,b}^{comp}V_2 \tag{2.6}$$

In equation 2.5 and 2.6, the idea is to isolate V_2:

$$V_2 = \frac{P_1^{comp} - P_1}{P_2 - P_2^{comp}}V_1 \tag{2.7}$$

and

$$V_2 = \frac{P_{1,b}^{comp} - P_{1,b}}{P_{2,b} - P_{2,b}^{comp}}(V_1 - V_b) \tag{2.8}$$

Thanks to equation 2.7 and 2.8 it is possible to link the volume of the ball to the volume V_1 with a set of measured pressure. The volume of the ball is known with a value of $7.0699\,\mathrm{cm}^3$, this gives a volume V_1 equal to $90\,\mathrm{cm}^3$ and a volume V_2 of $240\,\mathrm{cm}^3$.

2.8 Relative Humidity Regulation

In each scientific study, some parameters have to be kept under control as they could interfere with the results. The main objective of the Aerosol facility is to create a variation to investigate one aspect of the aerosol behaviour, the other aspects have to be kept identical to deduce the inherent mechanisms in play. The methodology used implies a control of different parameters, such as the humidity, to control the conditions in which the aerosol is formed. The humidity is defined as the ratio (see eq 2.9) between the partial water vapour pressure in the gas phase to the saturation pressure at a given temperature. The saturation pressure correspond to the maximal amount of liquid water one could evaporate in the gaseous phase, here air.

$$H(T) = \frac{P_v}{P_v^{sat}(T)} \tag{2.9}$$

Plans and principle validation

To control the humidity inside the EC, some active system has to be used. As a first design, the idea is to create a thermally controlled cold point inside the EC, where the water vapour will condensate because locally, the vapour pressure will decrease according to the Rankine formula (see eq 2.10). As the partial pressure of water in the vapour phase stays constant, the humidity (see eq 2.9) is rising to one due to the diminution of the saturation pressure. As thermodynamically, the humidity can't be over one, the excess water in the vapour phase will liquefy. This mechanism acts as a way to trap water in a liquid form locally. As the circuit is closed from the outside, the presence of liquid water will decrease the water contained in the vapour phase globally, leading to a decrease of humidity overall inside the EC.

$$P_v^{sat}(T) = P_0 \exp\left(13.7 - \frac{5120}{T}\right) \tag{2.10}$$

Here P_0 is the standard pressure of 1 atm and T the temperature in the gas phase. This process shall allow a local control of the humidity. Then, the humidity will vary as a diffusive process and allow a control of the humidity inside the EC via a cold point. To create this cold point, the following Peltier system is set and shown in figure 2.39 .

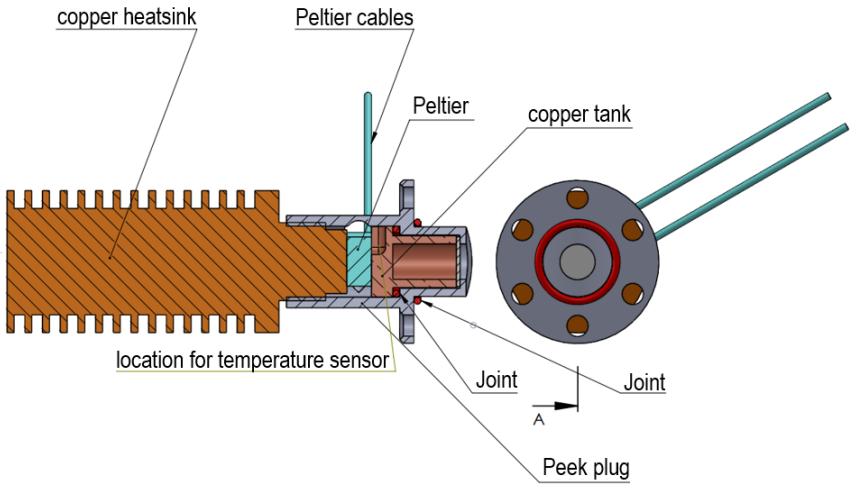

Figure 2.39: Plans of the regulative humidity system.

To create the cold point, a Peltier (from Laird Technologies, reference: CP0.8-7-06L) is used. As the EC is small and shall remains a cylinder, the cold point can not be too large. The following characteristics were chosen and are recorded in table 2.2. As shown previously, it is possible to control the humidity inside EC by controlling the temperature of the cold point. To do so, the system is piloted via Laird system.

Characteristic	**Value**
Cooling capacity	1 W
Maximal temperature difference	67 K
Maximal Current	2.1 A
Alimentation tension	0.85 V
Active area	6x6 mm
Thickness	3.4 mm

Table 2.2: Description of the Peltier Characteristics

The power supply is setting a tension of 24.1 V inside the electric circuit. As a result, and according to the alimentation tension of the Peltier documentation, it is not possible to have such a high value for this component. As the Peltier only has a small resistance, a voltage divider bridge is implemented with a 20 Ω resistance to adapt the tension to the Peltier's needs. The global system is piloted via Laird system. The software has to be paired with a physical system to execute the orders. Here the TC-XX-PR-59 programmable controller is supposed to supply a much stronger Peltier, that's also the reason why a voltage divider is used. The software offers a PID regulation, this allows a control of the power output once the targeted temperature is reached. The temperature is tracked by a probe in between the reservoir and the Peltier.

When activating the cooling system. After approximately five minutes, the temperature of the reservoir is stable at the targeted value, so on the next graphs, only the humidity curve is plotted as the cold point does not affect the temperature of the rest of the EC. As there is a cold point inside the EC, the saturation vapour pressure decreases. Locally, the humidity overpasses 100%. As a result the water contained in the gas phase liquefy on the reservoir's wall. The lower the temperature, the more water condensate and the lower the humidity inside the EC is by diffusion mechanism.

The idea was then to investigate the characteristic time necessary to decrease the humidity in the EC. The curve used to fit the data is based on an exponential equation (eq 2.11) and the fits are plotted in fig 2.40, H_{final} represents the lowest attainable humidity in these experimental conditions

(i.e at a percentage of the Peltier power), H_{decr} represents the decrease of humidity from the initial value to the minimal one and τ represents the characteristic time for this decrease to take place :

$$H(t) = H_{final} + H_{decr} \exp(-t/\tau) \tag{2.11}$$

For every experiments, the idea is to start at about 95% inside the EC and then create the cold point inside the EC to locally condensate and decrease the humidity. The power of the Peltier is fixed at the begining of the experiment with a value between 50 % and 100 % of its power. The evolution of the humidity is recorded in fig 2.40.

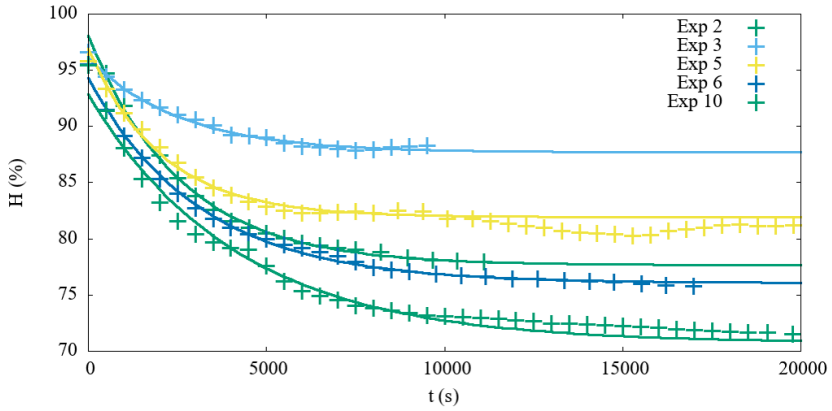

Figure 2.40: Plot of the humidity evolution and the exponential fit accordingly.

The different parameters of equation 2.11 could then be numerically computed by a standard least square method. The results are summarized in the table 2.3.

The different experiments have shown the possibility to decrease the humidity down to 70% thanks to a cold point inside the EC. The average characteristic time $< \tau >$ is 2726 s (experiment n°7 excluded) or approximately 45 min, if we consider that reaching 95% of the final value is acceptable to reach the targeted humidity, it takes three times the characteristic time (so 2 h 15) to reach the targeted humidity. It is not possible to have a time this long for the humidity control during a parabolic flight campaign.

Experiment	H_{final} (in %)	H_{decr} (in %)	τ (in s)
1	82.690928	15.615980	2181.379669
2	77.653211	20.414945	2595.747634
3	87.693166	8.407060	2574.169606
4	80.713800	14.655594	3149.572487
5	81.931301	14.976187	2057.655497
6	76.065156	18.206576	3139.888423
7	71.933461	13.295878	12657.611239
8	74.673277	22.793487	2249.620774
9	74.934457	21.189685	2435.067382
10	70.740702	22.089235	4154.750026

Table 2.3: Record of the fitting parameters, all errors are bellow 1% and are not shown, the exponential fit is a good approximation here.

Improvement of the process

Now that the concept is effective, the idea is to improve the cooling system in order to decrease the humidity more efficiently. To do so, a steel exchanger is set in derivation of the initial circuit. This allows the presence of much larger Peltier systems (see fig 2.41). Two Peltier elements are mounted in series (see table 2.4) to cool the exchanger faster. To support this new circuit an other pump is put in place and three electro-valves are added to separate this new circuit from the original one. This way, the secondary circuit, responsible for the regulation of the humidity, only has little impact to the primary circuit, used to form the aerosol.

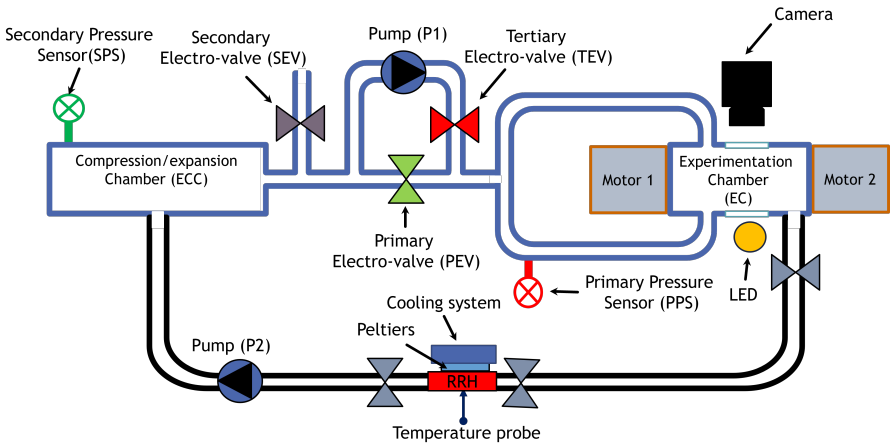

Figure 2.41: New set-up to regulate the humidity. A secondary circuit (in black) is added in addition to the initial one (see figure 2.5).

The thermostat used initially is a cooled bath controlled by a Huber Polystat CC3. This bath allows an accurate control of the temperature. However, this system is too large (bath dimensions: $50 \times 30 \times 15\,\mathrm{cm}^3$) and uses fluid (R 290) which is not allowed for parabolic flights campaign. As a result, an other system has to be found. To replace this system, a simple idea is to use the top steel rack plate which will have enough thermal inertia to tank the transferred heat from the Peltier.

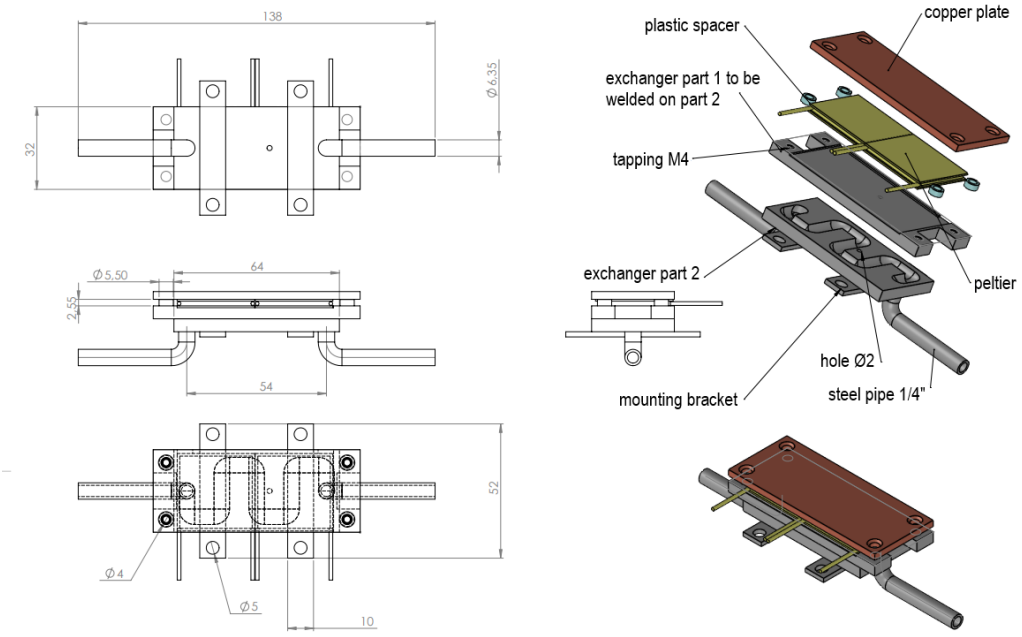

Figure 2.42: Display of the new Regulative Relative Humidity system (RRH).

The new system architecture is displayed in figure 2.42. The idea is to maximize the exchange between the cooled steel and the air to cool via a coil. The Peltiers are placed on top of the steel exchanger and plastic spacers are also used to decrease the mechanical pressure from the copper plate on top of the Peltiers. This copper plate is then in contact with the cooling system used to keep the heating plate of the Peltier cool.
The figure 2.43 shows the improvement of the cooling efficiency of the system. Now in less than eight minutes, it is possible to decrease the humidity inside the EC at a controlled value of 60%. At 70% humidity, the 59th parabolic flight campaign (October 2019) showed the feasibility to observe the evaporation process of the aerosol. This set-up was used with great success in the parabolic flight campaign of March 2023 allowing to set the initial humidity of each series of parabolas at 60%.

Characteristic	Value	Previous Montage
Cooling capacity	39.1 W	1 W
Maximal temperature difference	75 K	67 K
Maximal Current	3.9 A	2.1 A
Alimentation tension	16.4 V	0.85 V
Active area	29.7 × 29.7 mm	6x6 mm
Thickness	3.2 mm	3.4 mm

Table 2.4: Description of the Peltier characteristics used in the deported set-up of the RRH

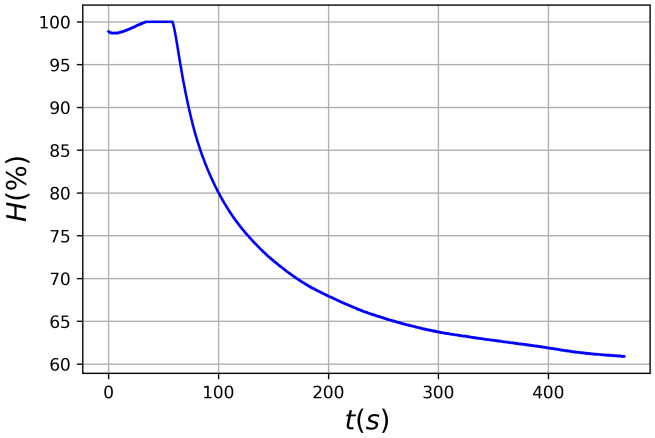

Figure 2.43: Evolution of the Humidity inside the EC on day 1 of the parabolic flight campaign (March 2023) to prepare the experimental conditions for evaporation investigation.

A numerical fitting gives a good correlation coefficient ($R^2_{corr} = 0.9709$) with an exponential law for the decreasing portion of the humidity with the following law:

$$H(t) = 60 + 44.68 \exp(-0.008t) \tag{2.12}$$

It gives us a characteristic time of 125 s or approximately two minutes, demonstrating the efficiency of this new control process.

2.8.1 Humidity regulation protocol and humidity stabilisation

During the parabolic flight campaign, the idea is to go fast to reduce humidity inside the EC because the time is limited. As a result, the Peltier are working at 100% of their power and the system stops as soon as the target value is reached, there is no stability conditions. The objective of this section is to establish a protocol that will produce a stable humidity inside the EC during the experiments without time restriction. The protocol is the following. First, the electro-valves PEV, EVAR, EVH1, EVH2 are open then the Pump 2 is started to homogenize the humidity. After three minutes, the thermal regulation of the Peltier system starts (three different temperature are tested). The idea is to reach a stable humidity target. Afterwards, the pump is stopped, the electrovalves are closed and the system is evolving, everything remains closed. The two graphs (figure 2.44a and figure 2.44b) are showing the evolution of the temperature and humidity inside the system over time.
For the three temperature of the Peltier system investigated, the temperature of the chambers is increasing (approximately 0.5 °C in the EC and 3.5 °C in the ECC). This is due to the electrovalves system and the pump. The electrovalves are heating up as current is going through to maintain them open and the pump is also warming up the gas due to the pumping mechanism that will heat the gas over time. The ECC is the first one to receive the pumped gas (see figure 2.41). The gas can't exchange enough heat in the ECC or pipes between the chambers and a raise in temperature is seen in the EC too. However, this increase is small. The variation of temperature in the EC is much more driven by the evolution of the room temperature as there is no insulation. The decrease of temperature in the EC and ECC could be seen as two phases, the convective one where the flow will exchange heat with the walls and the conductive one where the flow is damped out and the second phase where the temperature evolution is driven by the diffusion. This slow evolution of temperature will impact the humidity evolution on the long term. The dead area in the circuit will also diffuse water over time. Those phenomenon point out the difficulty to have a stable humidity inside the circuit.

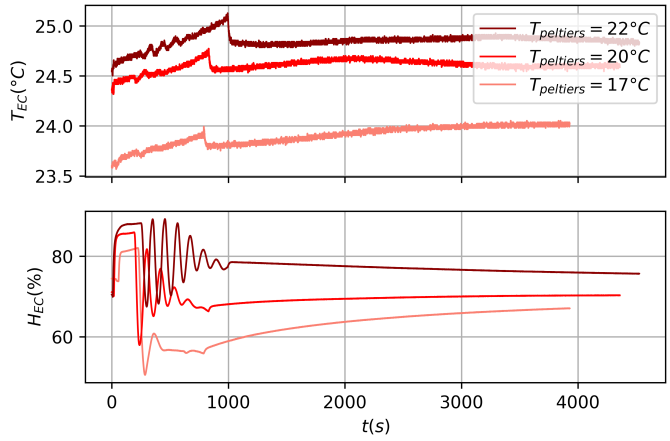

(a) Evolution of the temperature (top) and humidity (bottom) inside the EC.

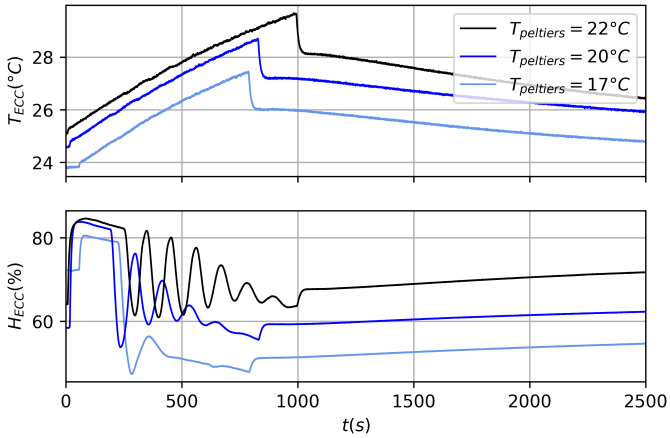

(b) Evolution of the temperature (top) and humidity (bottom) inside the ECC.

Figure 2.44: Evolution of the temperature and humidity in the EC and ECC as a function of time for three different Peltier temperature.

2.8.2 Consequences of a lack of thermal regulation

As mentioned in the previous section (2.8), a cold point (CP) could be used to reduce the humidity inside the EC. A non controlled cold point inside the EC will have the exact same impact on the humidity. It will slowly fix the humidity inside the entire chamber. The humidity inside the observed volume will then be the one described in eq 2.13 as the ratio of two water vapour saturation pressure with $T_{CP} < T_{EC}$ and T_{CP} the temperature of this cold point.

$$H_{obs} = \frac{P_v^{sat}(T_{CP})}{P_v^{sat}(T_{EC})} \tag{2.13}$$

This observed humidity can't exceed one and the main idea is to be as close as possible to saturation. This will allow studies on water aerosol on the long run, otherwise it will evaporate. The evaporation time is the time necessary for the aerosol to evaporate completely in the probed volume. The way to evaluate this time is explained in section 3.5. The evaporation time could be linked to the humidity as $t_{evap} = \frac{k_{exp}}{1-H}$ with a parameter k_{exp} that is determined experimentally during our parabolic flights (see section 3.5.1). The first hypothesis is to consider that the temperature of the CP instantaneously influences the humidity and impacts the aerosol observed via optical tomography. This will result in eq 2.14:

$$t_{evap} = \frac{k}{1 - H_{obs}} = \frac{k_{exp}}{1 - \frac{P_v^{sat}(T_{CP})}{P_v^{sat}(T_{EC})}} \tag{2.14}$$

The second option is to use the diffusion time necessary for a cold point to impact the humidity near the sensor or observed area in the EC. This study is described in section 2.8. The idea is then to modify the cold point observed temperature used to compute the humidity, to account for the diffusive nature of the process. According to section 2.8, the temperature will then evolve in an exponential manner (see eq 2.15) where τ is the characteristic diffusive time evaluated in section 2.8. The analogy with a thermal system, where τ is independent from the temperature difference or time, is applied. The EC temperature is fixed to 25 °C.

$$T_{CP,obs}(t) = T_{CP} + (T_{EC} - T_{CP})e^{-t/\tau} \tag{2.15}$$

The cold point observed temperature used to compute the evaporation time, will then be the average observed temperature used in eq 2.15 over the evaporation time. This leads us to the following equation:

$$t_{evap} = \frac{k_{exp}}{1 - \frac{P_v^{sat}(T_{CP,obs,avg})}{P_v^{sat}(T_{EC})}} \tag{2.16}$$

where $T_{CP,obs,avg} = \frac{1}{t_{evap}} \int_0^{t_{evap}} T_{CP,obs}(t)dt$. The solutions described in eq 2.14 and eq 2.16 are displayed in fig 2.45. The temperature of the EC,T_{EC} is fixed to 25 °C.

This approach is valid if the hypothesis that the factor k_{exp} is constant throughout time and for very high humidity levels is true (above 99%). This factor was determined experimentally during the parabolic flights campaigns,

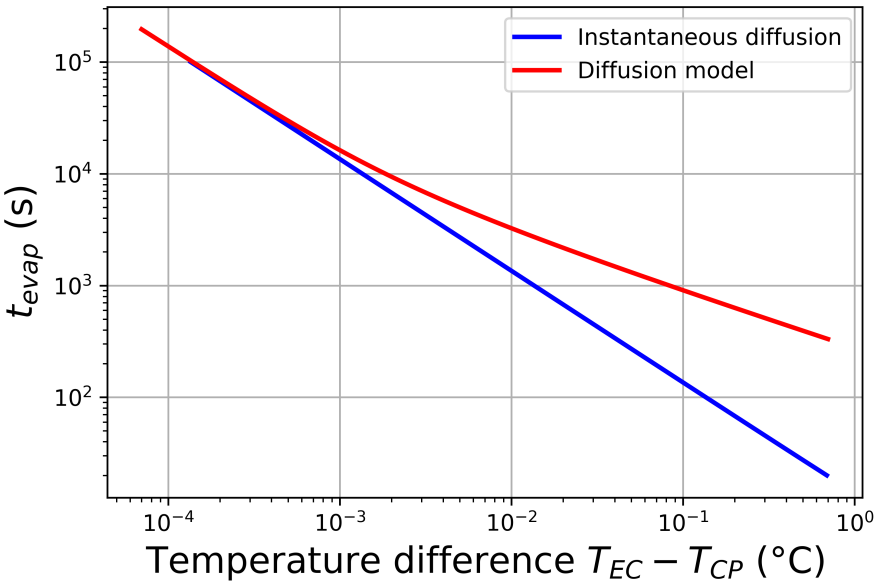

Figure 2.45: Evolution of the evaporation time as a function of the temperature of the cold point. The blue line describes the instantaneous diffusion model in equation 2.14, the red line describes the diffusive model and is based on the equation 2.16. The EC temperature is fixed at 25°C.

meaning that for longer periods of time (longer than 22 seconds), this is an extrapolation that was not observed yet.

The control of the dead volumes and the thermal regulation are key factors to control the humidity in long experiments. The system developed for this work is meeting the requirements and time restrictions of parabolic flight campaigns.

2.9 Secondary vapour injection

In order to study nucleation in mixtures and the composition of the gas phase in the EC with the FTIRS, a secondary vapour is introduced. It is key to know the volume injected of the secondary vapour (the primary being water vapour). To do so, on the secondary pumping circuit, a syringe is added as shown in figure 2.46.

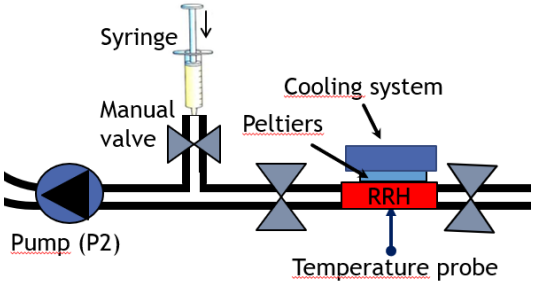

Figure 2.46: Scheme of the syringe used and its injection location into the secondary circuit (see figure 2.41).

This syringe is not pushed by hand as it will result in a lack of precision on the injected volume. It is pushed via a syringe pump from WPI model SP100i. The syringe used is an Hamilton syringe of 1 mL. The syringe is made of glass. If the syringe pump is started and the manual valve is closed and everything remains sealed, the increase of pressure could break the glass. This is an important security issue that could have prevented this system to be used in parabolic flight. To counter this issue, it was ensured that the screw thread was not tight between the syringe and the manual valve. As a result, when the syringe pump is started and the manual valve is closed, there is a leak and liquid is coming out via the screw thread (see figure 2.47).

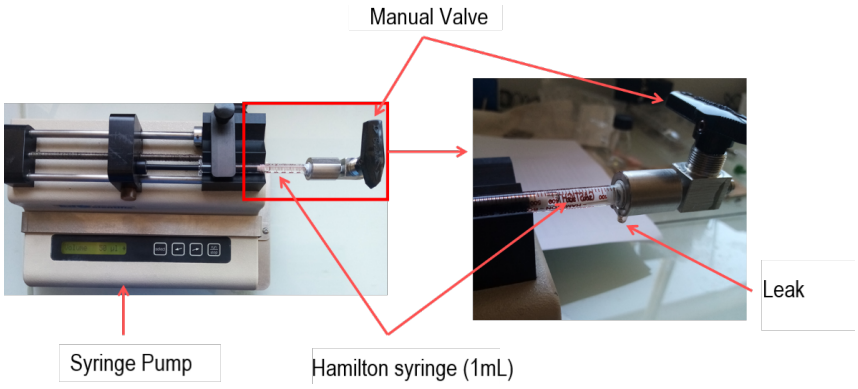

Figure 2.47: Picture of the syringe pump, the manual valve and the Hamilton syringe (1 mL).

2.10 Ground Qualification Tests

The objective of this section is to describe, understand and explain the aerosol production, the impact of relative humidity and the evolution of the temperature inside the EC during aerosol formation on the ground.

2.10.1 Aerosol production

The sequence that produces the aerosol is the same whether it is used on the ground or in parabolic flights. The sequence used for the aerosol production is the following:

- Configuration of the material and Hiris (software)
- Read Pressure (link with pressure sensor)
- Read camera position (for future tomography)
- Open TEV (To pump directly from the ECC)
- Start Pump P1
- Close Pump (when the target pressure value is reached in the EC or at the end of a timer)
- Wait (to let the gas inside the EC exchange with the walls and return to ambient temperature)
- Close TEV (end the circulation in the best circulation mode for the pump)
- Start Tomography with synchronized images and pressure data
- Open PEV (expansion start, leading to the creation of the aerosol)
- Close PEV (close the valve to go back to normal position and disconnect the EC and ECC)
- End of the recording
- Home Tomography (to ensure that the camera is at the right position for the next parabola)

This sequence is duplicated on the ground to ensure the conditions are known in parabolic flight. The following tests are done only in the ground.

2.10.2 Impact of relative humidity on aerosol formation

To understand the way the experimental set-up works precisely, it needs to be described quantitatively. The conditions, before expansion, have to be known in terms of pressure and temperature. The impact of humidity on those parameters is investigated hereafter.

Experimental protocol

The humidity of the whole system is set before the experiments are started. When the humidity is stable in the system (recorded by the humidity sensor), the following sequence is used: Start of temperature and pressure record inside the EC. Increase of EC pressure through the pump P1 to a controlled value (1800, 1900, 2000, 2100, 2200, 2300 mbar). Closure of TEV. Waiting time of 10 seconds to ensure reliable pressure and temperature conditions before the expansion. Opening of the PEV to expand brutally the gas and generate the aerosol. Record of the evolution of the droplets through Tomography microscopy. Every sequence is run three times then the sequence is changed to reach the next controlled pressure value. The figure 2.48 records the evolution of pressure and temperature through a run. Every part of the sequence can easily be identified. The files are not synchronised but the expansion is recorded by both signals and occur at the same real time, this allows for a recalibration of the signal.

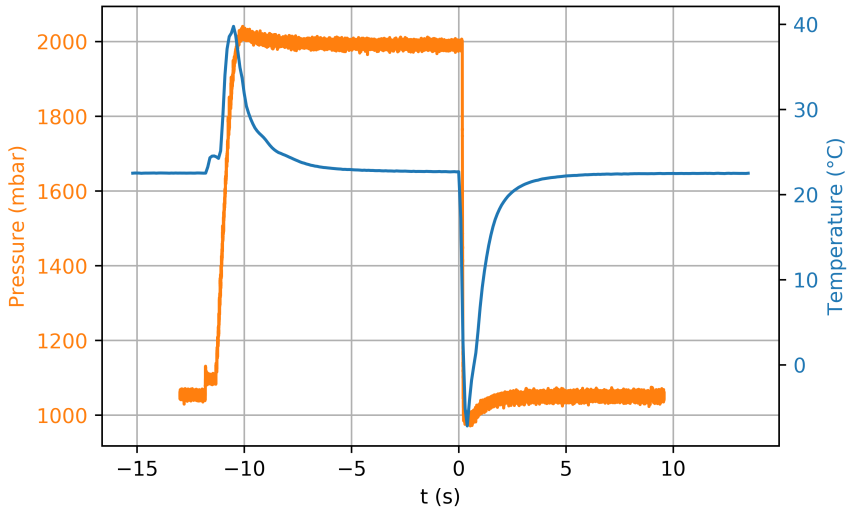

Figure 2.48: Evolution of temperature and pressure through a run.

Three phases could be observed in the figure 2.48, the first phase is the compression that increases the pressure and temperature. Then the gas

exchanges heat and cool down to its initial temperature. After that, the expansion decreases brutally the temperature and pressure. Finally the temperature goes back to its initial value. The objective is to describe the system accurately. Therefore, the information have to be quantified for every run. The following information will be analysed: highest temperature, time to go back to environment temperature after compression ($t_{cooling}$), lowest temperature (expansion), time to go back to environment temperature after expansion ($t_{warming}$) and pressure drop. As the fig 2.48 demonstrates, after the compression, the temperature cools down to the EC walls temperature.

Temperature evolution

The first idea is to evaluate the time required to go back to the EC walls temperature with a simple thermal model. The volume of air inside the chamber can be seen as a cylinder with air properties as water vapour only represents a small fraction of the gas mass even at saturation. The movement of the gas induced by the compression leads to strong turbulent exchanges inside the EC. As a result the temperature of the EC is considered homogeneous (0D model). With these hypothesis, a thermal balance can be established:

$$\rho_{air} V_{EC} C_{p_{air}} \frac{\partial T_{air}}{\partial t} = h_{cooling} S_{EC} (T_{wall} - T_{air}) \tag{2.17}$$

Letter	Meaning	value	unit
ρ_{air}	Air density	1.293	kg.m^{-3}
V_{EC}	Volume of the cylinder of the EC	4.24 10^{-5}	m^3
S_{EC}	Surface of this cylinder	7.068 10^{-3}	m^2
$C_{p_{air}}$	Air heat capacity	1006	J.kg^{-1}.K^{-1}
T_{air}	Air temperature inside the EC		K
T_{init}	Air temperature inside the EC at t=0		K
T_{wall}	Wall temperature of the EC		K
$h_{cooling}$	Heat exchange coefficient	7	W.m^{-2}.K^{-1}
$\tau_{cooling}$	Characteristic cooling time		s

This equation is a differential equation of the first order. The solution is:

$$T_{air}(t) = (T_{init} - T_{wall}) e^{-\frac{t}{\tau_{cooling}}} + T_{wall} \tag{2.18}$$

Here $\tau_{cooling}$ is the important factor as three times $\tau_{cooling}$ represents the time required to drop 95% of the initial temperature difference between the walls and the air inside the EC. It could be written as:

$$\tau_{cooling} = \frac{\rho_{air} V_{EC} C_{p_{air}}}{h_{cooling} S_{EC}} = 1.114\,\text{s} \tag{2.19}$$

Three times $\tau_{cooling}$ is 3.342 s. To reveal if the model is correct the idea is to compare $3\tau_{cooling}$ to $t_{cooling}$, the experimental cooling time recorded for every test after the compression.

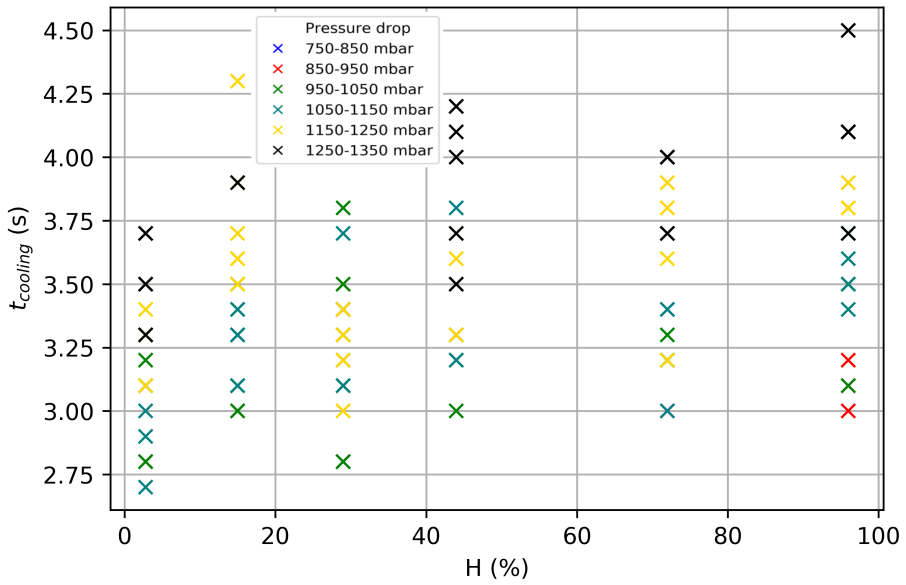

Figure 2.49: Cooling times as a function of humidity for different pressure drops. The legend indicates the pressure drop in mbar. Points are overlapping each other due to the lack of precise time resolution.

The pressure drop has little to no impact on the cooling time for the different humidities, at the end of the compression it takes the same time to go back to the EC walls temperature. The average time to go back after the compression to room temperature inside the EC is 3.50 s, so our simple thermal 0D model gives an approximation of the heat exchange coefficient h_{wall}. This cooling time gives a value for h_{wall} of $7\,\text{W.m}^{-2}\text{.K}^{-1}$. For an air flow, it corresponds to the high end of a naturally convected flow, or the very low end of a forced convective flow. This thermal model can be improved by looking up at the water presence in the vapour phase (increasing the thermal inertia) and challenging the homogeneous repartition of the temperature inside the EC (evolution towards a thermal model more complexed).

The relaxation time to warm up the volume is more relevant. As previously investigated, the pressure drop, and therefore how low the temperature goes, has little to no impact on the time necessary to warm up the gas after

the expansion. Unlike for the cooling time ($t_{cooling}$), the warming time shows a dependency in the humidity content (see figure 2.50), that is probably due to the aerosol being created, as after 40% humidity, droplets are visible for a short time. These droplets will require energy to evaporate, this process increases the time necessary to go back to the EC walls temperature.

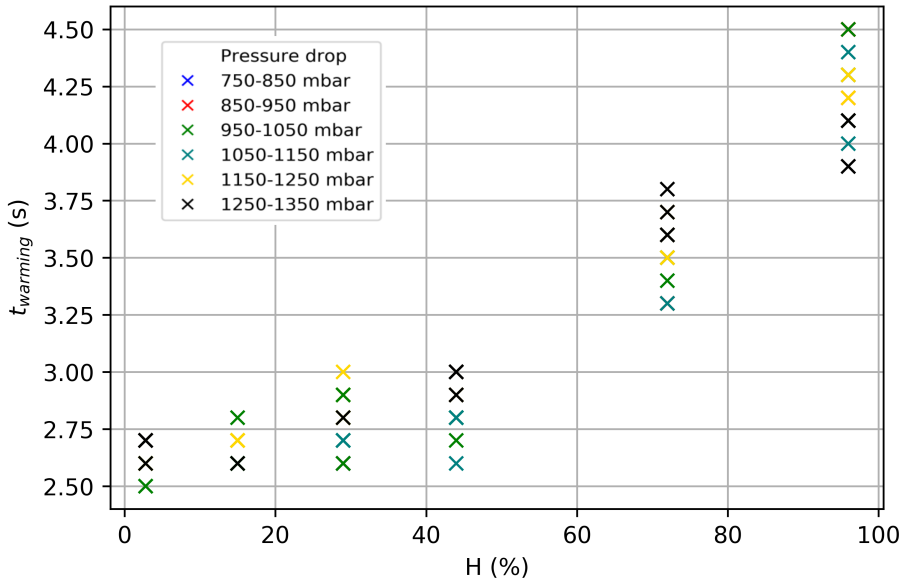

Figure 2.50: Record of the warming time as a function of the humidity. The legend indicates the pressure drop in mbar. Points are overlapping each other due to the lack of precise time resolution.

Temperature drop

The figure 2.51 shows the record for each experiment of the initial temperature, the maximal value and the minimal value. The temperature drop during the expansion $\Delta T = T_{initial} - T_{min}$ is recorded for each experiment, the relative humidity is also indicated on the legend.

For each experiment the initial and maximal temperatures stay the same no matter the pressure or relative humidity. This could be seen as expected for the initial temperature as when the sequence is fully executed, the system goes back to its initial conditions naturally as the figure 2.48 has shown previously. However the humidity has a role on the lowest temperature reached. First, it causes a raise in the thermal air capacity due to the water presence. Secondly, the nucleation of the droplets has an energetic cost, therefore a part of the energy previously used only to decrease the air temperature is now used to create the droplets. These reasons are limiting the temperature

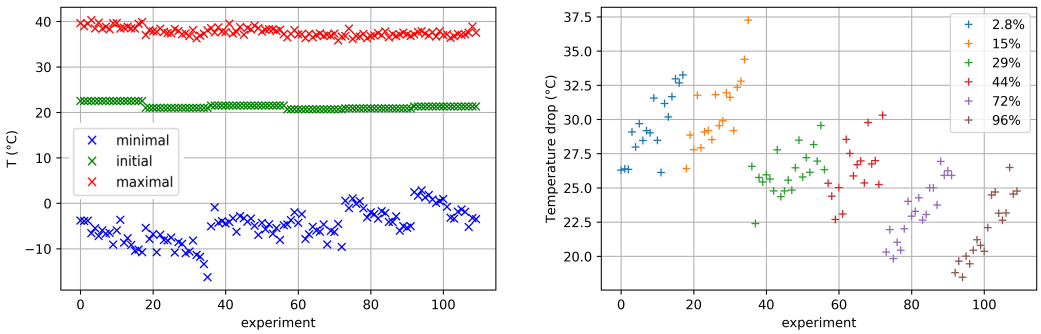

(a) Evolution of the temperature maximal, initial and minimal value for each experiment.

(b) Temperature drop for each run, in colour the relative humidity at the beginning of the run session.

Figure 2.51: Evolution of Temperature through a run.

drop. When looking at the temperature drop as a function of the pressure drop inside the EC (see figure 2.52) the impact of the humidity could be seen. For a particular pressure drop, the values with low humidity have a higher temperature drop.

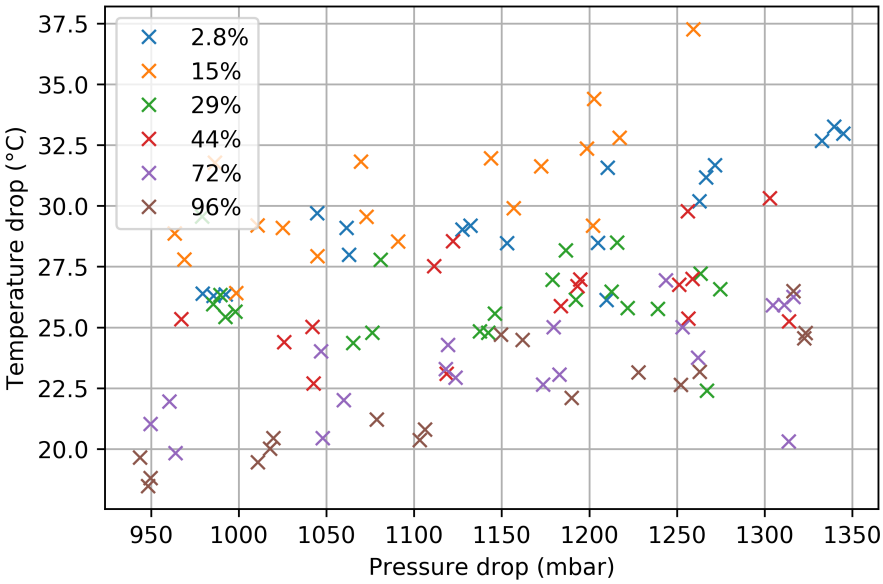

Figure 2.52: Record of the temperature drops as a function of the pressure drop.

Supersaturation

The supersaturation ratio is defined here as:

$$S = \frac{H(\%)P_v^{sat}(T_{initial})}{P_v^{sat}(T_{minimal})} = \frac{H(\%)P_v^{sat}(T_{initial})}{P_v^{sat}(T_{initial} - \Delta T)} \tag{2.20}$$

The supersaturation ratio is plotted for every experiment in figure 2.53 as a function of the temperature drop. The droplets are created by nucleation, as the air inside the circuit is not perfectly clean, it is most likely heterogeneous nucleation. The humidity inside the system allows for the creation of water droplets when the supersaturation is higher than 2.

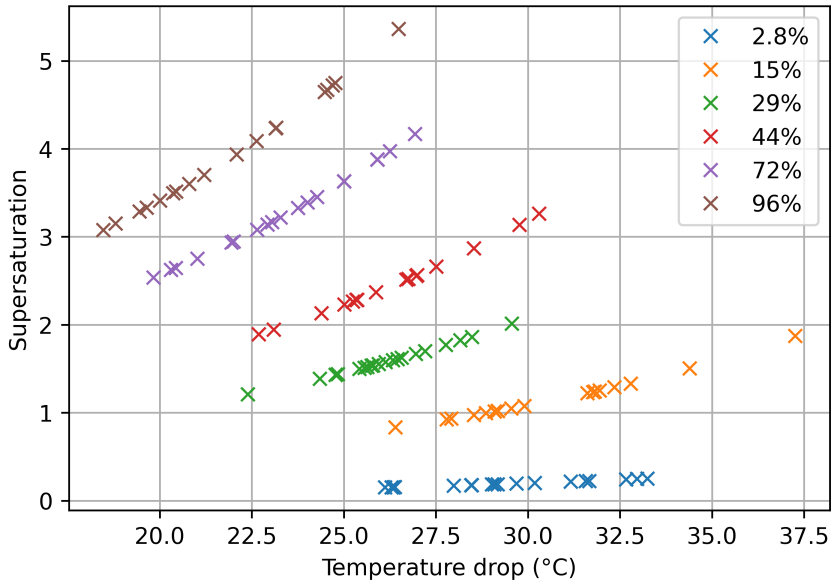

Figure 2.53: Record of the saturation investigated, droplets starts to appear at a saturation of 2. The legend indicates the humidity level.

For a fixed humidity, as the initial temperature is the same, only the minimal temperature (and therefore the temperature drop) will impact the supersaturation ratio. The lower the minimum temperature, and therefore the greater the temperature drop, the higher the supersaturation.

Chapter 3

Parabolic Flights investigation

An aerosol is subject to gravity on the ground and in high altitudes. However, in high altitudes, upward movements of warmer air keep the droplets in place and compensate gravity. This phenomenon allows droplets to have a high life time compared to what is possibly observable on the ground. On the ground, the gravity will drag the droplets down and settle the aerosol. The objective of this chapter is then to present experiment in microgravity using parabolic flights to have stable droplets levitating. Furthermore, the optical tomography microscopy technique needs coherence between two successive images, having a stable aerosol will increase the quality and the post processing of the data. This chapter will be presenting the course of a parabolic flight campaign, the results obtained about evaporation and the results when adding a second vapour to create a binary mixture water/HFE-7100.

3.1 Course of a campaign

One parabolic flight campaign is composed of two main parts, the preparation and validation of the experiment by the team of Novespace, and the flying part during which the experiment in microgravity happens. The process ahead of the flying part won't be presented. The flying part is composed of three days, each day has one flight during which 31 parabolas are performed. Each parabola is composed of three phases, during the first phase, the plane is tilting upwards to gain altitude, leading to an hyper gravity ($1.8\,g$) for 20 seconds. Then the engines are reduced to the minimum to start the microgravity phase, this phase is where the experiments could take place and last typically 22 seconds (as shown in figure 3.1). Finally there is the last phase where the plane is stabilizing to the starting altitude (hyper gravity again into normal gravity), a break of approximately two minutes is done and

the next parabola starts as indicated in figure 3.2. The figure 3.2 gives the timing of a parabolic flight. One scientific campaign is made of three flight like this. It gives 93 parabolas per campaign in total.

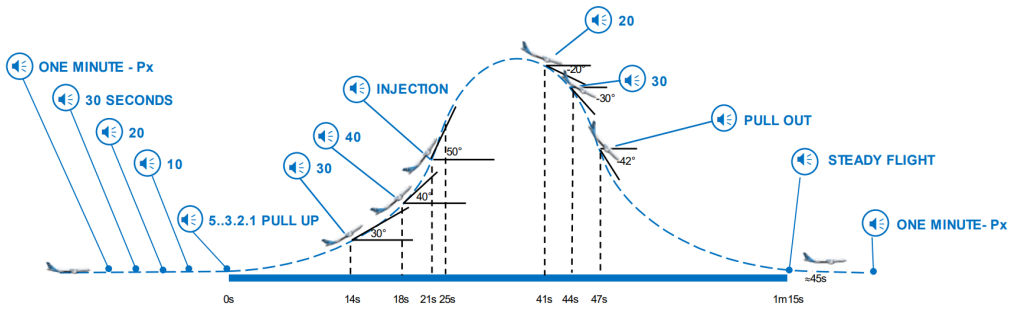

Figure 3.1: Timing and announcements made by the pilots during a parabola.

During each parabola, the objective is to form the aerosol at the beginning of the microgravity phase. Each parabola has the same timings and announcements, they are listed in the figure 3.1. The sequence, from the click on the run button to the expansion, takes approximately 17 seconds. The expansion has to occur at the beginning of the micro gravity phase. As a result, the sequence is started 8 seconds after the "pull up" announcement, this is adjusted in flight on the firsts parabolas as the timing may vary slightly from one pilot to an other.

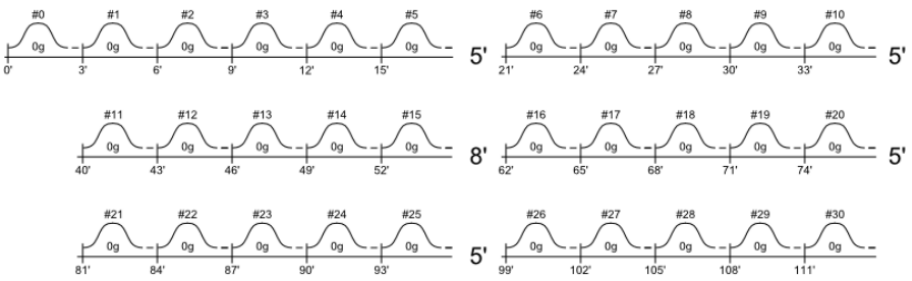

Figure 3.2: Parabolic flight, the times are given in minutes.

During the breaks, operation on the experiment could be done to modify parameters and prepare for the next round of parabolas.

3.2 Humidity evolution

During the parabolic flight campaigns, when evaporation was investigated, the key parameter is the humidity. As there is no time to circulate the gas between parabolas and stabilise the humidity, there is an evolution of the humidity conditions inside the EC. During the compression phase, water vapour is added from the ECC to the EC. Then, the nucleation process transforms water vapour into liquid water droplets, these droplets will globally stay inside the EC after the expansion. As a result, a part of the water vapour added during the compression phase stays in the EC. This increment is illustrated on figure 3.3 as the difference between the first ($H = 72.5\%$) and last value recorded ($H = 80\%$).

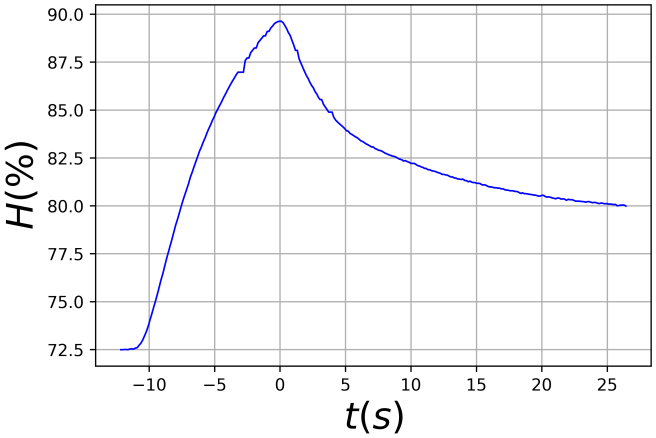

Figure 3.3: Humidity evolution throughout time for one parabola in the EC. At t=0 there is the expansion leading to nucleation and creation of the droplets in the EC.

This difference is adding up and causes the humidity to increase every time a compression/expansion is performed (see figure 3.4b). This increase of humidity is not controlled but corresponds to a gradual increase of the humidity and allows for the investigation of a large humidity range (see figure 3.4). This increment is reproducible whether on the ground or in parabolic flight campaign. This increment is plotted in figure 3.4b as the humidity jump as a function of the initial humidity.

The increment is decreasing linearly as the humidity is increasing (see figure 3.4a). To investigate evaporation over a large humidity range during the evaporation experiments, this phenomenon was used. For the first parabola, the idea is to have 75% humidity to start. After 15 parabolas, the humidity is high enough to have living droplets until the end of the parabola inside

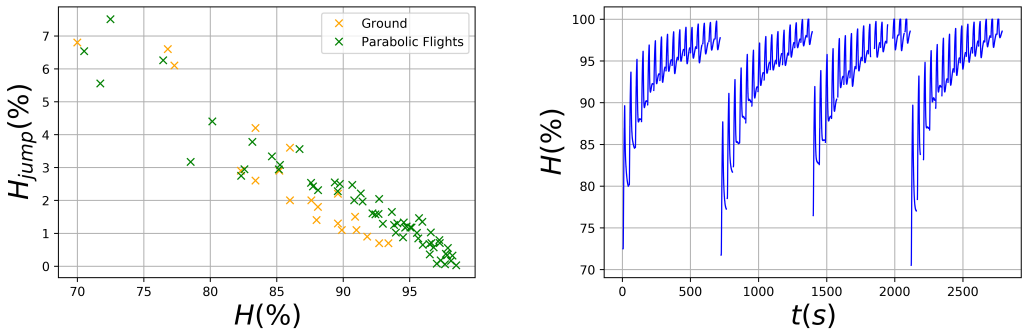

(a) Humidity jump as a function of the initial humidity.

(b) Compilation of humidity evolution in the EC.

Figure 3.4: Evolution of the humidity with compression/expansion.

the EC. It is not ideal as it is not controlled but during a parabolic flight campaign, there was not enough time to control the humidity and stabilise it with the CP produced by the Peltier system.

3.3 Initial flow and relaxation time

After typically 5 seconds, the initial flows are damped out and the droplets are stable. As a result, there is a high quality reconstruction of the aerosol because of the high coherence between consecutive images. Before that the reconstruction is not perfect but some data can still be extracted such as the average speed of the droplets in the (x,y) plan. The droplets average speed show an exponential decay during the first seconds (see fig 3.5), the decay is due to the viscous dissipation of the initial flow created by the expansion at $t = 0\,\mathrm{s}$, the acceleration at the end of the parabola (22 s and above) is due to the beginning of the hyper gravity phase of the parabola.

The droplets are liquid elements inside a flow, they are therefore submitted to a drag stokes force that is proportional and opposed to their speed. If gravity is considered negligible during this phase (the expansion is done at the beginning of the microgravity phase) then the only force applied on a droplet is this drag force (see equation 3.1).

$$\rho_{water}\frac{4}{3}\pi R^3\frac{d\mathbf{v}}{dt} = -6\pi\mu_{air}\mathbf{v}R \tag{3.1}$$

with $\mathbf{v}$ the droplet velocity and m its mass. This equation 3.1 is a first order equation for the velocity. The important factor here is the characteristic time $\frac{2\rho_{water}R^2}{9\mu_{air}}$. This time is low in our experiment (in the order of $10^{-4}\,\mathrm{s}$ for droplet

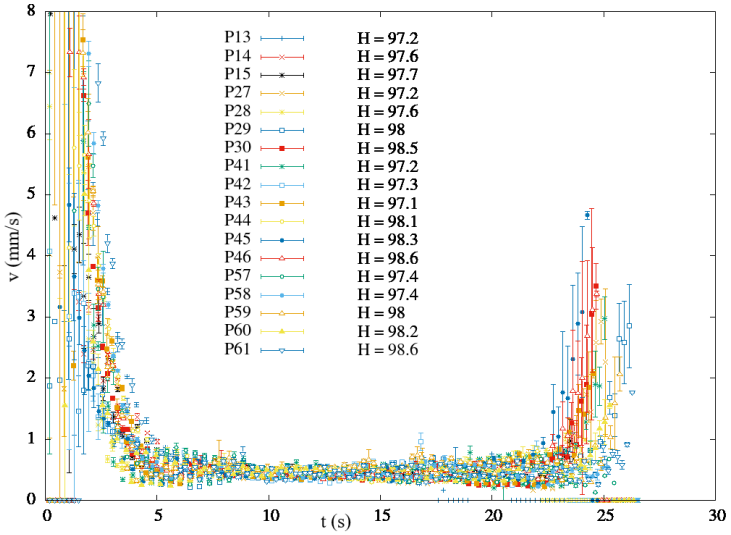

Figure 3.5: Average droplet velocity for different humidity recorded during the 64th parabolic flight campaign.

of 5 μm in diameter). This means that the droplets are instantaneously driven by the flow. So the droplets in the first seconds are acting as tracers for the flow, indicating the overall dynamic of the average speed decay due to the viscous dissipation. There, the characteristic time for the evolution of the flow could be evaluated as 1.333 s.

3.4 Reproducibility of experiments

When dealing with nucleation, it is important to be as reproducible as possible, that is the reason why there is a 10 seconds delay between the end of the compression and the expansion, this time allows the system to cool down and be in a reproducible and stable thermodynamic state before the expansion, resulting in a isothermal compression (see figure 2.48). When creating the aerosol, there is two things to look at in terms of reproducibility, the number of droplet in the probed volume and the size of the average droplet. Both of them would be analysed. The first thing analysed is the radius or the diameter of the average droplet. Figure 3.6 shows the average droplet diameter evolution throughout a parabola for the first parabolas of the 62nd parabolic flight campaign. As the environment is saturated in water, there is no evaporation, leading to droplets observation until the end of the parabola (occurring at 25 seconds).

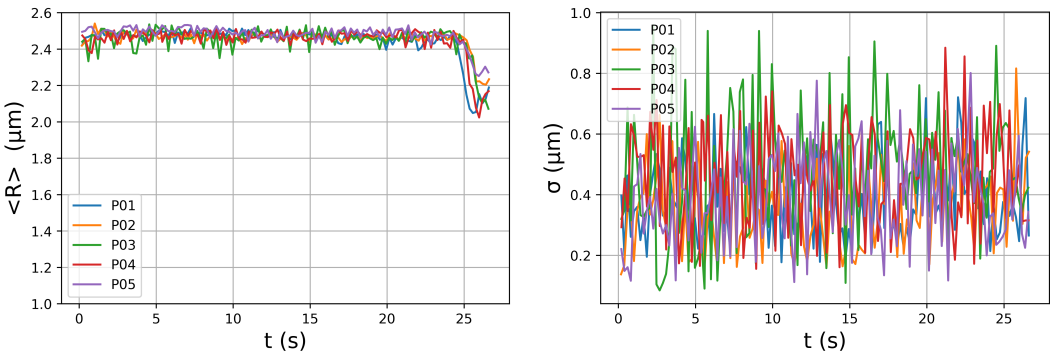

(a) Average droplet diameter evolution.

(b) Standard deviation evolution.

Figure 3.6: Average droplet diameter and standard deviation of the radius distribution evolution for the firsts parabola of the 62nd parabolic flight campaign. ($\Delta P = 1200\,\text{mbar}$, $T = 22\,^{\circ}\text{C}$)

The figure demonstrates that the diameter is reproducible from one experiment to another. For the experimentation of the 62nd parabolic flight campaign, the number of droplet in the probed volume is in between 100 and 200 (displayed in figure 3.7).

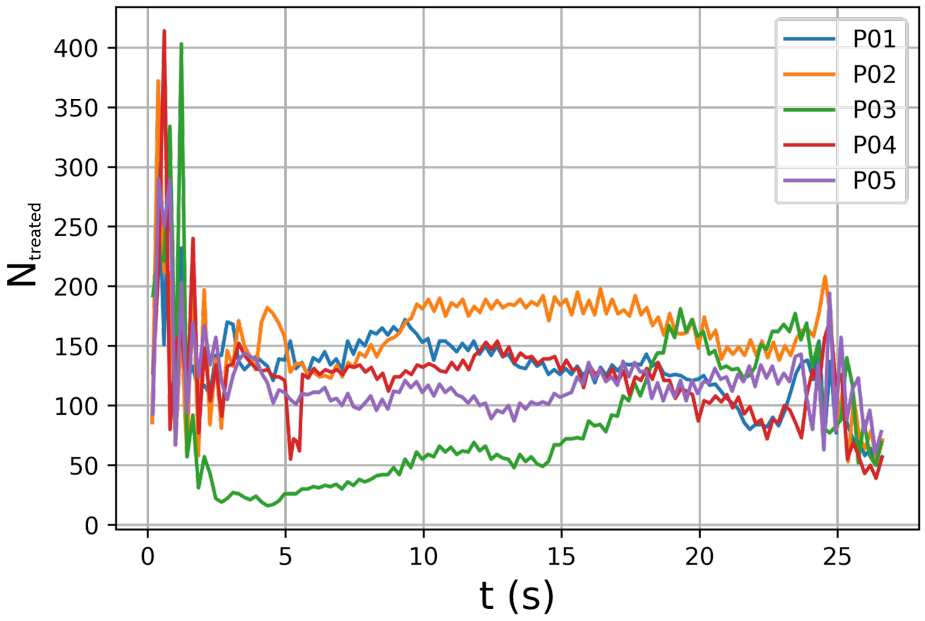

Figure 3.7: Number of droplets per scan in the probed volume, throughout time for the firsts parabolas of the 62nd parabolic flight campaign.

The number of droplet in the probed volume is not fully reproducible. For most of the experiments, it stays between 100 to 200 droplets. Some experiment show up to 400 droplets and some have low amount of droplets (around 50). As the nucleation process is heterogeneous, an exterior agent is used as a nucleus (here dusts present inside the EC and their amount is not controlled). This along with the small volume probed (only $2\,mm^3$) shall explain the variation from one parabola to another or from one campaign to another.

3.5 Evaporation of droplets

In this section, the results from the parabolic flight campaign obtained in march and October 2023 are described. The objective is to study the evaporation of an aerosol by varying the humidity inside the EC. Below 100% of humidity, thermodynamically there is no possibility to have droplets floating around. They will therefore evaporate to maximize the humidity inside the EC first. This evaporation mechanism is followed via the optical tomography.

3.5.1 Global evolution

The first thing to study is the time necessary to evaporate the aerosol and to compare it to the evaporation of a single droplet. This will help to understand the impact of a droplet population on the aerosol evaporation. The protocol used to regulate the humidity inside the cell is explained in section 2.8. It is important to keep in mind that during the evaporation experiments, the humidity is evolving by increments due to the cycle of compression-expansion described in section 2.10.1. For the 64th parabolic flight campaign, 62 points of data were gathered to ensure reproducibility. The time necessary to see a disappearing of the aerosol is called evaporation time and recorded in the figure 3.8. The humidity considered is the one at the end of a parabola.
The fitting curve used in the figure 3.8 is based on the evaporation model (eq 1.4) of a single droplet extracted from the review of H. Yildirim Erbil [36]. This model is from the first approach, developed in section 1.1.2. This model is given for a droplet of a millimetric size. Here as the droplets studied are of the micrometric order, this model might not be the perfectly adapted but it is a good first approach. The Knudsen number indicates whether fluid behaviour should be modeled using statistical mechanics or continuum mechanics in fluid dynamics. Here, the Knudsen number is equal to $Kn = \lambda_{mfp}/d = 0.0132$, where λ_{mfp} is the air mean free path (66 nm) and d the droplet diameter. In this context, the continuum physics shall still hold

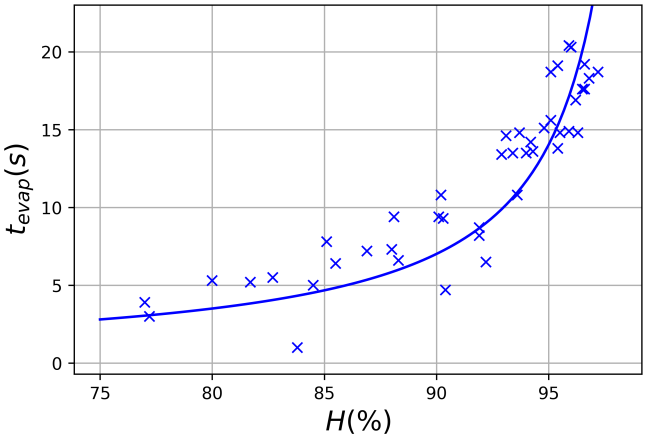

Figure 3.8: Evolution of the recorded lifetimes of the aerosol with humidity for the two first days of the 64th parabolic flight campaign. The fitting is based on the theory described in eq 1.7.

even if this is the very end of the continuum physics domain [165]. The figure 3.8 demonstrates the agreement of the results obtained in the parabolic flight campaign with equation 1.7. For the fitting in figure 3.8, values of a lifetime above 22 s are not taken into account, it corresponds to the end of the parabola and therefore it is likely that the aerosol would have lived longer if a longer microgravity phase was available. In this fit, the factor k_{exp} is estimated to be 0.71 s. The factor k_{exp} could also be evaluated from eq 1.6 with $k_{th} = \frac{R_0^2 \rho_{water} \mathcal{R} T}{2 D_{va} M P_v^{sat}(T)}$. With the values described in the table bellow:

Letter	**Meaning**	**value**	**unit**
ρ_{water}	Water density	998	kg.m^{-3}
R_0	Initial radius	2	μm
T	Air temperature	293	K
$\mathcal{R}$	Perfect gas constant	8.314	J.kg^{-1}.mol^{-1}
D_{va}	Diffusion coefficient of water in air	2.42 10^{-5}	m^2.s^{-1}
$P_v^{sat}(T)$	Saturation vapour pressure	2325	Pa
k_{th}	Millimetric model factor	0.00444	s
k_{exp}	Experimental factor	0.71	s

There is a difference by a factor 200 between the experimental value and the theoretical one. However, this simple theory is able to catch the fact that a single factor is necessary to fit the experimental data in the eq 1.7. The thermal approach has to be studied to capture at best the evolution of the aerosol as will be explained in section 3.6.

3.5.2 Numerical resolution: Temperature evolution

To understand properly the conditions in which the droplets are evaporating, it is key to understand the thermodynamic conditions in which the droplets evolve locally. This state is not accessible with a sensor and has to be numerically assumed. After the expansion and the damping of the initial flow, the temperature inside the EC evolves with conduction only. The hypothesis done for this simplified model is that the temperature is following the heat equation 3.2. This leads to a temperature following the equation of the form:

$$\frac{\partial^2 T(r,z)}{\partial r^2} + \frac{\partial^2 T(r,z)}{\partial z^2} + \frac{1}{r}\frac{\partial T(r,z)}{\partial r} = \frac{1}{a_m}\frac{\partial T(r,z)}{\partial t} \tag{3.2}$$

where T is the temperature in the gas phase, a_m is the moist air thermal diffusivity ($a_m = \frac{\lambda_{cond}}{\rho_{air} C_{p_{air}}}$, with λ_{cond} the thermal conductivity of moist air and $C_{p_{air}}$ the thermal capacity) and (r,z) the cylinder coordinates. This equation is discretized and solved via Python (explicit scheme). By symmetry, only one fourth of the EC is meshed. The radius of the chamber (R_{EC}) is 15 mm, respectively Z_{EC} = 30 mm and the space between two mesh nods (dr=dz) is 0.25 mm. The time increment (dt) is 0.1 ms for a total simulation time of 25 s. The CFL is calculated as $a_m dt/dr^2 = 0.036$, this number is below 0.25, this indicates that the resolution is stable. A division by 10 or 100 of the time increment does not change the quality of the solution (the temperatures curves are superimposed). The simulation is also stable when the space between two mesh nods is reduced by a factor 10.

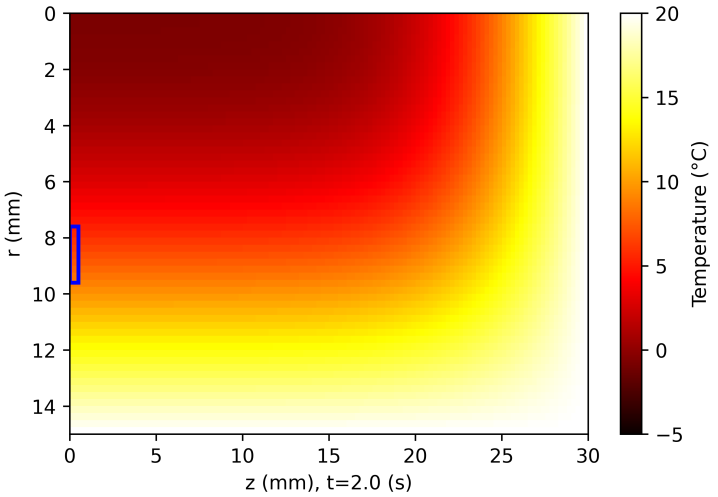

Figure 3.9: Temperature map of the EC, the blue rectangle represent the probed volume investigated by optical tomography. 2D model using conduction only. The centre of the EC is on the top left corner.

The initial conditions are fixed by $T(t=0,r,z) = -5\,°\text{C}$, because that is the temperature measured by the sensor after the expansion (see figure 2.48). The boundary conditions are fixed by $T(t,R_{EC},z) = T(t,r,Z_{EC}) = 20\,°\text{C}$ because when evaporation was investigated in the A310 zeroG of Novespace, the thermostat of the cabin was at 20 °C.

The first thing to notice is that the evolution of the temperature in the probed volume does not depend significantly of the z coordinates. This result will motivate a one dimensional approach for the next steps. This leads to a modification of equation 3.2 to 3.3.

$$\frac{\partial^2 T(r)}{\partial r^2} + \frac{1}{r}\frac{\partial T(r)}{\partial r} = \frac{1}{a_m}\frac{\partial T(r)}{\partial t} \tag{3.3}$$

With this one dimensional model, the temperature gradually evolves to reach the temperature of the wall of the EC (see figure 3.10).

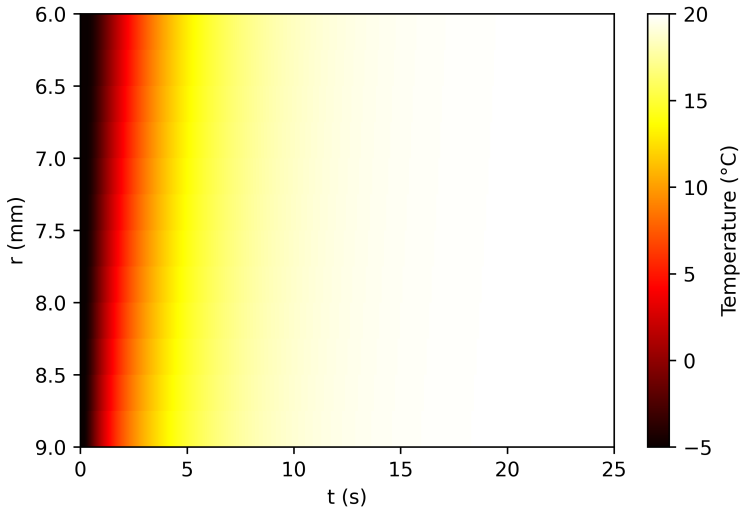

Figure 3.10: Temperature map of the probed volume investigated by optical tomography throughout time. 1D model using conduction only.

The objective of this section is to have the best simple numerical model to access the temperature and heat flow inside the chamber. So far, this model is only using conduction and it may be valid after the air flow is damped but the initial condition where $T(t=0,r) = -5\,°C$ and the conductivity is the one of still moist air might be far from reality. To cope with this issue the idea is to force convection into the conductive scheme without implementing a velocity field. To do so, a few elements are modified: on the limit ($r = R_{EC}$) the condition becomes:

$$-\lambda_{eff}(t)\frac{\partial T}{\partial r} = h(t)(T(t, R_{EC}) - T_{wall}) \tag{3.4}$$

Where T_{wall} is the wall temperature of the EC ($T_{wall} = 20\,°\mathrm{C}$) and h is the heat convective exchange coefficient between these walls and the air inside. The initial flows created by the expansion of the gas to form the aerosol are damped out fast, so the idea is to use this information as a way to evaluate h as follows:

$$h(t) = h_f + (h_0 - h_f)\exp(-t/\tau_h) \tag{3.5}$$

Here h_0 is the initial heat convective exchange coefficient value ($20\,\mathrm{W.K^{-1}.m^{-2}}$), h_f is the final value of the heat exchange coefficient when everything is settled down ($2\,\mathrm{W.K^{-1}.m^{-2}}$), and τ_h is the characteristic time of the flow speed evaluated as 1.33 s from section 3.3. The value of the thermal diffusion coefficient is also modified to reflect an effective thermal diffusion coefficient as :

$$\lambda_{eff}(t) = \lambda_{cond}\left[1 + \left(\frac{h_0}{h_f} - 1\right)\exp(-t/\tau_h)\right] \tag{3.6}$$

with $\lambda_{cond} = 0.025\,\mathrm{W.K^{-1}.m^{-1}}$. This way the conduction scheme reflect to some extent the convection happening inside the EC. The results are plotted in figure 3.11.

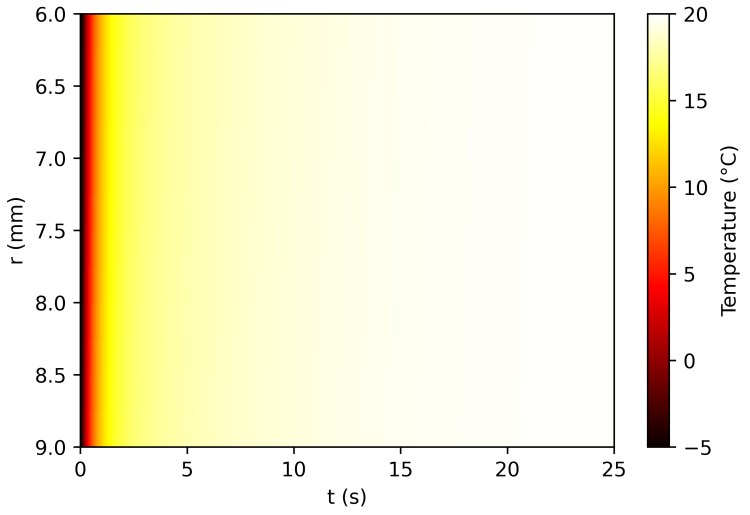

Figure 3.11: Temperature map of the probed volume investigated by optical tomography throughout time. 1D model using conduction and convection into the numerical scheme.

As the conduction can't truly develop before five seconds, the temperature profile in figure 3.11 is much straighter across the probed volume compared to the diffusion only scheme in figure 3.10. From those data, the heat flow across the probed volume could be estimated with the equation below.

$$\Phi_{conv}(t,r) = -\lambda_{eff}(t)\frac{T(r = 8.6\,\mathrm{mm}) - T(r = 6.6\,\mathrm{mm})}{2 \cdot 10^{-3}} \tag{3.7}$$

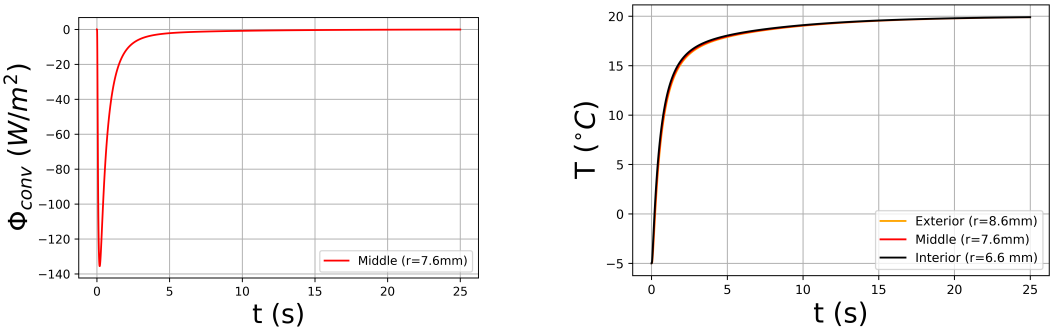

(a) Heat flux going through the probed volume as a function of time.

(b) Temperature evolution inside the probed volume as a function of time.

Figure 3.12: Thermodynamic conditions inside the probed volume as functions of time.

The colour code that will be used for the next sections reflects the fact that, even if it is a small thermal gradient, the deeper you are going towards the centre of the EC (decreasing values of r), the cooler the temperature is. This is based on the approach shown by figure 3.9. From these numerical resolution, the early evaporation from the outer regions of the probed volume could be linked to an early change in the thermodynamic conditions as known as an early rise in temperature. The model could be improved by implementing a thermal capacity model that takes into account the evaporation of the droplets.

3.6 Local evaporation

After the expansion, the temperature inside the volume is cold (see section 2.10.2) and the walls of the EC stay at a stable temperature even after the expansion as the thermal inertia of the steel is high compared to the gas in the EC. So, the heat flux coming from the walls will warm up the outer air layers first (see section 3.5.2). A higher temperature leads to an increase of the saturation pressure. So, for a fixed water vapour quantity,

the humidity decreases, which leads to a faster evaporation of the droplets surrounded by this water vapour. This is leading to an early evaporation of the outer layers of air compared to the centre of the EC. The walls of the cell will create inhomogeneities in term of temperature (see figure 3.12) in the probed volume. The fact that evaporation is influenced by the heat flux coming from the walls is illustrated in figure 3.13 where reconstructions across different times are displayed. Here, the evaporation starts from the bottom of the volume corresponding to the outer parts of the probed volume.

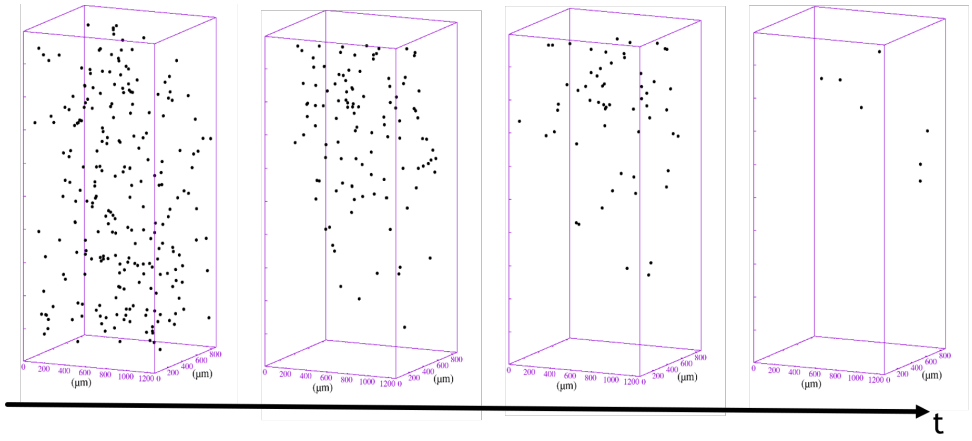

Figure 3.13: Record of the aerosol evolution through different stages showing the preferential evolution from the bottom of the volume which correspond to the higher values of r.

3.6.1 Local evolution of the droplet number

From this conclusion, the continuation that came in mind is to divide the probed volume into smaller ones and quantify the local evaporation. The volumes chosen have the same section as the probed volume in fig 3.13 ($1280\,\mu$m $\times$ $860\,\mu$m), the only thing that varies is the height. In figure 3.14, each smaller volume height is one fifth of the total probed volume height (that is 0.4 mm). It was chosen to divide the volume in five to have a number of boxes that can indicate a relevant spatial disparity and to keep enough droplets in each boxes to have statistically relevant averages. After the reconstruction of the aerosols, droplets are counted into their respective volumes to quantify the difference in terms of evaporation and understand the local evaporation dynamic.

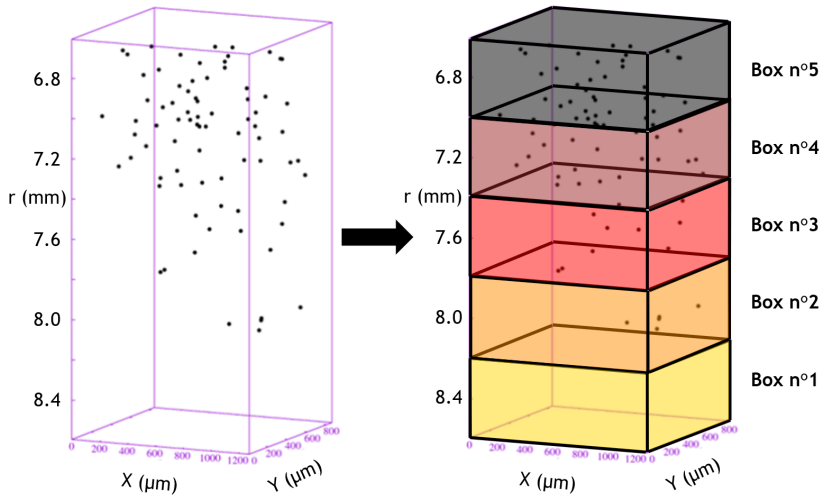

Figure 3.14: Decomposition of the probed volume into five smaller ones, $r = 0\,\text{mm}$ corresponds to the central axis of the EC. The box 1 is the closest to the wall where the heat flux is coming and directed towards the EC centre.

The result from the counting of the droplets is displayed in figure 3.15 (Parabola 6, 64th parabolic flight campaign), the first part of the graph (up to three seconds) can't be fully trusted as the initial flows are not relaxed yet (see section 3.3).

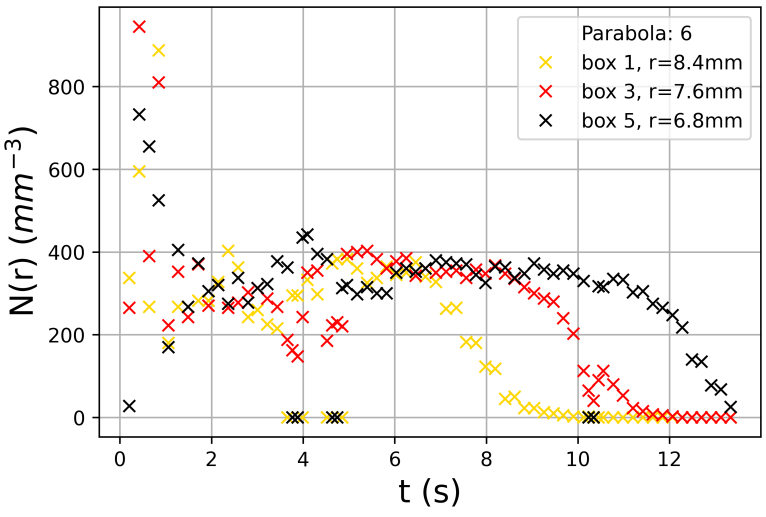

Figure 3.15: Record of the droplet number density per box per scan throughout time. Here only three of the five boxes are represented for visibility. These volumes are represented from the bottom to the top.

The idea is now to describe the aerosol evolution using hyperbolic fittings.

$$N(r,t) = A\left(1 + \tanh\left(\frac{t_{ev,N} - t}{\tau_{ev,N}}\right)\right) \tag{3.8}$$

The figure 3.16 shows the data for the five boxes and their associated fitting curves. The different fitting curves are hyperbolic tangents done to fit to its best the decay in terms of number of droplets detected inside the smaller volumes. From those data, it appears that there is a delay, the outer region of the volume tends to evaporate first (respectively the lower box number), this confirms the intuition and secondly, this delay could be measured to evaluate the heat flux and local humidity impacting the temperature of the smaller domains and therefore the local evaporation. The objective would then be to analyse the evolution of the fitting parameter $t_{ev,N}$ which correspond to the hyperbolic tangent half height.

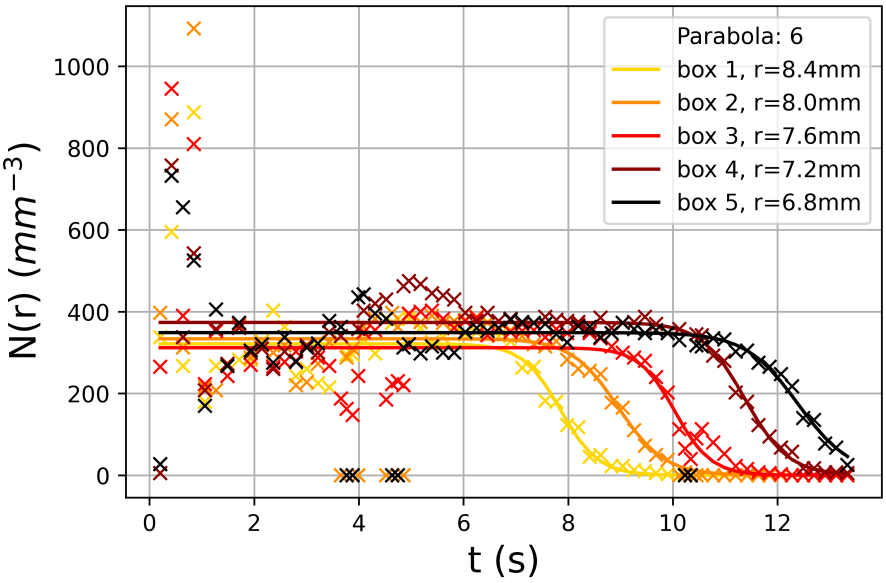

Figure 3.16: Record of the droplet number density per box per scan throughout time. In the same colour as the data, the corresponding fitting hyperbolic tangent. Parabola 6, 94.2% humidity

From that situation, the idea is to evaluate the different fitting parameters like the middle height tangent ($t_{ev,N}$) and have a look at the difference between these values for each boxes. This delay seems to be linear as there is roughly one second delay between each of the boxes. This difference in evaporation shall be triggered by a local difference in temperature or humidity. For this set of data (parabola 6 of the 64th parabolic flight campaign),

the humidity is quite high (94.2%), leading to an overall long lifetime. For lower humidity (this time 80%, parabola 0, same campaign), evaporation is happening faster. It means that the temperature inhomogeneities are not able to develop inside the probed volume leading to no visible discrepancies in the fitting lines. This is shown in figure 3.17 where the evaporative delay is a lot shorter if there is any at all.

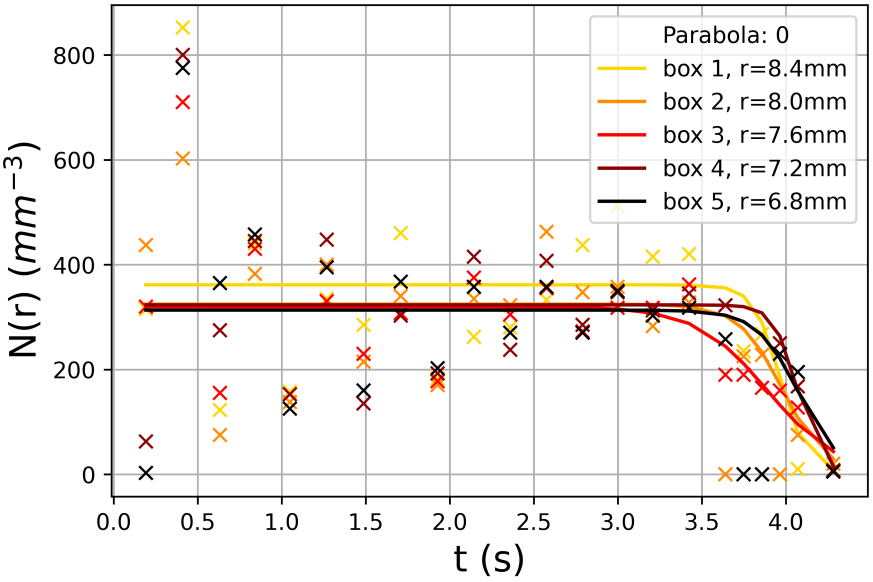

Figure 3.17: Record of the droplet number density per box per scan throughout time. In the same colour as the presented data, the fitting hyperbolic tangent. Parabola 0, 80% humidity.

In the same fashion, the results for the half height values ($t_{ev,N}$) for each boxes of the 64th parabolic flight campaign are displayed in figure 3.18 as a function of the humidity recorded at the end of the parabola. For humidity values lower than 86% the evaporation profile is relatively flat and there is no delay between the different boxes, as seen for parabola 0. For humidities higher than 86%, the delay from the inhomogeneous temperature is visible and its effect is seen the higher the humidity is. For values in humidity higher than 98% to 99% the aerosol is living until the end of the parabola, fitting these data would then not be pertinent as the aerosol is disappearing from a $1.8\,g$ gravity pull and not evaporation.

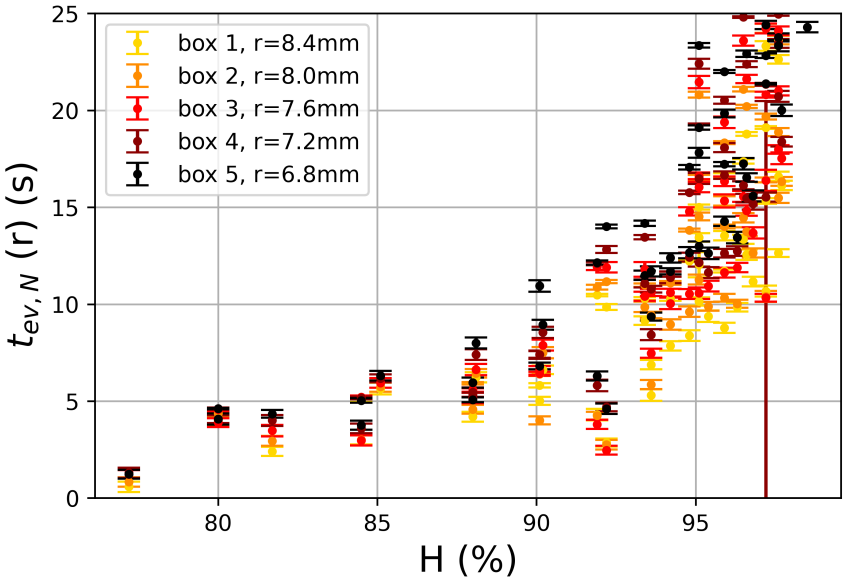

Figure 3.18: Record of the middle height tangent $t_{ev,N}$ for each boxes as a function of the humidity.

For a given humidity, the difference between the first box in gold ($r = 8.4\,\text{mm}$) and the last one in black ($r = 6.8\,\text{mm}$) is giving an idea of how long it takes to complete the evaporation. It is important to keep in mind that humidity is not the only parameter that will affect the aerosol evaporation in this case. As presented in section 3.3 there is movement in the first few seconds of the aerosol life, leading to convection and homogeneous thermodynamic properties inside the probed volume. When this flow stops, diffusive mechanisms will be prevalent leading to differences in humidity and the creation of a temperature gradient that will impact the aerosol evaporation along with the humidity. Figure 3.18, is probably the best representation to see the impact on the aerosol from the fluid regime occurring inside the EC. When the humidity is below 86%, the evaporation is taking place in less than 5 seconds the flow is then still moving, leading to homogeneous thermodynamic conditions around droplets. As a result, the evaporation between the boxes does not differ that much as it's only affected by the global humidity and temperature conditions. When the humidity is higher than 86%, the aerosol outlives the convective flows occurring inside the EC and as nothing is moving after that, diffusion will prevail. This will lead to linear temperature evolution inside the EC (see section 3.5.2), and therefore a linear humidity difference and this is the reason that shall explain the constant delay when looking at the evaporation in-between the boxes in figure 3.16. To capture the humidity difference between the boxes, the idea is to fit the

$t_{ev,N}$ for each boxes and induce a variation from the average. The fitting equation is represented via eq 3.9 based on the behaviour from the figure 3.8:

$$t_{ev,N} = \frac{k_{ev,N}}{1 - (H(\%) + \beta_{avg})} \tag{3.9}$$

The value of $k_{ev,N}$ is 0.90 s is slightly different from the global one k_{exp} (0.71 s) but the method is different and considers the middle height point not the total evaporation of the aerosol. The fitting, added to figure 3.18 is displayed in figure 3.19.

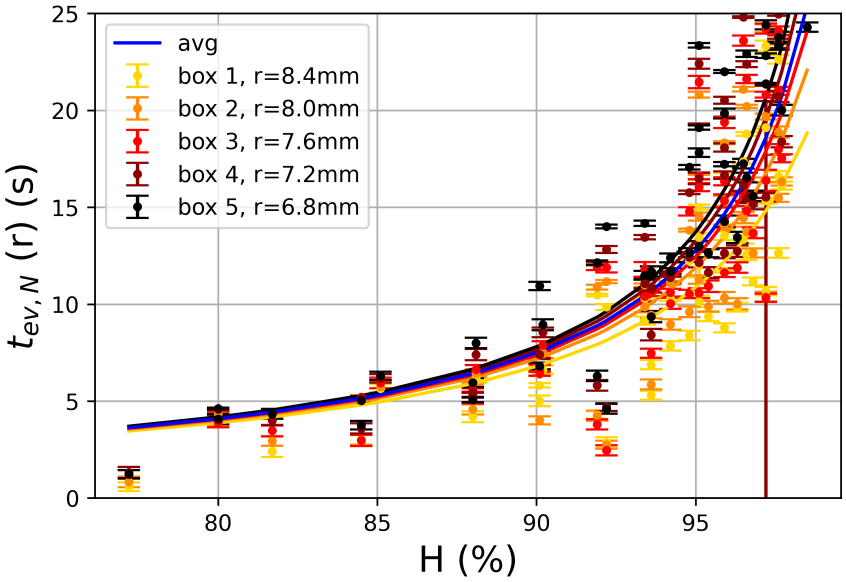

Figure 3.19: Record of the half height tangent $t_{ev,N}$ for each boxes as a function of the humidity. Along with the fitting values for each box based on eq 3.9. The average values for the data are in blue.

When doing the fitting for the boxes, the value $k_{ev,N}$ is kept constant and only β is allowed to change. The results are displayed in figure 3.20 for the difference between the box value of β and the average β_{avg}.

$$t_{ev,N} = \frac{k_{ev,N}}{1 - (H(\%) + \beta_{avg} + \beta_{ev,N})} \tag{3.10}$$

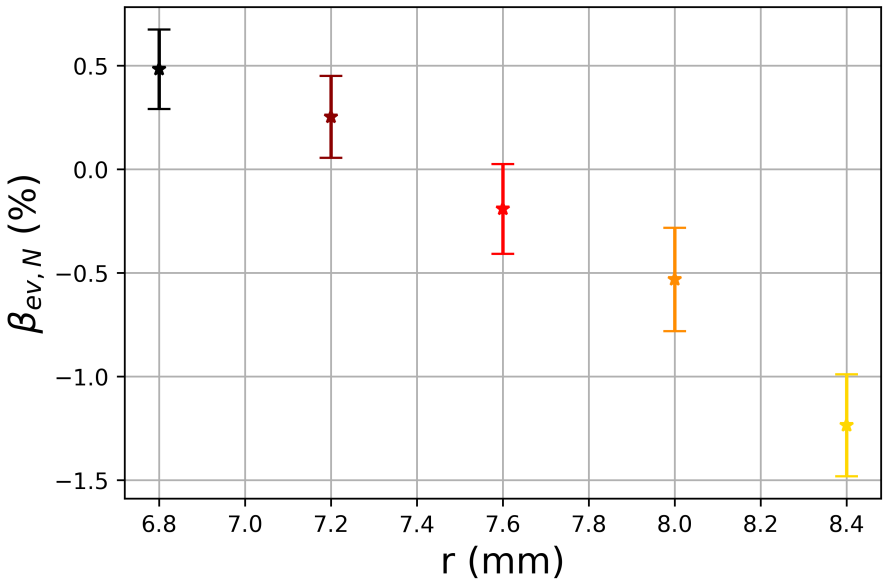

Figure 3.20: Record of the humidity correction $\beta_{ev,N}$ for each boxes as a function of the position.

So, to analyse these values, when positioned close to the centre of the EC, the correction has to be positive as the evaporation is more delayed than in the other boxes. When the box is on the outside of the probed volume, the humidity has to be reduced as the evaporation is happening faster. The comparison is made as a difference from the average, so as the middle volume is the closest to the average of what is happening in the entire box. It is normal to expect and see that this has the lowest correction. However, this difference is not linear, maybe the correction is based on the log as for standard problems in cylinder coordinates, such terms often appears. With the hypothesis that the liquid fraction is the same among the boxes (verified in section 3.7.3), the water vapour partial pressure shall also be equally distributed before evaporation starts. This leads to the following equation:

$$1 + \frac{\beta_{ev,N}}{H} = \frac{P_v^{sat}(T)}{P_v^{sat}(T + dT_{ev,N})} \tag{3.11}$$

To have numerical values, H is fixed at 90% and T at 20 °C, the result of equation 3.11 are plotted for each box in figure 3.21

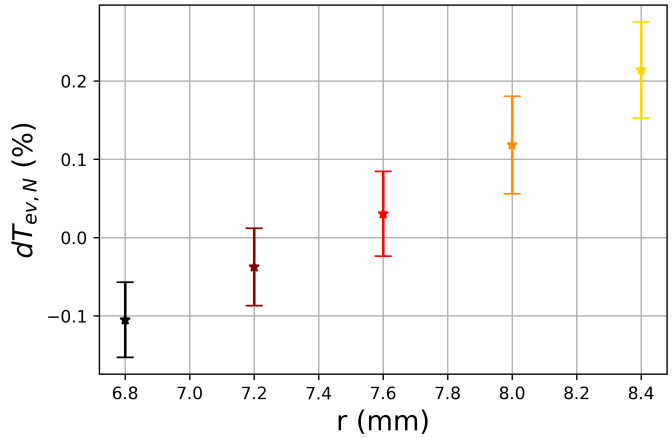

Figure 3.21: Record of the temperature correction $dT_{ev,N}$ for each boxes as a function of the position.

As expected, the closer from the centre, the lower the temperature. As the temperature plays a predominant role in the humidity, a higher temperature leads to early evaporation. This is verified via the temperature correction calculated in figure 3.21.

3.7 Vapour diffusion

The droplet concentration is about $300\,\mathrm{mm}^{-3}$ (see figure 3.16) that is giving an average distance between the droplets of $N^{-1/3} = 0.15\,\mathrm{mm}$ this distance is much greater than the diameter of the droplet (around $4\,\mu\mathrm{m}$). So the hypothesis that the droplets evaporates independently shall hold.

3.7.1 Evaporation of a single drop in our experimental conditions

According to Erbil [36], with a simple model, two equations shall govern the evaporation of the droplet, one transport equation and one heat transfer equation:

$$-\frac{dm}{dt} = 4\pi R D_{va} \frac{M P_v^{sat}(T)}{\mathcal{R}T}(1 - H(\%)) \tag{3.12}$$

$$-L\frac{dm}{dt} = 4\pi R \lambda_{cond} dT_{drop,th} \tag{3.13}$$

With those two equations it is easy to compute the evolution of the radius as a function of time along with the temperature of the droplet. The idea

is to simulate the life of a droplet in our conditions to see its evolution. For this simulation, the humidity is fixed at 90%.

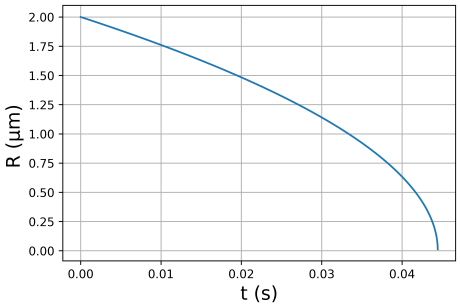

(a) Evolution of the radius corresponding to droplets seen on screen during the optical tomography.

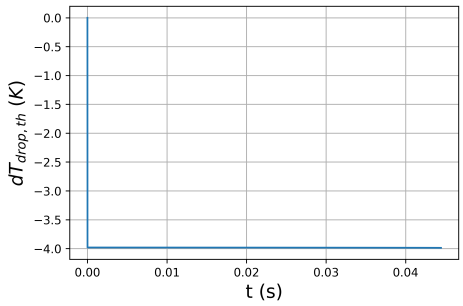

(b) Evolution of the droplet temperature compared to its initial value, the air temperature.

Figure 3.22: Evolution of the radius and temperature of a droplet that follows equation 3.12 and 3.13.

The issue is that the droplet is only living 0.044 s in those conditions. It does not correspond to the observed lifetime of the droplets. This lifetime could be linked to local parameters with the constant k_{th} from section 3.5.1, so that $t_{evap} = k_{th}/(1 - H(\%))$ with:

$$k_{th} = \frac{\rho_{water} R_0^2 \mathcal{R} T_{air}}{2 D_{va} M P_v^{sat}(T_{air})} = 0.00444\,\text{s} \tag{3.14}$$

3.7.2 Impact of the environment

There is some inconsistency in our model, the droplets are living for far too long, it has to be bridged. The idea is to focus on a single droplet in its own volume. The volume where this single droplet evaporates is $N^{-1}\,\text{mm}^3$. The idea is to see if the evaporation in its own volume is enough to reach the saturation of the volume. If it's true then the excess of water will have to migrate and eventually condensate on other droplets evaporating due to the fact that because of the evaporative cooling, they become cold point inside the volume. The comparison between the partial pressure and the saturation pressure is computed in equation 3.15:

$$\frac{P_v}{P_v^{sat}(T_{air})} = \frac{4\pi \rho_{water} R_0^3 \mathcal{R} T_{air}}{3 M P_v^{sat}(T_{air}) N^{-1}} = 0.58 \tag{3.15}$$

So, if there is at least 42% humidity in the single droplet volume before the evaporation, evaporating a droplet of $2\,\mu$m in radius will oversaturate this

volume. This will create a concentration gradient and by the Fick's law, the concentration in water vapour has to move towards adjacent volumes where droplets have not yet evaporated. This action will increase the local humidity and diminish the evaporation rate in the volume nearby. The diffusion coefficient of water vapour in air D_{va} is giving us indication about the distance travelled by this water vapour in a certain time.

$$D_{va} = \frac{d_{th}^2}{t_{th}} \tag{3.16}$$

The characteristic time t_{th} is fixed as the time necessary to evaporate a single droplet normally in its volume so 0.044 s. This rule of thumb gives a travelled distance of $d_{th} = 1.07\,\text{mm}$ this is around ten times the distance between two droplets in our experimental conditions.

3.7.3 Equation adaptation

The figure 3.23a is the evolution of the average droplet mass throughout time for each box. After the convection regime is finished (around 5 seconds) it looks like all the boxes have the same average droplet mass and the figure 3.23b suggests that each box has the same number of droplet. The liquid water quantity is calculated as the average droplet volume multiplied by the fitted values of the number of droplet per box.

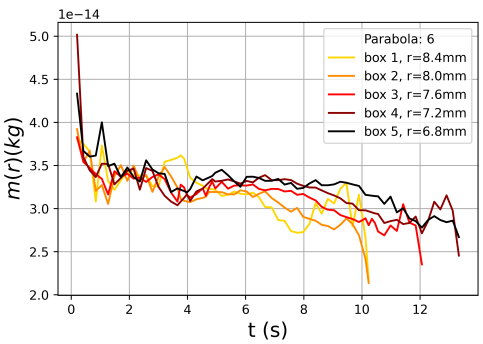

(a) Evolution of the mass of the average droplet.

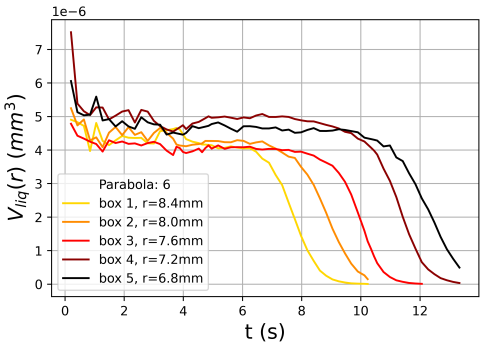

(b) Evolution of the total liquid water quantity.

Figure 3.23: Evolution of the average droplet mass and the total liquid water quantity in each boxes.

Equation 3.12 and equation 3.13 are giving the way the droplet shall behave. However the experimental results do not match. The average droplet in each of the boxes is living for far too long. The droplets that evolve in our

experimental set-up shall live a fraction of a second as suggested by section 3.7.1. So, the idea is to correct the transport equation and to add an other term that will count the mass flow allowing the average droplet to persist in time. This incoming mass flow is noted s. The evaporation rate for a single droplet, calculated as $4\pi R D_{va} \frac{M P_v^{sat}(T)}{\mathcal{R}T}(1 - H(\%))$ is named as f. With these terms, equation 3.12 becomes:

$$\frac{\partial m(r,t)}{\partial t} = -f(r,t) + s(r,t) \tag{3.17}$$

As we are looking at experimental data, equation 3.13 becomes:

$$-L\frac{\partial m}{\partial t} = 4\pi R \lambda_{cond} dT_{drop} \tag{3.18}$$

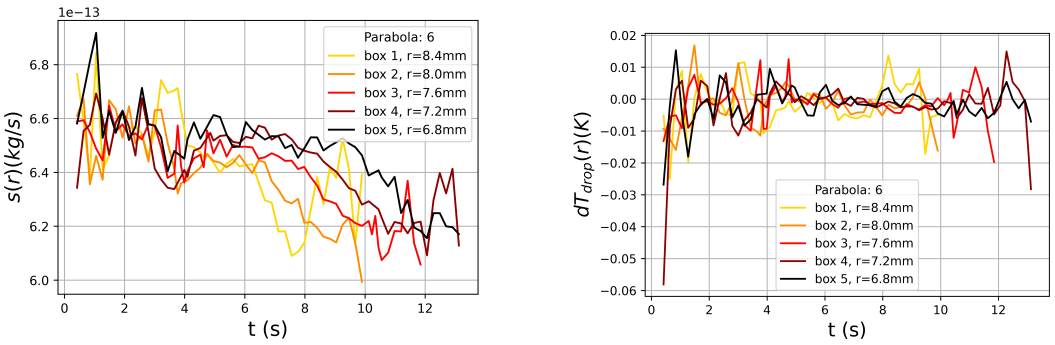

(a) Compensative mass flow evolution, calculated using equation 3.17.

(b) Experimental temperature drop, calculated using equation 3.18.

Figure 3.24: Evolution of the compensative mass flow and the experimental droplet temperature drop in each boxes.

The temperature evolution is not stable and the temperature difference from the surrounding air is much lower than in theory (presented in figure 3.22b). That was expected because the average droplet mass does not drop as fast as in theory. The compensative mass flow rate (s) is decreasing a little throughout time (see figure 3.24a). This mass flow has to be multiplied by a time so that it is comparable to the mass of the droplet itself. The time chosen is the theoretical lifetime of the droplet $t_{th} = k_{th}/(1 - H(\%))$. For this illustrative parabola, the humidity is 94.2%, that gives a theoretical lifetime of 0.0766 s. The figure 3.25a gives an idea of the mass that the average droplet receives over the time necessary for this droplet to evaporate in theory. The figure 3.25b shows that the droplet receives between 6.5 to 7.5 times its own mass to compensate the volume loss in equation 3.17.

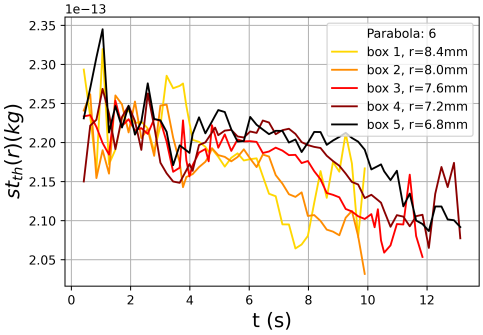

(a) Compensative mass flux multiplied by the theoretical lifetime of the average droplet.

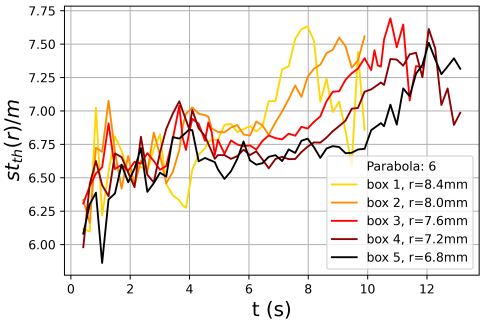

(b) Ratio of the incoming mass flux times the theoretical lifetime over the mass of the droplet.

Figure 3.25: Evolution and comparison of the compensative mass flux to the mass of the average droplet.

3.7.4 Equation closure

From then on, the idea is to link the compensation mass flux s to actual phenomenon occurring inside the volume especially f the evaporation of the droplets in the adjacent boxes. To do so, it is necessary to think about the total number of droplet per box instead of thinking on only one droplet. As a result, equation 3.17 becomes:

$$\frac{\partial N(r,t)m(r,t)}{\partial t} = -N(r,t)f(r,t) + N(r,t)s(r,t) \tag{3.19}$$

The figure 3.26 illustrate equation 3.19.

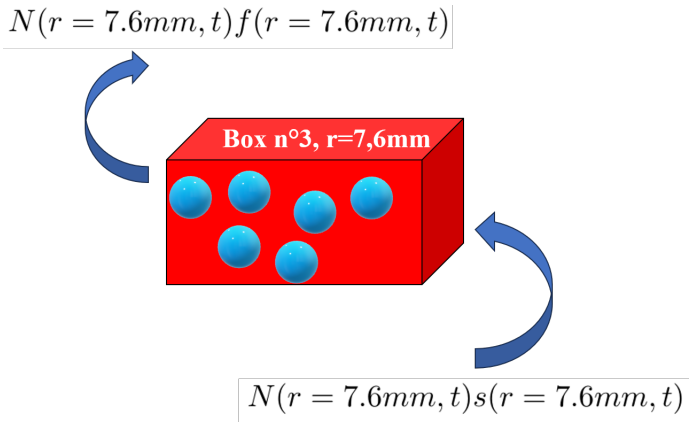

Figure 3.26: Mass balance for the box number 3, this figure is the illustration of equation 3.19.

The term s is a source term, it has to come from somewhere as there is no creation of mass in the volume, the main idea is that this term is the evaporative flux coming out of the box in $r+dr$. The comparison that comes to mind then is to compare the term $N(r,t)s(r,t)$ to what is evaporating from the box in $r+dr$, this is then the term $N(r+dr,t)f(r+dr,t)$. The figure 3.27 represent the compilation of the boxes (based on figure 3.26) and the reason to do the comparison. On the right, the arrows are pointing the term $N(r,t)s(r,t)$ that is coming inside the box in position r to compensate the evaporative flux of a single droplet that is too high (see section 3.7.3). On the left, the arrows are pointing the terms $N(r,t)f(r,t)$ this term is what comes out of each boxes.

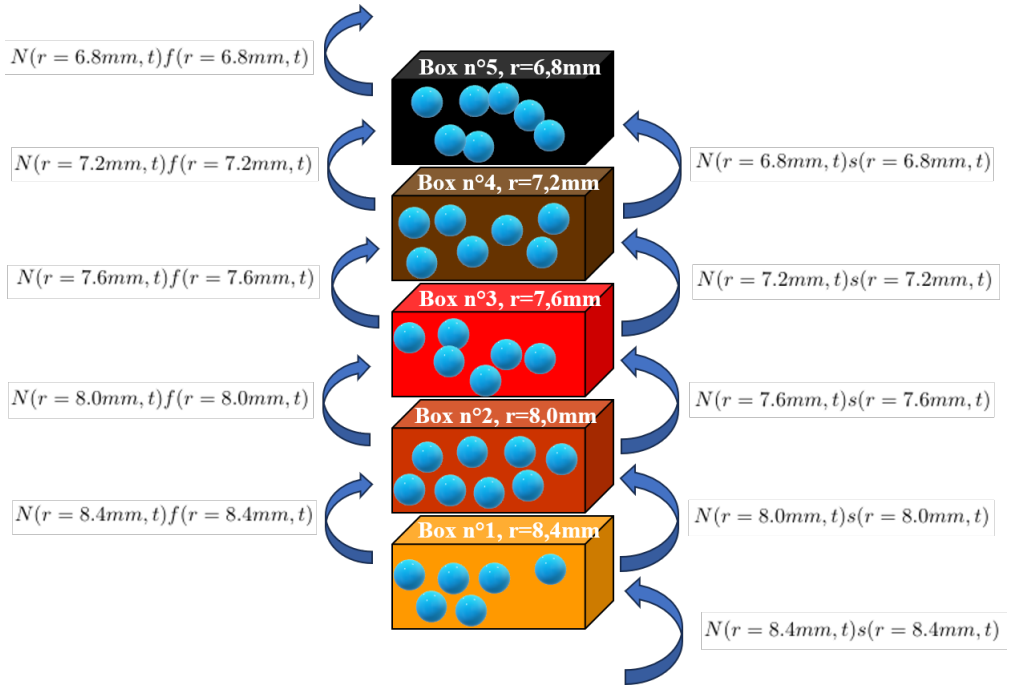

Figure 3.27: Mass balance for each boxes. On the left, the evaporative flux coming out of the boxes. On the right, the mass flux coming in the boxes. The comparison drawn is where the mass fluxes are on the same horizontal line (for example: $N(r=8.4\,\mathrm{mm},t)f(r=8.4\,\mathrm{mm},t)$ has to be compared to $N(r=8.0\,\mathrm{mm},t)s(r=8.0\,\mathrm{mm},t)$).

This idea is justified because the evaporation of the droplet is happening first in the outer layers of the EC. This evaporation will induce a gradient of water vapour concentration. This mass flux is then going towards the centre of the EC by the Fick's law. To do the comparison, the thermal flux ratio (φ_{TFR}), defined as $\varphi_{TFR} = \frac{N(r+dr,t)f(r+dr,t)}{N(r,t)s(r,t)}$ is plotted in figure 3.28.

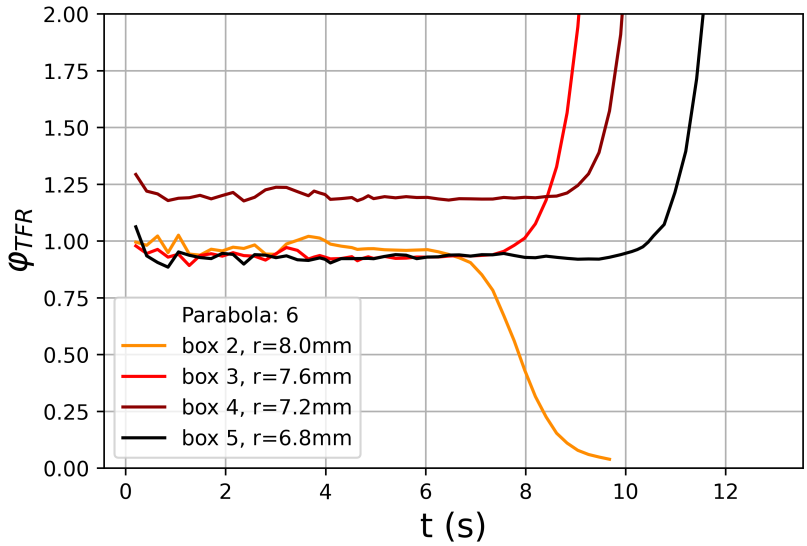

Figure 3.28: Evolution of the thermal flux ratio (φ_{TFR}) as a function of time.

The terms are globally equal, the divergence happens when the number of droplet is critically low in the outer volume $(r + dr)$. The terms are not perfectly equal because this ratio highly depends on the fitting quality of the prefactor A when calculating $N(r, t)$. Maybe an hyperbolic tangent is not the best function even if it captures well the decay for the droplet number. If we assume that $\varphi_{TFR}(r, t) = 1$, then equation 3.19 becomes:

$$\frac{\partial N(r,t)m(r,t)}{\partial t} = dr\frac{\partial N(r,t)f(r,t)}{\partial r} \tag{3.20}$$

This equation is similar to a spray equation 1.43 from Haselman and Westbrook [83].

3.8 Radius evolution

The radius also could be followed, like the droplet density, throughout time. However, the droplets are small (around 4 to 5 μm in diameter) which is only a few pixels. When following the evolution of the squared diameter to detect any d2-law. It appeared that different phases in the squared diameter evolution could be seen in figure 3.29. After the initial flows are damped out (around 4 to 5 seconds), the droplets have approximately the same size as this mixing process distribute the droplet evenly inside the probed volume and the nucleation process used to create the aerosol tends to create mono-disperse radius distribution (see figure 2.26). Like the droplet density, the diameter of the droplets closer to the wall start to diminish first. This change can be seen in the figure 3.29 as a break in the linear trend of the squared diameter evolution. This break in the trend could be seen in the box 1 around 6 seconds, 8 seconds for box 3 and 10 seconds for box 5.

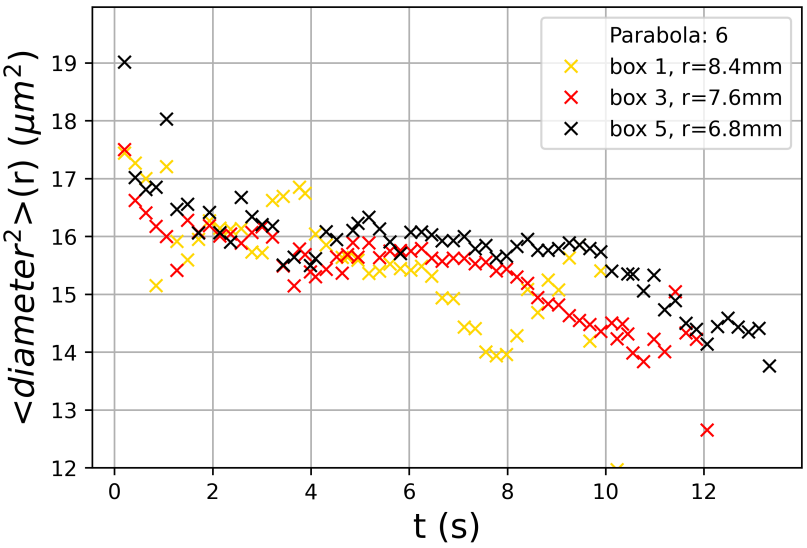

Figure 3.29: Evolution of the averaged squared diameter as a function of time for three boxes.

It is important to note that the latest evaluations of the radius are done on a small amount of droplets (see figure 3.15). The evaluation of the radius is based on an average of every droplet inside the box. Once the evaporation is well established, the number of droplets is not statistically significant to evaluate a representative averaged radius, these data are therefore remove from the fitting data. This corresponds to not taking the radius averaged data past $t_{ev,N}$. The data taken during the initial flows are also removed. The figure 3.30 is the figure 3.29 with the addition of the fitting trends.

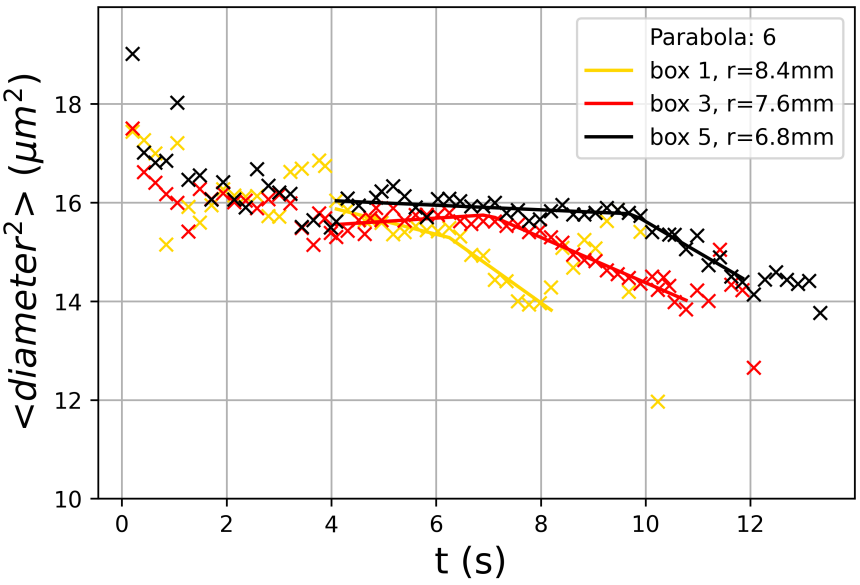

Figure 3.30: Evolution of the squared averaged diameter throughout time for three boxes. The linear piecewise interpolations are plotted in full line over the relevant data.

The function used to interpolate the averaged squared diameter is the following:

$$f_{ev}(t, t_{ev,R}, \alpha_1, \alpha_2, d^2_{ev,R}) = \begin{cases} \alpha_1(t - t_{ev,R}) + d^2_{ev,R} & \text{if } t < t_{ev,R} \\ \alpha_2(t - t_{ev,R}) + d^2_{ev,R} & \text{if } t \geq t_{ev,R} \end{cases} \tag{3.21}$$

The function f_{ev} is a piecewise linear function as the d2-law shall remain valid here. The idea is to gather information with the fitting done via the function f_{ev}. The main information that will be discussed about is the time when the break in the trends happens. This time, noted $t_{ev,R}$, is plotted for each boxes in figure 3.31.

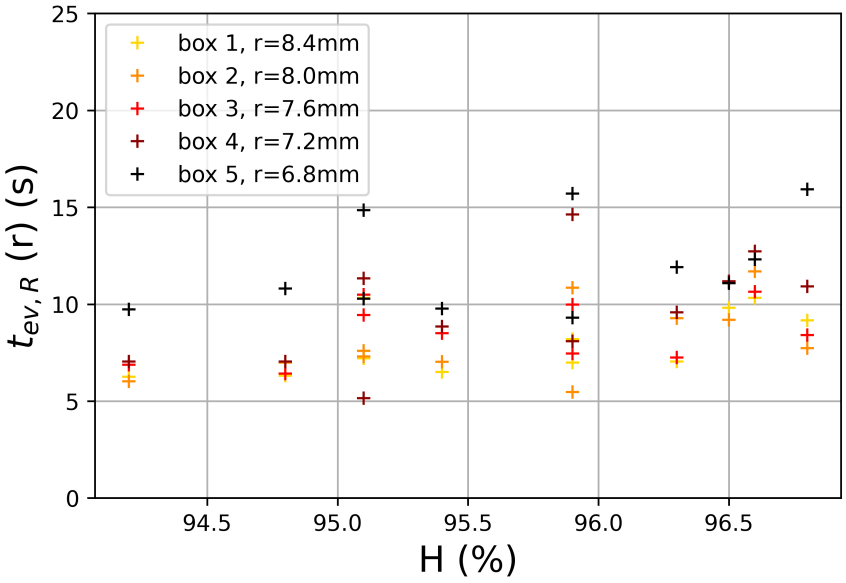

Figure 3.31: Evolution of $t_{ev,R}$ as a function of the relative humidity for each boxes.

It is important to note that in figure 3.31, for humidities lower than 94%, the evaporation of the aerosol is occurring too fast to see a proper break in the trend as the relevant data to see this phenomenon are only on a few points. For humidities higher than 97%, the disappearing of the droplets occurs much more due to the end of the parabola than due to evaporation, seeing breaks in trends at such long lifetimes would be debatable. This time ($t_{ev,R}$) can be seen as the initiation of the evaporation process as the number of droplet has not started to decrease yet (see figure 3.15). This time has to be compared to the evaporation time based on the fitting of the number of droplets $t_{ev,N}$ in the corresponding box. The figure 3.32 is the comparison between the two evaporation times.

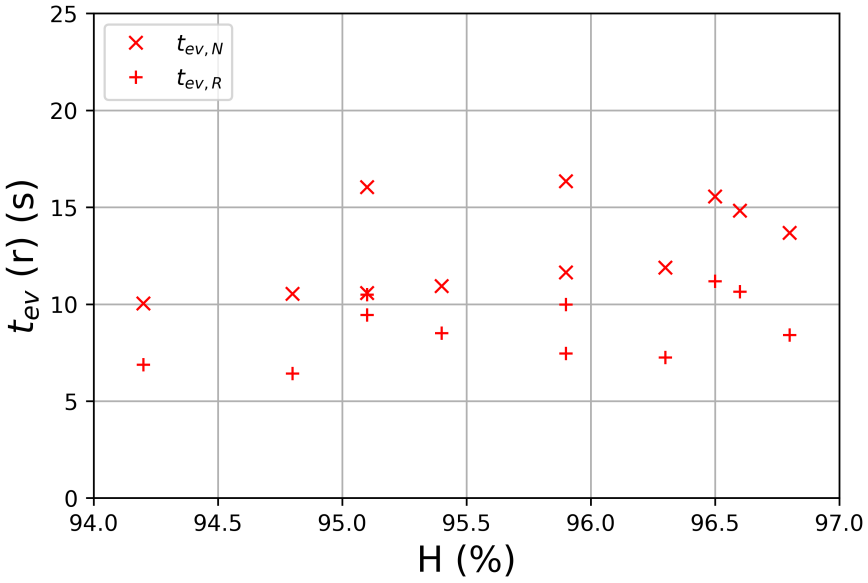

Figure 3.32: Comparison of the evaporation characteristic times based either on the number of droplets $t_{ev,N}$ or based on the squared diameter $t_{ev,R}$ for the box number 3.

Both evaporation times are following the same trend as the time difference between the two is approximately constant. Both times are increasing as the evaporation is delayed the higher the humidity is. The figure 3.33 summarize the results for every boxes inside the probed volume. The same trend could be seen occurring for each boxes similarly to what is happening in box number 3.

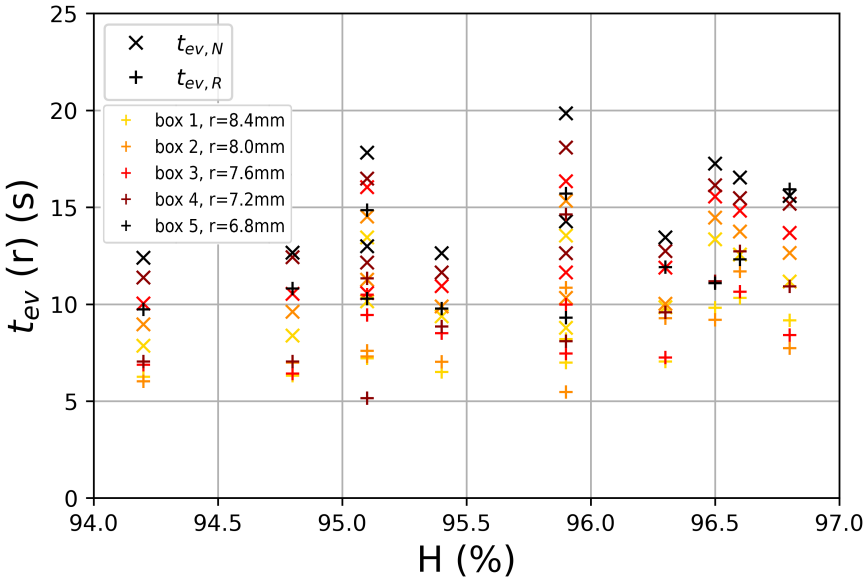

Figure 3.33: Comparison of the evaporation characteristic times based either on the number of droplets $t_{ev,N}$ or based on the squared diameter $t_{ev,R}$ for every boxes in the probed volume.

Looking at the number of droplets or the average squared diameter gives a similar trend when looking at the evaporation time. Counting the droplets require less numerical effort and might be a little bit easier to implement. However, the evaporation time based on the squared diameter $t_{ev,R}$ gives an information about when the evaporation process is most likely starting. The results on the trend evolution are in appendix G.

3.9 Infrared spectroscopy of water aerosols with HFE-7100 vapour

For the 67th parabolic flight campaign of CNES in October 2024, a fluid had to be chosen to investigate the binary gas mixture of water and secondary vapour. After some preliminary tests done by the intern C. GOUEROU, the HFE-7100 was chosen. The Perfluorobutyl Ether (HFE-7100), is a hydrofluoroether (HFE) belonging to the family of fluorinated fluids. Here are some key points about HFE-7100:

- HFE-7100 is a chemical compound made up of carbon, fluor, oxygen, and hydrogen atoms, which gives it specific properties. It is a clear,

colourless liquid with a relatively low boiling point (61°C). It is non-flammable, which makes it safe to handle in many industrial applications. It has low toxicity and is considered an environmentally friendly fluid.

- HFE-7100 is widely used as a cleaning agent in the electronics industry, particularly for the precision cleaning of sensitive electronic components such as circuit boards, chips, and connectors. It is effective at removing organic contaminants, and fine particles without leaving residues.
- HFE-7100 is compatible with a wide range of materials used in the electronics industry, including plastics, metals, coatings, and sensitive electronic components. It is non-corrosive and does not damage delicate materials. It offers excellent cleaning performance due to its ability to effectively dissolve organic contaminants. It evaporates quickly (saturation pressure at 20 °C: 21705 Pa) without leaving residues, which reduces drying time and improves productivity in electronic manufacturing processes.
- HFE-7100 is considered a safe fluid to handle under normal usage conditions, but appropriate precautions should be taken to avoid prolonged inhalation or skin contact. It is important to comply with local regulations and best practices regarding health and safety when using this product.

No clear effect was seen on the evaporation of the aerosol with the FTIRS set-up with or without the presence of HFE-7100. As a result, the spectroscope could be used as a non invasive measurement technique. The FTIRS was used to diagnose the nucleation and the evolution of the binary mixture water/HFE-7100 during the 67th parabolic flight campaign of CNES in October 2024. The idea of this campaign was to study the evolution of different specific spectral absorption bands to determine the behaviour of the chemical components of the aerosol during the different phases of the parabolas. The figure 3.34 is a display of the typical different spectral absorption bands for the HFE-7100 [166].

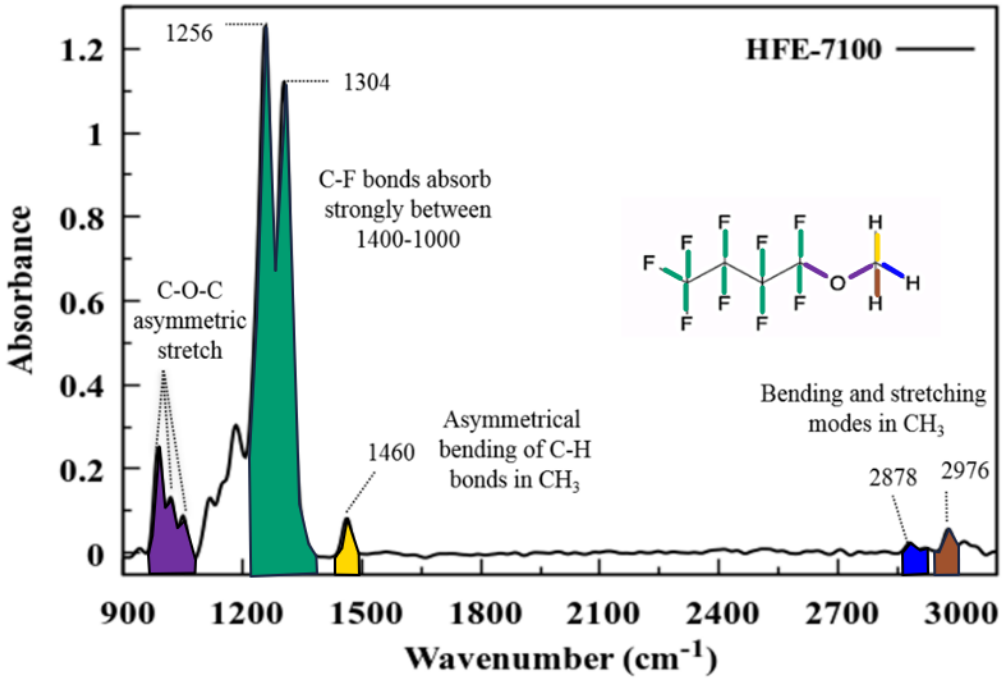

Figure 3.34: Absorption spectrum of the HFE-7100 with the explanation of the different chemical bond seen in the spectrum.

In the EC, several chemical species are present, in the following subsections, the behaviour of the baseline will be analysed. Then, the evolution of the CO_2 throughout time will be discussed. Lastly, the behaviour of the different specific spectral bands of the HFE-7100 will be analysed.

3.9.1 Evolution of the spectrum in the absence of HFE-7100

First, tests are conducted to see the behaviour of the FTIRS without the presence of HFE-7100. Are present in the system, water in saturation quantity and air (including CO_2). The full range absorption spectrum of parabola 8 is plotted for different times in figure 3.35. In this figure, the baseline is evolving during the different phases of the parabola. Ten seconds before the expansion, the baseline show no drastic distortion. In this moment, the plane is in hypergravity ($1.8\,g$) this line gives the behaviour of the FTIRS under this stress. Five seconds before the expansion, the compression is fully done, and the gas is in the thermodynamic conditions to be expanded (initial temperature and 2.2 bars in pressure). This operation brought matter as the pressure inside the EC is now 2.2 bars, this will affect the baseline as it can be seen on the green line in figure 3.35.

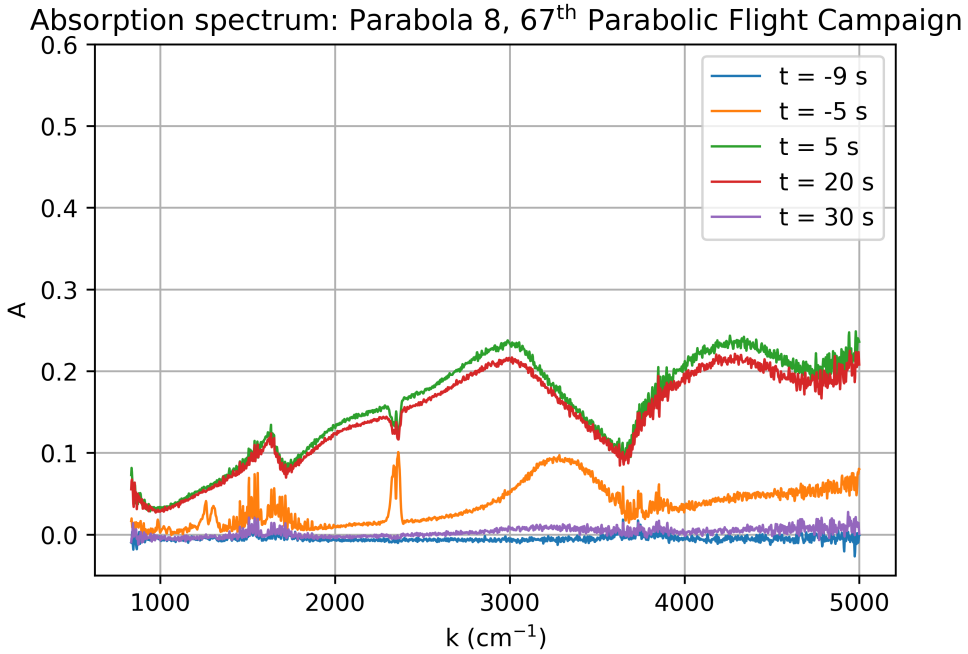

Figure 3.35: Full range absorption spectrum at five different times. t_0 is the time when expansion happens.

Then, the expansion happens and droplets are created via nucleation. These droplets will affect the IR signal and absorb/diffract the IR beam. As a result less power is coming back to the receptor. Then, the absorbance is rising compared to before the expansion. As there is little to no droplets evaporation during the parabola (the humidity is at 100% so water droplets will not evaporate), the absorption stays high, this could be seen in the orange line, fifteen seconds after the expansion (see figure 3.35). Twenty seven seconds after the expansion, the aircraft is in the hypergravity phase, the droplets do sediment due to the restored gravity. This disappearing of the droplets decreases the value of the baseline to its initial value before compression. Three phases could be seen on the evolution of the peak offset for the different characteristic absorption bands and are presented in figure 3.36.

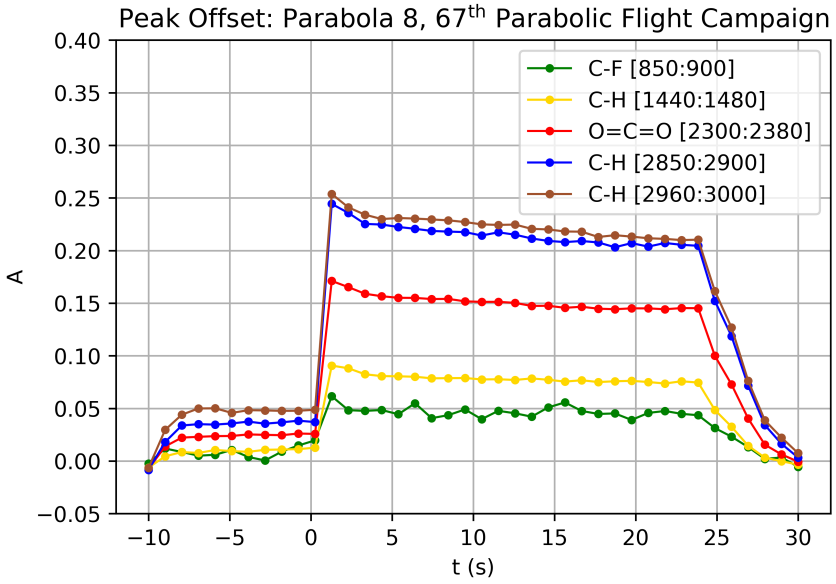

Figure 3.36: Peak offset corresponding to the increase of the baseline value as a function of time for five different absorption bands.

In a first time, the compression occurs. This leads to a raise in the offsets as there is more matter in EC. Then, the brutal expansion occurs leading to a higher offset due to the presence of liquid water droplets that will either diffract or absorb the IR beam. The nucleation and high velocity flows in the first seconds of the microgravity influence the behaviour of the absorption for the first two to three seconds. After this phase, the signal is slightly diminishing most likely due to a decrease of the droplet number or average size along the IR signal trajectory that has yet to be confirmed with the image analysis. After 22 seconds the parabola ends and the offset goes back to normal as the droplets sediment and leave the IR signal trajectory.

3.9.2 Evolution of the CO_2 peak

The CO_2 is characterized by a peak in the range 2300 to 2380 cm^{-1} [167]. The idea is then to take a zoom in this region to understand the behaviour of the CO_2 during the parabola (see figure 3.37).

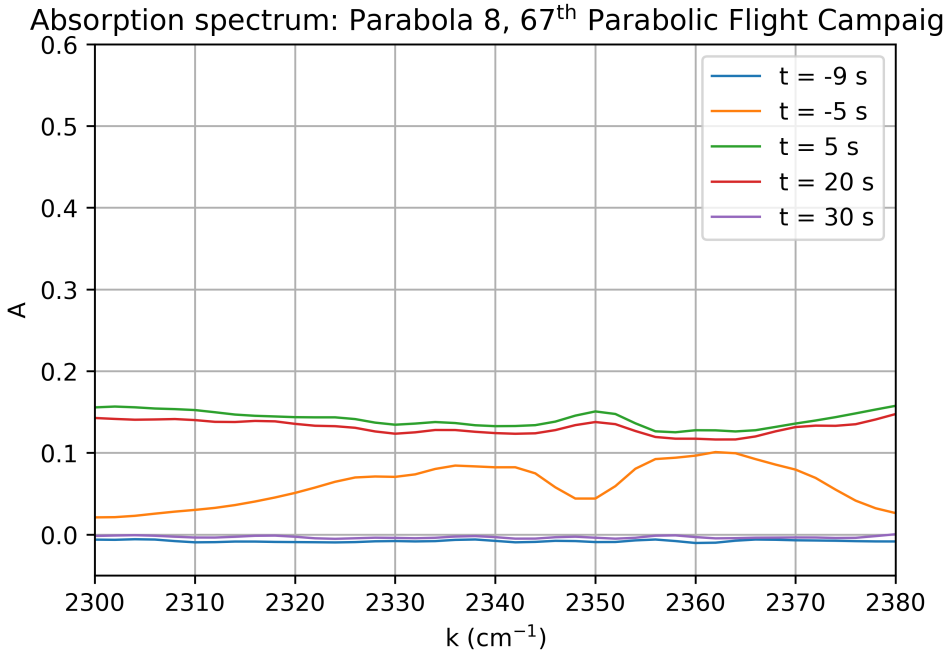

Figure 3.37: Zoom in the region 2300-2380 cm^{-1} of the absorption spectrum. This range is typical of the C=O stretching band.

After the compression is done, more CO_2 is present in the EC, leading to a raise in its absorbance. Then, after the expansion the CO_2 decrease in quantity below the baseline. One probable explanation is that the CO_2 is dissolved inside the liquid water droplets and therefore no longer present in the vapour phase. This phenomenon is leading to a drop below the baseline as the initial blank baseline contained CO_2. The surface peak is then calculated as the absorption integral between two wavenumber and the baseline value is subtracted. This evolution is recorded for each scans in the figure 3.38.

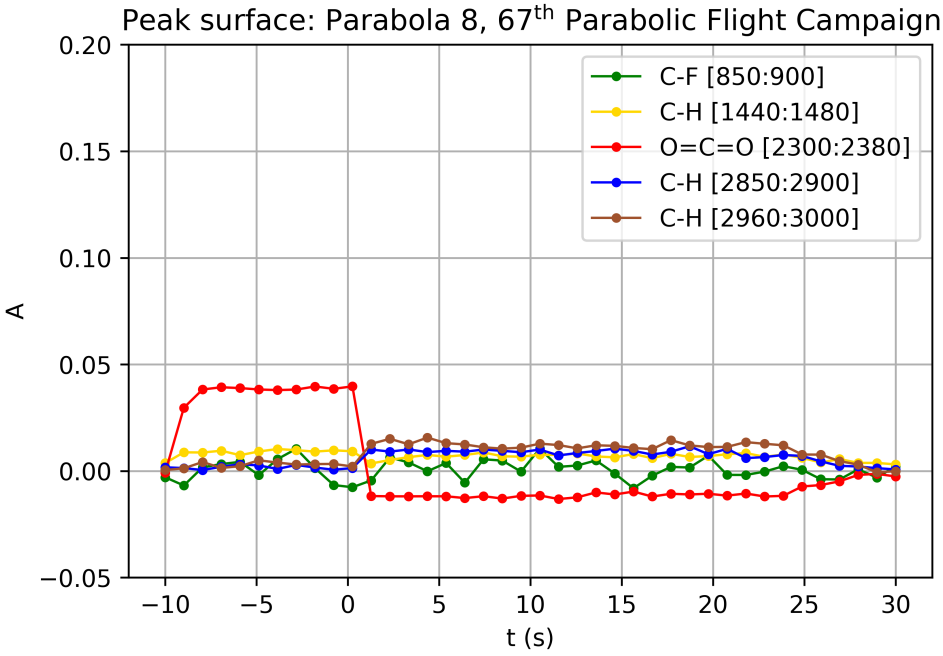

Figure 3.38: Peak surface for the CO_2 and the typical absorption bands of the HFE-7100. The legend indicates the wavenumber range over which each peak is integrated.

In figure 3.38, the evolution of the CO_2 could be seen, in a first time over the baseline and then dissolved inside the water droplets. The characteristic bands of the HFE-7100 are relatively close to 0 because there is no HFE-7100 in the EC for these parabolas.

3.9.3 Evolution of the spectrum in the presence of HFE-7100

The HFE-7100 is then introduced and the same experiments are run. The presence of HFE-7100 could be seen on the full spectral range in figure 3.39.

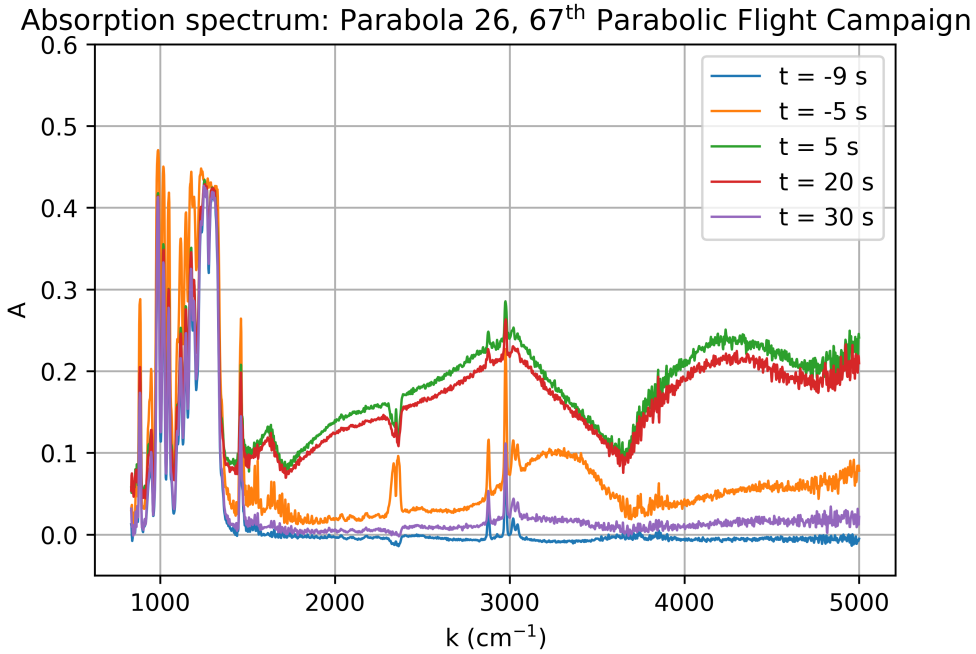

Figure 3.39: Full range absorption spectrum in the presence of HFE-7100.

In the presence of HFE-7100, new peaks are added to the spectrum in comparison to the figure 3.35. Like the CO_2, these peaks have to be characterized, and their peak surface have to be estimated in the corresponding ranges. The peaks determination are based on the figure 3.34 and the article published by Bravo [168]. The figure 3.34 gives the peaks values and their chemical correspondence for the HFE-7100, they are integrated over a known wavenumber range. The result of this integration could be seen in the figure 3.40 as a function of time.

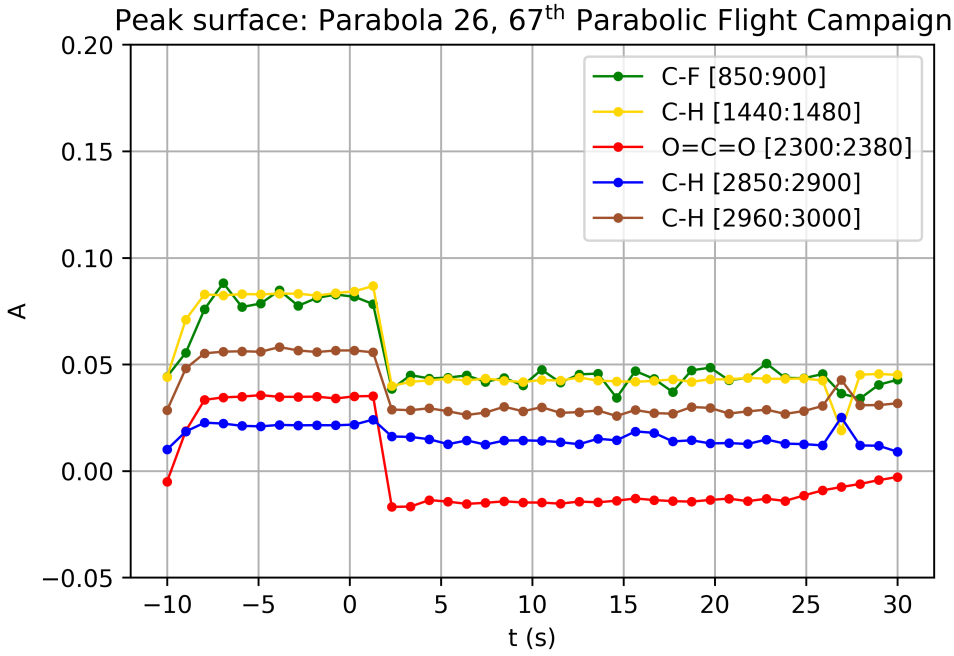

Figure 3.40: Peak surface for the CO_2 and the typical absorption bands of the HFE-7100. The range indicated in the legend corresponds to the range over which the peaks are integrated.

The saturation pressure of the HFE-7100 is given by the data sheet of the manufacturer for Antoine's exponent coefficient:

$$\ln\left(\frac{P_{HFE}^{sat}}{P_0}\right) = 22.415 - \frac{3641.9}{T + 273} \tag{3.22}$$

with P_{HFE}^{sat} in Pa and T in °C. As the HFE-7100 concentration is not high enough to reach saturation when the expansion occur, the surface peak increases and directly goes back to its initial value. Meaning that the HFE-7100 quantity is directly going back to the gas phase, without interacting much with the water droplets. However, when the concentration in HFE-7100 inside the EC is high enough to reach saturation, the HFE-7100 starts to nucleate like water does. It can be seen in the figure 3.41, where the surface peak drops is much more pronounced below its final level than at parabola 26 (see figure 3.40).

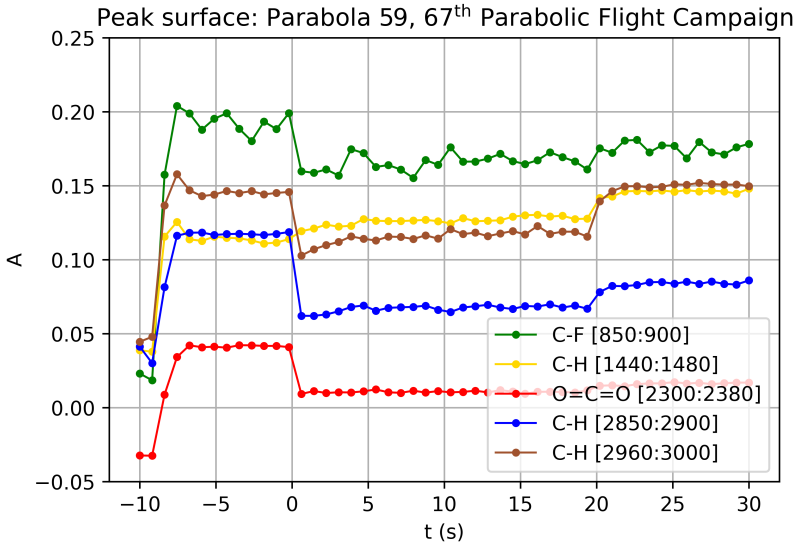

Figure 3.41: Peak surface for the CO_2 and the typical absorption bands of the HFE-7100. The range indicated in the legend correspond to the range over which the peaks are integrated.

The behaviour around 23-24 seconds after the expansion indicates that the droplets are leaving the IR signal trajectory. Therefore, the HFE-7100 had to nucleate either alone (homogeneous nucleation) or on something other than HFE-7100 (heterogeneous nucleation). This second option might be that the water droplet nucleate first on a molecule of HFE-7100 (acting as condensation nucleus) and then the HFE-7100 uses the water droplet as a nucleus on its own. As the droplets seemed to be a little larger and it costs less energy to do, the heterogeneous nucleation is the most reasonable hypothesis (it has to be confirmed with an imaging analysis that has not been conducted yet). When looking at figure 3.41, it looks like the surface of the peak is increasing during the microgravity phase, this may indicate that the HFE-7100 is evaporating from the droplets to go back to a vapour form as the saturation pressure of the HFE-7100 is hard to reach with low amounts of HFE-7100 in the EC (saturation pressure at 20 °C: 21705 Pa). After the end of the parabola, the droplets are falling and the surface peaks are all evolving back to their initial values. A phenomenon that may occur here is the saturation of peaks, especially the ones where the final value is comparable to the value before the expansion. This saturation is impacting the analysis of the IR signals.

Conclusion

In this work, the AEROSOL facility was presented. This experiment is a parabolic flight experimental rack that only hopes to fly in the ISS to have access to long periods of microgravity. These long microgravity periods would allow an exploration of new areas of clouds microphysics such as the nucleation of ice droplets. For the moment, this rack is used to do parabolic flight investigation. It is a great way to prove at a relatively minor cost that the experiment are conclusive and could be conducted in the ISS. A parabolic flight preparation starts with the development of the tools that will be used when flying. In the case of this work, the development of the humidity regulation would be taken as an example. The first idea is to define the physical properties that would be used and then try them with a coarse system, if the results are showing an effect on the targeted quantity (here humidity), then the system is developed to be more efficient on the ground, to eventually perform what it was supposed to do during the parabolic flight campaign. The different parabolic flight campaigns provided key results about the evaporation of the aerosol in microgravity by providing reference experiment for the scientists that can only simulate an aerosol or have access to single droplet levitation techniques. These campaigns also helped as a qualification process for the on-boarded instrument such as the FTIRS. After the campaign is finished, it is time to analyse the results. In this regard, a Python code was developed to do the imaging analysis using the library trackpy. This new technique comes also as a comparison and a verification to the code that was already done in Fortran. After that, different thermal models were done to investigate the evolution of the temperature inside the EC throughout time. There, conduction and convection were used to understand at best the behaviour of the temperature of the EC. This thermal study was done to understand the behaviour of the aerosol during its evaporation. Different fitting techniques were used to extract the physical parameters behind this behaviour. The possibility to investigate the evaporation of the aerosol was a great achievement that shyly started with putting a cold point in the EC and wait a few hours to see a decrease in humidity. After the evaporation

investigation, the second vapour was added, to do the investigation with the HFE-7100. This was a proper moment to have an introduction to IR spectroscopy techniques, the different absorption bands and what they actually represent. The possibility to investigate the nucleation of the binary mixture is a starting point to open the doors of the investigation of chemical reaction for aerosols in microgravity. The parabolic flight campaign are stressful to prepare but it is an amazing feeling to be able to evolve in a microgravity environment, I wish every experimenter could try it one day. As a next step for the experiment, I would humbly recommend to do the analysis of the droplet radius for the experiments of the 67th CNES parabolic flight campaign, maybe they will provide key information about the evaporation of binary mixtures. I would also recommend to achieve a thermal regulation of the rack to remove the cabin temperature dependency and to improve the temperature stability across a day of parabolic flight. The design, requirements and experimental design for the ISS insert are still on discussion, but are progressing at every meeting. The project has shown some issues with the new objectives of NASA based more on space exploration than material science but I have good hopes for the future of this project.

Appendix A

NI MAX

The appendices are a summary of the different things that did not belong to the main body of the manuscript but are useful to know about the experiment. The first thing discussed are the different software. The main program used for the incoming sections are displayed in figure A.1. These software are the ones to pilot most of the experimental set-up.

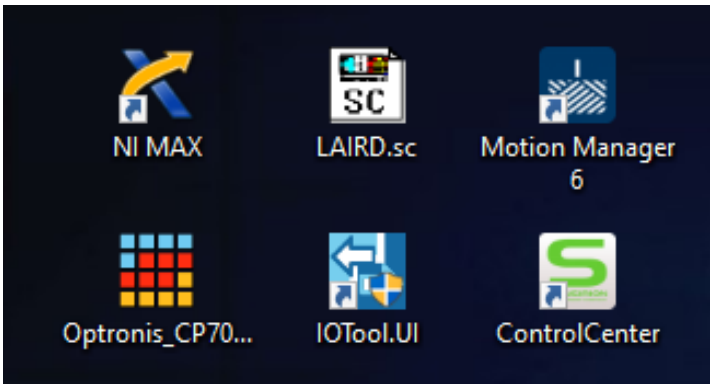

Figure A.1: Visialization of the different useful softwares on the desktop.

The software NI MAX is very useful to test the pumps and EV. To start the software double click on it, go to "Visoinage de données", then "Taches" and there you will find the two main programs, the first one is to control the EV, the second one is to follow the evolution of the pressure. For the program to run, click on "Executer".

You can turn on one component by clicking on the corresponding white circle. A second click on an activated component will turn it off. The list bellow will give an idea on how to do simple tasks:

- Compression: EV3, Pompe 1: ON, at the end of the compression, turn off both.

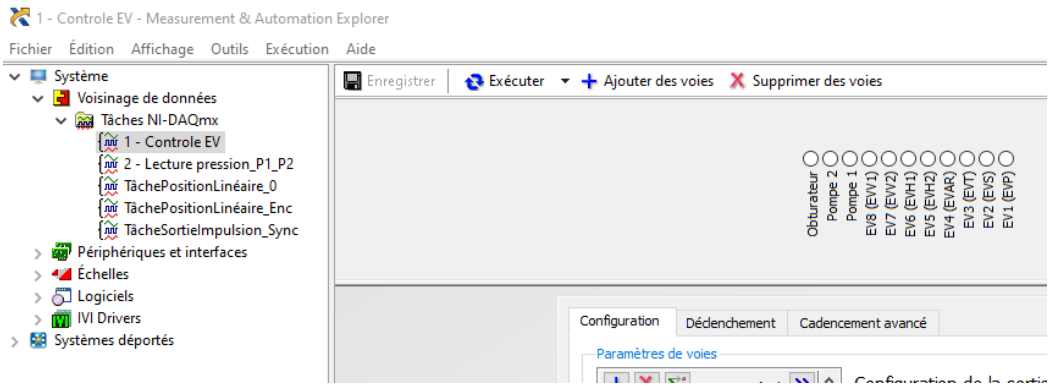

Figure A.2: Main control of NI MAX software.

- Expansion: EV1: ON, has to be done after the compression phase is completed
- Gas circulation: EV1, EV4, EV5, EV6, Pompe 2: ON
- Connect to exterior: EV2 : ON

It is important to note that the system to maintain the EV open is a magnetic one, therefore current is going through the material and this heats up the material over time, leading to malfunctions after 10 to 15 minutes of continuous use.

A.1 Control the leaks

To be able to control a leak it is key to detect it in the first place. To do so, do a compression as explained previously and then, note the pressure (use the value provided by the second program of NI-MAX). The sensor 1 tells the pressure in the EC and the second sensor in the ECC. If the pressure in the EC decrease or if the pressure in the ECC increases then you have a leak. To control a leak, you have two choices: either the leak is large and you can hear it when you create the compression or you can't. If you can't hear the leak, plug a gas bottle on EV2, open EV1 and EV2. Then, let the pressure rise (the sensors saturate around 3 bars so no need to go further). From then on use foam made of water and soap and apply it to where you think the leak could be to detect it. The air getting out of the system will make bubbles when you put foam on it, allowing you to detect the leak.

Appendix B

IOTool

This section is there to teach the basics of IOTool and handle this software. The first thing is to start the program. To do that first start the camera with the software OptronisCP70 first and then IOTool.UI.

B.1 How to load and start a sequence

To load a sequence, go to File and Open. The different routines usually have numbers and description. The best thing to do is to start with the sequence 0 named home tomography. Double click on the name to load. Ensure that every Electronical Boxes 1 and 2, the alimentation supply RS-3005P and the Laird TC-XX-PR-59 are switched on. Ensure also that the connexion is done nicely. To start a sequence, click on the "Run" button (see figure B.1).

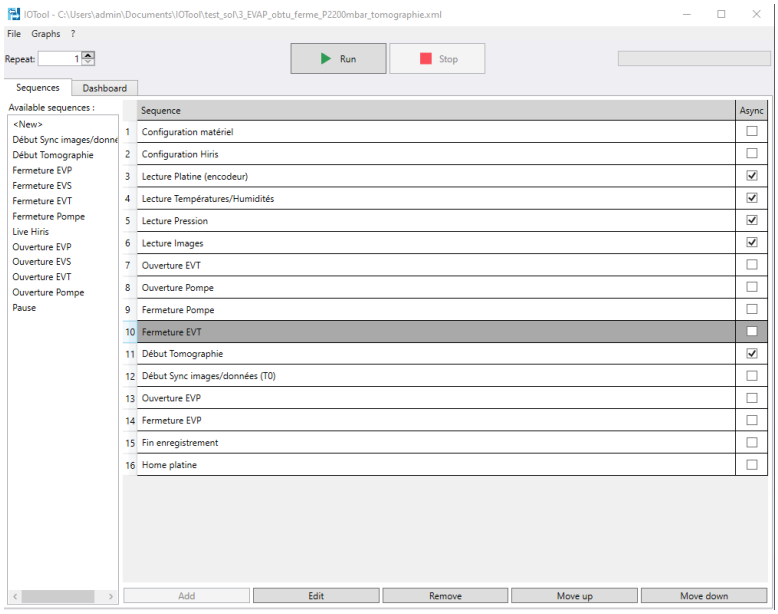

Figure B.1: IOTool interface after loading a sequence.

B.2 How to modify a sequence

To modify a sequence, the procedure is to click "Edit" when a sequence is loaded.

B.2.1 Modify targeted pressure

The figure B.2 is there to explain how to modify the targeted pressure during the compression phase. To modify the targeted pressure, edit the section named "Lecture Pression", click on the line that says "Compare Decimal", the value is in mbar. At the end of the modification, close the Sequence editor and save the sequence.

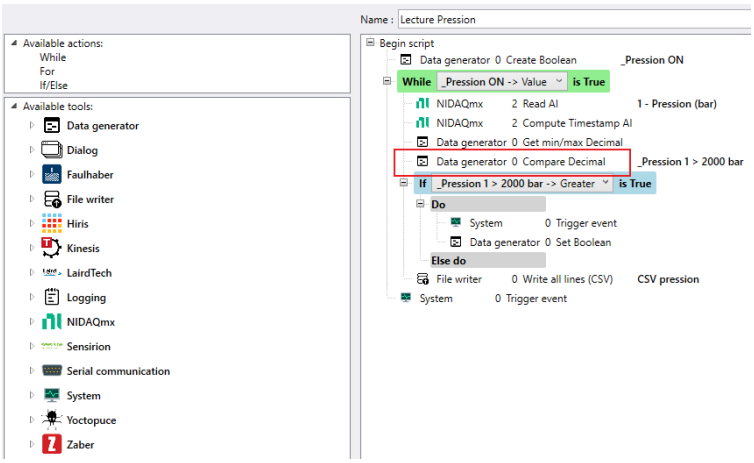

Figure B.2: Sequence editing window in IOTool.

B.2.2 Modify the maintaining pressure time

The idea after the compression is to let the system evolve and stabilize, this takes some time that has to be taken into account because usually, you want the expansion to be made at the beginning of the microgravity phase. To modify this time, edit the instruction named "Fermeture EVT" and modify the sleep delay. This delay is placed as a time to wait before the next instruction begin. The system is relaxed to stable conditions in about 5 to 10 seconds.

B.2.3 Modify the tomography length in time

To modify the time of the tomography, go to "Fin d'enregistrement" (see figure B.1) the first line is the total length of tomography sequence. This has to be in accordance with the parabola length, usually something like 22 seconds or a little more.

B.2.4 Modify the speed and engines start

To modify the engines rotation frequency and start time, first load the sequence, then edit the section named "Declanchement moteurs".

B.3 How to plug the COM port correctly

If the cables have to be unplugged for whatever reason, it is important to know how to do the plugging correctly of the different components. To do

the plugging, open the configuration panel (top right of the desktop). The idea is to find the peripheral manager (see figure B.3).

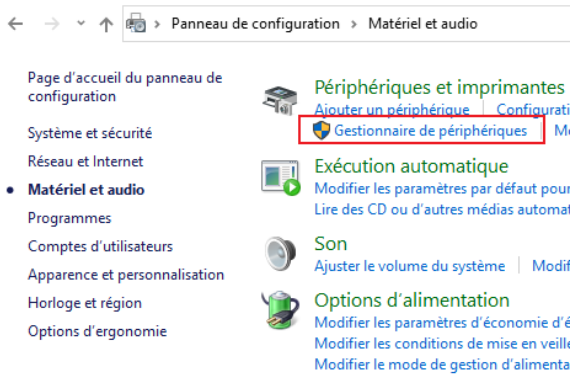

Figure B.3: How to open the device manager.

From this the idea is to go to the "Ports(COM and LPT)" (see figure B.3) menu and from then plug one component, the name of the component will appear on the menu, with the port number in mind, the idea is to go to configuration of the material (first instruction in the sequences) and modify the ports properties accordingly (click on "Edit", then on the tool instance properties name the port).

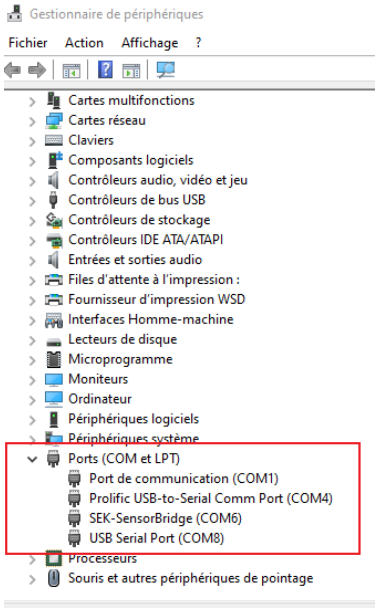

Figure B.4: Device manager.

B.4 How to deal with errors

There are a few types of errors, the first type is when the COM port is not connected properly, either you will have a message saying what is displayed in figure B.5, or the software will crash and close without any message. To ensure that there is no COM port conflict, it is necessary to disconnect the COM port when it is used by a separate software for example LAIRD or sensirion.

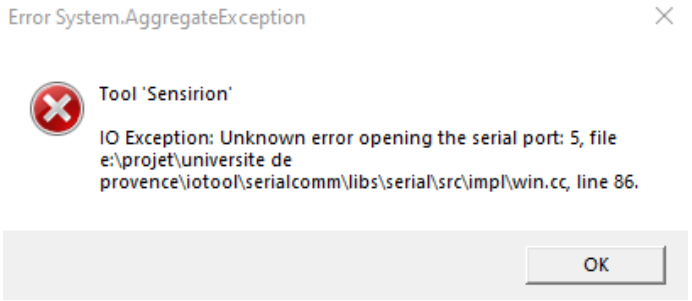

Figure B.5: Sensirion software typical error.

A type of error not seen every day is when the memory from the video disk (F:) is full, then the camera will have issue to save the images on the disk and will not be able to complete the sequence as shown in figure B.6

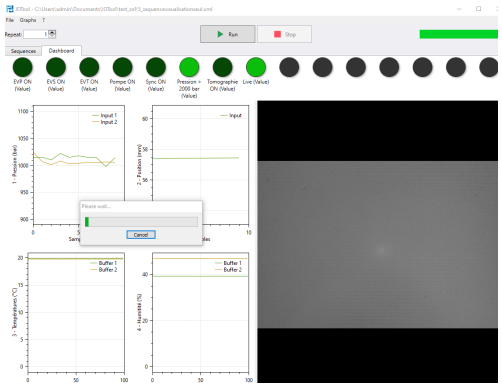

Figure B.6: Sequence error in IOTool due to the lack of disk space.

B.5 How to record with the camera live

It is important to be able to switch from the standard record via the programation to the live record to check different optical parameters. To do so start the camera software optronis, on the GenlCam Tool on the acquisition

control parameters, go from single frame to continuous in the acquisition mode section. Then click on the Setup button, on the acquisition mode go from External to Normal and click OK (see figure B.7). Check that the light is connected and you should have it working.

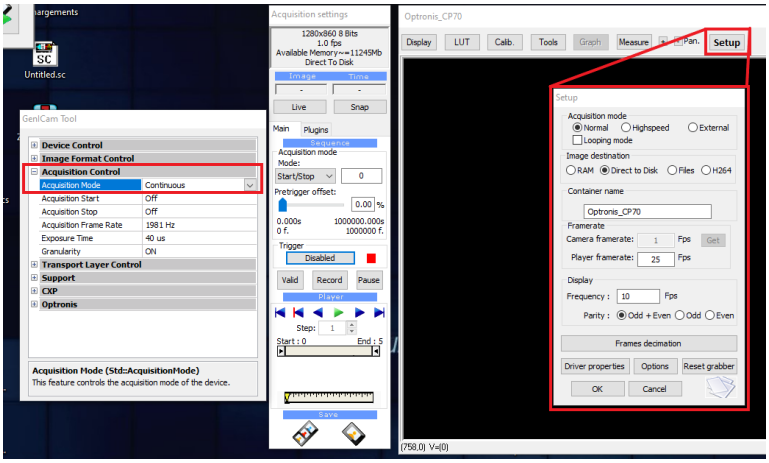

Figure B.7: How to record the live camera.

Appendix C

LAIRD

The LAIRD software is on the windows desktop (see figure A.1). This software is used to control the temperature of the cold point for the humidity regulation. To start the software double click on the icon. The first thing is to ensure that the device is powered and plugged in correctly. To connect the device to the correct COM port, go to "setup" then "global setup" then chose the correct COM port to connect (see figure C.1). Then on the "Regulator" menu click connect (do not forget to disconnect at the end of your use to prevent conflict with IOTool). The value "St1" is the target temperature and "Tr1" is the response from the main sensor. To start the regulation, send the parameters by clicking on "SEND" and then you can start the regulation using "START", the evolution could be followed on a graph via "Runtime".

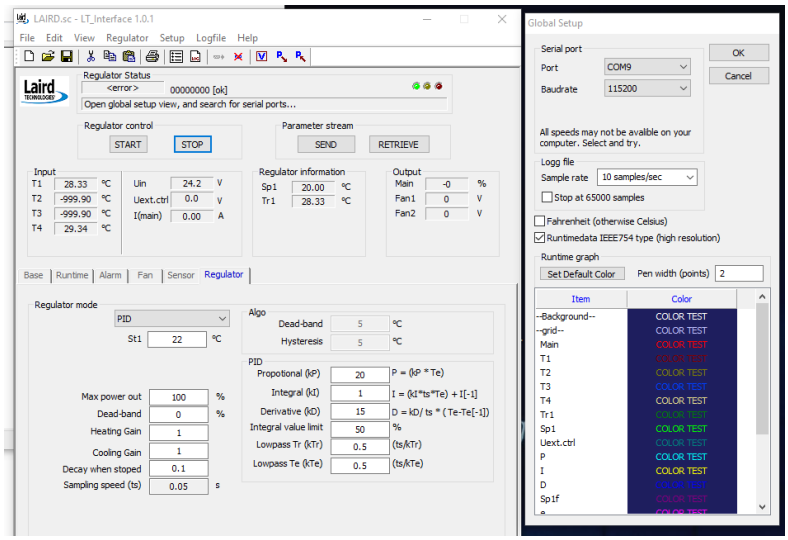

Figure C.1: Main control window of LAIRD software.

Appendix D

How to regulate the humidity inside the EC

The humidity regulation could be done in two ways, the first one is with the software IOTool, the second one is with a combination of software (LAIRD, NI-MAX and Sensirion). Both methods are described below.

D.1 With IOTool

To regulate the humidity inside the EC, load the regulation sequence, and then start it. For the configuration, edit "Regulation humidite". This sequence is done to decrease the humidity, usually from saturation to the target value most of the time 70% humidity. The target humidity could be modified by changing the value in the line "Targeted humidity" (the value is in percent). To reach this target the idea is to apply a cold point and reach the humidity by controlling the cold point temperature. The colder the cold point, the lower the humidity in the circuit. If the target temperature is reached and the targeted humidity is not then the temperature is decreased by an amount that could be modified in "Decrementation de la temperature". The initial target temperature could be selected via "St1 ($^{\circ}C$) var".

D.2 Manually controlling the humidity

So to manually control the humidity, the idea is to have NI-MAX started, this is for the circulation of the gas in the circuit that goes through the cold point. The other software necessary is Sensirion to monitor the humidity. And the last software is LAIRD. Once all these software are started: then

you can control the temperature of the cold point (via the LAIRD software) and follow its impact via Sensirion on the humidity evolution.

Appendix E

Operating the FTIRS

To operate the FTIRS, you have to connect it first, as shown in figure E.1, note it might be turned upside down.



Figure E.1: Connections to the FTIRS.

Then, open the software "ARCspectro Rocket". It is on the windows desktop along with the other software used to control the equipment. You then have to click on the button inside the black box on figure E.2 named "Connect to USB Device". Then wait for the connection to occur.

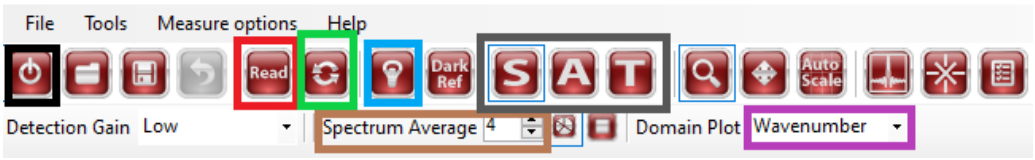

Figure E.2: ARCspectro Rocket software taskbar. The coloured boxes are there to guide and will be referred to in the different paragraphs.

If you want to, you can modify the X-axis units from the "Wavelength" to the "Wavenumber". To do so, modify it in the drop-down list (purple box in figure E.2). Then click on "Read" (red box in figure E.2). The double arrows are for a continuous read of the spectrum (green box). Place the mirror in front of the FTIRS to have a correct signal, you can "Auto Scale" it if you need to. To stop continuous read, click on the double arrows again. To diminish the noise, you can average the signal over more scans (important to note that the more scans, the longer in between each of them) 16 scans is the advised maximal value (brown box in figure E.2).

E.1 Baseline

You can import a base line or register the current spectrum as a base line.

To import the base line, click on the menu "Measure options" then "Load Reference baseline" from that point, select the baseline as a spectrum previously done. Click on "A" to show the absorbance, "T" to see the transmission and "S" to see the spectrum (grey box in figure E.2). If you want to change the baseline, close the software and restart this procedure.

To create a baseline, after a spectrum is established, click on the lightbulb icon named "Set baseline spectrum" (blue box in figure E.2). If this baseline will be used later, it would be better to save it and then import it via the procedure previously described.

E.2 Prepare a series of measure

It is possible to realise a series of scan with constant time increments. To do so, go on the "Tools" menu and chose "Sequence Measurement". There, you can choose the number of scans and the time between the start of two consecutive scans. It is important that this time increment is larger than the time necessary to take a scan (especially if it is an averaged scan, an average of 16 scans takes 4 seconds approximately). You can also chose the number

of measure to take (as the data generated for each scan are not that large, it is advised to take margins before and after the parabola).

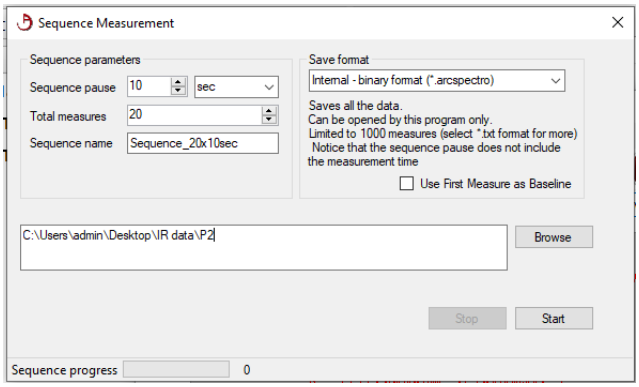

Figure E.3: Sequence Measurement panel of ARCspectro Rocket software.

The name of the sequence and the format are kept by default. For the folder where the data will be saved: create beforehand the folders (IRdata/-Calibration...) and select the folder with the "Browse" option. After everything is done, you can start the sequence.

E.3 Exploit Spectrum values

First, disconnect the instrument. Then click on "File", then "Export Multiple Arcspectro Files to Spreadsheets...", choose "Absorption Spectrum" or "Transmission Spectrum" depending on which spectrum you want. Choose the spectrum to convert. Go to the folder, where your spectrum is, a new ".txt" file appeared. When opened, the first column correspond to the wavenumber and the last one to the absorbance. You can copy paste the data on Excel or load them in python with the pandas library if you have multiples data to plot at the same time.

E.4 Modify the parameters of the scan

To decrease the time necessary for the spectrometer to make a scan, it might be useful to play on the resolution or on the spectral range. To modify one of these parameters, go on the "Tools" menu and chose "Device Status Params". You will end up in the window in figure E.4.

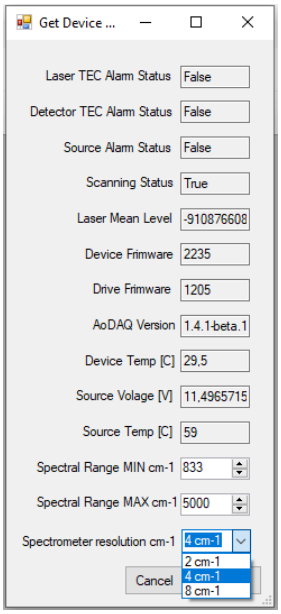

Figure E.4: Device status parameters

Appendix F

Impact of the engines on the temperature sensor

The engines are creating a disturbance in the sensors and their way to collect data. As seen previously in chapter 2.6 in the way these sensors work, a mechanical oscillating stress can create a slight disturbance. The temperature sensor is small and therefore has a small thermal inertia, a slight variation of temperature is therefore detected. Here however, the vibration induced by the engine seems to affect the physical parameters of the sensors and therefore the signal it provides. In the two following pictures (F.1a and F.1b) the probe is placed inside the EC, around the central axis, both engines are running at different spinning speed (0, 1000, 2000 $\mathrm{tr.min^{-1}}$) and the sequence described in section 2.10.1 is run. The attained pressure is 2.2 bars and the expansion is done after 1.5 s waiting time.

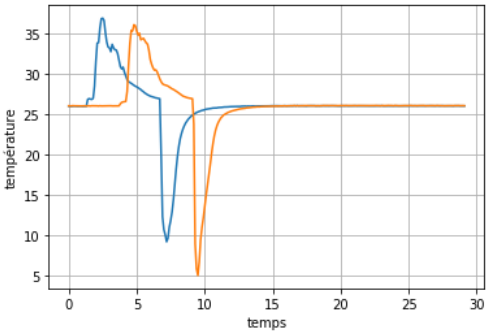

(a) Evolution of the Temperature during the experiment, without the engine.

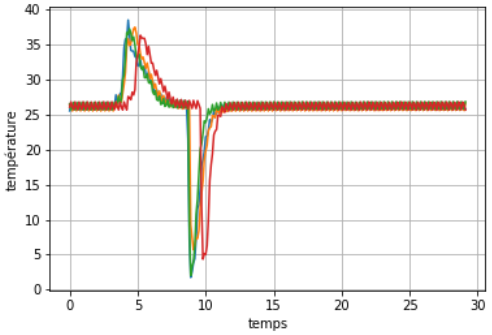

(b) Evolution of the Temperature during the experiment, with the engine running (1000 and 2000 $tr.min^{-1}$).

Figure F.1: Evolution of Temperature when the probe is inside the cell.

As the figure F.1 shows, the engines are creating a vibration due to the displacement of the mass centre of the axis away from the rotation axis. This vibration creates a sinusoidal perturbation on the temperature sensor due to it's low thermal inertia. The figure F.2 is a zoom in the stationary part of the figure F.1b, this allows a record of the oscillating parameters.

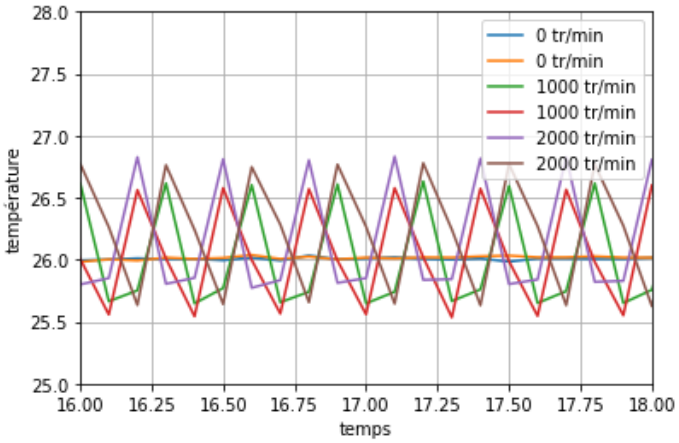

Figure F.2: Zoom on the stationary regime to see the impact of the engines on the temperature evolution.

The same study is run but this time the sensor is set to the limit of the EC in order to decrease the impact on the air flow inside the EC.

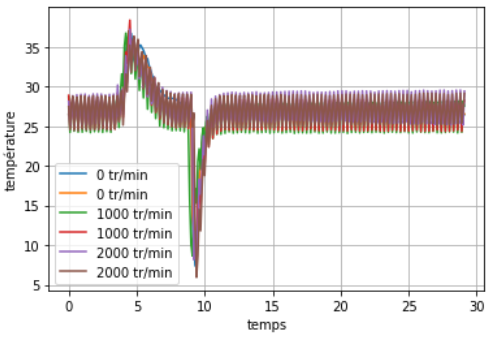

(a) Evolution of the Temperature during the experiment, without the engine and probe at the border of the EC

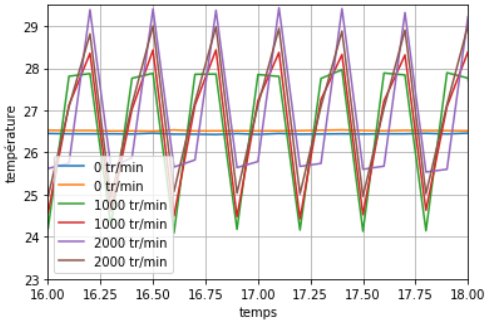

(b) Evolution of the Temperature during the experiment, with the engine running (1000 and 2000 $tr.min^{-1}$) and probe at the border of the EC

Figure F.3: Evolution of Temperature when the probe is at the border of the EC

As figure F.3b shows, the amplitude is much higher at the border of the EC. The table F.1, record the different values and allows the comparison

with the configuration in which the probe is deep in the EC. The hypothesis to explain the behaviour of the sensor under this vibrating stress is that due to the low mass of the thermal sensor, the vibrations are probably creating an irregular bending movement of the sensor at the tail of it's support. This movement might create hits of the sensor end on the support. These hits might affect the sensor and its ability to transmit the information as shown in figures F.1b and F.3a suggest.

Series	**Rotation speed**	**Amplitude** (K)	**Period**
1	$0\,\mathrm{tr.min^{-1}}$	0	0
2	$0\,\mathrm{tr.min^{-1}}$	0	0
3	$1000\,\mathrm{tr.min^{-1}}$	1	0.3 s
4	$1000\,\mathrm{tr.min^{-1}}$	1.1	0.3 s
5	$2000\,\mathrm{tr.min^{-1}}$	0.9	0.3 s
6	$2000\,\mathrm{tr.min^{-1}}$	1	0.3 s
7	$0\,\mathrm{tr.min^{-1}}$	0	0
8	$0\,\mathrm{tr.min^{-1}}$	0	0
9	$1000\,\mathrm{tr.min^{-1}}$	3.8	0.3 s
10	$1000\,\mathrm{tr.min^{-1}}$	4.1	0.3 s
11	$2000\,\mathrm{tr.min^{-1}}$	3.6	0.3 s
12	$2000\,\mathrm{tr.min^{-1}}$	4.0	0.3 s

Table F.1: Record of the oscillating parameters observed in fig F.3b and F.2, the series 1-6 are for the probe deep in the EC, the others when the probe is at the border of the EC

To solve this issue and minimise the effect of the engines on the sensors. It seems that twisting the wires of the temperature sensor is enough to suppress this effect. This effect were probably created by a rotating electro magnetic field of the engines.

Appendix G

Diameter evolution during evaporation experiments

The main equation used for the piecewise linear fitting of the data is the equation 3.21 that is:

$$f_{ev}(t, t_{ev,R}, \alpha_1, \alpha_2, d^2_{ev,R}) = \begin{cases} \alpha_1(t - t_{ev,R}) + d^2_{ev,R} & \text{if } t < t_{ev,R} \\ \alpha_2(t - t_{ev,R}) + d^2_{ev,R} & \text{if } t \geq t_{ev,R} \end{cases} \tag{G.1}$$

Here the focus will be on the trend coefficient (α_1 and α_2).

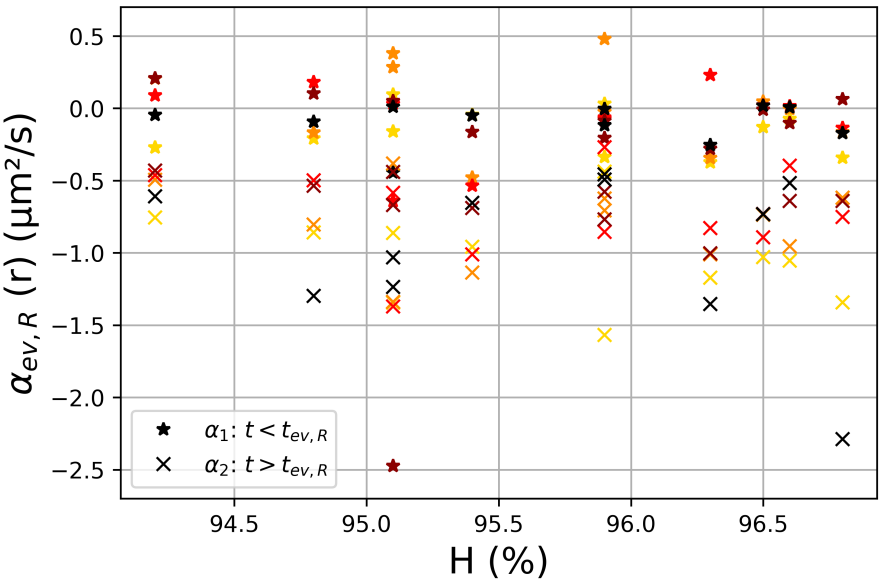

Figure G.1: D2-law trend coefficient before and after the break ($t_{ev,R}$).

Before the break, the trend coefficient are fairly centred around 0. This is an expected behaviour as, before the break, the evaporation has not started yet. After the break, the coefficients are approximately at a value $-1\,\mu m^2/s$ (see figure G.1).

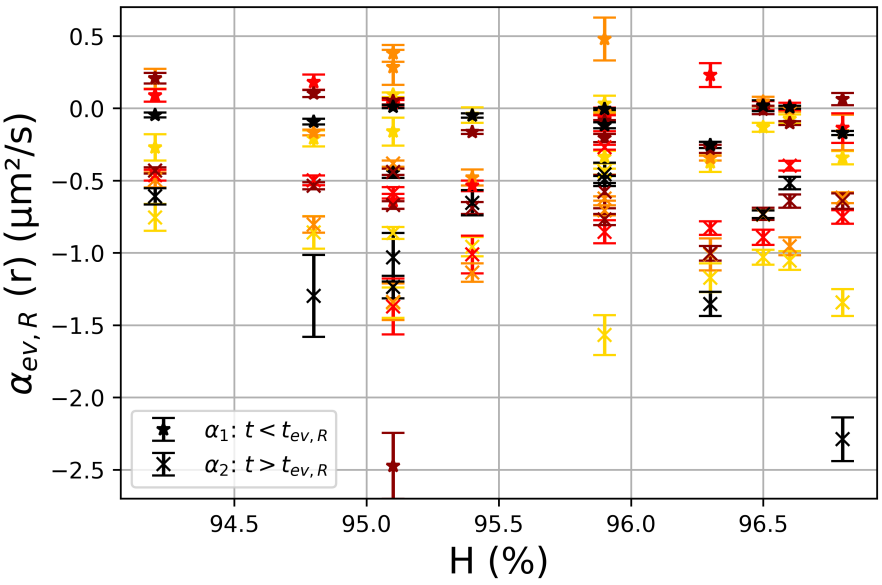

Figure G.2: D2-law trend coefficient before and after the break ($t_{ev,R}$) with the error bars.

The figure G.2 records the same values but the error bars are added. It is important to keep in mind that the last evaluations of the radius are not taken into account because there is not enough droplet in the volume so that the average radius is representative. With a better imaging techniques, key informations could also be extracted there.

Appendix H

Scaled Nucleation Theory

The scaled nucleation theory were introduced by B.Hale in 1986 [169]. In this theory, the nucleation rate per unit of time (here s^{-1}) per unit of volume (here cm^{-3}) is a function of the reduced pressure, reduced temperature and the reduce bulk liquid number density.

$$J(T, P, n) = f(\frac{T}{T_c}, \frac{P}{P_c}, \frac{\tilde{n}}{\tilde{n}_c}) \tag{H.1}$$

After some time a function was proposed in 1992 to evaluate the nucleation rate [170].

$$J(T, S) = J_0 \exp\left(-\frac{16\pi}{3}\frac{\Omega^3}{\ln(S)^2}\left(\frac{T_c}{T} - 1\right)^3\right) \tag{H.2}$$

where Ω is the excess surface entropy divided by k (Boltzmann constant) per molecule in the embryonic cluster. The value for Ω vary between 2 for ordinary liquids to 1.5 for associated liquids. J_0 is the kinetic prefactor. It was shown in reference [169] that this prefactor J_0 could be linked to the Becker-Doring theory [102]. As a result:

$$J_0 = J_c I \left(\frac{P_0}{P_c}\right) S^2 \tag{H.3}$$

where $I = 2\frac{\tilde{n}_c}{\tilde{n}}^{2/3}(\Omega(\frac{T_c}{T} - 1)^{1/2})(\frac{T_c}{T}^{3/2})$

Appendix I

Record of the different acceleration during parabolic flights

This section is a summary of the different quality in terms of microgravity for each parabola. One full acceleration record is displayed in fig I.1. The axis are designated as follow: X-axis from tail to front of the aircraft, Y-axis from left to right wings, when looking in cockpit direction while standing in the cabin, Z-axis from floor to ceiling direction.

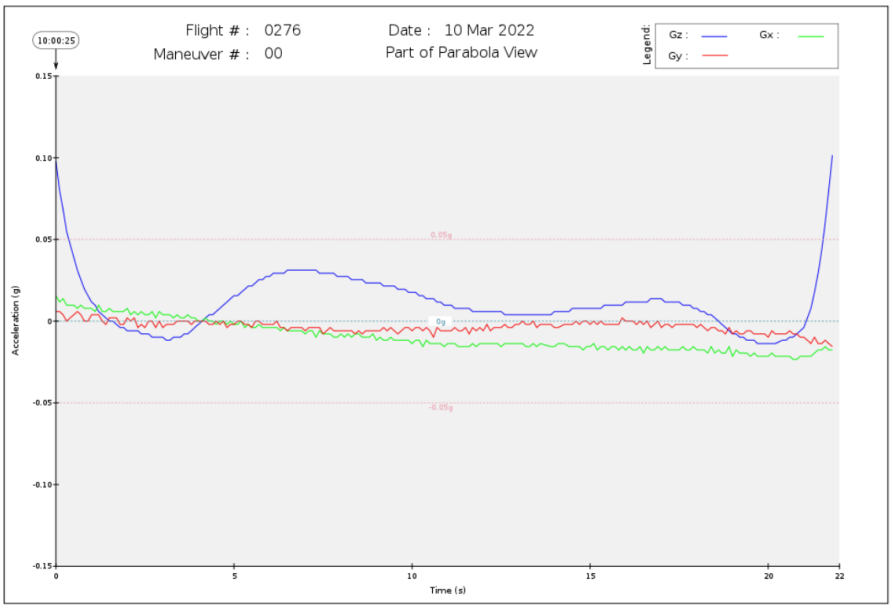

Figure I.1: Record for each of the axis the acceleration level

For the following records, each point is the absolute maximum value taken between 2 and 20 s of each parabola.

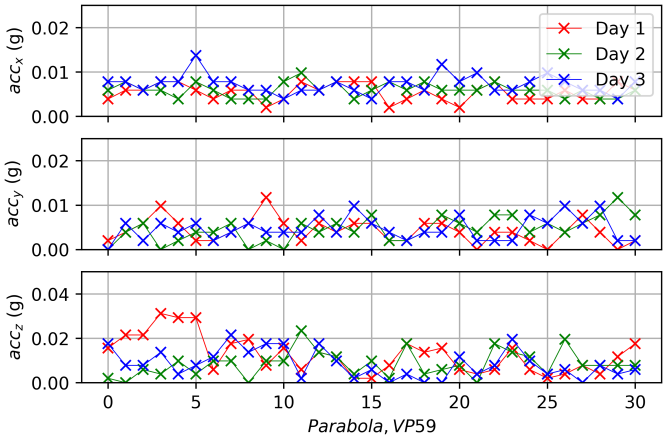

Figure I.2: Record of the acceleration level for each of the axis for the 59th parabolic flight campaign.

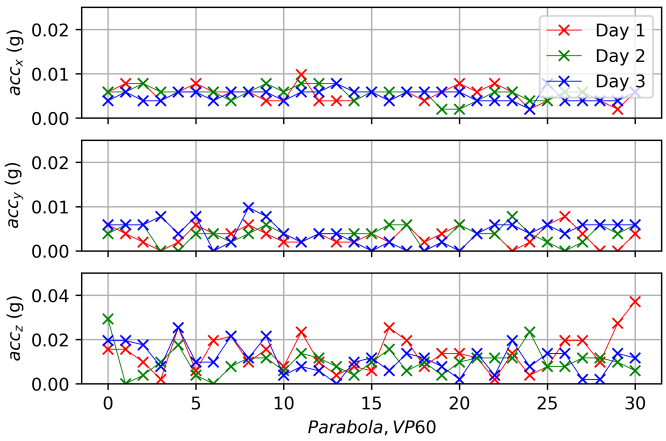

Figure I.3: Record of the acceleration level for each of the axis for the 60th parabolic flight campaign.

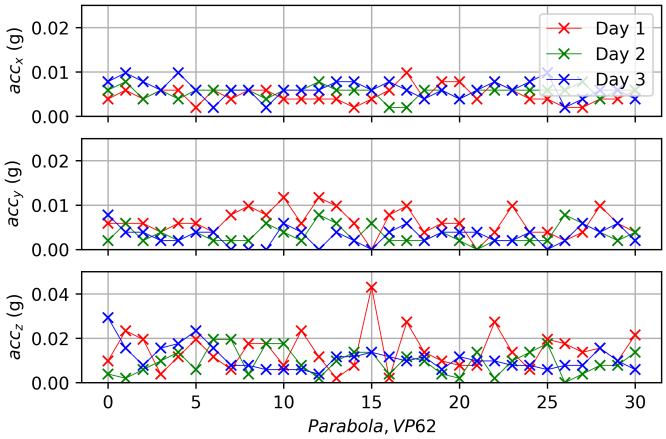

Figure I.4: Record of the acceleration level for each of the axis for the 62nd parabolic flight campaign.

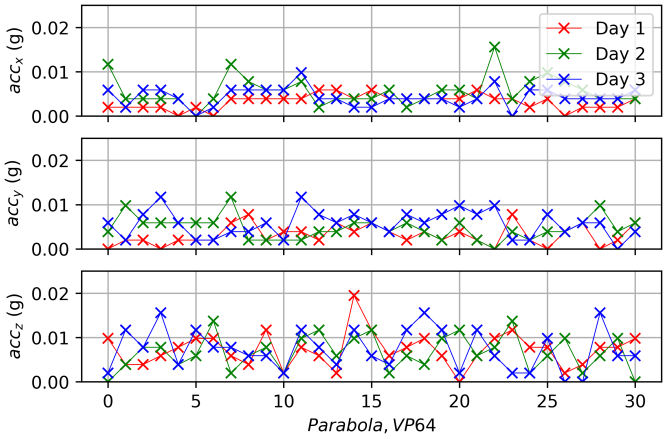

Figure I.5: Record of the acceleration level for each of the axis for the 64th parabolic flight campaign.

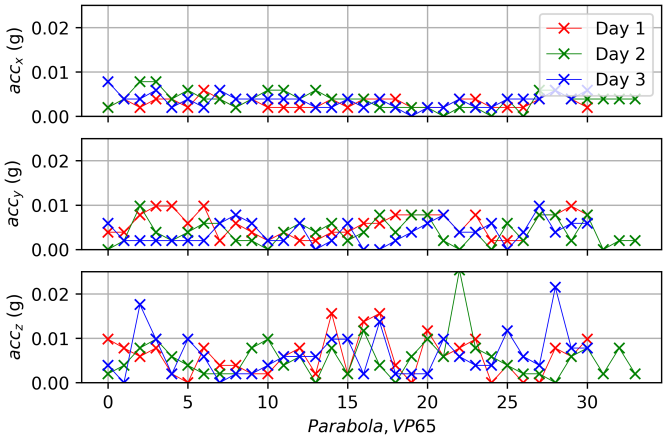

Figure I.6: Record of the acceleration level for each of the axis for the 65th parabolic flight campaign.

Appendix J

Record of Pressure, Temperature and Humidity during parabolic flights

This section displays the record of the Pressure, Temperature and Humidity over time for the parabolic flight campaign VP65, they are sorted by experience type (evaporation, evaporation under IR source and von-Kármán experiment)

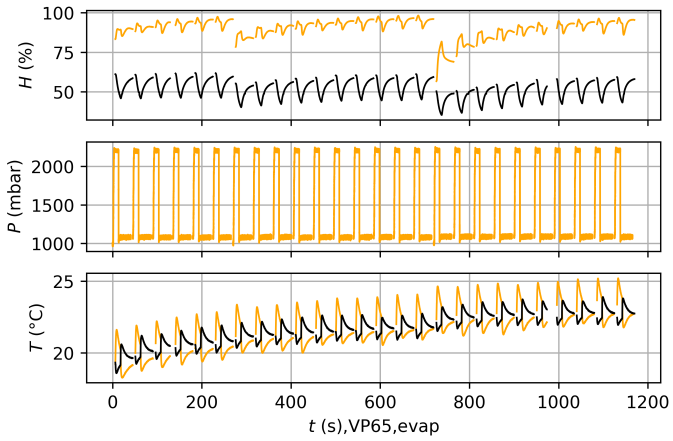

Figure J.1: Record for the Pressure, Temperature and Humidity for the evaporation experiment during the VP65

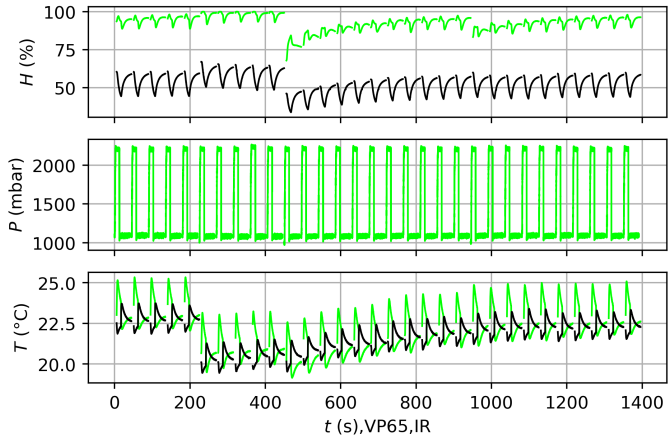

Figure J.2: Record for the Pressure, Temperature and Humidity for the evaporation experiment with the IR source impacting the aerosol during the VP65

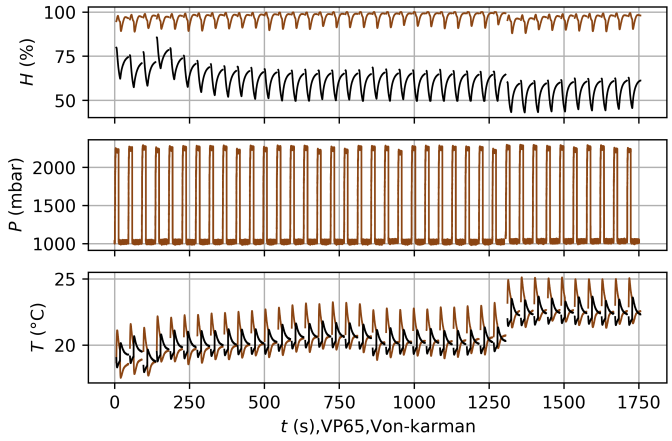

Figure J.3: Record for the Pressure, Temperature and Humidity for the von-Kármán flow experiment during the VP65

Appendix K

Code to solve the heat equation

```
import matplotlib.pyplot as plt
import numpy as np


T0=20
Ti=5
lambd=0.025
rho=1.23
cp=1805
a=lambd/(rho*cp)
R=0.015 #(15mm) rayon de la cellule
Z=0.03 #(30mm) longueur de la cellule
pos=0.007 #(7 mm) rayon
nb_r=60
dr=R/nb_r
nb_z=120
dz=Z/nb_z
T_init=-5.0
T_bords=20.0
init_Temp=np.full([nb_r,nb_z],T_init)
r = np.linspace(0, R, nb_r)
z = np.linspace(0, Z, nb_z)

temps_simu=25 #s

dt_0=0.0001
List_temps=np.linspace(0, temps_simu,int(temps_simu/dt_0))
```

```
s=a*dt_0/dr**2+a*dt_0/dz**2 #pour stabilite avoir s<0.25
print(s)
nb_s=int(temps_simu/dt_0)

h0=2
hinit=20
tau=1.3333

def h(t):
    return h0+(hinit-h0)*np.exp(-t/tau)

def lbd(t):
    return lambd*(1+(hinit/h0-1)*np.exp(-t/tau))

def a_th(t):
    return lbd(t)/(rho*cp)

def B(t):
    return dr*h(t)/lbd(t)

def T_suiv(u,dt,t):
    u_new = np.copy(u)
    for i in range(1,nb_r-1):
        for j in range(1,nb_z-1):
            radial_term=(u[i+1,j]-2*u[i,j]+u[i-1,j])
            central_term=(u[i,j+1]-2*u[i,j]+u[i,j-1])
            u_new[i,j] = u[i, j]
            +a*(1/dr)**2*dt*(radial_term+central_term)
            + a*dt*(1/r[i])*(u[i+1,j]-u[i,j])/dr

        u_new[:-1,0]=u_new[:-1,1]
        u_new[0,:-1]=u_new[1,:-1]
        for ii in range(len(u_new[:,0])-1):
            u_new[ii,-1]=u_new[ii,-2]/(1+B(t))
            +T_bords*B(t)/(1+B(t))
        for jj in range (len(u_new[0,:])-1):
            u_new[-1,jj]=u_new[-2,jj]/(1+B(t))
            +T_bords*B(t)/(1+B(t))
    u_new[-1,-1]=u_new[-1,-2]
    return u_new
```

```
#test=T_suiv(init_Temp,dt_0,0)

def solve_heat(dt):
nb_s=int(temps_simu/dt)
LL=[init_Temp]
for it in range(nb_s-1):
    LL.append(T_suiv(LL[-1],dt,it*dt_0))
return LL

sol_0=solve_heat(dt_0)
data_0=np.array(sol_0)
```

Bibliography

[1] J. Lucas, M. Ralaivao, B. N. Estevinho, and F. Rocha. "A new approach for the microencapsulation of curcumin by a spray drying method, in order to value food products". In: *Powder Technology* 362 (Feb. 2020), pp. 428–435.

[2] D. Song, J. Liu, and Y. Liu. "Reactive Paper Spray Ionization Mass Spectrometry for Rapid Detection of Estrogens in Cosmetics". In: *Molecules* 28.15 (July 2023), p. 5675.

[3] E. Boel, R. Koekoekx, S. Dedroog, I. Babkin, M. R. Vetrano, C. Clasen, and G. Van den Mooter. "Unraveling Particle Formation: From Single Droplet Drying to Spray Drying and Electrospraying". In: *Pharmaceutics* 12.7 (2020).

[4] J. Troyano, C. undefinedamur, L. Garzón-Tovar, A. Carné-Sánchez, I. Imaz, and D. Maspoch. "Spray-Drying Synthesis of MOFs, COFs, and Related Composites". In: *Accounts of Chemical Research* 53.6 (June 2020), pp. 1206–1217.

[5] A. Carné-Sánchez, I. Imaz, M. Cano-Sarabia, and D. Maspoch. "A spray-drying strategy for synthesis of nanoscale metal–organic frameworks and their assembly into hollow superstructures". In: *Nature Chemistry* 5.3 (2013), pp. 203–211.

[6] S. R. Bakshi, V. Singh, S. Seal, and A. Agarwal. "Aluminum composite reinforced with multiwalled carbon nanotubes from plasma spraying of spray dried powders". In: *Surface and Coatings Technology* 203.10 (2009), pp. 1544–1554.

[7] V. Caratelli, G. Fegatelli, D. Moscone, and F. Arduini. "A paper-based electrochemical device for the detection of pesticides in aerosol phase inspired by nature: A flower-like origami biosensor for precision agriculture". In: *Biosensors and Bioelectronics* 205 (2022), p. 114119.

[8] Z. Barker, V. Venkatchalam, A. N. Martin, G. R. Farquar, and M. Frank. "Detecting trace pesticides in real time using single particle aerosol mass spectrometry". In: *Analytica Chimica Acta* 661.2 (2010), pp. 188–194.

[9] R. Davydov, M. Sokolov, W. Hogland, A. Glinushkin, and A. Markaryan. "The application of pesticides and mineral fertilizers in agriculture". In: *MATEC Web of Conferences* 245 (2018). Ed. by A. Borodinecs, V. Sergeev, and N. Vatin, p. 11003.

[10] I. P. on Climate Change (IPCC). *Climate Change 2021 – The Physical Science Basis: Working Group I Contribution to the Sixth Assessment Report of the Intergovernmental Panel on Climate Change*. Cambridge University Press, 2023, pp. 2215–2256.

[11] World Bank. *World Bank Open Data*. 2024. URL: `https://data.worldbank.org/` (visited on 10/17/2024).

[12] V. Masson-Delmotte, P. Zhai, A. Pirani, S. L. Connors, C. Péan, S. Berger, N. Caud, Y. Chen, L. Goldfarb, M. I. Gomis, et al. "Summary for policymakers". In: (2021).

[13] A. Berk, P. Conforti, R. Kennett, T. Perkins, F. Hawes, and J. van den Bosch. "MODTRAN6: a major upgrade of the MODTRAN radiative transfer code". In: *SPIE Proceedings*. Ed. by M. Velez-Reyes and F. A. Kruse. SPIE, June 2014.

[14] M. Wild. "The global energy balance as represented in CMIP6 climate models". en. In: *Clim. Dyn.* 55.3 (May 2020), pp. 553–577.

[15] K. Sefiane. "Patterns from drying drops". In: *Advances in colloid and interface science* 206 (2014), pp. 372–381.

[16] V. Vancauwenberghe, P. Di Marco, and D. Brutin. "Wetting and evaporation of a sessile drop under an external electrical field: A review". In: *Colloids and Surfaces A: Physicochemical and Engineering Aspects* 432 (2013), pp. 50–56.

[17] F. Carle, B. Sobac, and D. Brutin. "Experimental evidence of the atmospheric convective transport contribution to sessile droplet evaporation". In: *Applied Physics Letters* 102.6 (Feb. 2013).

[18] S. David, K. Sefiane, and L. Tadrist. "Experimental investigation of the effect of thermal properties of the substrate in the wetting and evaporation of sessile drops". In: *Colloids and Surfaces A: Physicochemical and Engineering Aspects* 298.1-2 (2007), pp. 108–114.

[19] G. Dunn, S. Wilson, B. Duffy, S. David, and K. Sefiane. "The strong influence of substrate conductivity on droplet evaporation". In: *Journal of Fluid Mechanics* 623 (2009), pp. 329–351.

[20] I. Ríos-López, P. Karamaoynas, X. Zabulis, M. Kostoglou, and T. D. Karapantsios. "Image analysis of axisymmetric droplets in wetting experiments: A new tool for the study of 3D droplet geometry and droplet shape reconstruction". In: *Colloids and Surfaces A: Physicochemical and Engineering Aspects* 553 (2018), pp. 660–671.

[21] I. Ríos-López, S. Evgenidis, M. Kostoglou, X. Zabulis, and T. D. Karapantsios. "Effect of initial droplet shape on the tangential force required for spreading and sliding along a solid surface". In: *Colloids and Surfaces A: Physicochemical and Engineering Aspects* 549 (2018), pp. 164–173.

[22] R. Picknett and R. Bexon. "The evaporation of sessile or pendant drops in still air". In: *Journal of colloid and Interface Science* 61.2 (1977), pp. 336–350.

[23] T. A. Nguyen and A. V. Nguyen. "Increased evaporation kinetics of sessile droplets by using nanoparticles". In: *Langmuir* 28.49 (2012), pp. 16725–16728.

[24] C. Bourges-Monnier and M. Shanahan. "Influence of evaporation on contact angle". In: *Langmuir* 11.7 (1995), pp. 2820–2829.

[25] J. Stauber, S. K. Wilson, B. Duffy, and K. Sefiane. "Comment on "Increased evaporation kinetics of sessile droplets by using nanoparticles"". In: *Langmuir* 29.39 (2013), pp. 12328–12329.

[26] J. M. Stauber, S. K. Wilson, B. R. Duffy, and K. Sefiane. "On the lifetimes of evaporating droplets". In: *Journal of Fluid Mechanics* 744 (2014), R2.

[27] J. M. Stauber, S. K. Wilson, B. R. Duffy, and K. Sefiane. "Evaporation of droplets on strongly hydrophobic substrates". In: *Langmuir* 31.12 (2015), pp. 3653–3660.

[28] Z. Pan, S. Dash, J. A. Weibel, and S. V. Garimella. "Assessment of water droplet evaporation mechanisms on hydrophobic and superhydrophobic substrates". In: *Langmuir* 29.51 (2013), pp. 15831–15841.

[29] D. Hu and H. Wu. "Volume evolution of small sessile droplets evaporating in stick-slip mode". In: *Physical Review E* 93.4 (2016), p. 042805.

[30] D. Debuisson, A. Merlen, V. Senez, and S. Arscott. "Stick–Jump (SJ) evaporation of strongly pinned nanoliter volume sessile water droplets on quick drying, micropatterned surfaces". In: *Langmuir* 32.11 (2016), pp. 2679–2686.

[31] S. K. Wilson and B. R. Duffy. "Mathematical models for the evaporation of sessile droplets". In: (2022).

[32] S. K. Wilson and H.-M. D'Ambrosio. "Evaporation of Sessile Droplets". In: *Annual Review of Fluid Mechanics* 55.1 (Jan. 2023), pp. 481–509.

[33] S. Kumar, M. Medale, P. D. Marco, and D. Brutin. "Sessile volatile drop evaporation under microgravity". In: *npj Microgravity* 6.1 (Dec. 2020).

[34] P. Kelly-Zion, C. Pursell, S. Vaidya, and J. Batra. "Evaporation of sessile drops under combined diffusion and natural convection". In: *Colloids and Surfaces A: Physicochemical and Engineering Aspects* 381.1–3 (May 2011), pp. 31–36.

[35] C. Chauveau, M. Birouk, and I. Gökalp. "An analysis of the d2-law departure during droplet evaporation in microgravity". In: *International Journal of Multiphase Flow* 37.3 (Apr. 2011), pp. 252–259.

[36] H. Y. Erbil. "Evaporation of pure liquid sessile and spherical suspended drops: A review". In: *Advances in colloid and interface science* 170.1-2 (2012), pp. 67–86.

[37] B. Sobac, P. Talbot, B. Haut, A. Rednikov, and P. Colinet. "A comprehensive analysis of the evaporation of a liquid spherical drop". In: *Journal of Colloid and Interface Science* 438 (Jan. 2015), pp. 306–317.

[38] J. C. Maxwell. *Collected Scientific Papers. Vol. 2.* CUP, 1890.

[39] N. Fuchs. *Growth and evaporation of drops in gaseous media.* 1959.

[40] L. Consolini, S. K. Aggarwal, and S. Murad. "A molecular dynamics simulation of droplet evaporation". In: *International journal of heat and mass transfer* 46.17 (2003), pp. 3179–3188.

[41] J. Wang, G. Gréhan, Y. Han, S. Saengkaew, and G. Gouesbet. "Numerical study of global rainbow technique: sensitivity to non-sphericity of droplets". In: *Experiments in fluids* 51 (2011), pp. 149–159.

[42] R. B. Bird. "Transport phenomena". In: *Appl. Mech. Rev.* 55.1 (2002), R1–R4.

[43] B. Haut and P. Colinet. "Surface-tension-driven instabilities of a pure liquid layer evaporating into an inert gas". In: *Journal of colloid and interface science* 285.1 (2005), pp. 296–305.

[44] M. K. Yau and R. R. Rogers. *A short course in cloud physics*. Elsevier, 1996.

[45] S. Torquato and G. R. Stell. "An equation for the latent heat of vaporization". In: *Industrial and Engineering Chemistry Fundamentals* 21.3 (Aug. 1982), pp. 202–205.

[46] J. G. Leidenfrost. *De aquae communis nonnullis qualitatibus tractatus*. Ovenius, 1756.

[47] A.-L. Biance, C. Clanet, and D. Quéré. "Leidenfrost drops". In: *Physics of Fluids* 15.6 (June 2003), pp. 1632–1637.

[48] B. Sobac, A. Rednikov, S. Dorbolo, and P. Colinet. "Leidenfrost effect: Accurate drop shape modeling and refined scaling laws". In: *Physical Review E* 90.5 (Nov. 2014).

[49] L. Maquet, M. Brandenbourger, B. Sobac, A.-L. Biance, P. Colinet, and S. Dorbolo. "Leidenfrost drops: Effect of gravity". In: *EPL (Europhysics Letters)* 110.2 (Apr. 2015), p. 24001.

[50] G. Fantoni et al. "Assembly of mini and microparts: development of an electrostatic feeder". In: *PROCEEDINGS OF THE 6TH AI TE. M. CONFERENCE*. 2003, pp. 352–366.

[51] V. Vandaele, P. Lambert, and A. Delchambre. "Non-contact handling in microassembly: Acoustical levitation". In: *Precision engineering* 29.4 (2005), pp. 491–505.

[52] M. Zaeh, J. Zimmermann, A. Zitzmann, and M. Schilp. "Non-contact handling in microfabrication". In: *Proceedings of the Euspen International Topical Conference, Aachen, Germany*. 2003, pp. 325–328.

[53] F. Erzincanli, J. Sharp, and S. Erhal. "Design and operational considerations of a non-contact robotic handling system for non-rigid materials". In: *International Journal of Machine Tools and Manufacture* 38.4 (1998), pp. 353–361.

[54] J. Gao, C. Cao, and B. Wei. "Containerless processing of materials by acoustic levitation". In: *Advances in Space Research* 24.10 (1999), pp. 1293–1297.

[55] M. A. Andrade, N. Pérez, and J. C. Adamowski. "Review of progress in acoustic levitation". In: *Brazilian Journal of Physics* 48 (2018), pp. 190–213.

[56] H. Bruus. "Acoustofluidics 7: The acoustic radiation force on small particles". In: *Lab on a Chip* 12.6 (2012), pp. 1014–1021.

[57] Y. Sasaki, K. Hasegawa, A. Kaneko, and Y. Abe. "Heat and mass transfer characteristics of binary droplets in acoustic levitation". In: *Physics of Fluids* 32.7 (July 2020).

[58] Y. Maruyama and K. Hasegawa. "Evaporation and drying kinetics of water-NaCl droplets via acoustic levitation". In: *RSC Advances* 10.4 (2020), pp. 1870–1877.

[59] P. Wagner and R. Strey. "Homogeneous nucleation rates of water vapor measured in a two-piston expansion chamber". In: *The Journal of Physical Chemistry* 85.18 (1981), pp. 2694–2698.

[60] D. Brus, V. **Z**dímal, and J. Smolík. "Homogeneous nucleation rate measurements in supersaturated water vapor". In: *The Journal of chemical physics* 129.17 (2008).

[61] S. Kooij, R. Sijs, M. M. Denn, E. Villermaux, and D. Bonn. "What Determines the Drop Size in Sprays?" In: *Physical Review X* 8.3 (July 2018).

[62] S. Kooij, A. Astefanei, G. L. Corthals, and D. Bonn. "Size distributions of droplets produced by ultrasonic nebulizers". In: *Scientific Reports* 9.1 (Apr. 2019).

[63] T. Jackson, D. Deibert, G. Wyatt, Q. Durand-Moreau, A. Adisesh, K. Khunti, S. Khunti, S. Smith, X. H. S. Chan, L. Ross, N. Roberts, E. Toomey, T. Greenhalgh, I. Arora, S. M. Black, J. Drake, N. Syam, R. Temple, and S. Straube. "Classification of aerosol-generating procedures: a rapid systematic review". In: *BMJ Open Respiratory Research* 7.1 (Oct. 2020), e000730.

[64] G. de Leeuw, E. L. Andreas, M. D. Anguelova, C. W. Fairall, E. R. Lewis, C. O'Dowd, M. Schulz, and S. E. Schwartz. "Production flux of sea spray aerosol". In: *Reviews of Geophysics* 49.2 (May 2011).

[65] A. Qi, J. R. Friend, L. Y. Yeo, D. A. Morton, M. P. McIntosh, and L. Spiccia. "Miniature inhalation therapy platform using surface acoustic wave microfluidic atomization". In: *Lab on a Chip* 9.15 (2009), pp. 2184–2193.

[66] M. Faraday. "On the forms and states assumed by fluids in contact with vibrating elastic surfaces". In: *Phil. Trans. R. Soc. Lond.* 121 (1831), pp. 319–340.

[67] J. W. Strutt and J. W. S. Rayleigh. *The theory of sound*. Vol. 1. Macmillan, 1877.

[68] R. J. Lang. "Ultrasonic atomization of liquids". In: *The journal of the acoustical society of America* 34.1 (1962), pp. 6–8.

[69] E. Villermaux and B. Bossa. "Drop fragmentation on impact". In: *Journal of Fluid Mechanics* 668 (2011), pp. 412–435.

[70] A. H. Lefebvre and V. G. McDonell. *Atomization and sprays*. CRC press, 2017.

[71] J. R. Lake. "The effect of drop size and velocity on the performance of agricultural sprays". In: *Pesticide Science* 8.5 (Oct. 1977), pp. 515–520.

[72] S. Reichenberger, M. Bach, A. Skitschak, and H.-G. Frede. "Mitigation strategies to reduce pesticide inputs into ground- and surface water and their effectiveness; A review". In: *Science of The Total Environment* 384.1–3 (Oct. 2007), pp. 1–35.

[73] C. Stainier, M.-F. Destain, B. Schiffers, and F. Lebeau. "Droplet size spectra and drift effect of two phenmedipham formulations and four adjuvants mixtures". In: *Crop Protection* 25.12 (Dec. 2006), pp. 1238–1243.

[74] H. Kublik and M. Vidgren. "Nasal delivery systems and their effect on deposition and absorption". In: *Advanced Drug Delivery Reviews* 29.1–2 (Jan. 1998), pp. 157–177.

[75] M. B. Dolovich and R. Dhand. "Aerosol drug delivery: developments in device design and clinical use". In: *The Lancet* 377.9770 (Mar. 2011), pp. 1032–1045.

[76] P. Le Brun, A. de Boer, H. Frijlink, and H. Heijerman. In: *Pharmacy World and Science* 22.3 (2000), pp. 75–81.

[77] E. Villermaux. "Fragmentation". In: *Annual Review of Fluid Mechanics* 39.1 (Jan. 2007), pp. 419–446.

[78] H. B. Squire. "Investigation of the instability of a moving liquid film". In: *British Journal of Applied Physics* 4.6 (June 1953), pp. 167–169.

[79] D. Sharp. "An overview of Rayleigh-Taylor instability". In: *Physica D: Nonlinear Phenomena* 12.1–3 (July 1984), pp. 3–18.

[80] L. Rayleigh. "On The Instability Of Jets". In: *Proceedings of the London Mathematical Society* s1-10.1 (Nov. 1878), pp. 4–13.

[81] P. MARMOTTANT and E. VILLERMAUX. "On spray formation". In: *Journal of Fluid Mechanics* 498 (Jan. 2004), pp. 73–111.

[82] S. A. Basha and K. R. Gopal. "In-cylinder fluid flow, turbulence and spray models—A review". In: *Renewable and sustainable energy reviews* 13.6-7 (2009), pp. 1620–1627.

[83] L. Haselman and C. Westbrook. *A theoretical model for two-phase fuel injection in stratified charge engines*. Tech. rep. SAE Technical Paper, 1978.

[84] P. Vaillancourt, M. Yau, and W. W. Grabowski. "Microscopic approach to cloud droplet growth by condensation. Part I: Model description and results without turbulence". In: *Journal of the atmospheric sciences* 58.14 (2001), pp. 1945–1964.

[85] P. Vaillancourt, M. Yau, P. Bartello, and W. W. Grabowski. "Microscopic approach to cloud droplet growth by condensation. Part II: Turbulence, clustering, and condensational growth". In: *Journal of the atmospheric sciences* 59.24 (2002), pp. 3421–3435.

[86] J. F. Davies, A. E. Haddrell, and J. P. Reid. "Time-resolved measurements of the evaporation of volatile components from single aerosol droplets". In: *Aerosol Science and Technology* 46.6 (2012), pp. 666–677.

[87] G. Tsagkogeorgas, P. Roldin, J. Duplissy, L. Rondo, J. Tröstl, J. G. Slowik, S. Ehrhart, A. Franchin, A. Kürten, A. Amorim, et al. "Evaporation of sulfate aerosols at low relative humidity". In: *Atmospheric Chemistry and Physics* 17.14 (2017), pp. 8923–8938.

[88] G. Rovelli, R. E. Miles, J. P. Reid, and S. L. Clegg. "Accurate measurements of aerosol hygroscopic growth over a wide range in relative humidity". In: *The Journal of Physical Chemistry A* 120.25 (2016), pp. 4376–4388.

[89] J. F. Davies, A. E. Haddrell, R. E. Miles, C. R. Bull, and J. P. Reid. "Bulk, surface, and gas-phase limited water transport in aerosol". In: *The Journal of Physical Chemistry A* 116.45 (2012), pp. 10987–10998.

[90] L. Morawska. "Environmental aerosol physics". In: *Brisbane, Queensland University of Technology* (2003).

[91] T. Von Kármán. "Uber laminare und turbulente Reibung". In: *Z. Angew. Math. Mech.* 1 (1921), pp. 233–252.

[92] G. K. Batchelor. "Note on a class of solutions of the Navier-Stokes equations representing steady rotationally-symmetric flow". In: *The quarterly journal of mechanics and applied mathematics* 4.1 (1951), pp. 29–41.

[93] B. Saint-Michel. "L'écoulement de von Kármán comme paradigme de la physique statistique hors de l'équilibre". PhD thesis. Université Pierre et Marie Curie-Paris VI, 2013.

[94] E.-W. Saw, D. Kuzzay, D. Faranda, A. Guittonneau, F. Daviaud, C. Wiertel-Gasquet, V. Padilla, and B. Dubrulle. "Experimental characterization of extreme events of inertial dissipation in a turbulent swirling flow". In: *Nature communications* 7.1 (2016), p. 12466.

[95] A. E. Perry and B. Fairlie. "Critical points in flow patterns". In: *Advances in geophysics*. Vol. 18. Elsevier, 1975, pp. 299–315.

[96] W. W. Grabowski and L.-P. Wang. "Growth of Cloud Droplets in a Turbulent Environment". In: *Annual Review of Fluid Mechanics* 45.1 (Jan. 2013), pp. 293–324.

[97] K. Lau and H. Wu. "Warm rain processes over tropical oceans and climate implications". In: *Geophysical Research Letters* 30.24 (2003).

[98] R. Bousquet, O. Chaffard, M. Creff, D. Lucor, and C. Nore. "Large scale analysis of three-dimensional turbulent von Kármán swirling flows". In: *Physics of Fluids* 36.10 (2024).

[99] Wikipedia contributors. *Cloud*. `https://en.wikipedia.org/wiki/Cloud`. 2024.

[100] V. Kalikmanov. *Nucleation Theory*. Springer Netherlands, 2013.

[101] T. Koop, B. Luo, A. Tsias, and T. Peter. "Water activity as the determinant for homogeneous ice nucleation in aqueous solutions". en. In: *Nature* 406.6796 (Aug. 2000), pp. 611–614.

[102] R. Becker and W. Döring. "Ann. Phys." In: *Ann. Phys.* Vol. 24. 1935, p. 719.

[103] Y. B. Zeldovich. "On the theory of new phase formation: cavitation". In: *Acta Physicochem., USSR* 18 (1943), p. 1.

[104] M. Volmer. "Kinetik der phasenbildung". In: *(No Title)* (1939).

[105] R. C. Miller, R. J. Anderson, J. Kassner Jr, and D. E. Hagen. "Homogeneous nucleation rate measurements for water over a wide range of temperature and nucleation rate". In: *The Journal of Chemical Physics* 78.6 (1983), pp. 3204–3211.

[106] C. T. R. Wilson. "XI. Condensation of water vapour in the presence of dust-free air and other gases". In: *Philosophical Transactions of the Royal Society of London. Series A, Containing Papers of a Mathematical or Physical Character* 189 (1897), pp. 265–307.

[107] P. Coulier. "de Pharm. et de Chim". In: *Par.(Ser. 4)* 22 (1875), p. 254.

[108] J. L. Kassner Jr and R. J. Schmitt. "Homogeneous nucleation measurements of water vapor in helium". In: *The Journal of Chemical Physics* 44.11 (1966), pp. 4166–4170.

[109] J. L. Schmitt. "Precision expansion cloud chamber for homogeneous nucleation studies". In: *Review of Scientific Instruments* 52.11 (1981), pp. 1749–1754.

[110] B. N. Hale and P. Plummer. "Molecular model for ice clusters in a supersaturated vapor". In: *The Journal of Chemical Physics* 61.10 (1974), pp. 4012–4019.

[111] Y. Viisanen, R. Strey, and H. Reiss. "Homogeneous nucleation rates for water". In: *The Journal of chemical physics* 99.6 (1993), pp. 4680–4692.

[112] J. Wölk and R. Strey. "Homogeneous nucleation of H2O and D2O in comparison: the isotope effect". In: *The Journal of Physical Chemistry B* 105.47 (2001), pp. 11683–11701.

[113] D. Brus, V. Zdimal, and H. Uchtmann. "Homogeneous nucleation rate measurements in supersaturated water vapor II". In: *The Journal of chemical physics* 131.7 (2009), p. 074507.

[114] R. J. Charlson and T. M. Wigley. "Sulfate aerosol and climatic change". In: *Scientific American* 270.2 (1994), pp. 48–57.

[115] M. Lazaridis, M. Kulmala, and A. Laaksonen. "Binary heterogeneous nucleation of a water-sulphuric acid system: The effect of hydrate interaction". In: *Journal of aerosol science* 22.7 (1991), pp. 823–830.

[116] N. H. Fletcher. "Size effect in heterogeneous nucleation". In: *The Journal of chemical physics* 29.3 (1958), pp. 572–576.

[117] H. Köhler. *Zur Kondensation des Wasserdampfes in der Atmosphäre.* I kommission hos Cammermeyers boghandel, 1921.

[118] G. McFiggans, P. Artaxo, U. Baltensperger, H. Coe, M. C. Facchini, G. Feingold, S. Fuzzi, M. Gysel, A. Laaksonen, U. Lohmann, et al. "The effect of physical and chemical aerosol properties on warm cloud droplet activation". In: *Atmospheric Chemistry and Physics* 6.9 (2006), pp. 2593–2649.

[119] J. Sun and P. A. Ariya. "Atmospheric organic and bio-aerosols as cloud condensation nuclei (CCN): A review". In: *Atmospheric Environment* 40.5 (2006), pp. 795–820.

[120] M. Andreae and D. Rosenfeld. "Aerosol–cloud–precipitation interactions. Part 1. The nature and sources of cloud-active aerosols". In: *Earth-Science Reviews* 89.1-2 (2008), pp. 13–41.

[121] S. N. Pandis, A. S. Wexler, and J. H. Seinfeld. "Secondary organic aerosol formation and transport—II. Predicting the ambient secondary organic aerosol size distribution". In: *Atmospheric Environment. Part A. General Topics* 27.15 (1993), pp. 2403–2416.

[122] S. Thorpe. "Bubble clouds and the dynamics of the upper ocean". In: *Quarterly Journal of the Royal Meteorological Society* 118.503 (1992), pp. 1–22.

[123] H. R. Pruppacher, J. D. Klett, and P. K. Wang. *Microphysics of clouds and precipitation.* 1998.

[124] L. Qi, Q. Li, C. He, X. Wang, and J. Huang. "Effects of the Wegener–Bergeron–Findeisen process on global black carbon distribution". In: *Atmospheric Chemistry and Physics* 17.12 (2017), pp. 7459–7479.

[125] T. Storelvmo, J. E. Kristjánsson, U. Lohmann, T. Iversen, A. Kirkevåg, and Ø. Seland. "Modeling of the Wegener–Bergeron–Findeisen process—Implications for aerosol indirect effects". In: *Environmental Research Letters* 3.4 (2008), p. 045001.

[126] A. Korolev and J. Milbrandt. "How are mixed-phase clouds mixed?" In: *Geophysical Research Letters* 49.18 (2022), e2022GL099578.

[127] A. V. Korolev, G. A. Isaac, S. G. Cober, J. W. Strapp, and J. Hallett. "Microphysical characterization of mixed-phase clouds". In: *Quarterly Journal of the Royal Meteorological Society* 129.587 (Jan. 2003), pp. 39–65.

[128] A. Tremblay, A. Glazer, W. Yu, and R. Benoit. "A mixed-phase cloud scheme based on a single prognostic equation". In: *Tellus A* 48.4 (1996), pp. 483–500.

[129] A. Wegener. *Thermodynamik der atmosphäre.* JA Barth, 1911.

[130] T. Bergeron. "On the physics of clouds and precipitation". In: *Proc. 5th Assembly UGGI, Lisbon, Portugal, 1935* (1935), pp. 156–180.

[131] Z. Findeisen. "Kolloid meteorologische vorgange bei neiderschlagsbildung". In: *Meteorologische Zeitschrift* 55 (1938), p. 121.

[132] A. Korolev. "Limitations of the Wegener–Bergeron–Findeisen Mechanism in the Evolution of Mixed-Phase Clouds". In: *Journal of the Atmospheric Sciences* 64.9 (Sept. 2007), pp. 3372–3375.

[133] J. Huang. "A Simple Accurate Formula for Calculating Saturation Vapor Pressure of Water and Ice". In: *Journal of Applied Meteorology and Climatology* 57.6 (June 2018), pp. 1265–1272.

[134] A. V. Korolev and I. P. Mazin. "Supersaturation of water vapor in clouds". In: *Journal of the atmospheric sciences* 60.24 (2003), pp. 2957–2974.

[135] P. Jonas. "Turbulence and cloud microphysics". In: *Atmospheric Research* 40.2–4 (May 1996), pp. 283–306.

[136] S. Moss and D. Johnson. "Aircraft measurements to validate and improve numerical model parametrisations of ice to water ratios in clouds". In: *Atmospheric research* 34.1-4 (1994), pp. 1–25.

[137] A. Korolev, G. McFarquhar, P. R. Field, C. Franklin, P. Lawson, Z. Wang, E. Williams, S. J. Abel, D. Axisa, S. Borrmann, J. Crosier, J. Fugal, M. Krämer, U. Lohmann, O. Schlenczek, M. Schnaiter, and M. Wendisch. "Mixed-Phase Clouds: Progress and Challenges". In: *Meteorological Monographs* 58 (Jan. 2017), pp. 5.1–5.50.

[138] R. A. Shaw. "Particle-turbulence interactions in atmospheric clouds". In: *Annual Review of Fluid Mechanics* 35.1 (2003), pp. 183–227.

[139] J. MacPherson and G. Isaac. "Turbulent characteristics of some Canadian cumulus clouds". In: *Journal of Applied Meteorology and Climatology* 16.1 (1977), pp. 81–90.

[140] O. Ayala, B. Rosa, and L.-P. Wang. "Effects of turbulence on the geometric collision rate of sedimenting droplets. Part 2. Theory and parameterization". In: *New Journal of Physics* 10.7 (July 2008), p. 075016.

[141] W. W. Grabowski and T. L. Clark. "Cloud-environment interface instability: Part II: Extension to three spatial dimensions". In: *Journal of the Atmospheric Sciences* 50.4 (1993), pp. 555–573.

[142] A. Seifert, C. Köhler, and K. Beheng. "Aerosol-cloud-precipitation effects over Germany as simulated by a convective-scale numerical weather prediction model". In: *Atmospheric Chemistry and Physics* 12.2 (2012), pp. 709–725.

[143] D. Rosenfeld, M. O. Andreae, A. Asmi, M. Chin, G. de Leeuw, D. P. Donovan, R. Kahn, S. Kinne, N. Kivekäs, M. Kulmala, et al. "Global observations of aerosol-cloud-precipitation-climate interactions". In: *Reviews of Geophysics* 52.4 (2014), pp. 750–808.

[144] P.-L. Ma, P. J. Rasch, M. Wang, H. Wang, S. J. Ghan, R. C. Easter, W. I. Gustafson Jr, X. Liu, Y. Zhang, and H.-Y. Ma. "How does increasing horizontal resolution in a global climate model improve the simulation of aerosol-cloud interactions?" In: *Geophysical Research Letters* 42.12 (2015), pp. 5058–5065.

[145] R. Srivastava. "Growth of cloud drops by condensation: A criticism of currently accepted theory and a new approach". In: *Journal of Atmospheric Sciences* 46.7 (1989), pp. 869–887.

[146] S. A. Orszag. "Spectral methods for problems in complex geometrics". In: *Numerical methods for partial differential equations*. Elsevier, 1979, pp. 273–305.

[147] P. Bartello, O. Métais, and M. Lesieur. "Coherent structures in rotating three-dimensional turbulence". In: *Journal of Fluid Mechanics* 273 (1994), pp. 1–29.

[148] N. P. Sullivan, S. Mahalingam, and R. M. Kerr. "Deterministic forcing of homogeneous, isotropic turbulence". In: *Physics of Fluids* 6.4 (1994), pp. 1612–1614.

[149] W. W. Grabowski and P. Vaillancourt. "Comments on "preferential concentration of cloud droplets by turbulence: effects on the early evolution of cumulus cloud droplet spectra"". In: *Journal of the atmospheric sciences* 56.10 (1999), pp. 1433–1436.

[150] A. S. Lanotte, A. Seminara, and F. Toschi. "Cloud droplet growth by condensation in homogeneous isotropic turbulence". In: *Journal of the Atmospheric Sciences* 66.6 (2009), pp. 1685–1697.

[151] N. L. Miles, J. Verlinde, and E. E. Clothiaux. "Cloud Droplet Size Distributions in Low-Level Stratiform Clouds". In: *Journal of the Atmospheric Sciences* 57.2 (Jan. 2000), pp. 295–311.

[152] NASA. *Sounding Rockets*. Accessed: 2023-10-03. 2022.

[153] NASA. *Sounding Rockets*. Accessed: 2023-10-09. 2023.

[154] European Space Agency. *ZARM's Drop Tower in Bremen*. Accessed: 2023-10-03. 2017.

[155] European Space Agency. *Drop Towers*. [Online; accessed 1-November-2023]. 2023.

[156] Air Zero G. *Prestations Science*. Accessed: 2023-10-03. 2022.

[157] Air Zero G. *Airbus A310 Zero-G*. Accessed: 2023-10-03.

[158] NASA. *International Space Station Reference*. Accessed: 2023-10-03. 2022.

[159] M. Schmitt, S. Limage, D. Grigoriev, J. Kragel, V. Dutschk, S. Vincent-Bonnieu, R. Miller, and M. Antoni. "Transition from spherical to irregular dispersed phase in water/oil emulsions". In: *Langmuir* 30.16 (2014), pp. 4599–4604.

[160] M. Schmitt, S. Limage, R. Denoyel, and M. Antoni. "Effect of SPAN80 on the structure of emulsified aqueous suspensions". In: *Colloids and Surfaces A: Physicochemical and Engineering Aspects* 521 (2017), pp. 121–132.

[161] T. T. D. Team. *TrackPy: A Python Package for Particle Tracking*. Accessed: 2023-10-01. 2023.

[162] J. C. Crocker and D. G. Grier. "Methods of digital video microscopy for colloidal studies". In: *Journal of colloid and interface science* 179.1 (1996), pp. 298–310.

[163] I. Ermolli, K. Matthes, T. D. de Wit, N. A. Krivova, K. Tourpali, M. Weber, Y. C. Unruh, L. Gray, U. Langematz, P. Pilewskie, E. Rozanov, W. Schmutz, A. Shapiro, S. K. Solanki, and T. N. Woods. "Recent variability of the solar spectral irradiance and its impact on climate modelling". In: *Atmospheric Chemistry and Physics* 13.8 (Apr. 2013), pp. 3945–3977.

[164] G. Rusu, M. Diciu, C. Pirghie, and E. Popa. "Structural characterization and optical properties of ZnSe thin films". In: *Applied Surface Science* 253.24 (Oct. 2007), pp. 9500–9505.

[165] G. Karniadakis, A. Beskok, and N. Aluru. *Microflows and nanoflows: fundamentals and simulation*. Vol. 29. Springer Science & Business Media, 2006.

[166] R. Ritu. "Experimental Investigations of Mass Transfer Kinetics in Liquid/liquid and Liquid/gas Systems". PhD thesis. 2019.

[167] SpectraBase. *Spectrum for CO_2, IR Spectrum - G4CBuKNSKtQ*. Accessed: 2024-10-18. 2024.

[168] Y. Díaz-de-Mera, A. Aranda, I. Bravo, E. Moreno, E. Martínez, and A. Rodríguez. "Atmospheric HFEs degradation in the gas phase: Reaction of HFE-7500 with Cl atoms at low temperatures". In: *Chemical Physics Letters* 479.1-3 (2009), pp. 20–24.

[169] B. N. Hale. "Application of a scaled homogeneous nucleation-rate formalism to experimental data at T much inferior to T c". In: *Physical Review A* 33.6 (1986), p. 4156.

[170] B. N. Hale. "The scaling of nucleation rates". en. In: *Metallurgical Transactions A* 23.7 (July 1992), pp. 1863–1868.